Symmetry-Breaking Degrees of Freedom in Molecular Perovskites



Hanna L. B. Boström

Exeter College

A Thesis submitted to the University of Oxford for the degree of

Doctor of Philosophy

Inorganic Chemistry Laboratory

University of Oxford

Trinity 2018

The work presented in this Thesis was carried out between October 2015 and June 2018 in the Inorganic Chemistry Laboratory under the supervision of Professor Andrew L. Goodwin. All the results are my own unless otherwise stated and have not been submitted previously for any degree at this or any other university.

Hanna Lilly Birgit Boström
August 2018

Symmetry-breaking degrees of freedom in molecular perovskites

Hanna L. B Boström, Exeter College

D.Phil., Trinity Term 2018

Perovskite oxides are functionally and structurally very diverse materials largely due to their abundance of symmetry-lowering degrees of freedom. A related and more nascent area of research is *molecular* perovskites: systems where at least one of the constituent ions is a polyatomic species. As a result of the topological congruence, molecular perovskites can often be understood in terms of the concepts developed for their inorganic congeners; yet the presence of polyatomic components imparts a higher level of flexibility. This Thesis addresses the structural chemistry of molecular perovskites with regards to the effects of introducing molecular moieties. A special emphasis is placed on the existence and ramifications of "unconventional degrees of freedom"—deformations unrealisable in conventional perovskites.

Three main themes are developed. First, the presence of polyatomic linking anions means that the BX_6 octahedra are no longer corner sharing. Consequently, translational rigid unit phonon modes emerge, where columns or planes of octahedra displace relative to each other. These vibrations are referred to as "columnar shifts" and often constitute soft modes. Hence, they are prone to condensation upon cooling and can drive displacive phase transitions—like tilts in conventional perovskites. Second, as molecular linkers enhance the separation of the neighbouring metal units, the energy scale for B-site correlation is reduced. This is apparent in the cooperative Jahn-Teller distortions in Cu-based systems, *e.g.* $[C(NH_2)_3]Cu(HCOO)_3$, $CuPt(CN)_6$ and $Cu_3[Co(CN)_6]_2$. Dilution of the Cu^{2+} cations by Mn^{2+} generates orbitally disordered states at seemingly lower dilution levels than in solid solutions of inorganic perovskites. Third, it is demonstrated how the unconventional degrees of freedom expand the library of symmetry-breaking distortions. A key result is that molecular perovskites exhibit a comparatively high propensity for the adoption of acentric space groups *via* hybrid improper mechanisms; an impossible occurrence in conventional perovskites in the absence of layered order.

Acknowledgements

First of all, I'm extremely grateful to my supervisor, Andrew Goodwin, for accepting me as a DPhil student and designing such a wonderful and blue project for me; yet allowing me to colour nitrogen atoms in orange. His constant patience, enthusiasm, empathy and ability to explain difficult concepts continue to amaze me. A better and kinder supervisor can only be found in the World of Ideas and, even so, the improvement would be negligible.

Moreover, I'm fortunate enough to have had Mark Senn as my "academic godfather". Few people have an equally contagious excitement for representation analysis and without him this Thesis would be devoid of irreps.

No DPhil can be carried out without funding and I'd like to acknowledge the University of Oxford for awarding me an Oxford Graduate Scholarship, and the generous donation from Neil Woodford and Craig Newman in support of this scholarship. On a related note, I owe thanks to Sharon for helping me to get here.

I'm incredibly lucky to have been surrounded by a truly amazing research group, and everyone deserves a special mention for being so nice and for putting up with me. Extra-special mentions go to my cyanide sister Chloe, for friendship and for always being willing to procrastinate with me; to Emily, for endless encouragement and energy and enthusiasm; to Josh, for looking after me so well in my first year and for keeping in touch since then; to Hamish, for being everything you want a research fellow to be; to Arkadiy, for coding and crystallography and the cuddly ESRF teddy bear; to Andrew C, for being so very supportive and friendly; to Harry, for helping me with complicated technology such as laptops and staplers; to my fellow Scandi Peter, for telling me about ABC; to Phil W, for inspiring bravery; and to Ali, for teaching me FORTRAN and for saying the right thing at the right time. And, of course, not to forget Nick, Will, Phil M, Trees, Carl, Sneha, Emma, and Xiao for their help and friendship. Chloe, Emily, Mark, Hamish, and Phil W thoroughly proofread everything I asked them to, which is greatly appreciated. I

also owe thanks to Nick, Mark, Emily, and Hamish for their kind help in the lab.

I'm grateful to Peter Battle and Nicola Spaldin for agreeing to act as my examiners and for their useful comments and questions. I'd also like to thank my supervisor and examiners, particularly Peter, for the very swift viva rearrangement and to shame the tick that caused the delay.

I've had plenty of help from a range of people with the research presented here and they are acknowledged in the relevant Chapters. Moreover, I wish to thank those who helped me more generally or with aspects of my work that didn't make it into the Thesis: Ines and Andrew C for the high-pressure experiment and for making it so fun, the staff at I11 for keeping the beamline up and running, Simon and Danny for the very patient help with the SQUID and I11, Simon and Jack for being such great conference companions, and Matt for sharing his PyMOL scripts. Finally, I also want to thank the support staff in receptions, college offices, finance, IT, HR, *etc.* for ensuring that the matters that so often are taken for granted run smoothly.

As for non-ICL friends, I wish to thank Ondřej for supreme wonderfulness and for taking me on adventures, Myriam (and Jess) for being the best housemate(s) I could have found, Daniel for friendly action at a distance, and also Adam, Andy, and Charlotte. I'm lucky to have been part of an MCR as friendly and social as Exeter's and would like to thank Tory, Luke, Parker amongst others. Thanks also go to OUWO for introducing me to crazy modern wind music and for making me practise those 7/8 bars.

Slutligen vill jag tacka släkt och vänner (både två- och fyrbenta) hemma i Sverige som har hållit kontakten med mig trots min långa utlandsvistelse och stått ut med mig när jag inte har kunnat prata om annat än om kemi och kristaller. Särskilt tack till Jonas för att du har matat mig med naturvetenskap sedan jag var liten.

Dear reader, who this page now face,

in-depth information

on polarisation,

perovskite relations,

some shift/tilt notation,

MC simulations,

mode hybridisation,

and RUM condensations,

you'll certainly find in this place.

Contents

1 Introduction **1**

1.1 Overview . . . 1

1.2 Conventional perovskites . . . 3

1.3 Degrees of freedom in conventional perovskites . . . 5

1.4 Molecular perovskites . . . 22

1.5 Degrees of freedoms in molecular perovskites . . . 49

1.6 Thesis outline . . . 56

2 Methods **58**

2.1 Structure determination . . . 58

2.2 Representation analysis . . . 76

2.3 Lattice dynamics . . . 82

2.4 Atomic absorption spectroscopy . . . 93

2.5 Monte Carlo techniques . . . 94

3 Columnar Shifts in Molecular Perovskites **97**

3.1 Chapter overview . . . 97

3.2 Rigid unit modes . . . 98

3.3 Dynamic shifts . . . 102

3.4 Static shifts . . . 106

3.5 Case studies . . . 112

3.6 Shift trends . . . 118

3.7 Implications . . . 123

4 Cooperative Jahn-Teller Effects in Molecular Perovskites **126**

4.1 Chapter overview . . . 126

4.2 Background . . . 127
4.3 Methods . . . 135
4.4 Primitive cubic systems . . . 141
4.5 Face-centred cubic systems . . . 149
4.6 Comparative discussion . . . 161
4.7 Implications . . . 165

5 Hybrid Improper Ferroelectricity in Molecular Perovskites 169
5.1 Chapter overview . . . 169
5.2 Background . . . 170
5.3 Methods . . . 176
5.4 Results . . . 181
5.5 Propolar perovskites . . . 185
5.6 Implications . . . 188

6 Outlook 191

Bibliography 197

Appendix A: Dynamical Matrices 228
A1 Conventional perovskites . . . 229
A2 Molecular perovskites . . . 232

Appendix B: Alternative Monte Carlo Simulations 236
B1 Finite size effects . . . 236
B2 Alternative vacancy distributions . . . 236

Appendix C: Supplementary Crystallographic Results 240
C1 $[C(NH_2)_3]Mn_{1-x}Cu_x(HCOO)_3$ . . . 240
C2 $B_{1-x}Cu_x[Pt(CN)_6]$ . . . 240
C3 $(B_{1-x}Cu_x)_3[B'(CN)_6]_2$ . . . 273

Appendix D: Hidden Vacancy Order in Prussian Blue Analogues 291

Appendix E: Supplementary Group-Theoretical Results 315

Publications

N. L. Evans, P. M. M. Thygesen, **H. L. B. Boström**, E. M. Reynolds, I. E. Collings, A. E. Phillips, and A. L. Goodwin, Control of multipolar and orbital order in perovskite-like $[C(NH_2)_3]Cu_xCd_{1-x}(HCOO)_3$ metal–organic frameworks, *J. Am. Chem. Soc.*, 2016, **138**, 9393–9396.

H. L. B. Boström, J. A. Hill, and A. L. Goodwin, Columnar shifts as symmetry–breaking degrees of freedom in molecular perovskites, *Phys. Chem. Chem. Phys.*, 2016, **18**, 31881–31894.

E. A. Donlan, **H. L. B. Boström**, H. S. Geddes, E. M. Reynolds, and A. L. Goodwin, Compositional nanodomain formation in hybrid formate perovskites, *Chem. Commun.*, 2017, **53**, 11233–11236.

A. Sapnik, X. Liu, **H. L. B. Boström**, C. S. Coates, A. R. Overy, E. M. Reynolds, A. Tkatchenko, and A. L. Goodwin, Uniaxial negative thermal expansion and metallophilicity in $Cu_3[Co(CN)_6]$, *J. Solid State Chem.*, 2018, **258**, 298–306.

H. L. B. Boström, M. S. Senn, and A. L. Goodwin, Recipes for improper ferroelectricity in molecular perovskites, *Nat. Commun.*, 2018, **9**, 2380.

H. L. B. Boström, I. E. Collings, A. B Cairns, C. P. Romao, and A. L. Goodwin, High-pressure behaviour of Prussian blue analogues: interplay of hydration, Jahn-Teller distortions and vacancies, *Dalton Trans.*, 2019, **48**, 1647–1655.

C. S. Coates, H. J. Gray, J. M. Bulled, **H. L. B. Boström**, A. Simonov, and A. L. Goodwin, Ferroic multipolar order and disorder in cyanoelpasolite molecular perovskites, *Philos. Trans. R. Soc., A*, in press.

List of Figures

1.1 The degrees of freedom of a perovskite . . . 3
1.2 Common compositional ordering patterns . . . 7
1.3 Crystal field splitting . . . 10
1.4 The Q_2 and Q_3 Jahn-Teller distortions . . . 12
1.5 Second-order Jahn-Teller distortions . . . 16
1.6 Glazer notation . . . 18
1.7 Multiferroicity . . . 21
1.8 Molecular perovskite analogues . . . 22
1.9 Antiferroquadrupolar cation order in $(CH_3NH_3)PbI_3$ . . . 27
1.10 Charge compensation in Prussian blue analogues . . . 30
1.11 Exotic structures based on Prussian blue analogues . . . 32
1.12 Common A-site cations . . . 35
1.13 Binding modes of the formate anion . . . 36
1.14 Magnetoelectric coupling in $[(CH_3)_2NH_2]Mn(HCOO)_3$ . . . 38
1.15 Mixed X-site formate hypophosphite perovskites . . . 41
1.16 Pressure dependence of the phase transitions in $[Pr_4N]B[N(CN)_2]_3$ . . . 45
1.17 Phase transitions in dicyanometallate perovskites . . . 46
1.18 Supramolecular molecular perovskites . . . 48
1.19 Tilting modes in molecular perovskites . . . 53
1.20 Matrix notation for unconventional tilts . . . 54

2.1 Crystal structure as a convolution of lattice and motif . . . 59
2.2 Scattering from a pair of particles . . . 61
2.3 The first Brillouin zone for two cubic lattices . . . 65
2.4 Powder diffraction *vs.* single-crystal diffraction . . . 69
2.5 A synchrotron light source . . . 73

2.6 Correlated disorder in square ice 76
2.7 Group-theoretical classes and irreducible representations 78
2.8 Irreps in periodic structures 80
2.9 Propagation of phonons in extended solids 83
2.10 Phonon dispersion curves for monoatomic crystals in 1D and 3D . . 85
2.11 The phonon dispersion curve for NaCl 86
2.12 The tension and RUM models 91

3.1 Periodicities of columnar shifts 102
3.2 Phonon dispersion curves of molecular perovskites 104
3.3 Shifts in 2D 107
3.4 Crystallographic aspects of certain shift patterns 108
3.5 Literature examples of shifted compounds 114
3.6 Complex shift patterns 118
3.7 Binding angles of azide and cyanide 120
3.8 The templating effect of the A-site cation for shifts 122

4.1 Phase diagram of $La_{1-x}Ca_xMnO_3$ 129
4.2 Symmetry relationships in $[C(NH_2)_3]Cd_{1-x}Cu_x(HCOO)_3$ 133
4.3 The endmembers of the mixed-metal series 134
4.4 Mixed-metal molecular perovskites 136
4.5 The order parameter space of Jahn-Teller distortions 138
4.6 Experimental data for $[C(NH_2)_3]Mn_{1-x}Cu_x(HCOO)_3$ 142
4.7 Intensity of the 210 reflection as a function of x 145
4.8 Monte Carlo results for primitive cubic systems 147
4.9 Nanoregions in mixed-metal formate perovskites 150
4.10 Experimental data for $Mn_{1-x}Cu_x[Pt(CN)_6]$ 152
4.11 Experimental data for $(Mn_{1-x}Cu_x)_3[Co(CN)_6]_2$ 155
4.12 The influence of synthesis conditions on the phase behaviour 157
4.13 Monte Carlo results for face-centred cubic systems 158
4.14 Semaphore diagrams 162
4.15 Summary of orbital order–disorder in molecular perovskites 166

5.1 Hybrid improper ferroelectricity in $[C(NH_2)_3]Cu(HCOO)_3$ 171

5.2 Landau energy expansions for proper and improper ferroelectrics . . 173
5.3 Spherical harmonics 178
5.4 Coupling schemes of distortion modes 182
5.5 Inversion symmetry breaking in 2D molecular perovskites 184

6.1 Mineralomimetic structures 192
6.2 Chiral density wave in $[NEt_4]Ag_3(CN)_4$ 195
A1.1 Lattice-dynamical model for a 2D perovskite 230
A2.2 Vectorisation of a molecular perovskite 233
B1.1 Finite size effects 237
B2.2 Effect of different vacancy arrangements on the orbital order 238
C2.1 Constrained Rietveld fits for $Mn_{1-x}Cu_x[Pt(CN)_6]$ at ambient conditions 242
C2.2 Pawley fits for $Mn_{1-x}Cu_x[Pt(CN)_6]$ at 100 K 243
C2.3 Constrained Rietveld fits for $Mn_{1-x}Cu_x[Pt(CN)_6]$ at 100 K 244
C2.4 Pawley fits for $Mn_{1-x}Cu_x[Pt(CN)_6]$ at 500 K 245
C2.5 Constrained Rietveld fits for $Mn_{1-x}Cu_x[Pt(CN)_6]$ at 500 K 246
C2.6 Pawley fits for $Fe_{1-x}Cu_x[Pt(CN)_6]$ at ambient conditions 249
C2.7 Constrained Rietveld fits for $Fe_{1-x}Cu_x[Pt(CN)_6]$ at ambient conditions 250
C2.8 Pawley fits for $Fe_{1-x}Cu_x[Pt(CN)_6]$ at 100 K 251
C2.9 Constrained Rietveld fits for $Fe_{1-x}Cu_x[Pt(CN)_6]$ at 100 K 252
C2.10 Pawley fits for $Fe_{1-x}Cu_x[Pt(CN)_6]$ at 500 K 253
C2.11 Constrained Rietveld fits for $Fe_{1-x}Cu_x[Pt(CN)_6]$ at 500 K 254
C2.12 Pawley fits for $Zn_{1-x}Cu_x[Pt(CN)_6]$ at ambient conditions 257
C2.13 Constrained Rietveld fits for $Zn_{1-x}Cu_x[Pt(CN)_6]$ at ambient conditions 258
C2.14 Pawley fits for $Zn_{1-x}Cu_x[Pt(CN)_6]$ at 100 K 259
C2.15 Constrained Rietveld fits for $Zn_{1-x}Cu_x[Pt(CN)_6]$ at 100 K 260
C2.16 Pawley fits for $Zn_{1-x}Cu_x[Pt(CN)_6]$ at 500 K 261
C2.17 Constrained Rietveld fits for $Zn_{1-x}Cu_x[Pt(CN)_6]$ at 500 K 262
C2.18 Pawley fits for $Cd_{1-x}Cu_x[Pt(CN)_6]$ at ambient conditions 264

C2.19 Constrained Rietveld fits for $Cd_{1-x}Cu_x[Pt(CN)_6]$ at ambient conditions . . . 265
C2.20 Pawley fits for $Cd_{1-x}Cu_x[Pt(CN)_6]$ at 100 K . . . 267
C2.21 Constrained Rietveld fits for $Cd_{1-x}Cu_x[Pt(CN)_6]$ at 100 K . . . 268
C2.22 Pawley fits for $Cd_{1-x}Cu_x[Pt(CN)_6]$ at 500 K . . . 270
C2.23 Constrained Rietveld fits for $Cd_{1-x}Cu_x[Pt(CN)_6]$ at 500 K . . . 271
C3.24 Constrained Rietveld fits for $(Mn_{1-x}Cu_x)_3[Co(CN)_6]_2$ at ambient conditions . . . 275
C3.25 Pawley fits for $(Mn_{1-x}Cu_x)_3[Co(CN)_6]_2$ at 100 K . . . 276
C3.26 Constrained Rietveld fits for $(Mn_{1-x}Cu_x)_3[Co(CN)_6]_2$ at 100 K . . . 277
C3.27 Pawley fits for $(Mn_{1-x}Cu_x)_3[Co(CN)_6]_2$ at 500 K . . . 278
C3.28 Constrained Rietveld fits for $(Mn_{1-x}Cu_x)_3[Co(CN)_6]_2$ at 500 K . . . 279
C3.29 Experimental data for $(Mn_{1-x}Cu_x)_3[Fe(CN)_6]_2$. . . . 281
C3.30 Constrained Rietveld fits for $(Mn_{1-x}Cu_x)_3[Fe(CN)_6]_2$ at ambient conditions . . . 283
C3.31 Pawley fits for $(Mn_{1-x}Cu_x)_3[Fe(CN)_6]_2$ at 100 K . . . 284
C3.32 Pawley fits for $(Mn_{1-x}Cu_x)_3[Fe(CN)_6]_2$ at 500 K . . . 285
C3.33 Experimental data for $(Cd_{1-x}Cu_x)_3[Co(CN)_6]_2$ . . . 287
C3.34 Pawley fits for $(Cd_{1-x}Cu_x)_3[Co(CN)_6]_2$ at 100 K. . . . 288
C3.35 Pawley fits for $(Cd_{1-x}Cu_x)_3[Co(CN)_6]_2$ at 500 K. . . . 290
E0.1 Visual representation of key irreps for molecular perovskites . . . 317

List of Tables

2.1 The seven crystal systems 60

3.1 Parameter values used for the lattice-dynamical model 103
3.2 The symmetry aspects of the 2D shift systems 110

5.1 Degrees of freedom in molecular perovskites and their irreps 180
5.2 The coupling schemes of known acentric molecular perovskites . . . 183

C1.1 Crystallographic data for $[C(NH_2)_3]Mn_{1-x}Cu_x(HCOO)_3$ at ambient conditions 240
C2.2 Crystallographic data for $Mn_{1-x}Cu_x[Pt(CN)_6]$ at ambient conditions 241
C2.3 Crystallographic data for $Mn_{1-x}Cu_x[Pt(CN)_6]$ at 100 K 241
C2.4 Crystallographic data for $Mn_{1-x}Cu_x[Pt(CN)_6]$ at 500 K 241
C2.5 Crystallographic data for $Fe_{1-x}Cu_x[Pt(CN)_6]$ at ambient conditions 248
C2.6 Crystallographic data for $Fe_{1-x}Cu_x[Pt(CN)_6]$ at 100 K 248
C2.7 Crystallographic data for $Fe_{1-x}Cu_x[Pt(CN)_6]$ at 500 K 248
C2.8 Crystallographic data for $Zn_{1-x}Cu_x[Pt(CN)_6]$ at ambient conditions 256
C2.9 Crystallographic data for $Zn_{1-x}Cu_x[Pt(CN)_6]$ at 100 K 256
C2.10 Crystallographic data for $Zn_{1-x}Cu_x[Pt(CN)_6]$ at 500 K 256
C2.11 Crystallographic data for $Cd_{1-x}Cu_x[Pt(CN)_6]$ at ambient conditions 266
C2.12 Crystallographic data for $Cd_{1-x}Cu_x[Pt(CN)_6]$ at 100 K 269
C2.13 Crystallographic data for $Cd_{1-x}Cu_x[Pt(CN)_6]$ at 500 K 272
C3.14 Crystallographic data for $(Mn_{1-x}Cu_x)_3[Co(CN)_6]_2$ at ambient conditions 274
C3.15 Crystallographic data for $(Mn_{1-x}Cu_x)_3[Co(CN)_6]_2$ at 100 K 274
C3.16 Crystallographic data for $(Mn_{1-x}Cu_x)_3[Co(CN)_6]_2$ at 500 K 274

C3.17 Crystallographic data for $(Mn_{1-x}Cu_x)_3[Fe(CN)_6]_2$ at ambient conditions 281
C3.18 Crystallographic data for $(Mn_{1-x}Cu_x)_3[Fe(CN)_6]_2$ at 100 K 282
C3.19 Crystallographic data for $(Mn_{1-x}Cu_x)_3[Fe(CN)_6]_2$ at 500 K 282
C3.20 Crystallographic data for $(Cd_{1-x}Cu_x)_3[Co(CN)_6]_2$ ambient conditions 287
C3.21 Crystallographic data for $(Cd_{1-x}Cu_x)_3[Co(CN)_6]_2$ at 100 K 289
C3.22 Crystallographic data for $(Cd_{1-x}Cu_x)_3[Co(CN)_6]_2$ at 500 K 289
E0.1 The conversion of irreps upon an origin change 316
E0.2 Third-order couplings with polarisation (Γ_4^-) 317
E0.3 Fourth-order couplings with polarisation (Γ_4^-) 318

Abbreviations

,

1D	one dimension(al)
2θ	scattering angle (diffraction)
2D	two dimension(al)
3D	three dimension(al)
AAS	atomic absorption spectroscopy
Bn	benzyl, C_6H_5
Bu	butyl, C_4H_9
BZ	Brillouin zone
CFSE	crystal field stabilisation energy
CP	coordination polymer
DAB	dabconium cation
DFT	density functional theory
DSC	differential scanning calorimetry
EPR	electron paramagnetic spectroscopy
FCC	face-centred cubic
FOJT	first-order Jahn-Teller
GULP	general utility lattice program
HIF	hybrid improper ferroelectricity
HIm	imidazolium cation
Im	imidazolate anion
INS	inelastic neutron scattering
irrep	irreducible representation
IUPAC	International Union of Pure and Applied Chemistry

JT	Jahn-Teller
LFSE	ligand field stabilisation energy
MA	methylammonium cation
MC	Monte Carlo
MOF	metal–organic framework
NLC	negative linear compressibility
NMF	non-negative matrix factorisation
NMR	nuclear magnetic resonance
NTE	negative thermal expansion
OPD	order parameter direction
PB	Prussian blue
PBA	Prussian blue analogue
PDF	pair distribution function
Ph	phenyl, C_6H_5
PPN	bis(trisphenylphosphine)iminium cation
Pr	propyl, C_3H_7
PTE	positive thermal expansion
PXRD	powder X-ray diffraction
RUM	rigid unit mode
SHG	second harmonic generation
SOJT	second-order Jahn-Teller
Trz	triazolium cation
XAS	X-ray absorption spectroscopy
XRD	X-ray diffraction
ZIF	zeolitic imidazolate framework

Chapter 1

Introduction

1.1 Overview

One of the ultimate aims of material science is the ability to rationally design and tune functionality. This objective underpins the immense interest in developing structure–property relationships: if the structural dependence of the desired property is known, functional control can hopefully be obtained by judicious manipulation of the crystal symmetry: so-called crystal engineering.[1–4] Albeit a straightforward concept in theory, the realisation of such an approach in practice is frequently associated with profound challenges, as detailed structure–property relationships may be elusive and precise structural design is often difficult.

In many cases, the symmetry of a given solid-state compound is derived from a high-symmetry parent structure (aristotype). The addition of symmetry-lowering distortions to the aristotype gives access to a range of hettotypes (daughter structures) with space groups corresponding to subgroups of the aristotype space group. By way of illustration, numerous minerals—including perovskite, cristobalite and quartz—exhibit thermally induced polyhedral rotations that can drive phase transitions into states with reduced symmetry.[5] For these materials, rational design of functionality requires (i) a knowledge of the accessible distortions and their effect on the symmetry, (ii) means by which to exert control over distortions, and (iii)

symmetry–property relationships. In general, the first criterion is greatly simplified by the use of group-theoretical methods, whereas the latter two points can entail prominent challenges. Nevertheless, such approaches are sometimes feasible, particularly in cases when the symmetry dictates the potential functionality. This link is especially prominent for ferroelectricity—the presence of a field-switchable electronic polarisation—where a polar space group is required. A notable example is the targeted development of a novel multiferroic perovskite derivative through the analysis and activation of appropriate octahedral rotations in order to lift the global inversion symmetry.[6]

Consequently, a sound understanding of the distortions—more generally referred to as degrees of freedom—accessible to a given aristotype is vital for research into new functional materials. Degrees of freedom are also of interest from a fundamental viewpoint and frequently shed light on *e.g.* dynamic behaviour such as thermal expansion.[5,7] This Thesis investigates some unexplored degrees of freedom that occur in molecular perovskites, with a view towards the eventual exploitation of these distortions in rational materials design. Although it is becoming increasingly clear that interesting and novel degrees of freedom can emerge in molecular perovskites, this is still relatively poorly understood. Throughout, the results are placed in the context of the research carried out on the well-known conventional perovskites with a particular focus on degrees of freedom unfeasible in ceramic materials. For this reason, this introductory Chapter commences by an overview of perovskite oxides, followed by the corresponding discussion of the molecular counterparts. Lastly, a more detailed overview of the aims and structure of the Thesis is given.

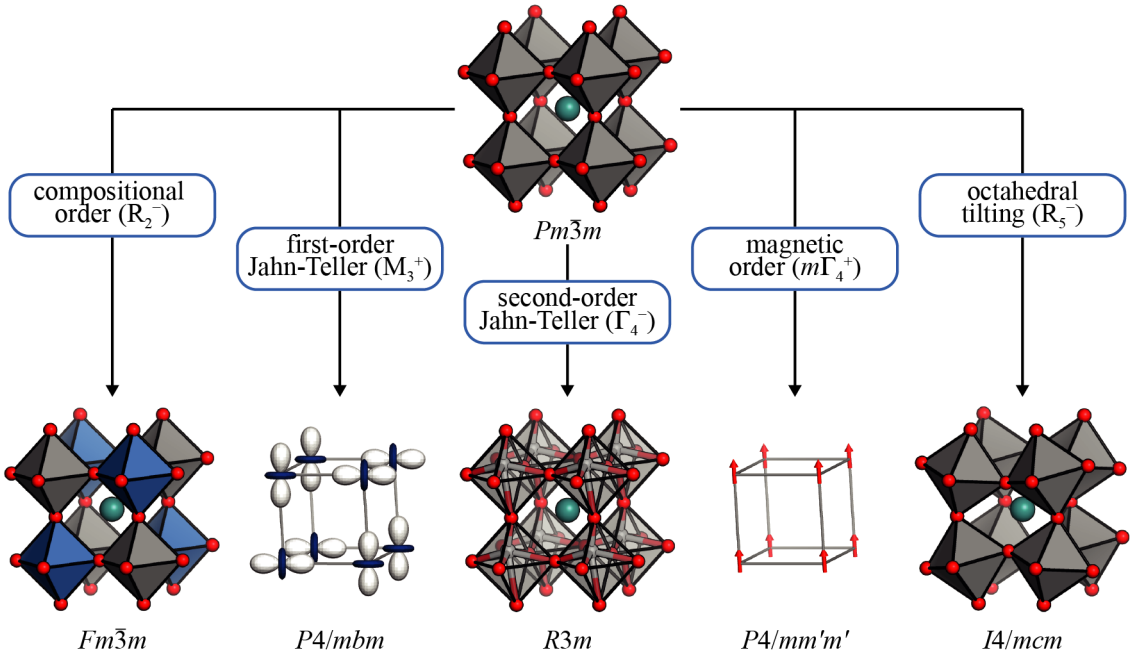


Figure 1.1: The aristotype perovskite in $Pm\bar{3}m$ along with representative examples of the degrees of freedom and the resulting hettotypes. The space group and irreducible representation (irrep) are provided for each symmetry-lowering distortion.

1.2 Conventional perovskites

The perovskite structure type derives its name from the mineral perovskite, $CaTiO_3$, which in turn was named after the Russian count Lev Perovski in the 19th century.[8] It is arguably the most prevalent and important topology adopted by inorganic compounds with ABX_3 stoichiometry, where A and B are cations and X is an anion.[8] The structure is appealingly simple and consists of a three-dimensional network of corner-sharing BX_6 octahedra and the A-site cation residing in the centre of the resulting cavity [Fig. 1.1]. In the aristotype phase, the space group is $Pm\bar{3}m$ and all ions are located at special positions.

The relative stability of the perovskite structure type is stipulated by the ratio of the sizes of the three ions. As the X-site usually is decorated by oxide anions, the

relative sizes of the cations tend to be the variable factor. By using a hard-sphere approach, the German chemist Goldschmidt quantified the stability range in terms of the tolerance factor now named after him:[9]

$$\alpha = \frac{r_{\mathrm{A}} + r_{\mathrm{X}}}{\sqrt{2}(r_{\mathrm{B}} + r_{\mathrm{X}})}, \tag{1.1}$$

where r_i is the ionic radius of site i. Empirically, the perovskite structure is found to be stable for $0.8 < \alpha < 1.0$ and deviations from this range lead to the preferential adoption of alternative topologies, such as ilmenite ($FeTiO_3$).[10] This stability window is remarkably large and allows for the incorporation of nearly every metal in the periodic table, thus explaining the compositional diversity of perovskites.[11]

Here, it is pertinent to mention the connection between the tolerance factor and crystal structure deformations, although these distortions are treated more fully in Sections 1.3.3–1.3.4. In the ideal case of $\alpha = 1$, the bonding environments of both the A- and B-site cations are optimal, favouring formation of the cubic aristotype structure. However, this situation is rarely realised.[12] The tolerance factor is frequently less than unity, leading to octahedral rotations in order to improve the bonding environment of the A-site cation. Indeed, these tilting distortions occur in the mineral perovskite itself.[13] Conversely, in systems with $\alpha > 1$—of which $BaTiO_3$ is a canonical example—the B-site cation is underbonded and consequently displaces from the centre of the octahedron.[14] These examples illustrate the crucial role of the tolerance factor in understanding both the existence and symmetry of conventional perovskites.

Additionally, there are many topological variations of perovskites, often resulting from an ordered intergrowth of another phase. A common variant of relevance is the Ruddlesden-Popper (RP) structure, described by the general formula $A_{n+1}B_nX_{n+1}$.[15] It consists of n perovskite layers interspersed by single rocksalt layers, such that the octahedral units are no longer stacked directly on top of each other and the percolating network of corner-sharing octahedra is broken. The layered nature of Ruddlesden-Popper phases lowers the aristotype space group to tetragonal $I4/mmm$ and the implications of the reduced symmetry will be discussed further in Chapter 5.

1.3 Degrees of freedom in conventional perovskites

As alluded to above, perovskites support a manifold of symmetry-lowering structural distortions [Fig. 1.1] and hence encompass a vast range of possible hettotypes. In conjunction with the considerable scope for compositional variation, these distortions engender a very diverse functionality, including ferroelectricity,[16,17] superconductivity,[18,19] and colossal magnetoresistance.[20,21] This Section reviews the degrees of freedom inherent to perovskite oxides, with the aim of providing the necessary background rather than giving a complete and balanced overview of the field. Certain degrees of freedom have little bearing on the results presented in this Thesis and are only briefly introduced, whereas others—particularly Jahn-Teller distortions—are highly relevant and so explained in more detail.

1.3.1 Compositional and charge order

Perovskites often contain a mixture of distinct ions at one or more of the sites—so-called complex perovskites[22]—which further expands the playground for the development and optimisation of desirable properties. Frequently, solid solutions between two endmembers can form, for example $La_{1-x}Ca_xMnO_3$[23] and $Y_{1-x}La_xVO_3$,[24] where the aliovalent doping of the former is compensated by mixed valence of manganese. Solid solutions allow for tuneable properties, as illustrated by the continuously variable coefficient of thermal expansion of $Bi_{1-x}Ln_xNiO_3$,[25] or the range of colours displayed by $Ca_{1-x}La_xTiO_2N$.[26] Alternatively, the behaviour of solid solutions can be more dramatic than that of any endmember, such as the strong enhancement of the piezoelectric response at the morphotropic phase boundary in $PbZr_{1-x}Ti_xO_3$ (PZT).[27,28] As a result, the synthesis and understanding of solid solutions is an area of intense research effort within the perovskite community.

When several ions occupy the same site (whether A, B, or X), ordered or disordered arrangements may occur and the former is manifested as a change in the symmetry. For double perovskites, $AA'B_2X_6$ or $A_2BB'X_6$, cation order is generally favoured when there is a substantial difference in ionic radii and/or charge between the two constituent ions. The possible ordered arrangements are rocksalt (R-point), layered (X-point) and columnar (M-point) order [Fig. 1.2].[29] The letters R, X and M denote the periodicity of the particular type of ordering and are introduced formally in Section 2.1.2. Naturally—and as is true more generally—order and randomness simply constitute the opposite abscissa on a spectrum and partial cation order is also feasible.[30,31] The extent of order often affects the properties of a complex perovskite

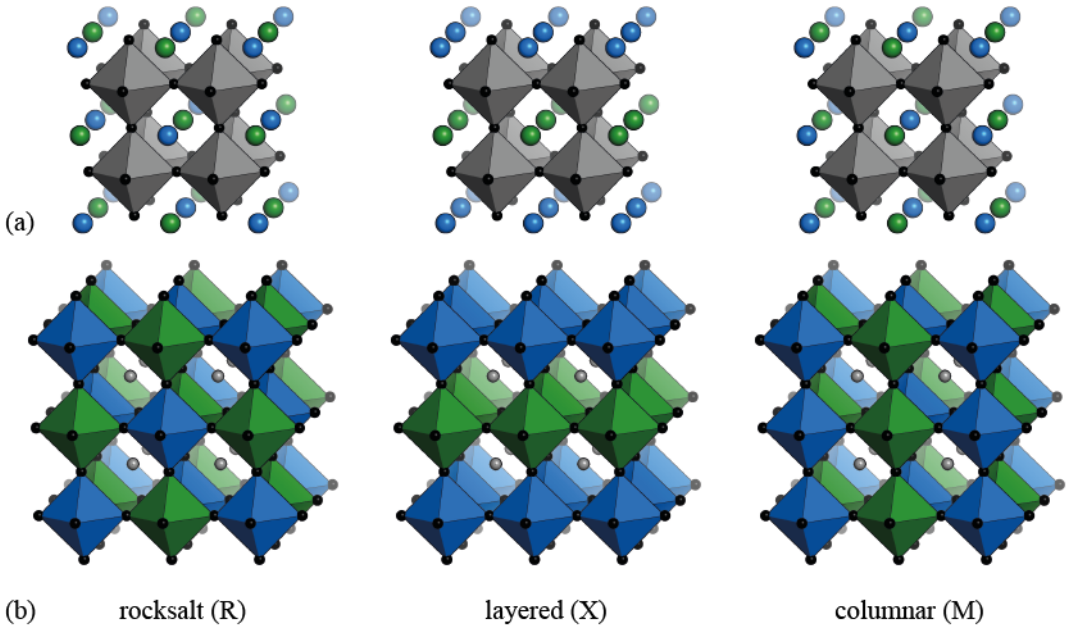


Figure 1.2: The three types of cation order, illustrated for (a) A-site cations and (b) B-site cations. The relevant point in reciprocal space for each of the ordering patterns is shown in brackets.

and can be an important design element, especially as it may sometimes be subject to synthetic control.[32]

The preference for a particular ordered arrangement varies between the three ion sites. Random distribution of A-site cations is very common and if any order occurs, it is nearly always layered.[33] The symmetry induced by A-site layering allows for an oxide displacement to optimise the bonding environment of the distinct A-site cations, explaining the predominance of layered A-site order.[34] Conversely, rocksalt arrangements are favoured at the B-site, which changes the aristotype to the face-centred cubic $Fm\bar{3}m$ structure.[34,35] This cation pattern maximises the separation of the two B-site cations; a crucial consideration as these species tend to be highly charged. Double–double perovskites with coexisting order on both cation sites also exist, but are relatively scarce.[36] The scope for substitution on the X-site is smaller, but compounds of formula ABO_2X (where $X = N^{3-}$ or F^-) are known and the anion

order in such systems is less straightforward.[37,38] The X^- anions normally appear in a *cis*-arrangement around the octahedra, often leading to planes of correlated anion disorder within the structure.[39,40]

Cation order is intimately related to the presence of charge order. In a charge order transition, itinerant (delocalised) electrons become localised at specific ions and render previously equivalent metal sites crystallographically independent.[41] It is seen mainly in compounds with semi-valent ions, such as doped manganites or cobaltates, or systems containing ions prone to charge disproportionation.[42–47] As for cation order, a range of various ordered states are known, including layered and rocksalt order as well as more complicated patterns.[48–51] Unambiguous determination of charge-ordered states is often nontrivial and may, for some systems, be further complicated by charge-order polymorphism.[41] In addition, electrons can delocalise over a small number of ions to form a polaron, as exemplified by the e_g electron in $LaMnO_3$.[52] Despite its complexity, charge order is of interest, as it is implicated in electronic conductivity as well as electronic and magnetic functionality.[53–55]

Another means of compositional variation is the introduction of vacancies on the A- or X-sites.[56,57] From a materials design perspective, oxygen non-stoichiometry is particularly appealing as it directly affects the performance of oxide ion conductors and (electronic) superconductors.[56,58–60] Furthermore, it depends strongly on the atmosphere during synthesis, which allows control over defect incorporation.[58] Oxygen defects are often disordered at high temperature, but ordering can occur upon cooling.[61] For sufficiently high defect concentrations, the ordering may lead to the adoption of another structure type, *e.g.* brownmillerite ($A_2B_2X_5$).[61,62]

1.3.2 First-order Jahn-Teller distortions

In 1937, Jahn and Teller used group-theoretical arguments to demonstrate the structural instability of nonlinear molecules in electronically degenerate states.[63] These compounds undergo a symmetry-lowering distortion in order to lift the degeneracy. Now known as the Jahn-Teller (JT) theorem, this result applies to a multitude of systems, although the most familiar example—and the one of importance to this Thesis—concerns unequal occupancy of *d*-orbitals in octahedral transition metal complexes.[64,65] The term first-order Jahn-Teller (FOJT) distortion is also sometimes used, to differentiate from the second-order Jahn-Teller distortions discussed below.

Before elaborating on the JT theorem, it is necessary to outline the basics of crystal and ligand field theory. In the absence of external perturbations, orbitals with a given value of orbital angular quantum number, l, are degenerate for a free ion [Fig. 1.3(a)–(b)]. The degeneracy is removed by the application of a nonspherical electrostatic field, as explained by crystal field theory (CFT).[66] In the case of a transition metal ion in an octahedral crystal field, the *d*-orbitals split into two levels separated by an energy difference Δ_o [Fig. 1.3(c)]. The two energy levels are labelled t_{2g} and e_g, in accordance with the irreducible representation they form a basis for in the octahedral point group [Section 2.2]. Population of the t_{2g} set of orbitals leads to a net stabilisation relative to the spherical field case, quantified by the crystal field stabilisation energy (CFSE) and usually written in terms of fractions of Δ_o. The simplicity of crystal field theory does not allow for an accurate measure of Δ_o; however, the closely related ligand field theory—an extension of CFT with the

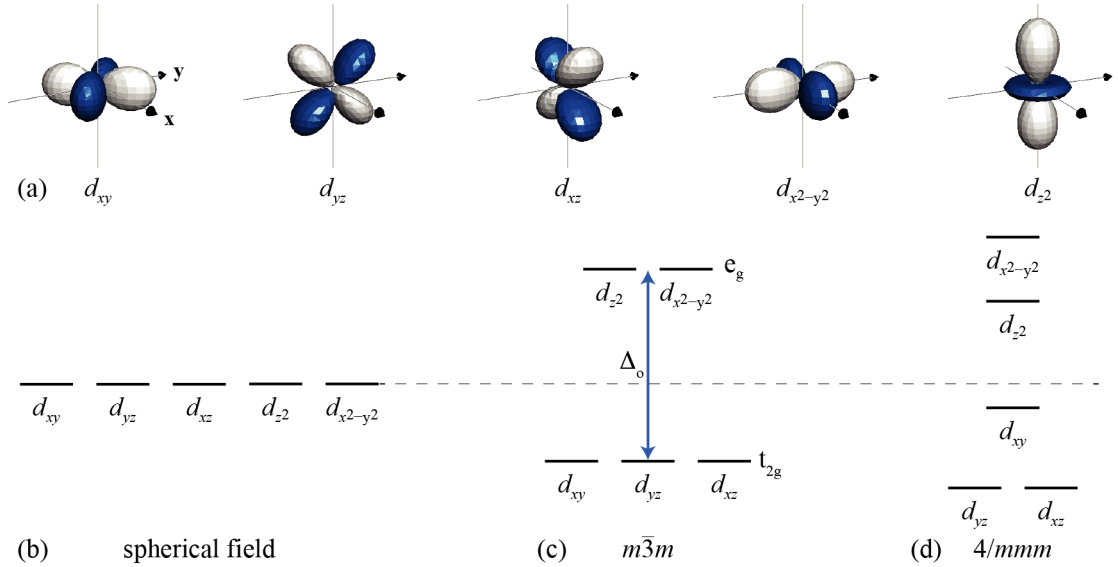


Figure 1.3: (a) The shape of the five d-orbitals in an octahedral field. They are degenerate for (b) a spherical crystal field, whereas in (c) an octahedral crystal field, the orbitals split into two levels. In order to remove electronic degeneracy associated with unequal occupancy of the e_g level, a (d) FOJT distortion occurs, leading to further splitting. Here, the tetragonal Q_3 distortion is shown.

allowance for covalent bonding—enables calculation of Δ_o and *ligand* field stabilisation energies (LFSE) from experimental data. The magnitude of Δ_o is a function of the radial extent of the orbitals at the central metal, the metal oxidation state, and the nature of the ligand, where the latter is expressed by the spectrochemical series.[65] Ligands able to act as π-acceptors (*e.g.* CO and CN^-) enforce very large splittings and reside at the high-field end of the spectrum, whereas π-donors (*e.g.* Cl^- and Br^-) are usually weak-field ligands. For electronic configurations of d^4–d^7, strong crystal fields favour double occupation of the t_{2g} set prior to occupying e_g orbitals, known as low spin (LS), whereas for weak crystal fields, Δ_o is lower than the electron pairing energy and so the electrons are arranged according to Hund's rule.[67] The latter scenario maximises the number of unpaired electrons and is labelled high spin (HS).

Electronic configurations with odd numbers of e_g electrons, such as d^9 and HS d^4,

are electronically degenerate and thereby susceptible to a first-order Jahn-Teller distortion [Fig. 1.3(d)]. Electronic degeneracy within the t_{2g} level can also occur,[68,69] although the ensuing distortion is often smaller than for the e_g level and is not discussed here.[70] In the simple approximation, FOJT distortions can assume two different forms, denoted Q_2 and Q_3 [Fig. 1.4(a)].[71,72] The former manifests as an elongation along the x-axis and compression along the y-axis, whereas the latter corresponds to an octahedral elongation along the z-axis and compression within the perpendicular plane. Put another way, Q_2 is described by orthorhombic strain and Q_3 by tetragonal strain of the aristotype octahedron. The tetragonal elongation is more prevalent as it arises from occupation of the d_{z^2} orbital, which is symmetry equivalent to the $4s$-orbital in the $4/mmm$ (D_{4h}) point group. This allows for an additional stabilisation by mixing of the two orbitals into a low-lying hybrid orbital.[70,73] Yet, the Q_2 distortion is occasionally realised, as in the canonical orbitally ordered perovskite $LaMnO_3$.[74,75]

As Q_2 and Q_3 constitute the two basis functions of the e_g distortion mode, they are orthogonal and can be represented in the complex plane [Fig. 1.4(a)].[76] Any linear combination of these modes also comprises a valid FOJT distortion, which is conveniently expressed by defining the phase angle ϕ relative to a specified axis in the diagram. Consequently, if Q_3 is defined as the horizontal axis and Q_2 as the vertical, their phase angles are equal to 0 and $\frac{\pi}{2}$, respectively. Rotational equivalents of the two basis modes are described by angles of $\phi \pm \frac{2\pi}{3}$; for example $\phi = \frac{2\pi}{3}$ corresponds to a Q_3 mode elongated along the x-axis, here denoted Q_3^x. The energy landscape of such a system is similar to a "Mexican hat" potential with local minima at integer

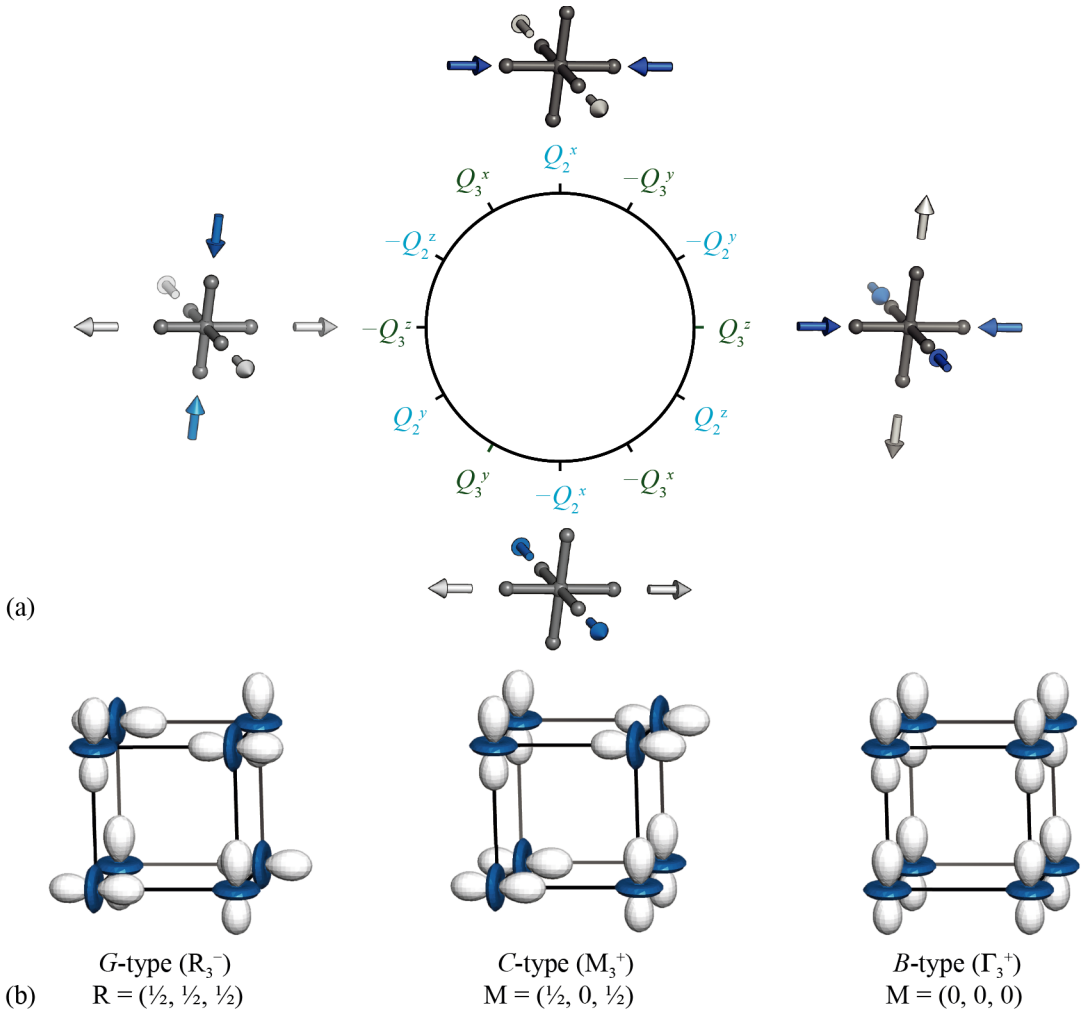


Figure 1.4: (a) The distortion space available for a first-order Jahn-Teller distortion, along with representations of the distortions for Q_2 and Q_3 distortions. (b) G-, M- and B-type orbital orderings with the corresponding irrep and crystal momentum.

multiples of $\phi = \frac{2\pi}{3}$.[70] However, there is no reason to restrict the phase angle to these discrete values and, in theory, symmetries with both Q_3 and Q_2 character are feasible. This will become evident in Chapter 4.

When JT-active species are arranged on a lattice, the distortions on individual cations can interact and drive a macroscopic symmetry lowering. This is known as cooperative Jahn-Teller effects or orbital ordering and is not restricted to perovskites, but occurs in a large range of structures.[77] As the perovskite structure is topologically cubic, there is no unique arrangement of the tetragonal (Q_3) or or-

thorhombic (Q_2) distorted BX_6 octahedra. Staggering of the elongated axes is generally favoured, leading to planes of Jahn-Teller distorted octahedra with the long axes on neighbouring sites arranged in a perpendicular manner. Packing of these sheets directly on top of each other yields C-type orbital order (M-point), as observed in $LaMnO_3$,[74] whereas offsetting forms G-type (R-point), which is exhibited by $KCuF_3$ [Fig. 1.4(b)].[78] The nomenclature is derived from the names of various orderings of magnetic spins.[79] Zone-centre ordering patterns of orbitals are not unprecedented, but are considerably rarer.[80,81] Altogether, cooperative Jahn-Teller distortions can give rise to a wide range of symmetry-distinct states in perovskite materials.

Orbital ordering is crucial for many of the intriguing properties exhibited by perovskites. First, the precise nature of the orbital overlap dictates the type of magnetic ordering of unpaired spins, as formalised by the Goodenough-Kanamori rules.[23,82,83] For example, the ferromagnetic exchange pathways of $BiMnO_3$ and the one-dimensional nature of the magnetism in $KCuF_3$ can be understood in light of orbital arrangements.[78,84] Second, several Jahn-Teller distorted manganites exhibit colossal magnetoresistance (CMR), *i.e.* a drastic decrease in resistivity upon the application of a magnetic field. This technologically interesting phenomenon is believed to originate from a complex interplay between orbital order, spin and charge degrees of freedom.[85–88] Third, as Jahn-Teller distortions lower the point symmetry and cause a splitting of energy levels, they influence electronic transitions and thus luminescence.[89] Hence, the understanding of orbital correlations is not only of fundamental interest, but also useful for potential applications.

In many perovskites, long-range orbital order is lost at elevated temperatures,

leading to an orbitally disordered state. For example, the canonical $LaMnO_3$ exhibits an isosymmetric order–disorder transition at $T_o = 750\,K$ and the development of a microscopic picture of the disordered state has remained a significant challenge despite intense research effort.[74,90,91] Ahmed *et al.* introduced an anisotropic three-state Potts model—a higher-dimensional version of the Ising model—where each site is allowed one of three states corresponding to octahedral elongation along x, y or z.[92–95] A recent study found some evidence in favour of this model as a descriptor for the orbital disorder in $LaMnO_3$, although other models could not conclusively be eliminated.[90] Aliovalent substitution of La^{3+} in $LaMnO_3$ for a divalent metal—*e.g.* Ca^{2+}, Sr^{2+} or Ba^{2+}—leads to mixed-valent manganites, which are frequently orbitally disordered at ambient conditions.[96] These systems often display highly intricate phase diagrams and many are also associated with CMR.[43,97,98] The complexity of the disordered phases and their intriguing functionality render orbital correlations a worthwhile area for further study.

1.3.3 Second-order Jahn-Teller distortions

A few decades after the publication of the FOJT theorem, Öpik *et al.* demonstrated that structural instabilities may persist even in non-degenerate systems, if the energy difference between the two electronic states is small.[99,100] This is referred to as the second-order (or pseudo) Jahn-Teller distortion (SOJT) and is of profound importance for many near-degenerate compounds.[101] In contrast to the FOJT, the magnitude of the SOJT distortion can be very large and even lead to dissociation for small molecules.[102,103] Moreover, the second-order Jahn-Teller distortion is a dipolar degree of freedom, in contrast to the quadrupolar nature of the first-order

distortion. In extended solids, the importance of the SOJT stems from its generation of acentric coordination environments and it is therefore a key driving force for ferroelectricity.[16,104]

In perovskites, the two main classes of SOJT-distorted materials are those containing (i) octahedral d^0 metal ions and (ii) cations with a non-bonding lone pair. For compounds in the first category, the hybridisation of the empty metal *d*-orbitals with the filled oxide *p*-orbitals leads to a near-degenerate state. As a result, the central metal ion becomes susceptible to a displacement from the centre of the octahedron in order to remove the degeneracy [Fig. 1.5(a)].[104] This distortion is typical of perovskites with underbonded B-site cations characterised by a high tolerance factor. The canonical example is $BaTiO_3$, where the correlated off-centring of the Ti^{4+} cation induces a macroscopic polarisation, rendering $BaTiO_3$ a material of high commercial value.[105–107] The hybridisation in perovskites with lone-pair cations is more complex, and involves both the *s*- and *p*-orbitals on the metal as well as the *p*-orbitals of the oxide anion, but the net effect is a stereochemically active electron pair [Fig. 1.5(b)–(c)].[108–111] Lone pair formation mainly occurs for the heavier main group elements and is responsible for ferroelectricity in compounds such as the multiferroic $BiFeO_3$.[112,113]

Despite the utility of the SOJT-driven ferroelectricity, it only occurs in a limited number of compounds and is not readily exploitable in the search for new ferroelectric materials.[114] Furthermore, the requirement for empty *d*-orbitals makes the coexistence and coupling to magnetic order difficult[115,116] and many of the heavy main group elements—in particular Pb—are toxic. As a result, there is a need

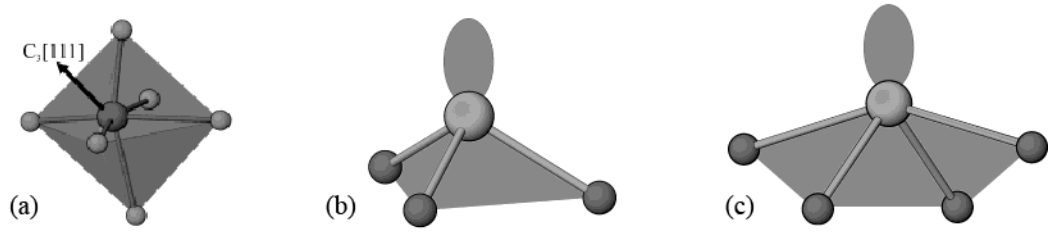


Figure 1.5: Second-order Jahn-Teller distortions. Schematic depictions of (a) the B-site off-centring and stereochemically active lone pairs in (b) tricoordinated and (c) tetracoordinated ions. Adapted with permission from P. S. Halasyamani, *Chem. Mater.*, 2004, **16**, 3586–3592. Copyright 2004 American Chemical Society.[104]

to develop alternative mechanisms for inversion symmetry breaking and one such mechanism, hybrid improper ferroelectricity, is the focus of Chapter 5.

1.3.4 Octahedral tilting

Second-order Jahn-Teller distortions occur in systems with $\alpha > 1$ and are driven by the need to improve the bonding environment of the small B-site cation. Conversely, when $\alpha < 1$, the A-site cation is of insufficient size for the cavity spanned by the surrounding framework and its bonding requirements are not satisfied.[117] This situation is ubiquitous in perovskites and is usually remedied by rotations (tilting) of the octahedral network.[117] Octahedral tilting can be described by the theory of rigid unit modes (RUMs), *i.e.* phonon modes that propagate whilst preserving the connectivity and geometry of the coordination polyhedra.[118] Upon cooling, the modes may soften and ultimately condense, which induces a phase transition from the aristotype untilted structure. By way of example, $SrTiO_3$ adopts the aristotype cubic crystal structure at elevated temperatures and undergoes a phase transition at 105 K to the tetragonal space group $I4/mcm$ as a result of the octahedral rotations.[119]

A notation to describe the various possible tilting patterns was been developed

by Glazer in 1972 and is now widely used.[120] A symbol of the form λ^{μ} is used for each axis of the pseudo-cubic perovskite unit cell. The superscript denotes the presence of tilting: "0" indicates the absence of tilting, "+" corresponds to in-phase tilting (ferrodistortive, $\mathbf{k} = 0$), and "−" indicates out-of-phase tilting (antiferrodistortive, $\mathbf{k} = \frac{1}{2}$) [Fig. 1.6(a)–(c)]. In order to retain the connectivity of the corner-sharing octahedral network, adjacent octahedra perpendicular to the direction of the propagation vector are required to tilt in opposite directions [Fig. 1.6(d)]. The symbol λ indicates the equivalence—or lack thereof—of the tilts down the three axes. As an example, the very common tilt pattern in $GdFeO_3$[121] is denoted $a^+b^-b^-$, showing an in-phase tilt polarised along one axis, and out-of-phase tilts of equal magnitude along the remaining two axes. This tilt pattern is highly prevalent and accounts for more than half of the tilted simple perovskites.[122] Conversely, some tilt systems have not yet been experimentally realised.[122]

Altogether, there are 15 distinct tilt systems and their effect on the global symmetry has been analysed by group-theoretical methods by Howard and coworkers [Fig. 1.6(e)–(f)].[12,81,123] Tilts frequently constitute the primary order parameter* and, therefore, the space group symmetry can often be inferred from the tilt pattern. Indeed, by inspection of Fig. 1.6(e), it is clear that the tilts of $GdFeO_3$ are predicted to give rise to the space group $Pnma$, as verified empirically.[121] Since the underlying factors governing the activation of tilts are known, the space group of a perovskite can, in principle, be controlled by judicious choice of composition.[6,124] Therefore, tilts have established themselves as prime candidate distortions exploitable for targeted materials design, as illustrated by the "tilt engineering" approaches employed

*The primary order is the distortion mode responsible for the observed space group symmetry.

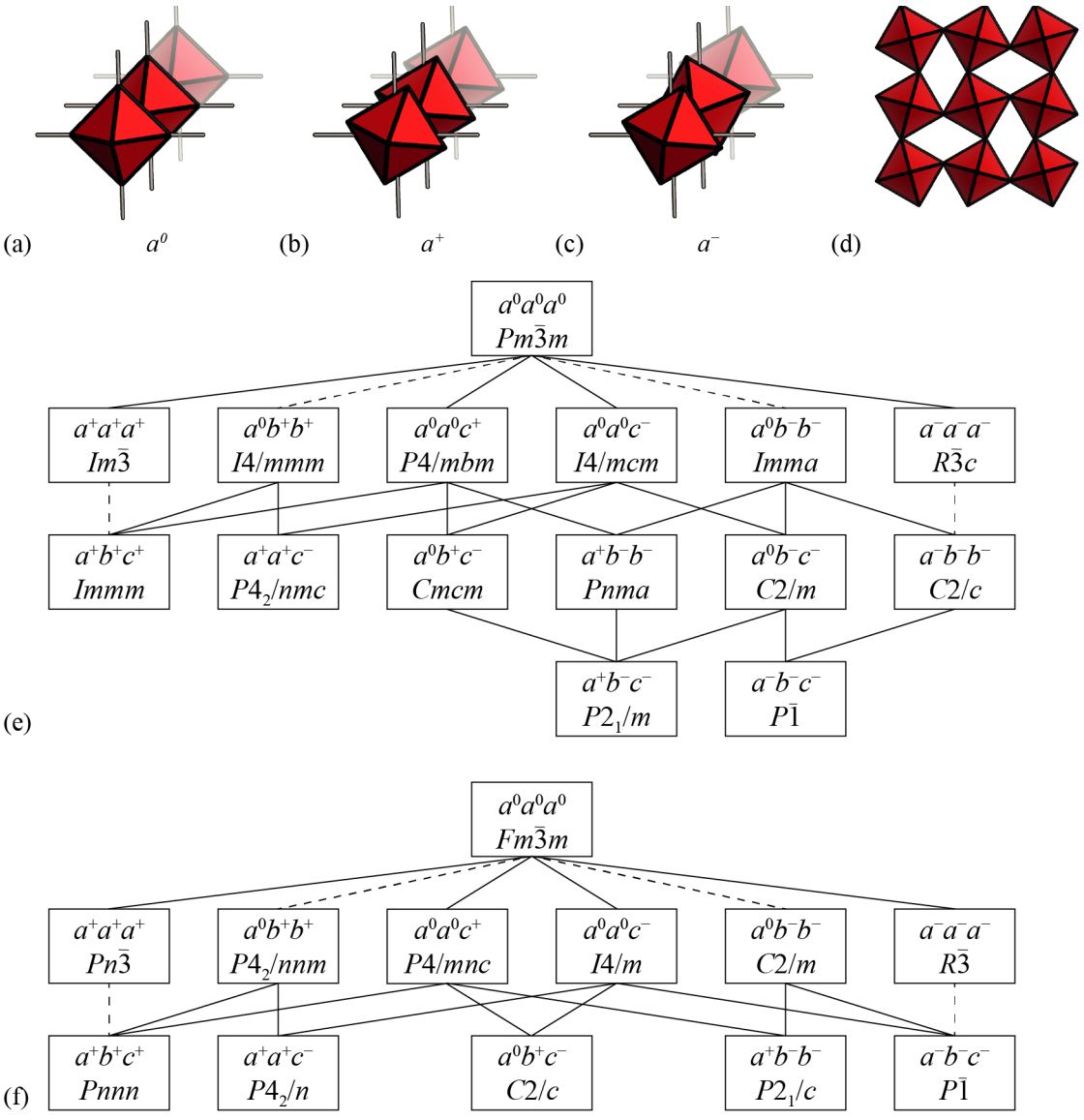


Figure 1.6: Simple tilt patterns in a conventional perovskite and the corresponding Glazer notation: (a) no tilts, (b) an in-phase tilt and (c) an out-of-phase tilt. (d) Within the plane perpendicular to the propagation vector, the tilt angles necessarily alternate in sign as a corollary of the corner sharing. The symmetry tree showing the relationships between the 15 tilt patterns and the resulting space group symmetry for (e) simple and (f) double perovskites. Dashed lines indicate transitions required to be first order. Data in panel e and f reproduced from Ref. 12 and 123 with permission of the International Union of Crystallography.

to synthesise systems capable of multiferroic response.[6]

1.3.5 Magnetic order

Magnetism has little bearing on this Thesis, but is briefly mentioned here for completeness. Long-range spin order arises from the coupling of unpaired electrons and

hence requires paramagnetic cations connected by exchange or superexchange pathways. Perovskites frequently contain magnetic species that are strongly coupled and so ordered states at ambient conditions are readily achievable.[125,126] The mediation of spin interactions is usually rationalised by the Goodenough-Kanamori rules.[23,82,83] In essence, the angle of overlap between partially filled orbitals dictates the nature of the interaction (ferromagnetic or antiferromagnetic) and, hence, spin correlations are functions of orbital order. Further understanding can be gained by the use of representation theory with the inclusion of time reversal symmetry.

1.3.6 Coupling

Functional materials design often seeks to exploit the strong interdependence that can exist amongst the various degrees of freedom discussed above. For example, the activation of one degree of freedom can affect, induce or inhibit another. A particularly desirable scenario is multiferroicity, where *e.g.* the magnetic and electronic degrees of freedom are coupled such that the electronic polarisation can be switched by the application of a magnetic field and *vice versa*.[127] This is desirable for the development of faster and more efficient data storage devices.[127] The word coupling is also used to describe scenarios when two independent distortions collectively act to achieve a given symmetry or property.

The interdependence of individual degrees of freedom (charge, spin and orbital) is often valuable, but it may also complicate the study of perovskites.[48,80,128,129] As an illustration, both colossal magnetoresistance in manganites and superconductivity in cuprates are believed to arise from strong interplay between electronic, magnetic

and lattice degrees of freedom, although the precise mechanisms remain poorly understood.[18,86,130–132] Degrees of freedom cannot normally be studied in isolation due to strong coupling and hence it can be challenging to untangle their individual roles in driving a particular phenomenon. To take a concrete example, it is clear that the Jahn-Teller distortion is pertinent to CMR in manganites, but it arises as a function of the charge order and will also affect the magnetic interaction pathways. Thus, in order to understand the effect of a single distortion on a system, model systems are often required to avoid the strong interdependence with other degrees of freedom.

A considerable amount of attention has been devoted to the development and understanding of multiferroic systems.[133–135] As the name suggests, a multiferroic material exhibits two or more ferroic orders: ferromagnetism, ferroelectricity and ferroelasticity [Fig. 1.7]. They can be further classified as "Type I"—where the two orders have different origins—or "Type II"—where the orders are of the same origin and normally strongly coupled.[136] In addition to magnetoelectric and electromagnetic effects mentioned above, piezoelectricity—strain-induced polarisation—is a noteworthy example. This is exhibited by *e.g.* the perovskite $PbZr_{1-x}Ti_xO_3$ or the mineral quartz, as exploited in quartz watches.[27,28]

Hybrid improper ferroelectricity

Coupling sometimes also refers to the activation of two or more independent distortions to collectively achieve a desired effect. A particularly intriguing example is that of hybrid improper ferroelectricity (HIF), where the different symmetries of two or more disparate distortions are exploited to break global inversion symmetry.[137] This is an appealing concept, as ferroelectricity is a commercially useful property

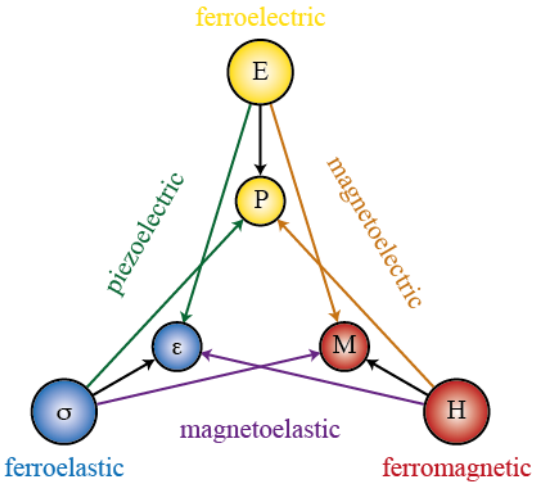


Figure 1.7: Multiferroic couplings between the three ferroic order parameters.

with a wide range of potential applications.[138] Moreover, HIF does not rely on the absence of *d*-electrons, in contrast to SOJT distortions, and is therefore easier to couple to magnetic functionality.

To take a concrete example, the aristotype symmetry of Ruddlesden-Popper phases ($I4/mmm$) is sufficiently low that the inversion centres can be lifted through a combination of octahedral tilts. In order to break the symmetry, two tilt modes that preserve *different* inversion centres have to be activated. In group-theoretical language, a polar secondary order parameter arises as a response to the two superimposed primary order parameters—*i.e.* the two tilts. This was firstly demonstrated for $Ca_3Mn_2O_7$, where the presence of an in-phase tilt along [001] and an out-of-phase tilt in the perpendicular direction gives the polar space group $A2_1am$ ($\equiv Cmc2_1$).[137] As tilting is often controllable, HIF is a strongly attractive mechanism and underpins the tilt engineering approaches referred to earlier.[6]

An important point that will become crucial to the analysis presented in Chapter 5 is that simple ABX_3 perovskites are not amenable to inversion lifting solely by means of tilting.[17] The accessible structural distortions are tilting modes and

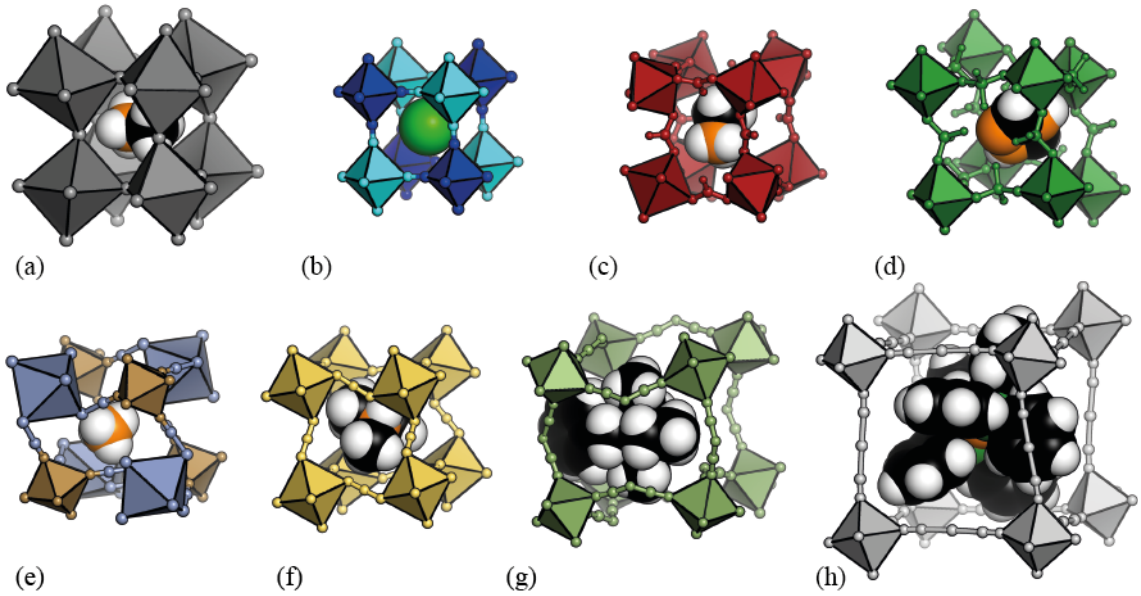


Figure 1.8: Perovskite unit cells of the different families of molecular perovskites drawn to scale. An (a) organic halide perovskite, (b) Prussian blue analogue, (c) formate, (d) hypophosphite, (e) thiocyanate, (f) azide, (g) dicyanamide, and (h) dicyanometallate. The A-site cations are shown as space filling with carbon in black, hydrogen in white, nitrogen in orange, and phosphorus in green.

FOJT distortions and irrespective of how they are combined, at least one centre of symmetry is always retained.

1.4 Molecular perovskites

So far, the structural chemistry of conventional perovskites has been considered, *i.e.* ceramic materials where A, B and X are all monoatomic, inorganic components. However, the A- or X-site of the perovskite structure can also be decorated with molecular components to afford molecular perovskites, which form the focus of this Thesis [Fig. 1.8]. These compounds commonly fall into the category of metal–organic frameworks (MOFs) or coordination polymers (CPs), consisting of a metal cation or metal cluster as the nodes, joined by anionic molecular linker species.

Here, a note on nomenclature is in place. The International Union of Pure and

Applied Chemistry (IUPAC) defines coordination polymer as a coordination compound extending in one or more dimensions,[139] with higher-dimensional structures being referred to as coordination networks. The molecular perovskites considered here are three dimensional and the term coordination network would be the most precise. However, in practice, coordination polymer (CP) is a more widespread expression throughout the inorganic community and will be the term used in this Thesis.* Metal–organic frameworks are a subset of coordination polymers, where the linkers are organic (taken as containing CH moieties) anionic species and the material is potentially porous.[139]

Many concepts developed for conventional perovskites are also applicable to these molecular analogues, although some adaptations are often necessary. For example, an extension of the Goldschmidt tolerance factor to molecular perovskites requires the definition of a set of sensible effective radii for molecular ions. Kieslich *et al.* approached this problem by treating the ions as freely rotating rigid units.[140] The radius of the A-site cation, r_{Aeff}, is taken as the sum of the ionic radius of the outermost non-hydrogen atom and its distance to the centre of mass, whereas the X-site anions are treated as cylinders with an effective radius, r_{Xeff}, and height, h_{Xeff}. Thus, the tolerance factor can be computed by

$$\alpha = \frac{r_{\mathrm{Aeff}} + r_{\mathrm{Xeff}}}{\sqrt{2}(r_{\mathrm{B}} + 0.5h_{\mathrm{Xeff}})}. \tag{1.2}$$

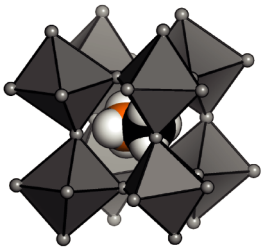
As for conventional perovskites, most molecular perovskites have tolerance factors

*Moreover, the obvious abbreviation of coordination network is CN, which—in the context of the work with cyanide-containing materials presented here—is a potential source of confusion.

$0.8 < \alpha < 1.0$, reflecting the importance of purely geometric considerations in determining the accessibility of this structure type.[140] The tolerance factors of a large number of hybrid perovskites have been calculated, which serves as a useful approximation as to whether a given ion combination might form a stable perovskite.[141] Nevertheless, issues regarding the universality of a simplistic tolerance factor approach have been raised and the approach should not be considered infallible.[142–144]

This Section gives an introduction to the classes of molecular perovskites of current interest in the field. The Section is ordered by the approximate linker length of the structural families and emphasises their structural chemistry and its effect on functionality. Some families are particularly pertinent to the research in this Thesis—notably Prussian blue analogues and metal formate frameworks—and, consequently, these families are presented in more detail than the other systems.

1.4.1 Organic halide perovskites



$(CH_3NH_3)PbI_3$[145]

The X-site in the ABX_3 structure can be decorated with a large halide anion (Cl^-, Br^-, or I^-) and this has important compositional implications. Firstly, the increased dimensions of the cavity enable the incorporation of bulkier cations on the A-site than is possible in conventional perovskites.[146,147] Small organic cations such as methylammonium and formamidinium are ideal candidates, which gives rise to the family of organic halide perovskites [Fig. 1.8(a)]. In general, larger cations lead to preferential formation of the hexagonal perovskite structure or layered materials,[148–151] but a

very recent advance in the field is the inclusion of divalent ethylenediammonium ($NH_3CH_2CH_2NH_3^{2+}$) concomitant with the expulsion of B and X cations to form "hollow perovskites".[152,153] Secondly, the large size of the anion introduces a lower limit to the size of the B-site cation, which in principle impedes the formation of 3D transition metal-based halide perovskites with the exception of fluoride perovskites.*[143,156] Indeed, the majority of organic halide perovskites contain heavy *p*-block elements on the B-sites and organic halide perovskites are less compositionally diverse than the oxide systems.

The first organic halide perovskites were synthesised in the 1970s,[157–159] and in 2009, compounds of formula $(CH_3NH_3)PbX_3$ (X = Br^- and I^-) were used as sensitisers in a photovoltaic cell, achieving a photoconversion efficiency of 3.8%.[160] This spurred intense research interest into the novel field of perovskite solar cells, encouraged by their inexpensiveness and ease of manufacture relative to silicon-based materials.[161] Since then, the efficiencies have increased dramatically and recently surpassed 22%, constituting an unprecedented rate of improvement.[162] As the research on organic halide perovskites is largely motivated by their photovoltaic performance, nearly all known compounds comprise heavy main group elements on the B-site, due to the importance of the stereochemically active lone pair in the enhancement of the optical absorption coefficients.[149,163–166] In fact, the majority of studies focus on the key compound $(CH_3NH_3)PbI_3$, although its toxicity and low stability present a problem for commercialisation.[167–173]

*However, low-dimensional perovskite derivates incorporating transition metals are experimentally accessible.[151,154] as well as "alloys" of transition metals and $(CH_3NH_3)PbX_3$, although the inclusion mechanism of the latter is not yet well understood.[155]

At face value, the structural chemistry of $(CH_3NH_3)PbI_3$ closely resembles that of conventional perovskites, even though the origin of the structural distortions likely differs. At elevated temperatures, $(CH_3NH_3)PbI_3$ exists in a plastic phase with orientational disorder of the A-site cation, leading to the aristotype $Pm\bar{3}m$ symmetry.[174] As the temperature decreases, a sequence of phase transitions occurs, accompanied by a gradual descent in symmetry: first to tetragonal $I4/mcm$ followed by orthorhombic $Pnma$.[175] This is consistent with the change in tilt system from $a^0a^0a^0$ to $a^0a^0c^-$ and subsequently $a^-a^-c^+$ in Glazer notation.[12,120] In oxide perovskites, the tilting is driven by size differences between the cations, but for $(CH_3NH_3)PbI_3$, it is believed to arise as a result of hydrogen bonding between the methylammonium and the iodide.[145,176] Irrespective of the origin, the phase transition highlights the interplay between two of the key distortions available to organic halide perovskites: tilting and A-site cation order.

The degrees of freedom arising from the molecular nature of the A-site cation are interesting and vital for the structure of $(CH_3NH_3)PbI_3$. All prolate (rod-like) cations possess quadrupolar symmetry and the cation arrangement can be described as an ordering of the quadrupole moment. For example, in the orthorhombic phase, the $CH_3NH_3^+$ cation exhibits antiferroquadrupolar order that is strongly coupled to the tilting pattern [Fig. 1.9(a)–(c)].[177] In the more symmetric phases, the cation is dynamically disordered (paraquadrupolar), which has been the focus of several studies in attempts to unravel the link between cation reorientation and charge carrier lifetime [Fig. 1.9(d)].[178–182] In addition, the polyatomic nature of the $CH_3NH_3^+$ cation opens up for internal degrees of freedom in the form of conformational changes. Due

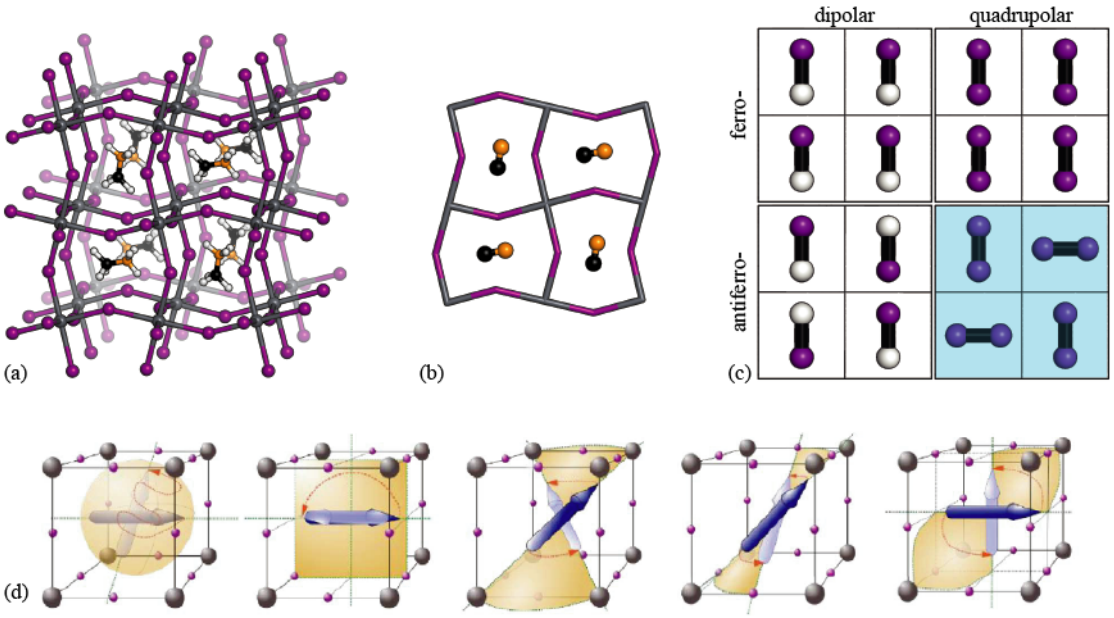
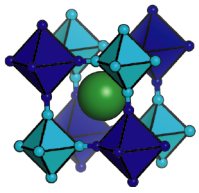


Figure 1.9: (a) The structure of $(CH_3NH_3)PbI_3$ with C in black, H in white, N in orange, Pb in grey and I in purple.[175] (b) The antiferroquadrupolar arrangement of methylammonium cations in a plane (H omitted) and (c) schematic representations of ferro- and antiferroorder of dipolar and quadrupolar moment with the antiferroquadrupolar arrangement highlighted. (d) The possible reorientation pathways of the methylammonium cation within the cage. Panel d adapted from Ref. 179 under a Creative Commons Attribution 4.0 International License.

to steric considerations, the ideal HNCH torsion angle for a free methylammonium cation is 180°, but it has been suggested that slightly lower values are favoured when the cation is enclosed in a perovskite cage.[183] Both the orientational cation order and the conformational changes represent "unconventional" degrees of freedom, *i.e.* they have no analogue in conventional inorganic perovskites.

1.4.2 Prussian blue analogues



$RbMn[Fe(CN)_6]$[184]

Organic halide perovskites are the sole family of molecular perovskites with a monoatomic anion and all remaining examples contain polyatomic linkers. Prussian blue (PB), $Fe_4^{3+}[Fe^{2+}(CN)_6]_3$ was serendipitously synthesised by a German draper in the early 18th century and is considered the first example of a coordi-

nation compound.[185] Its vivid colour, originating from charge transfer between the metal centres, has made it an attractive pigment.[186]

Despite the popularity of PB, understanding its structure has posed a prominent challenge. In 1936, Keggin and Miles proposed the first structural model of the series of compounds with assumed stoichiometry $AFe[Fe(CN)_6]$ (where A is an alkali metal or ammonium), based on a powder X-ray diffraction (XRD) study.[187] They postulated two interpenetrating cubic lattices of Fe^{2+} and Fe^{3+} joined by cyanide anions, reminiscent of the rocksalt structure. The resulting voids (Wyckoff position 4*c*) were occupied by A cations, if present [Fig. 1.8(b)].[187] Hence, each of the distinct Fe species only occupies one crystallographic site. Decades later, Ludi and coworkers carried out a single-crystal XRD study on different crystals of alkali-free Prussian blue of formula $Fe_4^{3+}[Fe^{2+}(CN)_6]_3$, and found the primitive space group $Pm\bar{3}m$ to be the most accurate.[188] In this space group, each metal ion decorates two crystallographically independent sites. As the 4:3 stoichiometry suggests 25% of the $Fe^{2+}(CN)_6$ moieties to be absent, the primitive space group allows for a predominant vacancy concentration on one of the two sites, *i.e.* vacancy order. The coordination spheres of the Fe^{3+} ions are completed by water molecules and there is also interstitial water encapsulated by the cavities.[189] The Ludi model is now generally accepted as the correct structure of alkali-free Prussian blue.

The utility of Prussian blue stems from the possibility of replacing the Fe ions with other transition metals, leading to the broad family of Prussian blue analogues (PBAs). The wavelength of the intense charge transfer excitation is strongly dependent on the nature of the metals and PBAs usually display a wide range of colours.

In addition to optical properties, the large scope for structural modification leads to a wealth of intriguing functionality including negative thermal expansion,[190,191] catalytic properties,[192] photo-induced magnetism,[193,194] electroactivity,[195] and photoabsorption relevant to biomedical applications.[196,197] Here, an overview of the structural chemistry of PBAs will be given and the effect on the properties highlighted.

The discrepancy between the models proposed by Keggin-Miles and Ludi highlights the complexity of Prussian blue and its analogues, as well as the challenges associated with accurate structure determination. The simplest version of PBAs resembles an A-site deficient double perovskite (α-Po topology) with cyanide as the bridging anion and symmetry $Fm\bar{3}m$ [Fig. 1.10]. The formula is therefore $B[B'(CN)_6]$* and examples include $Mn^{2+}[Pt^{4+}(CN)_6]$ and $Fe^{3+}[Fe^{3+}(CN)_6]$, known as Berlin green.[187,191] As the charges on the transition metals exactly balance the negative charge arising from the cyanide ligands, no additional charge compensation is required and a well-ordered structure is formed. However, for transition metals in other oxidation states, the need to maintain electroneutrality often introduces a certain degree of defects and/or disorder, rendering structure determination nontrivial.

One of the most common combinations of oxidation states in PBAs is that of an N-bound B^{2+} metal and C-bound B'^{3+}, which stipulates a stoichiometry of 3:2. Thus $B'(CN)_6$ vacancies are generally required, as also present in Ludi's model of Prussian blue itself. Consequently, the average coordination number of the B-

*Most literature on PBA uses $M[M'(CN)_6]$ as the generic formula. However, the letter "B" is employed throughout this Thesis, to emphasise the structural similarity to perovskites. This should not be confused with the element boron.

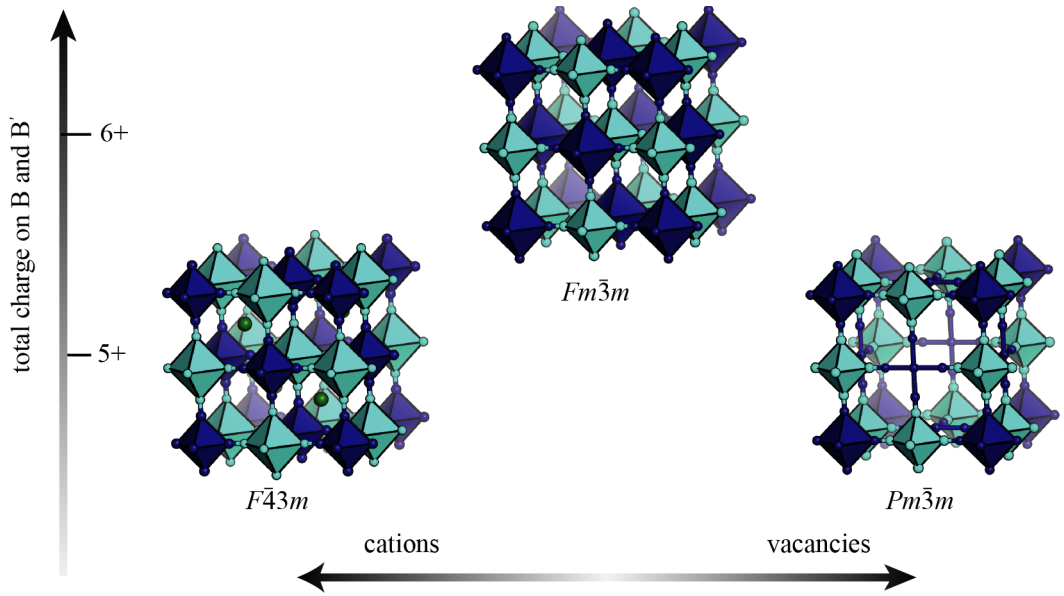


Figure 1.10: Ordered structures of Prussian blue analogues. When the charges on the two metal ions amount to +6, a fully ordered α-Po structure is formed.[198] As the charges are lowered, charge compensation *via* univalent cations gives the noncentrosymmetric perovskite structure with half of the A-sites vacant.[184] Alternatively, ordered arrangements of $B'(CN)_6$ vacancies can lower the symmetry to $Pm\bar{3}m$.[188] In the case of cation or vacancy disorder, the average structure is described by $Fm\bar{3}m$. To emphasise the similarity between the structures, all B cations are shown in dark blue, B′ cations in cyan and A-site cations in green.

sites is reduced from 6 to 4. The altered local environment induces a displacement of the B-site metal ions, away from the special position, manifesting as a diffuse contribution to the background in XRD data.[199,200] Given their drastic impact on the local structure, it is unsurprising that these defects can have significant effects on the functionality of the framework: they increase the pore volume and give rise to—following dehydration—coordinatively unsaturated metal sites; both of which are important factors for gas absorption and catalysis.[192,201] The magnetic behaviour is also influenced by defects, especially if B′ is a paramagnetic species.[185,202,203]

The vacancy distribution in defective PBAs is an intriguing and challenging consideration that is not yet well understood. The limiting case of a fully ordered structure is only achievable for the 4:3 stoichiometry (25% vacancies) and corresponds

to $Pm\bar{3}m$ symmetry with a void at the centre of the unit cell [Fig. 1.10]. There are two environments for the B-sites: the unperturbed $B(NC)_6$ and the square planar $B(NC)_4(OH_2)_2$, located at the unit cell corner and faces respectively. However, the more prevalent 3:2 stoichiometry (33% vacancies) cannot exhibit complete order on a cubic lattice and thus some vacancy disorder is inevitable.[190,200,201] Whilst the disorder is often presumed to be random, there is evidence in favour of non-random (correlated) disorder. Firstly, weak superlattice reflections inherent to the ordered $Pm\bar{3}m$ structure are sometimes observed in the powder XRD patterns.[186] Secondly, single-crystal studies reveal the presence of structured diffuse scattering, consistent with the presence of correlated vacancy disorder.[204–206] Thirdly, a solid-state NMR study of a series of $Cd_3[Co(CN)_6]_2$ systems discovered a predominant *trans*-arrangement of vacancies, in line with the $Pm\bar{3}m$ model.[207,208] The situation is complicated by the intimate link between vacancies and synthesis conditions,[188] which intermittently leads to irreproducibility.[201,209] As the nature of the vacancy disorder is not just a crystallographic curiosity, but also has implications for the functionality,[210] further studies will be worthwhile.

An alternative method of ensuring electroneutrality for the metal combination B^{2+}–B'^{3+} is the introduction of cations into the tetrahedral sites of the face-centred unit cell. Cation inclusion acts in competition to vacancy formation,[203,211] and even trace amounts of alkali metal present during synthesis may be incorporated into the framework, thereby reducing the number of vacancies.[188] Often, the cations are randomly distributed over the 8*c* sites in the space group $Fm\bar{3}m$,[208,212–214] but they may also order as to break the inversion centres, lowering the crystal symmetry to $F\bar{4}3m$

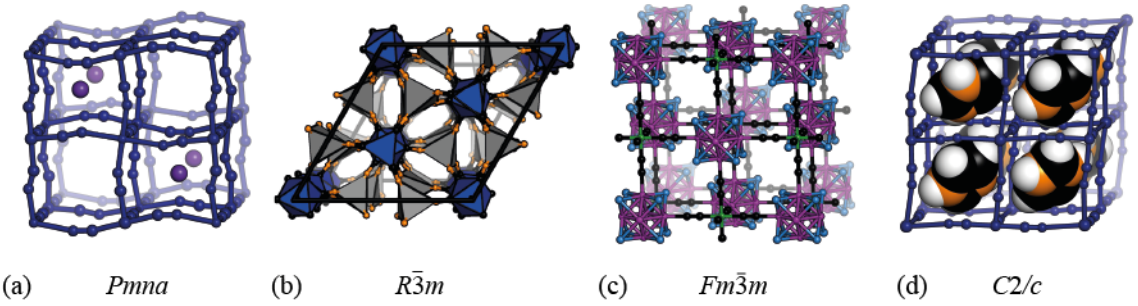


Figure 1.11: Variations on the theme of Prussian blue. (a) The tilted $RbCu[Fe(CN)_6]$ with a rod-like cation arrangement[216] with the framework shown in blue and Rb in purple;[216] (b) the rhombohedral polymorph of $Zn_3[Co(CN)_6]_2$[221] with Zn in grey, Co in blue, C in black, N in orange, and the unit cell in black; (c) the cluster-expanded $Ga_4[Re_6Se_8(CN)_6]_3$[222] with cyanide in black, Ga in green, Se in blue, and Re in purple; and (d) the cyanoelpasolite $(HIm)_2K[Fe(CN)_6]$ (HIm = the imidazolium cation)[223] with the framework in blue, C in black, H in white, and N in orange. The structures are not drawn to scale.

[Fig. 1.10].[190,215] Given that these two space groups display identical reflection conditions, differentiation based solely on crystallographic techniques is nontrivial. When coupled to distortions of the enclosing framework, more unusual rod-like ordering patterns can appear [Fig. 1.11(a)].[216] As for vacancies, the cations are pertinent to the functionality of PBAs and affect *e.g.* electrochemical performance, the affinity towards small adsorbates, and the electronic bandgap.[217–220]

In addition to symmetry lowering arising from the need for charge compensation, a range of other variations on the theme of Prussian blue can be composed. First, tetrahedral coordination is not disfavoured for B-site metal ions with low CFSE—*e.g.* Zn^{2+} or Mn^{2+}—and PBA-like structures with mixed tetrahedral-octahedral metal coordination exist [Fig. 1.11(b)].[200,209,221,224] Second, the cyanide anion can isomerise, although this appears to mainly occur for systems based on hexacyanochromates.[225–228] The vast majority of Prussian blue analogues appears predisposed to cyanide order, but it should be noted that XRD—the most common structure determination method—is largely insensitive to cyanide disorder due to the low and

similar scattering factors of C and N. Third, the B-site metal may be replaced by a large metal-containing cluster without disrupting the underlying topology. These systems exhibit tuneable porosity as a function of the size of the metal cluster [Fig. 1.11(c)].[222,229] Fourth, double interpenetration of a Prussian blue compound has been suggested,[230] although this proposition might benefit from further study due to the lack of crystallographic evidence. As these examples highlight, PBAs are a remarkably versatile playground for structural chemists.

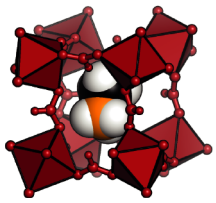
If the B-site is decorated with an alkali metal cation, the more exotic class of materials known as cyanoelpasolites* is obtained [Fig. 1.11(d)].[232–236] These have the general formula $A_2^+B^+[B^{3+}(CN)_6]$ and neither vacancies nor positional cation disorder are applicable here since cyanoelpasolites are stoichiometric phases. Yet, the increased pore volume allows for the A-site to be occupied by organic cations, which frequently display thermally induced order–disorder transitions of the same type as discussed for $(CH_3NH_3)PbI_3$.[237,238] As a result, these materials are of particular currency for their dielectric properties: the onset of rotation of a polar A-site cation at a critical temperature greatly enhances the dielectric constant, sometimes by a factor or four or more.[223,239] This feature is potentially exploitable in the development of switchable dielectrics. Moreover, employing cations with an inherent dipole moment can yield compounds predisposed to ferroelectric ordering.[240]

As parts of this Thesis are focused on Jahn-Teller distortions, it is appropriate to briefly consider the peculiar behaviour of copper-containing Prussian blue analogues. The cyanide ligand is a strong σ-donor and donates electron density from the weakly

*By analogy with the mineral elpasolite, K_2NaAlF_6.[231]

antibonding 5σ molecular orbital into the e_g set of the metal. Moreover, metal t_{2g} orbitals backbond into the 2π orbitals, which leads to a slight weakening of the CN bond.[241] The σ-donation is particularly favourable for Cu^{2+} ions, since it gives rise to an electronic configuration close to $3d^{10}$. As a result, the cyanide ligand in copper-containing PBAs exhibits very high vibrational frequencies as its bond order is increased upon coordination.[242] Additionally, in series of $B_3^{2+}[B'^{3+}(CN)_6]_2$ (B′ = Co or Fe), the smallest unit cell, strongest magnetic coupling and lowest degree of hydration are all exhibited by the B = Cu system.[200,209,242] Overall, copper-based PBAs typically display extreme and unique behaviour.

1.4.3 Metal formate perovskites



$(CH_3NH_3)Mn(HCOO)_3$[243]

Perovskite-like compounds based on the formate anion ($O–CH–O^-$) are a populous and compositionally versatile family [Fig. 1.8(c)], mainly as a result of the large selection of suitable A-site cations.[244] The length of the formate linker enables incorporation of small and mid-sized cations on the A-site, including methylammonium, dimethylammonium, guanidinium, imidazolium *etc.* [Fig. 1.12].[243,245,246] It is even possible to omit the A-site cation by employing a trivalent metal on the B-site and CO_2 or formic acid as a template, but these compounds are relatively rare.[247–249] Furthermore, there is a substantial scope for substitution on the B-site; with both small alkali metals and large transition metals included.[250,251] Double perovskite structures can be constructed by replacing the divalent B-site metal by a 1:1 combination of uni- and trivalent ions.[252] Due to the vast substitutional scope, formates are arguably the compositionally most diverse family

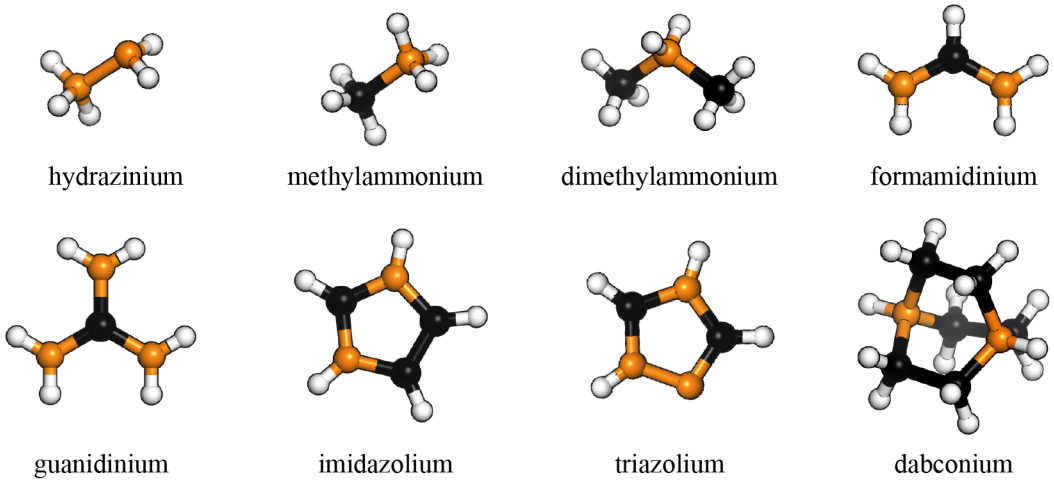


Figure 1.12: A selection of common A-site cations for medium-sized molecular perovskites, *i.e.* cyanoelpasolites, formates and hypophosphites. Carbon is shown in black, nitrogen in orange and hydrogen in white.

of molecular perovskites and also the best understood from a structural chemistry perspective.

The nature of the formate linker itself has a significant impact on the relative stability of the perovskite structure type for metal formate frameworks. The formate anion has three available binding modes: *anti–anti*, *syn–anti* and *syn–syn* [Fig. 1.13(a)–(c)], which are intimately linked to the tolerance factor, α. In metal formate perovskites, *anti–anti* is predominant (denoted perovskite I) and occurs for tolerance factors in the range 0.8–1.0 [Fig. 1.13(d)].[9,253,254] This is a similar tolerance factor range for stable perovskite oxides. If $\alpha < 0.8$, the binding mode of the formate anion switches to a mixture of *syn–anti* and *anti–anti* whilst retaining the corner-sharing network (the so-called perovskite II phase).[253,254] In addition, there are a few formate perovskites with exclusive *syn–anti* binding geometry (perovskite III).[250,254] The link between binding mode, tolerance factor and topology is complicated by the chiral hexagonal niccolite-type phase occurring for certain ion combinations, despite

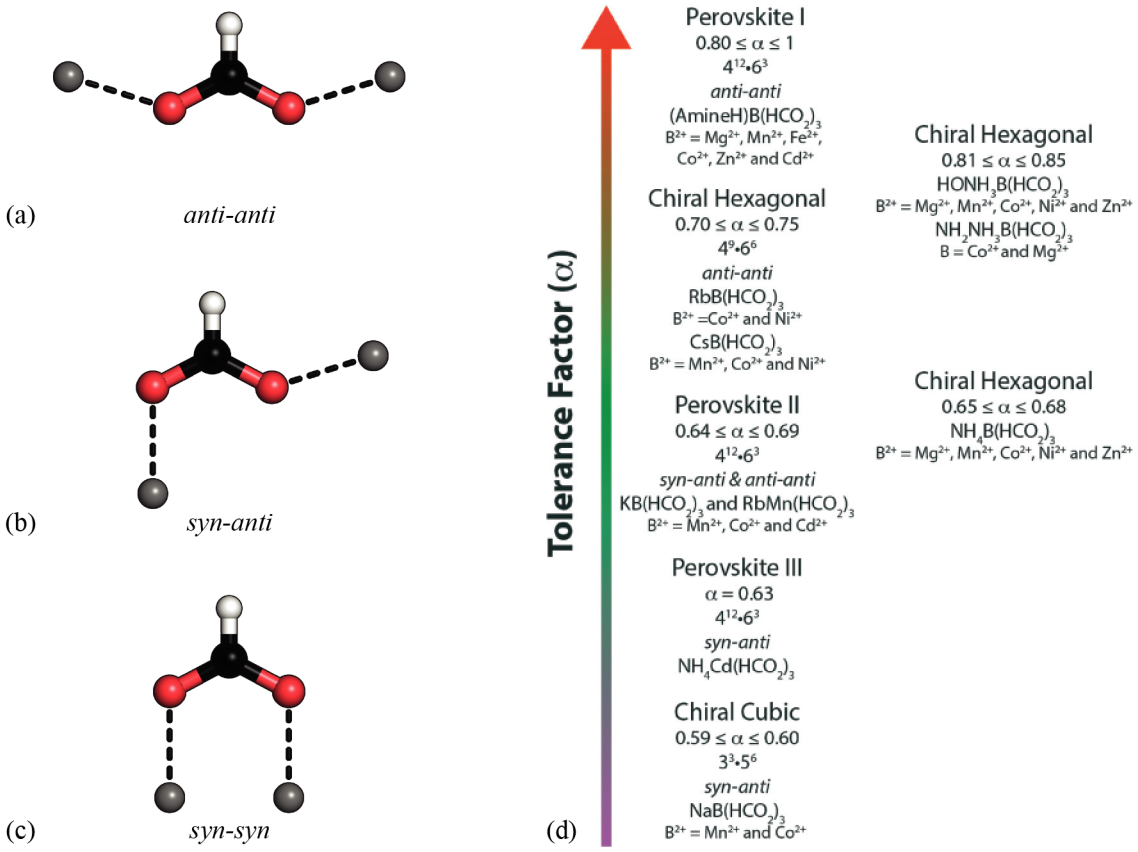


Figure 1.13: The binding geometries of the formate anion: (a) *anti–anti*, (b) *syn–anti*, and (c) *syn–syn*. Carbon is shown in black, hydrogen in white and oxygen in red. The metal ion is shown in grey, with dashed coordination bonds to the formate oxygen atoms. (d) The tolerance factors for formate perovskites. Note that the letter "B" does refer to boron in this figure. Panel d reproduced from Ref. 253 with permission from The Royal Society of Chemistry.

the tolerance factor being in the range expected for a perovskite.[253,255–257] For systems at the intersection of the stability regions, polymorphism can occur, reflecting the role of entropic effects in addition to the purely geometric considerations of the tolerance factor.[142,258] Partially as a result of the nonlinear M–O–C–O–M moiety, formate perovskites usually crystallise in low-symmetry space groups* and do not adopt the aristotype symmetry even at high temperature.[244] The flexible binding modes and low point symmetry of the formate anion are consequently crucial features of formate-based perovskites.

*Some A-site deficient formates allegedly exhibit cubic $Im\bar{3}$ symmetry,[247] indicating that the asymmetry of the A-site cations also contributes to the symmetry lowering of formate perovskites.

There is a multitude of intriguing functionality associated with formate perovskites and a prominent example is dipolar order. Under ambient conditions, the dimethylammonium cation in $[(CH_3)_2NH_2]B(HCOO)_3$ is dynamically disordered over three sites, consistent with $R\bar{3}c$ symmetry.[243,259] Upon cooling, the reorientational motion becomes energetically inaccessible and the cation undergoes a disorder–order transition, concomitant with a symmetry lowering to the polar space group Cc.[259–261] Early studies suggested antiferroelectric ordering, but it is now generally believed to be ferroelectric.[261–264] The transition temperature is a function of the strength of the hydrogen bonds between the ordered dimethylammonium and the formate anion and by employing a hard B-site cation, the transition temperature can be tuned to occur close to room temperature.[264–266] Interestingly, coexistence of the paraelectric and ferroelectric phases has been observed, perhaps indicating a progressive freezing process of the dynamic motion.[266] Moreover, ^{13}C NMR studies on the related $[(CH_3)_2NH_2]Zn(HCOO)_3$ revealed the formation of polar nanodomains prior to the phase transition, which provides an explanation for the relaxor-like behaviour observed in these systems.[267] Thus, formate perovskites may find applications as dielectric materials.

Another interesting property of metal formate frameworks is their magnetism, which can, in principle, couple to the dipolar ordering to give multiferroic materials.[268] The *anti–anti* binding mode of the formate anion generally mediates antiferromagnetic exchange interactions between unpaired spins and its noncentrosymmetric character induces spin canting.[269–272] As a consequence, many formate perovskites sustain weak ferromagnetism and there is often coexisting electric ordering

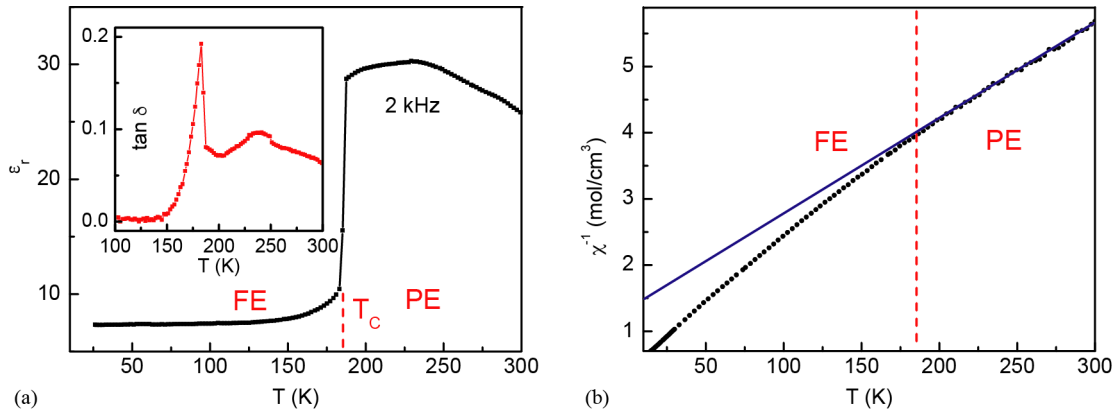


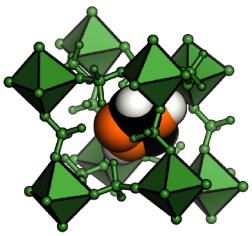
Figure 1.14: Magnetoelectric couplings in $[(CH_3)_2NH_2]Mn(HCOO)_3$. (a) The dielectric constant as a function of temperature with the dielectric loss displayed in the inset. The dielectric phase transition at $T_c = 185\,\mathrm{K}$ is evident. (b) The temperature dependence of the inverse magnetic susceptibility where the blue curve gives the fit to the Curie-Weiss law. A deviation from the Curie-Weiss behaviour appears at T_c, which is indicative of an enhancement of the short-range antiferromagnetic correlations at this temperature, *i.e.* magnetoelectric coupling. Adapted from Ref. 279 under a Creative Commons Attribution Noncommercial license.

at low temperatures, rendering these compounds Type I multiferroics.[243,264,270] Type II multiferroics (coupling of magnetic and electric orders) are more desirable and since the formate anion is involved in both the electric ordering of the A-site cation and the mediation of magnetic interactions, such states can be expected.[273] Indeed, both direct[274,275] and inverse magnetoelectric couplings[268,275–277] have been reported [Fig. 1.14], although some aspects are still debated.[278]

The structural diversity of perovskite-like formates and their dependence on weak interactions (*i.e.* hydrogen bonding between the A-site cation and framework) render them good model systems for structure–property relationships. There are numerous cases where the functional response can be tuned by chemical substitution on the A- or B-site. First, the hardness of the B-site cation influences the ordering transition temperature in $[(CH_3)_2NH_2]B(HCOO)_3$,[264–266] whereas substitution on the A-site affects the magnitude of the polarisation.[257,280] Second, a detailed study

of a large range of metal formates explored the relationship between thermal response and the size *and* shape of the A-site cation.[281] The direction of framework hingeing upon heating was found to be reversible upon alteration of the shape of the cation from oblate to prolate.[281] Third, the mechanical properties are also dependent on the hydrogen bonding and the Young's moduli vary drastically as a function of the hydrogen bonding capability of the A-site cation.[282] These studies highlight the extensive crystallographic attention devoted to the understanding of metal formate perovskites.

1.4.4 Metal hypophosphite perovskites



[Trz]$Mn(H_2POO)_3$[283]

Hypophosphite perovskites are the most recent addition to the various families of molecular perovskites [Fig. 1.8(d)], with just a handful of very recent publications known to date (August 2018).[283–285] The hypophosphite anion (H_2POO^-) spans a similar distance to the formate anion and, hence, there is a plethora of organic cations available to act as A-site species. Inclusion of a very wide range of various amine ions has been demonstrated,[284] which shows promise for the development of hypophosphite perovskites into a diverse and tuneable family in due course. Manganese is the sole cation to have been used as a B-site cation, but there is no reason to assume that it is the only suitable candidate.

Despite the very recent discovery of hypophosphite perovskites, some unusual structural features are already evident. First, hypophosphite does not appear to

have a strong preference for the B–O–P angle; this is in contrast to the two distinct binding modes adopted by the formate anion. The framework of hypophosphite perovskites is often deformed to a greater extent than the corresponding formate system, perhaps as a result of the less strict binding requirements.[284] Second, some unprecedented arrangements of the A-site cations are also known. By way of example, dimethylammonium preferentially resides in the windows between adjacent voids as opposed to the centre of the cavity.[283] Moreover, the partially A-site deficient $[DAB]_{0.5}Mn(H_2POO)_3$ (DAB = dabconium) has an extraordinary cation order consisting of layers along the [111] direction of the perovskite pseduo-unit cell.[284] Neither window occupation nor A-site deficiency is common in other classes of molecular perovskites, and so further studies into these various phenomena will be of interest.

Another recent development in the field is the partial replacement of formate ligands with hypophosphite anions to create mixed X-site perovskites [Fig. 1.15].[285] Given the considerable differences in the structural chemistry of formate and hypophosphite perovskites, these results are intriguing for the development of new functional materials. To date, only two mixed X-site compounds have been synthesised: $[C(NH_2)_3]Mn(HCOO)_{3-x}(H_2POO)_x$ ($x = 0.3$ and 0.5). These systems exhibit a pillared-layer order of the two anions, accompanied by an incommensurate anion displacement in the $x = 0.3$ compound. In brief, hypophosphite perovskites exhibit a plethora of interesting characteristics and further studies can be anticipated and encouraged.

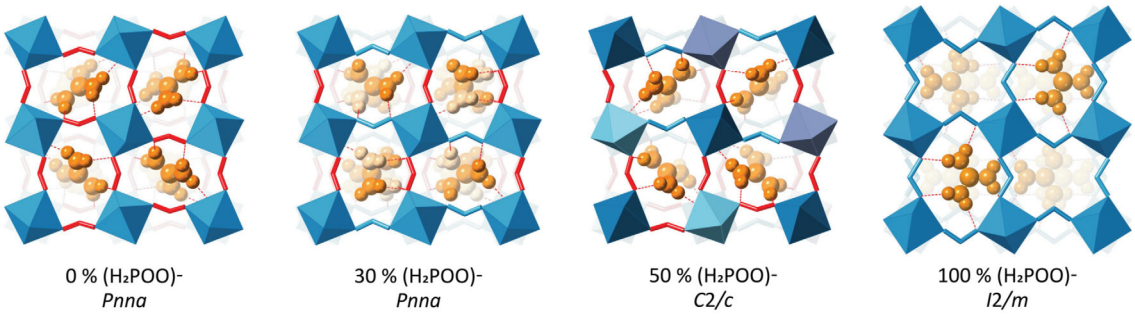
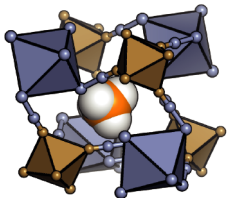


Figure 1.15: The structures of $[C(NH_2)_3]Mn(HCOO)_{3-x}(H_2POO)_x$ for different values of x, where the MnO_6 octahedra are shown in blue and $C(NH_2)_3$ in yellow. Red and blue linkers denote formate- and hypophosphite-rich sites respectively. Adapted from Ref. 285.

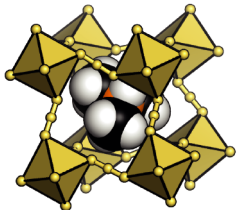
1.4.5 Metal thiocyanate perovskites



$(NH_4)_2NiCd(SCN)_6$ [286]

At time of writing, there have been few studies into thiocyanate (SCN^-) perovskites and only a handful of structures exist [Fig. 1.8(e)]. In 1980, two compounds of composition $ACd(SCN)_3$ ($A = Rb^+$, Cs^+) were reported, with $CsCd(SCN)_3$ crystallising as a perovskite.[287] More recently, Xie *et al.* synthesised $(NH_4)_2NiCd(SCN)_6$, which forms a double perovskite in space group $P2_1/n$ with heavily tilted octahedra.[286] Upon heating, it undergoes an isosymmetric phase transition associated with orientational disorder of the ammonium cation. Thiocyanate can also partially replace the halide in organic halide perovskites, thereby improving stability as well as causing unusual optical properties.[288–290] This process is not yet well understood from a structural viewpoint. However, as for the hypophosphite systems, thiocyanate perovskites represent a relatively understudied field and reports of further compounds may be expected in the future. Thiocyanate acts as a pseudohalide in the mediation of magnetic interactions and may perhaps be a useful building block in the search for new magnetic molecular perovskites.[291,292]

1.4.6 Metal azide perovskites



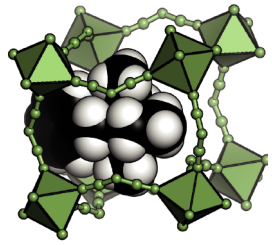
$[(CH_3)_3NH]Mn(N_3)_3$[293]

The family of azide (N_3^-) perovskites [Fig. 1.8(f)] is not as compositionally diverse as *e.g.* formates, yet they display a marked structural versatility. The B-site is commonly decorated by divalent Ca, Cd, or Mn[294–296] and bimetallic double perovskite structures with equimolar mixture of alkali metals and transition metals are known, as for the formates.[297] Methylammonium cations of general formula $(CH_3)_nNH_{4-n}$ are the predominant A-site species,[293,294] although cations with longer alkyl chains can also be included.[298,299] The azide-metal linkage is highly flexible, which renders the framework very adaptable to the shape of the interstitial A-site cation. Hence, the A-site cation has a large influence on the symmetry of the azide perovskites and the possible space groups span the entire range from triclinic to cubic.[293,300,301] Additionally, azide perovskites are predisposed to displaying a range of thermally induced phase transitions. These often feature drastic symmetry changes and complex structural alterations involving both disorder and displacement of the molecular moieties, as well as distortions of the framework.[293–297,300,302] Indeed, azides are perhaps the most flexible family of molecular perovskites.

With regards to functionality, azide perovskites are mainly associated with magnetic and dielectric properties. The early studies were primarily focussed on their magnetic behaviour, in an attempt to design molecular magnets.[295,303] Despite the ability of the azide anion to mediate both ferro- and antiferromagnetic coupling between the metal centres,[304,305] azide-bridged perovskites are generally antiferromagnets with relatively high ordering temperatures (*ca* 70 K).[293,295] This can be con-

trasted with the formates, where the Néel temperatures rarely exceed 30 K.[243–245,275] Moreover, cation-dependent magnetic bistability has been observed in the series $[(CH_3)_nNH_{4-n}]Mn(N_3)_3$ (n = 1–4).[293] As $[(CH_3)_4N]Mn(N_3)_3$ also exhibits a ferroelastic phase transition as well as antiferroelectric cation order, it presents an example of a coordination polymer with three coexisting ferroic orders.[306] Furthermore, their temperature sensitivity and the ease of deformation render azides highly thermoresponsive dielectric materials.[300] Despite the intriguing chemistry of azide perovskites, it should be remembered that azide is a highly explosive anion,[307,308] which hampers both research and applications in commercial devices.

1.4.7 Metal dicyanamide perovskites



$[Et_3NBn]Fe[N(CN)_2]_3$[309]

The pentatomic dicyanamide anion, $N(CN)_2^-$, is the longest nonlinear ligand amongst those found in molecular perovskites [Fig. 1.8(g)]. In contrast to the rather rigid formate anion, dicyanamide is relatively flexible and displays a slightly variable C–N–C angle.[310] Indeed, some unusual conformations have been postulated from partial structural solutions, but additional studies would be beneficial to corroborate this proposed geometry.[310] As a consequence of the considerable intermetallic distance in dicyanamide perovskites, sizeable A-site cations are required, such as ammonium or phosphonium ions coordinated to long (propyl, phenyl, butyl *etc.*) alkyl chains.[309,311] A more unusual A-site cation is the sulfur-based SPh_3 (Ph = phenyl).[312] Similar to the azides, the dicyanamide framework is highly flexible and so the A-site cation has a strong templating effect: the framework distorts to accommodate its size and shape.[312,313]

As expected for large and deformable frameworks, dicyanamide perovskites undergo a multitude of thermal phase transitions, commonly involving several structural changes, *e.g.* off-centring of the A-site cation, framework distortions, and order–disorder transitions of both the A-site cation and the ligands.[309–311,314,315] The transition may also impart interesting functionality with potential technological applications. For example, the transitions from noncentrosymmetric $P2_12_12_1$ to centrosymmetric space groups in $[Et_3RP]Mn[N(CN)_2]_3$ (Et = ethyl, R = propyl, methoxymethyl) and $[Et_3PrP]Cd[N(CN)_2]_3$ render these systems suitable for use as nonlinear optic switches.[310,313] Furthermore, the large entropy change associated with order–disorder transitions of the propyl and dicyanamide moieties causes a significant barocaloric effect in $[NPr_4]Mn[N(CN)_2]_3$ at modest pressures of relevance to refrigeration.[316]

Due to their flexible nature, dicyanamide perovskites are highly sensitive to external stimuli, *e.g.* temperature or pressure. For example, $[Et_3PrP]Cd[N(CN)_2]_3$ exhibits photoluminescence in the visible region and the emitted intensity can be tuned by temperature.[310] Moreover, members of the series $[Pr_4N]B[N(CN)_2]_3$ (B^{2+} = Fe, Co, Ni) undergo three thermal phase transitions, leading to a temperature-dependent dielectric response.[314] The first and third transition temperatures are functions of the external pressure with positive and negative signs of the dependence, respectively [Fig. 1.16(a)]. Hence, at a critical pressure, the two transition temperatures coalesce and thereby suppress the intermediate phases, reducing the number of phase transitions to one.[314,315] A similar effect is achieved by decreasing the size of the B-site cations, which in turn decreases the tolerance factor and en-

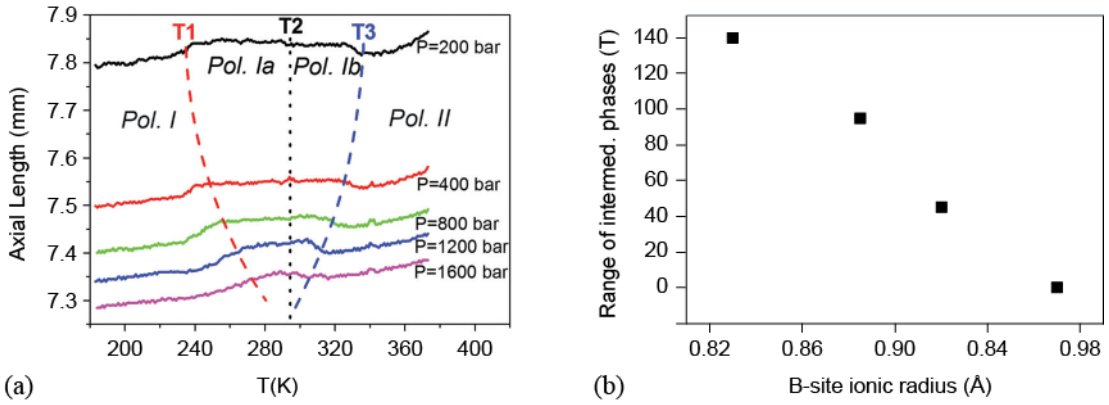
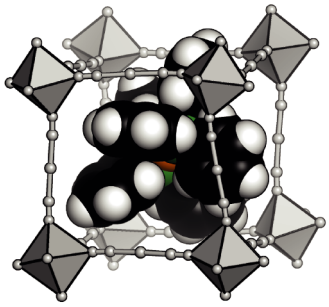


Figure 1.16: (a) The length of $[Pr_4N]Co[N(CN)_2]_3$ as a function of temperature and axial pressure, as measured by pressure-volume-temperature analysis. The transition temperatures are indicated by dashed lines and highlight the disappearance of the two intermediate polymorphs at a critical pressure. (b) The correlation between the crystal radius of the B-site cation[317] and the temperature range of the intermediate phases, *i.e.* the difference between the two phase transition temperatures (T3−T1) found on heating from differential scanning calorimetry (DSC).[314,315] Adapted from Ref. 314 published by The Royal Society of Chemistry.

hances the chemical pressure [Fig. 1.16(b)].[314] This sophisticated degree of control of phase transition temperatures may be an important element in crystal engineering.

1.4.8 Metal dicyanometallate perovskites



$[PPN]Cd[Ag(CN)_2]_3{\cdot}3EtOH$[318]

The almost linear dicyanometallate anion $M(CN)_2^-$ (M^+ = Ag, Au) forms an impressive range of very diverse CPs; however the subset of perovskite-like compounds is relatively small [Fig. 1.8(h)].[318–320] The dicyanometallate anion spans about a nanometre and naturally, the selection of isotropic cations of sufficient size to occupy the A-site is limited. Indeed, virtually all known dicyanometallate perovskites contain the bulky bis(trisphenylphosphine)iminium cation (PPN) as the interstitial species and smaller, more anisotropic cations lead to the adoption of other structure types.[318]

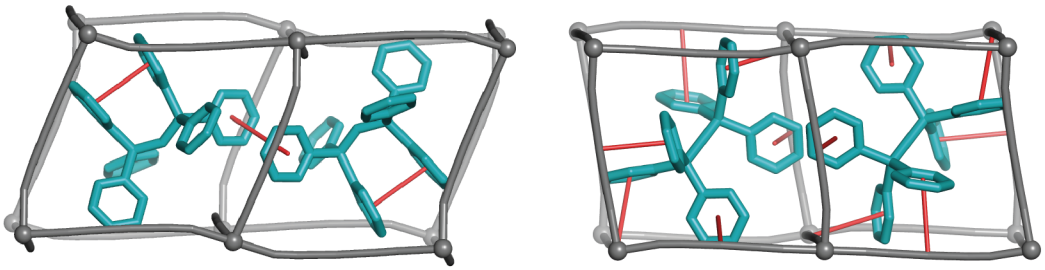


Figure 1.17: The monoclinic and rhombohedral phases of [PPN]B[Au(CN)$_2$]$_3$. In the monoclinic phase, the phenyl rings are orientated as to maximise the inter- and intramolecular π-π interactions, whereas in the rhombohedral phase, the aromatic rings are oriented towards the dicyanometallate linkers. Reproduced from Ref. 322.

Despite the paucity of known dicyanometallate perovskites and their compositional resemblance, there is a reasonable extent of variability in structural behaviour. For example, members of the series [PPN]B[Au(CN)$_2$]$_3$ (B^{2+} = Mn, Co, Ni, Cd) are isostructural ($R\bar{3}c$) at elevated temperature, but the Mn and Cd analogues undergo a phase transition to $I2/a$ upon cooling. This is driven by a change in tilting from $a^-a^-a^-$ to $a^-a^-c^-$ and a reorientation of the A-site cation [Fig. 1.17].[318,321] The lack of phase transitions for the Ni and Co analogues was hypothesised to arise from their nonzero ligand field stabilisation energy, in contrast to Mn^{2+} and Cd^{2+}.[318] A very different symmetry (cubic $Pa\bar{3}$) is obtained for the solvated [PPN]Cd[Ag(CN)$_2$]$_3$·3EtOH.[318] The structure of this system is discussed further in Section 1.5.1 in the context of its unconventional tilting.

The significant sizes of the cavity and pore windows of dicyanometallate perovskite facilitate direct interactions between adjacent A-site cations. The monoclinic phase of [PPN]B[Au(CN)$_2$]$_3$ contains π-π interactions between the phenyl rings, made feasible by the unusual conformation of PPN [Fig. 1.17]. The A-site can also be occupied by a combination of several smaller ions, as observed in the

tetragonal $[Bu_4N]Mn[Au(CN)_2]_3{\cdot}[Bu_4N]ClO_4$ ($P4/nnc$).[322] The formula may be abstracted as $ABX_3{\cdot}AY$: *i.e.* the usual BX_3 framework, but the Y *anion* is now located in the centre of the void and the A-site cations reside in four of the six faces of the perovskite pseudo-cube. A reconstructive phase transition occurs at higher temperatures, with loss of the perovskite topology. This salt inclusion perovskite can be considered as an inorganic co-crystal, representing a complex structural example unique to the large frameworks.

1.4.9 Other molecular perovskites

The examples considered above all consist of metal cations with coordinative bonds to covalent, anionic ligands. However, there are also numerous molecular perovskites held together by supramolecular interactions or delocalised bonds. Although not considered in any detail in this Thesis, a few examples are briefly mentioned here for interest.

Firstly, there are several examples of perovskites containing 3c–2e bonds with X = $BH_4^-/BF_4^-/ClO_4^-$ and these systems display some interesting and unusual features [Fig. 1.18(a)].[323–329] By way of example, inclusion of both protonic and hydridic hydrogen in the same compound has been demonstrated for $NH_4Ca(BH_4)_3$, leading to potential applications as hydrogen storage materials.[323] The presence of hydrides also opens up for new mechanisms for engineering lattice distortions, *e.g.* ferroelectricity induced by hydride order or rotational instabilities stabilised at *high* temperatures.[326] In most other perovskite materials, the rotational instabilities are the result of the condensation of a soft mode at low temperatures, and high-temperature

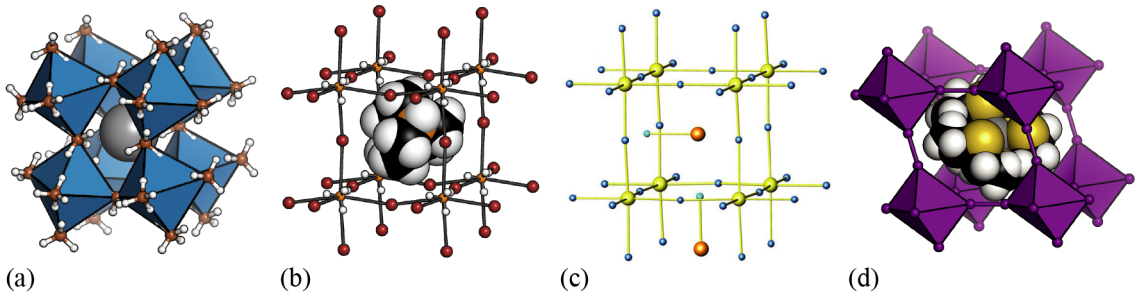


Figure 1.18: Molecular perovskites assembled by weak interactions. (a) The borohydride perovskite $CsSr(BH_4)_3$,[325] with Cs in white, Sr in blue, B in brown, and H in white; (b) a metal-free perovskite $[MDAB]NH_4Br_3$,[330] with C in black, N in orange, H in white, and Br in brown; (c) the postulated structure for the high-pressure phase of H_2S,[331] with S in yellow, and H in blue; and (d) the iodine-based $\{Ag[18]aneS_6\}I_7$,[332] with I in purple, and S in yellow. Panel c is adapted from Ref. 331. The figure is not to scale.

structures are likely to possess the aristotype symmetry.

Secondly, another intriguing case of perovskites based on tetrahedral moieties is that of metal-free perovskites, where the B-site is decorated by ammonium cations [Fig. 1.18(b)].[330] These are joined by halide ions to form a perovskite framework enclosing a divalent organic cation. By employing design strategies guided by the Curie symmetry principle[333]—the symmetry of a composite crystal cannot be higher than the largest common subgroup of its components—room-temperature ferroelectricity was recently demonstrated in $[MDAB]NH_4X_3$ (MDAB = methyldabconium and X = I^- or Br^-).[330] Moreover, the enclosure of chiral organic cations on the A-site allows access to optically active ferroelectric systems.[330]

Thirdly, it has been proposed that H_2S undergoes a pressure-induced decomposition to H_3S and SH^-.[331] On the basis of density functional theory (DFT) calculations, an antiperovskite structure was suggested, with SH_3 as the cationic framework and SH^- anions situated on the A-site [Fig. 1.18(c)].[331] This gives rise to a configurationally underconstrained state with correlated disorder of the SH vector. However, a recent study did not find any evidence of the postulated phase transition,

so the results are debated.[334] The high-pressure phase of H_2S is a conventional high-temperature superconductor, presenting an additional incentive for further study into the alleged phase transition.[335]

Finally, a more tangential example of a perovskite is provided by the supramolecular framework $\{Ag[18]aneS_6\}I_7$ [Fig. 1.18(d)], where $Ag[18]aneS_6$ denotes Ag^+ complexed by the sulfur-containing crown ether $[18]aneS_6$.[332] The formula may be recast as $\{Ag[18]aneS_6\}I(I_2)_3$ to emphasise the ABX_3 stoichiometry. Although this compound does not conform to the conventional definition of perovskite (*e.g.* species of distinct charge on the B- and X-site), it nevertheless constitutes a "cation in a box"* analogous to the perovskite structure.

1.5 Degrees of freedoms in molecular perovskites

The degrees of freedom in ceramic perovskites have been studied for over a century, uncovering many valuable relationships and phenomena. In light of the recent heightened interest in molecular perovskites, the obvious question arises: how are the degrees of freedom of a perovskite oxide altered upon molecular substitution at the A- and/or X-sites? At the onset of my DPhil project, this question had not been studied in any detail; however, a few remarks can be made based on simple considerations regarding the nature of molecular perovskites.

First, the charges of the A-site cations and X-site anions employed for molecular perovskites are typically limited to ± 1, which restricts the substitutional scope. In consequence, divalent B-site cations are necessary to maintain electroneutrality

*Not to be confused with a cat in a box, as famously and cruelly devised by Schrödinger.[336]

and the charge difference between distinct B-site metals never exceeds 2, as exemplified by the formate $(CH_3CH_2NH_3)Na^{+}_{0.5}Fe^{3+}_{0.5}(HCOO)_3$.[337] The smaller compositional playground also limits the possible cation orderings. Rocksalt patterns are predominant for bimetallic systems, driven either by cation differences or by asymmetric linkers such as cyanide and thiocyanate.[286,337] In contrast to conventional perovskites, aliovalent A-site substitution in the molecular congeners is very rare and isovalent substitution yields disordered structures.[258,338] Although some solid solutions of molecular perovskites have been synthesised, this is still a relatively nascent area, especially for solid solutions across the entire compositional range.[339] Overall, the substitutional degree of freedom is less versatile in molecular perovskites relative to conventional ceramics.

Second, the enhanced spatial separation of the B-sites due to the longer linker decreases the energy scale associated with intermetallic correlation. This is reflected by the reduced temperatures for the onset of magnetic order—with the exception of Prussian blue analogues specifically designed for this purpose[340]—and the lack of itinerant charge carriers in molecularly bridged frameworks. Thus, all X-site substituted molecular perovskites tend to be insulators or semiconductors with magnetic order only at very low temperatures, if at all present.[341] The weak coupling also prevents the formation of the strongly correlated electronic states commonly observed in oxide perovskites. As a result, the degrees of freedom relying on intermetallic correlations are likely to be more prone to disorder in molecular perovskites relative to the oxide congeners.

Third, second-order Jahn-Teller distortions are scarce in molecular perovskites,

although symmetry-equivalent deformations are feasible. B-site off-centring within an octahedron is rarely observed in coordination polymers[342] and in fact, the only genuine example of the SOJT effect is the lone-pair formation in organic halide perovskites, as discussed above.[150,343] Nevertheless, the SOJT distortions effectively comprise the emergence of a local dipole at the B-site and conceptually analogous distortions in molecular perovskites exist. For example, vacancies in defective PBAs can lead to the adoption of square pyramidal geometry and thereby an effective dipole moment. In response to the altered coordination environment, the B-site cation is predicted to displace from its high-symmetry position, reminiscent of a SOJT distortion.[199] Furthermore, a local polarisation of the Sr^{2+} ions in $(NH_4)Sr[Fe(CN)_6]$ develop upon hydration, as the water molecules coordinate to the Sr^{2+} ion in an ordered fashion.[344] Therefore, molecular perovskites exhibit deformations related to second-order Jahn-Teller distortions, albeit the underlying mechanisms differ.

Finally, the propensity for defects and their manifestation likely differ between molecular and inorganic systems. Oxide non-stoichiometry is well-known in canonical perovskites;[61,345] yet, defects in MOFs are an incipient area of research and few studies regarding molecular perovskites—with the exception of PBAs—have been carried out.[346–349] Hypothetically, the flexibility and directional bonding of molecular species may provide access to other low-energy structure types in addition to perovskite and so defects may perhaps facilitate the preferential formation of other topologies. By this argument, vacancies should be less prevalent in molecular perovskites relative to their inorganic counterparts. On the contrary, non-stoichiometry

is often difficult to probe experimentally and it is not impossible for molecular perovskites to harbour a wealth of defective states yet to be discovered. In any case, although there is currently little evidence in support of any significant defect concentration in molecular perovskites, it should certainly not be ruled out. Furthermore, molecular perovskites are a populous and heterogeneous class of compounds and the prevalence of structural defects is likely to be system dependent.

It is clear that molecular perovskites are less predisposed to certain degrees of freedom prevalent in conventional oxide perovskites, but the question still remains as to whether the presence of molecular species may facilitate additional distortions? In fact, a few examples of precisely these "unconventional" degrees of freedom—internal and conformational changes of a molecular A-site cation—were highlighted above, although they are not normally recognised as such [Section 1.4.1 and 1.4.8]. Furthermore, a rotational phonon mode, unconventional tilting, was investigated by a former DPhil student in this research group (Joshua Hill) and is presented below, as it will be of relevance for Chapter 3.

1.5.1 Unconventional tilting

Tilting in conventional perovskites was discussed in Section 1.3.4 and this analysis is also applicable to molecular perovskites. However, the requirement for out-of-phase tilting in directions perpendicular to the propagation vector is lifted in molecular perovskites and tilt patterns with new periodicities can appear [Fig. 1.19].[350] Glazer nomenclature is not sufficient to fully describe these unconventional tilting patterns, as it only captures the periodicity in one direction per axis. A full notation neces-

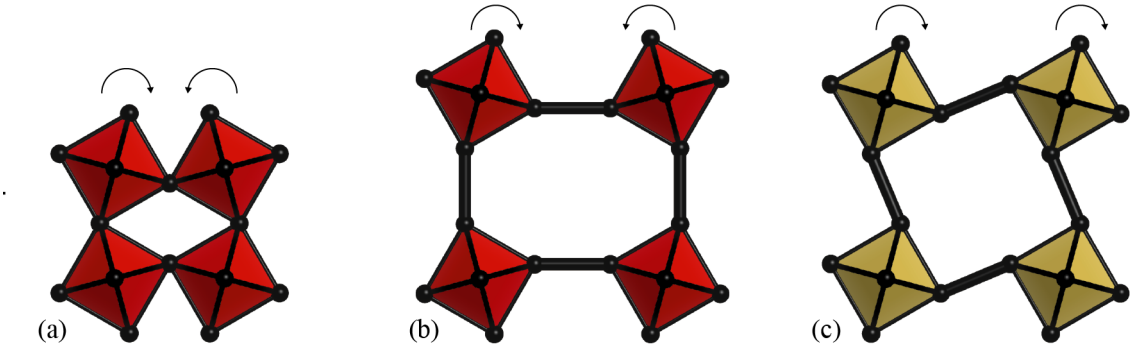


Figure 1.19: (a) Tilts in conventional perovskites are required to propagate with alternating signs of the tilt angle in the plane normal to the propagation axis. (b) This so-called conventional tilting is also realisable in molecular perovskites; yet the presence of polyatomic linkers also enables (c) unconventional tilting, where the tilt angles of neighbouring octahedra are in-phase correlated within the plane.

sitates a 3×3 matrix as introduced in Ref. 318 [Fig. 1.20]. Here, the element ij corresponds to the sense of the tilts around i propagating along direction j, giving:

$$\begin{bmatrix} aa & ab & ac \\ ba & bb & bc \\ ca & cb & cc \end{bmatrix}.$$

By way of example, the $a^+b^-b^-$ tilt in $GdFeO_3$ is described by

$$\begin{bmatrix} + & - & - \\ - & - & - \\ - & - & - \end{bmatrix},$$

where "+" and "−" refer to in-phase ($\mathbf{k} = 0$) and out-of-phase tilts ($\mathbf{k} = \frac{1}{2}$), respectively. The diagonal of this matrix is identical to the set of superscripts in Glazer notation and for a conventional perovskite, the off-diagonal elements are necessarily "−". As a result, unconventional tilting can be identified by non-negative

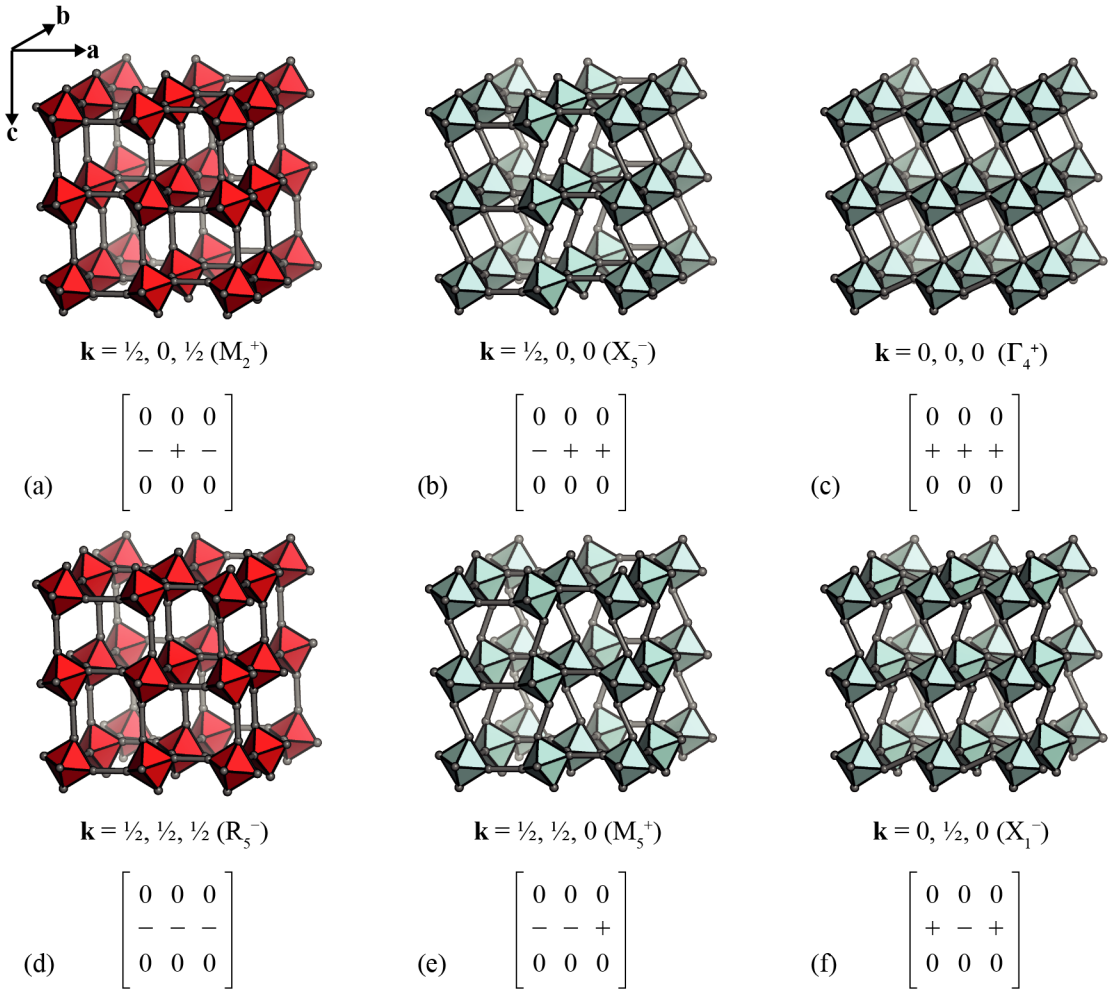


Figure 1.20: The tilt systems in a molecular perovskite generated by zone-centre and zone-boundary periodicities, including the relevant propagation vector and the notation in matrix form from Ref. 318. Tilt patterns realisable in inorganic perovskites are shown in red and those unique to molecular perovskites in cyan.

off-diagonal entries in the tilt matrix. An illustrative example is the dicyanometallate $[PPN]Cd[Ag(CN)_2]_3{\cdot}3EtOH$, introduced in Section 1.4.8.[318] It crystallises in the cubic space group $Pa\bar{3}$ with a tilt system of

$$\begin{bmatrix} - & - & + \\ + & - & - \\ - & + & - \end{bmatrix}.$$

In other words, the tilt pattern comprises out-of-phase tilts along the rotation axis, in-phase (unconventional) tilts in one of the perpendicular directions and out-of-phase tilts along the remaining perpendicular direction (irrep M_5^+) [Fig. 1.20(e)]. The Glazer notation for this tilt pattern is $a^-a^-a^-$, which thus fails to capture the unconventional (off-diagonal) component.

Although the tilt matrix is a useful tool, it does not adequately describe tilting at less symmetrical points in reciprocal space. Tilts with $\mathbf{k} = \frac{1}{4}$ have been reported in both conventional and molecular perovskites[284,351] and for these systems, the use of **k**-vectors instead of $+/-$ is advantageous. With this formalism, the tilt system of [PPN]Cd[Ag(CN)$_2$]$_3$·3EtOH is given by

$$\begin{bmatrix} \frac{1}{2} & \frac{1}{2} & 0 \\ 0 & \frac{1}{2} & \frac{1}{2} \\ \frac{1}{2} & 0 & \frac{1}{2} \end{bmatrix}.$$

Here, caution must be exerted to avoid confusion arising from the Glazer index "0" (denoting absence of tilts) and the **k**-vector "0" (denoting infinite periodicity). The $+/-$ indices employed in Glazer notation can be converted to the components of the propagation vector, $0/\frac{1}{2}$, through $+1 = \exp 2\pi\mathrm{i}\cdot 0$ and $-1 = \exp 2\pi\mathrm{i}\cdot\frac{1}{2}$. Given these relations, an alternative means of representing low-symmetry tilts is the use of imaginary components as entries in the tilt tensor, by recognising that $\mathrm{i} = \exp 2\pi\mathrm{i} \cdot \frac{1}{4}$.

1.6 Thesis outline

The aim of this Thesis is to investigate degrees of freedom in molecular perovskites in the context of the vast research already carried out on conventional perovskites. A particular focus is placed on the unconventional distortion modes and their implications for the functional and structural response. It is hoped that these results will provide a foundation for understanding these systems in more detail, with a view towards the prospect of targeted materials design. The methods employed range from analysis of previously published crystal structures to theoretical simulations and experimental studies. These various methods are discussed in detail in the ensuing Chapter.

Chapter 3 concerns a previously unexplored degree of freedom named columnar shifts, which consists of columns of octahedra collectively displacing relative to each other.[352] As for tilting, this degree of freedom corresponds to a rigid unit mode and has a strong influence on the structure and properties of the host compound, both in its dynamic and static forms. It will be shown that shifts are likely to drive negative thermal expansion in molecular perovskites and they can also act as primary order parameters in phase transitions. The Chapter concludes with a discussion of the factors affecting the prevalence and periodicity of shifts in various families of molecular perovskites, which may form the basis for simple design rules.

Chapter 4 is focussed on Jahn-Teller distortions, which have received relatively little attention in molecular perovskites despite their importance in the physics of conventional perovskites. The compositional dependence of orbital order is investi-

gated in the three systems $[C(NH_2)_3]Mn_{1-x}Cu_x(HCOO)_3$, $(Mn_{1-x}Cu_x)_3[B'(CN)_6]_2$ and $Mn_{1-x}Cu_x[Pt(CN)_6]$ using crystallographic and Monte Carlo techniques. The Monte Carlo model is adapted from the literature on conventional perovskites and predicts continuously variable JT distortions, analogous to XY magnets. The predisposition towards orbital order or disorder within a given system is found to be strongly dependent on the topology of the lattice, including the presence or absence of defects.

Chapter 5 considers the role played by the unconventional degrees of freedom in breaking the global inversion symmetry *via* hybrid improper ferroelectricity. Representation theory is used to reveal a profound enhancement of the number of accessible polar coupling schemes as a direct result of molecular substitution. Hence, it is demonstrated that simple molecular perovskites are more prone to crystallising in acentric space groups than their inorganic counterparts and a few as-yet unrealised molecular perovskites are predicted to adopt polar space groups. Not only is this of relevance for the development of candidates for ferroelectric applications, but also for nonlinear optic materials and other applications relying on the absence of centrosymmetry.

Lastly, the final Chapter summarises the results presented and places them in the context of other molecular mineral analogues. There are a vast number of such "mineralomimetic" materials and they frequently exhibit analogues of the unconventional distortions investigated here.[353,354] This illustrates how the concept of "unconventional" degrees of freedom is quite general and can readily be extended beyond perovskites.

Chapter 2

Methods

This Chapter provides the necessary background to the theory and techniques exploited throughout this Thesis with a particular emphasis on crystallography and symmetry. The theory follows standard textbook treatment.[119,355–357]

2.1 Structure determination

2.1.1 Crystal structures and symmetry

A crystal is defined as a repeating arrangement of particles (ions, atoms or molecules) with translational symmetry. This can be restated mathematically as the convolution of a motif with a lattice, *i.e.*

$$\rho(\mathbf{r}) = \text{lattice} \otimes \text{motif}, \tag{2.1}$$

where $\rho(\mathbf{r})$ is the electron density of a crystal and $\mathbf{r}$ is a vector [Fig. 2.1]. A 3D lattice is a regular array of points in space stipulated by the lengths and orientations of the three linearly independent basis vectors $\mathbf{a}$, $\mathbf{b}$, and $\mathbf{c}$. Thus, the location of electron density within a motif can be specified by coordinates x, y, z, where:

$$\mathbf{r} = x\mathbf{a} + y\mathbf{b} + z\mathbf{c}. \tag{2.2}$$

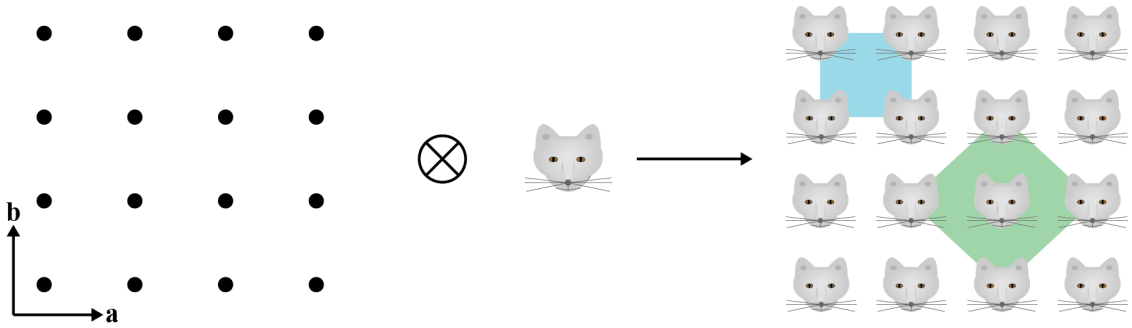


Figure 2.1: Schematic depiction of a 2D crystal structure as a convolution of a lattice with a motif, in this case an arctic fox. The basis vectors are indicated by arrows and two choices of unit cells are shown: a primitive cell (blue) and a centred cell (green). The plane group is pm.

As a consequence of translational symmetry, a crystal structure can also be viewed as a three-dimensional tiling of a repeating parallelepiped or unit cell. Primitive cells contain one single lattice point, whereas centred cells comprise additional lattice points, usually situated at the cell face(s) or centre. There is not a unique choice for the unit cell; rather, it is generally chosen to emphasise the underlying symmetry of the crystal structure.

The majority of crystal structures contains additional symmetry elements in addition to the inherent translational symmetry. The presence of any rotation axes—proper or improper—imposes strict rules on the allowed relative cell parameters (a, b, c) and angles (α, β, γ) of the unit cell. As a result, only seven geometries are allowable, which are known as the seven crystal systems [Table 2.1]. Combining these crystal systems with the possible centrings produces the 14 Bravais lattices. Moreover, the addition of further symmetry elements to the minimum symmetry defining the seven crystal systems generates the 32 crystallographic point groups. They form groups in a mathematical sense, rendering group theory a particularly useful approach to analyse changes in symmetry, for instance during a phase transition. However, as crystals extend in three dimensions, space groups—or, more correctly,

Table 2.1: The minimum symmetry, lattice parameters and allowed centrings for the seven crystal systems. Only standard settings are considered.

Crystal system	Minimum symmetry	Lattice parameters	Allowed centrings
Triclinic	none	$a \neq b \neq c$ $\alpha \neq \beta \neq \gamma$	P
Monoclinic	one two-fold or mirror	$a \neq b \neq c$ $\alpha = \gamma = 90° \neq \beta$	P, C
Orthorhombic	three two-folds or mirrors	$a \neq b \neq c$ $\alpha = \beta = \gamma = 90°$	P, C, I, F
Tetragonal	one four-fold	$a = b \neq c$ $\alpha = \beta = \gamma = 90°$	P, I
Trigonal	one three-fold	$a = b \neq c$ $\alpha = \beta = 90°$, $\gamma = 120°$	P, R
Hexagonal	one six-fold	$a = b \neq c$ $\alpha = \beta = 90°$, $\gamma = 120°$	P
Cubic	four three-folds	$a = b = c$ $\alpha = \beta = \gamma = 90°$	P, I, F

space group types—are needed for a full description of the symmetry. These arise from the combination of the Bravais lattices with the relevant point groups. All crystalline materials belong to one of the 230 crystallographic space groups and detailed information regarding their properties is listed in the International Tables of Crystallography.[358] The 2D analogues are known as plane groups, sometimes also colloquially referred to as wallpaper groups. By virtue of the higher dimensions, space groups—and also to some extent, plane groups—can comprise translational symmetry elements such as glide planes and screw axes, which do not occur in point groups.

2.1.2 Scattering theory and reciprocal space

Structure determination is at the very heart of solid-state science and several Nobel prizes have been awarded in honour of significant accomplishments within the development of X-ray diffraction (XRD) and related techniques.[359] These methods

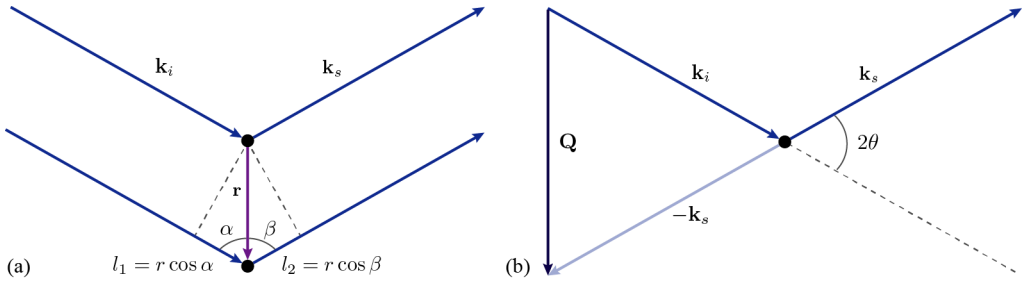


Figure 2.2: (a) The scattering of radiation from a pair of particles and (b) the geometric relationship between $\mathbf{k}_\mathrm{i}$, $\mathbf{k}_\mathrm{s}$, $\mathbf{Q}$, and 2θ.

are based on the underlying idea that radiation scattered by a material produces a pattern of scattered radiation, where the intensities are proportional to the square of the structure factor, $F(\mathbf{Q})$, of the material. $F(\mathbf{Q})$ corresponds to the Fourier transform of the electron density distribution* and so provides information regarding the crystal structure. The expression for $F(\mathbf{Q})$ can be derived by first treating the scattering of radiation from a pair of particles followed by extension to an arbitrary number of particles, as is now to be demonstrated.

Consider incident radiation with propagation vector $\mathbf{k}_\mathrm{i}$ (where $|\mathbf{k}_\mathrm{i}| = \frac{2\pi}{\lambda}$) scattered by a pair of point particles separated by the vector $\mathbf{r}$ [Fig. 2.2(a)]. The radiation scatters elastically in all directions, but the focus here is on the wave exiting with propagation vector $\mathbf{k}_\mathrm{s}$. The two beams are in phase prior to the interaction with the particles; yet the second beam travels a longer distance and thus its phase is shifted relative to the first beam. Consequently, the two rays are no longer perfectly in phase after the scattering event. The task is to understand how the amplitude of the incident radiation is altered upon scattering as a result of the phase shift of the second beam. The difference in path lengths between the beams is given by $l_1 + l_2$, which, by trivial geometry, can be shown to equal

*For the diffraction of X-rays.

$$l_1 + l_2 = \frac{\lambda}{2\pi}[(\mathbf{k}_\mathrm{i} - \mathbf{k}_\mathrm{s}) \cdot \mathbf{r}] \tag{2.3}$$

and consequently the phase difference, ϕ, is given by

$$\phi = (\mathbf{k}_\mathrm{i} - \mathbf{k}_\mathrm{s}) \cdot \mathbf{r} = \mathbf{Q} \cdot \mathbf{r}, \tag{2.4}$$

by defining the scattering vector $\mathbf{Q} = \mathbf{k}_\mathrm{i} - \mathbf{k}_\mathrm{s}$. The importance of $\mathbf{Q}$ becomes apparent when considering its magnitude, *i.e.*

$$|\mathbf{Q}| = Q = \frac{4\pi}{\lambda} \sin\theta, \tag{2.5}$$

where 2θ is the angle between $\mathbf{k}_\mathrm{i}$ and $\mathbf{k}_\mathrm{s}$ [Fig. 2.2(b)]. This formula is reminiscent of Bragg's well-known diffraction law,

$$\lambda = 2d \sin\theta, \tag{2.6}$$

where $d = |\mathbf{r}|$. It can hence be deduced that

$$Q = \frac{2\pi}{d}. \tag{2.7}$$

Therefore, $\mathbf{Q}$ is related to the phase difference between the two scattered beams, which in turn depends on the inverse interatomic spacings. The wave equation of the radiation after the scattering event is the sum of the wave equations for the two

beams, *i.e.*

$$\exp(\mathrm{i}\mathbf{k}_\mathrm{s}\mathbf{x}) + \exp(\mathrm{i}\mathbf{k}_\mathrm{s}\mathbf{x} \times \mathbf{Q} \cdot \mathbf{r}) = \exp(\mathrm{i}\mathbf{k}_\mathrm{s}\mathbf{x})[1 + \exp(\mathrm{i}\mathbf{Q} \cdot \mathbf{r})], \tag{2.8}$$

where $\mathbf{x}$ is the axis along which the wave propagates. The quantity $[1 + \exp(\mathrm{i}\mathbf{Q} \cdot \mathbf{r})]$ is known as the structure factor, $F(\mathbf{Q})$, and gives the particle interference function of the radiation following scattering. In the case of a collection of particles—as in an extended solid—$F(\mathbf{Q})$ is easily generalised to give

$$F(\mathbf{Q}) = \exp(\mathrm{i}\mathbf{Q} \cdot 0) + \exp(\mathrm{i}\mathbf{Q} \cdot \mathbf{r}_1) + \exp(\mathrm{i}\mathbf{Q} \cdot \mathbf{r}_2) + ... = \sum_j \exp(\mathrm{i}\mathbf{Q} \cdot \mathbf{r}_j). \tag{2.9}$$

This expression describes the scattering of radiation from a system comprising an arbitrary number of point-like identical particles. Allowing for a continuous distribution of electron density instead of discrete particles leads to the integral

$$F(\mathbf{Q}) = \int \rho(\mathbf{r}) \exp \mathrm{i}\mathbf{Q} \cdot \mathbf{r} \mathrm{d}\mathbf{r}. \tag{2.10}$$

Hence, the structure factor corresponds to the Fourier transform of the crystal structure, which is a convolution of a motif and a lattice. The convolution theorem states that the Fourier transform of a convolution is equal to the product of the Fourier transforms of the individual components in the convolution. Therefore, the structure factor is a product of the Fourier transforms of the lattice and the motif, which allows for a deeper understanding of the form of the structure factor. The Fourier transform of a lattice yields another lattice, known as the reciprocal lattice.

This is described by the reciprocal basis vectors ($\mathbf{a}^*$, $\mathbf{b}^*$, $\mathbf{c}^*$), which are related to the real lattice vectors:

$$\mathbf{a}^* = \frac{2\pi}{V_{\text{cell}}}\mathbf{b} \times \mathbf{c}, \tag{2.11}$$

where V_{cell} is the volume of the unit cell. Similar formulae can be obtained for $\mathbf{b}^*$ and $\mathbf{c}^*$ by cyclic permutation. For crystal systems with orthogonal basis vectors (*i.e.* orthorhombic, tetragonal and cubic), $\mathbf{a}^*$ is parallel to $\mathbf{a}$ with length $\frac{2\pi}{a}$. The locations of the reciprocal lattice points are given by the reciprocal lattice vector

$$\mathbf{Q} = h\mathbf{a}^* + k\mathbf{b}^* + l\mathbf{c}^*, \tag{2.12}$$

for integer values of the Miller indices $\{hkl\}$. In real space, the Miller indices label the set of crystal planes intersecting the unit cell axes at $(\frac{a}{h}, \frac{b}{k}, \frac{c}{l})$. The appearances of diffraction patterns should now be apparent: $F(\mathbf{Q})$ correlates with the intensity distribution in a scattering experiment and Eq. 2.12 shows that intensity is only observed when $\mathbf{Q}$ is equal to a reciprocal lattice point. Reciprocal space is an imperative concept in condensed matter physics and—as will be elaborated upon in subsequent Sections—a particularly useful construction is the first Brillouin zone (BZ), *i.e.* the Wigner-Seitz cell located at the origin of reciprocal space [Fig. 2.3]. High-symmetry points within the BZ are labelled by their Bradley-Cracknell symbols and this notation will be widely used throughout this Thesis.[360]

The Fourier transform of the motif also requires the application of the convolution theorem, as the motif is a convolution of the atomic positions with their electron density (and thermal motion). As the atomic positions are described by

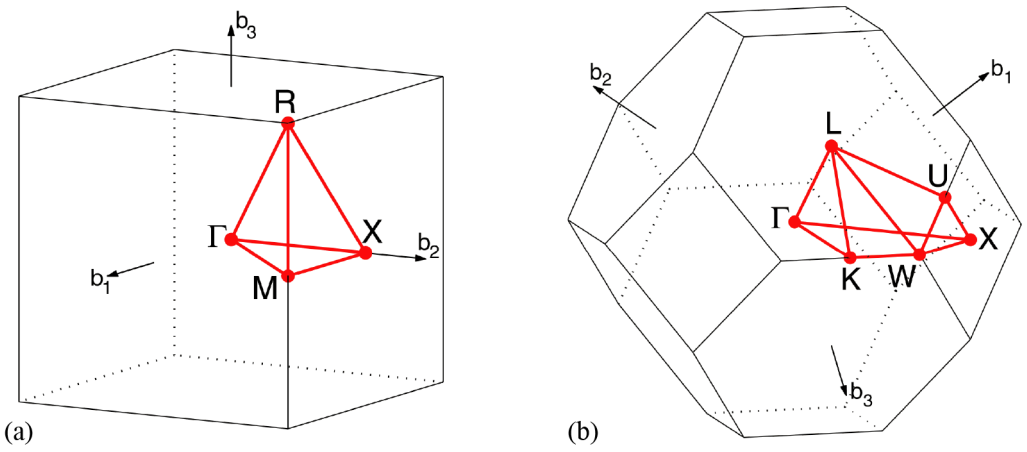


Figure 2.3: The first Brillouin zone for (a) a primitive cubic and (b) a face-centred cubic unit cell. The high-symmetry points are labelled by the Bradley-Cracknell notation. Reprinted from *Comput. Mater. Sci.*, **49**, W. Setyawan and S. Curtarolo, "High-throughput electronic band structure calculations: Challenges and tools", 299–312, Copyright 2010, with permission from Elsevier.[361]

delta functions in real space, their Fourier transforms are exponential functions of the form $\exp(\mathrm{i}\mathbf{Q}\cdot\mathbf{r})$. The Fourier transform of the electron density is a $\mathbf{Q}$-dependent function known as the atomic scattering factor, $f_j(\mathbf{Q})$, where j indexes the different atoms in the motif. So by applying the convolution theorem, the description of the motif in reciprocal space is determined as $\sum_j f_j(\mathbf{Q})\exp(\mathrm{i}\mathbf{Q}\cdot\mathbf{r}_j)$. By substituting the explicit definitions of $\mathbf{Q}$ and $\mathbf{r}$, it emerges that

$$\mathbf{Q}\cdot\mathbf{r}_j = (h\mathbf{a}^* + k\mathbf{b}^* + l\mathbf{c}^*)\cdot(x_j\mathbf{a} + y_j\mathbf{b} + z_j\mathbf{c}) = 2\pi(hx_j + ky_j + lz_j) \qquad (2.13)$$

and therefore

$$F(\mathbf{Q}) = \sum_j f_j(\mathbf{Q})\exp(\mathrm{i}\mathbf{Q}\cdot\mathbf{r}_j) = \sum_j f_j(\mathbf{Q})\exp[2\pi\mathrm{i}(hx_j + ky_j + lz_j)]. \qquad (2.14)$$

As $\{hkl\} \in \mathbb{N}$ (where $\mathbb{N}$ is the set of natural numbers), it is clear that $F(\mathbf{Q})$ is only nonzero at well-defined locations in space and zero valued everywhere else, as

noted above. Eq. 2.14 also indicates that the positions of the diffraction spots are related to the symmetry and dimensions of the real lattice, whereas the intensity correlates with the type of atoms present and their arrangement in the unit cell. The scattering factor is an exponential function whose magnitude decays with $\mathbf{Q}$ and so the intensity of reflections in an XRD pattern decreases as the scattering angle increases.

2.1.3 Diffraction experiments

When carrying out a diffraction experiment on a single crystal, the crystal is mounted in a small loop in the diffractometer, aligned with the beam direction and subsequently illuminated with X-rays. An area detector is usually employed to record the scattered radiation and by rotating the crystal, diffraction from a large fraction of reciprocal space can be collected. Following the data collection, the task at hand involves determining the unit cell and space group, obtaining a structural model (structure solution) and finally refining this initial model. Since the symmetry of the reciprocal lattice is related to that of the real lattice, the crystal system and dimensions of the unit cell can be determined by the positions of the diffracted reflections—a process known as indexing.

Finding the correct space group can be less straightforward, but is aided by the search for systematically absent reflections, also known as reflection conditions. These are positions in reciprocal space where a reflection would be predicted based on the crystal system, but where symmetry dictates intensities of zero. Systematic absences occur for structures with centred cells and/or translational symmetry el-

ements. As an illustration, consider a 2_1 screw axis along **c**. For every atom at x, y, z, there is another symmetry-related atom located at $\bar{x}$, $\bar{y}$, $z + \frac{1}{2}$ and thus the structure factor for these two positions becomes

$$F(hkl) = f_j(\mathbf{Q})\{\exp[2\pi\mathrm{i}(hx_j + ky_j + lz_j)] + \exp[2\pi\mathrm{i}(-hx_j - ky_j + l\{z_j + \frac{1}{2}\})]\} \quad (2.15)$$

and so for $F(00l)$,

$$\begin{aligned} F(00l) &= f_j(\mathbf{Q})[\exp(2\pi\mathrm{i}lz_j) + \exp(2\pi\mathrm{i}l\{z_j + \frac{1}{2}\})] \\ &= f_j(\mathbf{Q})\exp(2\pi\mathrm{i}lz_j)[1 + \exp(\pi\mathrm{i}l)] \\ &= f_j(\mathbf{Q})\exp(2\pi\mathrm{i}lz_j)[1 + (-1)^l]. \end{aligned} \quad (2.16)$$

As a result, the structure factor only assumes nonzero values along the $00l$ line in reciprocal space if l is even. Similar relations can be derived for the various unit cell centrings and glide planes. In this manner, systematic absences can be useful as a means to limit the choice of candidate space groups; however, many space groups show identical reflection conditions—such as $Pmmm$ and $Pmm2$. Consequently, space groups cannot generally be uniquely defined solely by the observation of systematic absences and other techniques may be required. A situation where two space groups can be discriminated based on their reflection conditions will be demonstrated in Chapter 4.

Following determination of a suitable space group, an initial starting model has to be found. As the structure factor corresponds to the Fourier transform of the crystal structure, performing the reverse Fourier transform of $F(\mathbf{Q})$ will generate

the spatial electron density distribution. However, the structure factor is a complex number and only $|F(\mathbf{Q})|^2$ is accessed from a diffraction experiment. Hence, the amplitudes of the structure factor can be measured, whereas the phases remain unknown. This is known as the "phase problem" and has presented a significant challenge for crystallographers during the development of diffraction techniques. Various tools have been designed to overcome the phase problem, including the Patterson synthesis,[362] Sayre's equation,[363] direct methods,[364] and, more recently, charge flipping.[365] These methods allow for structural solution and the development of a starting structural model. This initial model subsequently has to be refined, usually by a nonlinear least squares method as explained in the next Section in the context of Rietveld refinement. Nowadays, modern software and powerful computation mean that structure solution and refinement is largely automated and can be performed routinely for high-quality crystals.

2.1.4 Powder diffraction

Sometimes, single crystals of sufficient dimensions cannot be grown or they may be prone to intergrowth, preventing structure determination by the approach outlined above. Fortunately, powder X-ray diffraction (PXRD) provides an alternative analytic pathway, which—despite limitations compared to analysis of single crystal data—is a powerful tool. Powdered samples contain small crystallites with random orientations and the resulting powder pattern therefore consists of a large number of superimposed single crystal patterns [Fig. 2.4]. Hence, instead of well-resolved single reflections, 2D powder rings are observed. Due to the peak overlap, reliable intensities cannot necessarily be extracted in order to determine $|F(\mathbf{Q})|^2$. Direct

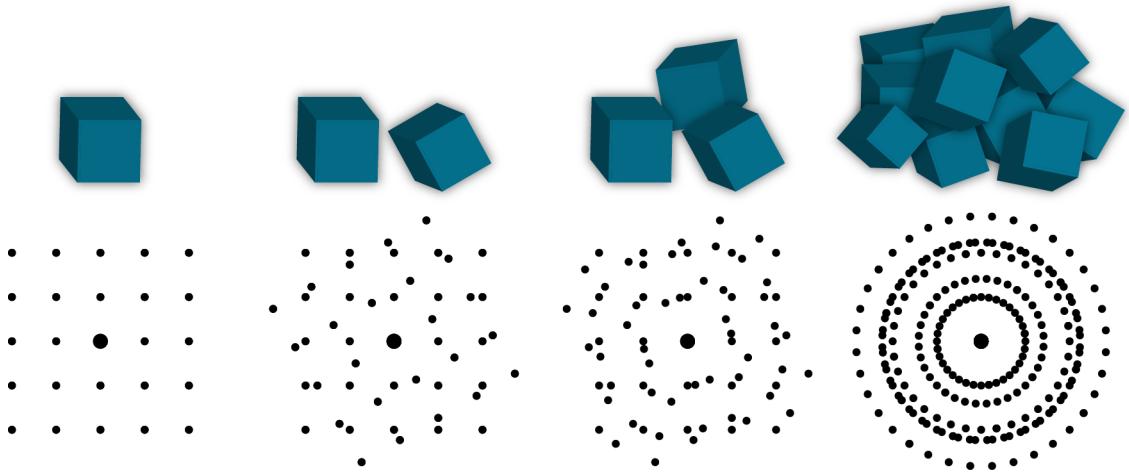


Figure 2.4: The presence of infinitely many crystallites in a powder sample leads to overlap of the single crystal diffraction pattern and the characteristic powder rings. Compression of the pattern yields the one-dimensional powder pattern as a function of $\mathbf{Q}$ or 2θ.

structure solution is therefore much less straightforward. Nevertheless, the position of the rings in the radial direction—usually plotted on a 1D scale—and their Miller indices still provide information about the size and symmetry of the unit cell by the process of indexing.

Powder diffraction relies on the presence of infinitely many randomly oriented crystallites to give a perfect averaging of the intensities, yet this does not always occur. Sometimes a particular arrangement of the crystallites is strongly favoured; a phenomenon known as preferred orientation. As a result, the intensity distribution is distorted and weak reflections may not be observed at all. Preferred orientation mainly occurs for systems with a propensity for the formation of crystallites with plate- or needle-like morphology and is exacerbated by small sample volumes. The problem can be partially overcome by careful grinding prior to the experiment and by rotating the sample during data collection.

Rietveld refinement

In cases where a starting model for the crystal structure is available, the method now known as Rietveld refinement enables structural determination from powder diffraction data.[366] The calculated powder pattern of the starting model is compared to the experimental data profile and the agreement is quantified by the weighted R-factor

$$R_{\mathrm{wp}} = \sqrt{\frac{\sum w_i (Y_{i,e} - Y_{i,c})^2}{\sum w_i Y_{i,e}^2}}, \tag{2.17}$$

where $Y_{i,e}$ and $Y_{i,c}$ represent the experimental and calculated intensity at position i and w is a weighting factor. Usually, the weights are defined as the inverse of the variance of the observed intensity.[357] By employing a nonlinear least squares refinement algorithm, the parameters of the starting model are gradually and iteratively adjusted in order to minimise R_{wp}. Common refineable parameters include the lattice parameters, the atomic positions and their thermal displacement parameters, as well as instrument parameters. It should be noted that a low R-factor is not necessarily indicative of a sensible solution and care must be taken when evaluating the result from a refinement.[367]

Pawley refinement

Prior to Rietveld refinement, it is often advisable to carry out a whole pattern fitting through the Pawley or Le Bail method.[368,369] These techniques fit the experimental profile to a given unit cell and space group, but without consideration of an explicit structural model. Instead, a Pawley refinement treats the intensities as freely adjustable parameters. This enables accurate determination of the unit cell and

peak shape, which may then be fixed in a subsequent Rietveld refinement. Whole pattern fitting is also valuable when monitoring the change in lattice parameter as a function of some external stimulus or when determining the space group for an unknown structure.

Despite the shortcomings of powder diffraction compared to the single crystal counterpart, it is widely used due to its simplicity and availability. There are a number of software packages implementing the Rietveld method—*e.g.* TOPAS,[370] GSAS,[371] and FullProf[372]—and as long as a sufficiently accurate starting model is accessible, structural analysis using high-quality PXRD data is certainly feasible.

2.1.5 Radiation sources

The interference effects exploited in scattering techniques are most pronounced for radiation with wavelengths similar to the spacings of the scattering objects. By consequence, diffraction by electromagnetic waves requires the use of X-rays, as these feature wavelengths ($\lambda \approx 1\,\text{Å}$) of the same order of magnitudes as the interatomic distances. As the production of X-rays is relatively straightforward, it is the most widespread and available type of radiation for diffraction experiments.

In lab-based diffractometers, X-ray vacuum tubes generate the incident radiation by firing a high-energy beam of electrons at a heavy metal target. The incoming electrons are sufficiently energetic to expel a core electron from the metal, leading to the relaxation of a higher-energy electron to fill the vacant orbital. This process leads to the emission of X-rays with discrete energies, each of which is characteristic of the metal and electronic transition in question. Usually, the transition between

the L and K shell is used, giving rise to Kα radiation. As a result of spin-orbit coupling, two sharp lines of X-rays with similar wavelength are produced, denoted Kα_1 and Kα_2 in Siegbahn notation.* Often, but not always, the radiation will be monochromated such that only the more intense Kα_1 emission is utilised. In any case, the sharp emission lines must always be filtered from the broad Bremsstrahlung (braking radiation), created by the deceleration of the incident electrons during the interaction with the metal.

The wavelength of the produced X-rays is a function of the particular heavy element used as the target. Copper is the predominant choice of metal ($\lambda = 1.541\,\text{Å}$), but molybdenum ($\lambda = 0.709\,\text{Å}$) and silver ($\lambda = 0.559\,\text{Å}$) sources are also in use.[374] The most suitable wavelength for a given system depends on the characteristics of the sample, in particular its volume and composition. Higher diffraction intensities are obtained with longer wavelengths, which can be useful for weakly scattering and/or small crystals. On the contrary, shorter wavelengths are less prone to absorption and this is especially relevant for metal-containing samples. Shorter wavelengths also enable the collection of a larger **Q**-range and thereby an enhanced real-space resolution. It follows that the choice of wavelength is a vital consideration for the success of a diffraction experiment.

Sometimes the intensity and resolution offered by lab-based diffractometers are insufficient, or specialist equipment is required. In those cases, the use of synchrotron radiation is necessary, *i.e.* the radiation generated by a charged particle during acceleration. In a synchrotron light source, electrons are accelerated to relativistic speeds

*Although the use of Siegbahn notation is discouraged by IUPAC,[373] it will be used here due to its prevalence within the crystallography community.

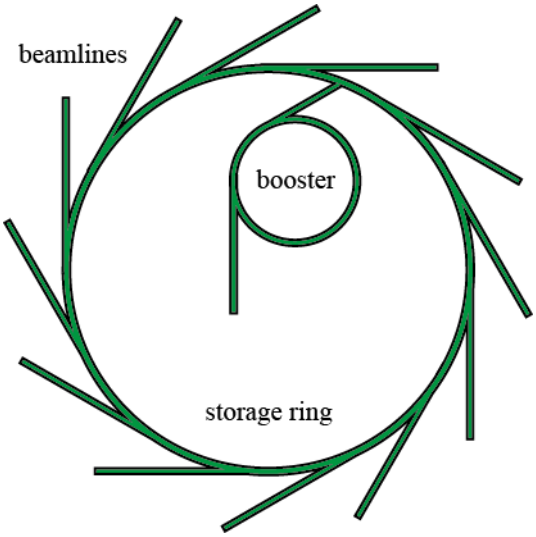


Figure 2.5: A schematic depiction of a synchrotron light source.

prior to entering a large storage ring, which tends to measure several hundred metres in diameter [Fig. 2.5]. Despite its name, a storage ring is not circular, but rather a multi-edged polygon with bending magnets located at the corners. These steer the electrons and thus generate synchrotron radiation from the electronic acceleration. The straight sections contain arrays of magnets known as insertion devices that induce an oscillation of the electrons and the emission of electromagnetic radiation of even higher intensity. The emitted light is focussed and filtered in beamlines, where the experiments are conducted. In general, each beamline is optimised for a certain application—*e.g.* extreme conditions, high resolution, or high energy—and the wavelength and flux of the beam will be fine-tuned to meet the specific needs. In the UK, Diamond Light Source (DLS) is a synchrotron light source located in Oxfordshire, featuring almost 40 beamlines with applications from X-ray diffraction under various conditions to spectroscopy and imaging.[375] The PXRD patterns presented in Chapter 4 were collected at beamline I11, which specialises in high-resolution powder diffraction.[376]

The focus so far has been on diffraction by X-rays, but particle beams such as thermal neutrons or electrons can also be employed. In neutron scattering, the atomic scattering factor, $f_j(\mathbf{Q})$, is replaced by the $\mathbf{Q}$-invariant neutron scattering length, b_j. Consequently, nuclear neutron data does not feature the decrease of intensity with scattering angle that is characteristic of XRD patterns. Moreover, the neutron scattering length varies nonlinearly with atomic number and so the differentiation between elements with similar numbers of electrons, such as C and N, is facilitated. The sensitivity to light elements in the presence of heavier congeners is also greatly augmented as neutrons are not scattered by the electron density. However, due to the inefficiency of the production of thermal neutrons, the flux is significantly lower than synchrotron radiation, leading to the requirement of large samples and long collection times. There are no lab-based neutron sources and so national facilities are required. A further drawback of neutron scattering in the context of the present study is the large incoherent scattering length of hydrogen, which reduces the resolution and increases the background. Hence, although neutron scattering offers a number of advantages, it is less straightforward to apply to systems with organic moieties—such as most molecular perovskites—relative to XRD.

Electrons accelerated through a potential difference of 10–50 keV also possess suitable wavelengths for scattering by crystals.[356] These high-energy electrons are strongly scattered by matter and electron diffraction allows for the study of crystals of insufficient size for analysis by X-rays.[377] The high interaction strength also facilitates rapid data collection, enabling ultrafast dynamical processes to be probed.[378] However, the high energies often lead to degradation of fragile moieties within beam-

sensitive samples, which limits the range of suitable systems.[377] As a result, electron diffraction is rarely used for coordination polymers.

2.1.6 Limitations of diffraction techniques

Despite the utility of diffraction techniques, their limitations should not be underestimated. Coherent diffraction relies on the presence of long-range order within the sample and this has important ramifications. The crystal structure observed by scattering techniques constitutes a temporary and spatially averaged structure, which may be significantly different from the local structure.[90,106,177] Moreover, there is little information regarding the dynamic processes in a material and randomly distributed defects are normally not detected. In those cases, local characterisation techniques, such as pair distribution functions (PDF), X-ray absorption spectroscopy (XAS) or nuclear magnetic resonance (NMR) are required.

Nevertheless, scattering techniques are sensitive to the presence of *non-random* disorder. In certain materials, the interactions governing order may not be sufficient to yield a unique ground state, or act in competition to give frustration.[379] Such states are not random, although the long-range order is absent. These scenarios are encapsulated in the concept of correlated disorder and manifest as highly structured streaks of intensity—in addition to the Bragg reflections—in single crystal diffraction patterns, known as diffuse scattering [Fig. 2.6]. In powder patterns, diffuse scattering is often merged with the background and in-depth analysis is more difficult. The extraction of information regarding local correlations from diffuse scattering is desirable, as it features in a wide range of ostensibly different materi-

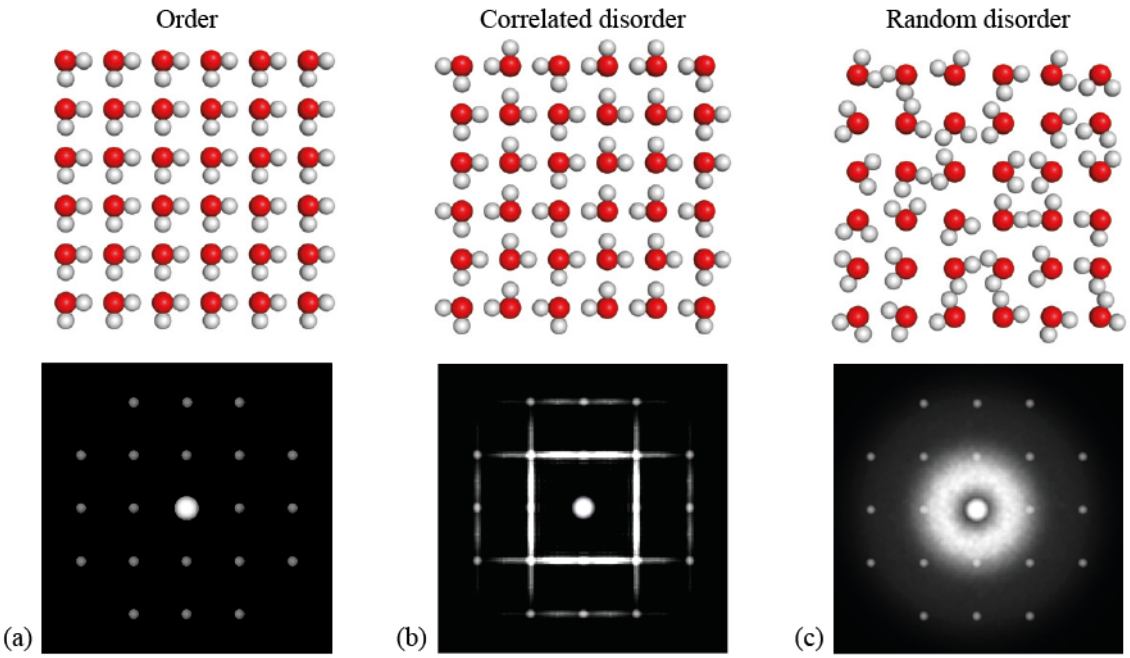


Figure 2.6: The effect of different types of disorder on the diffraction pattern, exemplified by the hypothetical square ice, with oxygen shown in red and hydrogen in white. (a) A long-range ordered structure of square ice, where all water molecules are identically oriented. The corresponding diffraction pattern features only sharp Bragg reflections. (b) The "two-in-two-out" rule stipulates that each oxygen atom should form two linear hydrogen bonds and two covalent bonds. This leads to a state of correlated disorder where each water molecule is in an identical environment, but there is no long-range periodicity. The resulting diffraction pattern exhibits highly structured diffuse scattering in addition to the Bragg peaks. (c) Random disorder, where the water molecules may assume any orientation, leads to unstructured diffuse scattering centred around the origin. Adapted by permission from Springer Nature Limited, "The crystallography of correlated disorder", D. A. Keen and A. L. Goodwin, Copyright 2015.[379]

als, including molecular crystals, superconductors and conventional perovskites.[380] At present, diffuse scattering analysis remains a relatively complex task; however, it can be successfully be applied to interrogate the disorder within suitable systems.[381]

2.2 Representation analysis

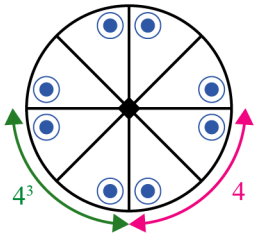
The mathematical theory regarding groups underlies many areas of chemistry, although its fundamental role is perhaps not always obvious. As crystallography constitutes a practical application of group theory and representation theory, significant insight into structural aspects can be gained by explicit use of group-theoretical

methods. Nowadays, the availability of web-based software such as the ISOTROPY suite and Bilbao Crystallographic Server facilitate routine representation analysis of crystal structures even for non-specialists.[382–385] Furthermore, group theory can be invoked to understand spectroscopic selection rules, rationalise bonding in organic and organometallic complexes, explain magnetic orderings and so on.[119,386] The present Section gives a brief introduction to the basics of group theory, largely based on Ref. 386, which provides a more thorough background.

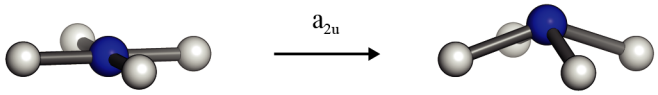
Formally, groups are mathematically defined as collections of elements that obey the four group axioms regarding closure, associativity, identity and invertibility. The size of the group, *i.e.* the number of elements, is known as the order of the group and given the symbol h. In crystallographic point/space groups, the group elements are the symmetry elements and h is thus a measure of the symmetry of the group. For example, the order of the orthorhombic point group $mm2$ (C_{2v}) is 4, whereas the cubic group $m\bar{3}m$ (O_h) has $h = 48$, reflecting the higher symmetry of cubic crystal systems relative to orthorhombic. The group elements can be further divided into classes—sets of conjugate elements*—and in crystallography, the classes encompass sets of symmetry elements interconvertible by application of another symmetry operation from the group. In Fig. 2.7(a), it can be seen that the rotations 4 and 4^3 in the point group $4/mmm$ (D_{4h}) are symmetry related through the mirror planes. Hence, 4 and 4^3 belong to the same class.

It is often valuable to understand how a particular distortion breaks the symmetry of a parent point group; *i.e.* how it transforms under the application of each

*Conjugate elements are similarity transforms of each other, *i.e.* if $B = X^{-1}AX$ for any X that is also an element in the group, A and B are conjugate and belong to the same class.



(a)



(b)

	E	$2C_4$ (z)	C_2	$2C'_2$	$2C''_2$	i	$2S_4$	σ_h	$2\sigma_v$	$2\sigma_d$
A_{2u}	1	1	1	−1	−1	−1	−1	−1	1	1

(c)

Figure 2.7: (a) The 4-fold and 4^3-fold rotation operations (magenta and green) are interconvertible through the mirror planes and, hence, 4 and 4^3 belong to the same crystallographic class in the point group $4/mmm$ (D_{4h}). (b) The off-centring of the central atom in a square planar molecule with point symmetry $4/mmm$ forms a basis for the a_{2u} irrep. (c) Excerpt from the $4/mmm$ character table.

symmetry operation of the point group. Consider the out-of-plane bending of a square planar molecule with point group $4/mmm$ (D_{4h}) [Fig. 2.7(b)]. This mode breaks the horizontal mirror plane and 2-fold axes, whereas the vertical mirror planes and the 4-fold axis are retained. Such information is concisely summarised in character tables, which are easily available for each point group [Fig. 2.7(c)].[383,387] The retention/loss of each class of symmetry elements is indicated by a positive/negative integer. There are only a finite number of possible permutations of these values—equal to the number of classes—known as irreducible representations (irreps). Irreps are linearly independent and cannot be broken down into constituent representations, *i.e.* they are irreducible. In more crystallographic terms, the irreps of a point group can be viewed as the complete set of distinct manners of breaking the symmetry of the aristotype. All distortion patterns, including rotations and translations, form a basis for an irrep or for a linear combination of a finite number of irreps: a reducible representation. Thus, if two states possess the same symmetry, they also form bases for the same irrep. In addition to structural distortions, any function or pattern may act as a basis for an irrep, as exploited in the labelling of orbitals and electronic states according to their irrep.

The conventional nomenclature for irreps (Mulliken notation) entails a certain extent of information regarding their transformation properties. The capital letter A/B denotes one-dimensional irreps that are symmetric/antisymmetric with respect to the principal rotation axis, whereas e and t are used for 2D and 3D—*i.e.* doubly and triply degenerate—irreps, respectively. A subscripted number indicates the retention (1) or loss (2) of a horizontal 2-fold axis and the subscripted letter g or u reveals whether an inversion centre has been lifted or not. The name of the irrep a_{2u} in Fig. 2.7(b) should now be apparent. An additional example is provided by the Q_3 Jahn-Teller distortion of an octahedron [Fig. 2.8(a)], which forms a basis for the e_g irrep, together with the Q_2 distortion . Its degeneracy has already been discussed and its centrosymmetry is evident in the subscript "g".

The above notation is only applicable to point groups, whereas in crystals, a different nomenclature for the irreps is required to account for translational periodicity. The irreps are now described by $K_n^{+/-}$, where K represents the Bradley-Cracknell symbol for the high-symmetry points in reciprocal space, n is a tabulation number and $+/-$ provide information regarding centrosymmetry.[360,388] For example, the FOJT mode of a perovskite belongs to either of the Γ_3^+, X_4^-, M_3^+, or R_3^- representations, depending on the corresponding crystal momentum [Fig. 2.8(b)]. It should be noted that the irrep labels are not invariant under origin shifts of the unit cell. The irreps listed in Fig. 2.8(b) are derived relative to a parent perovskite with the A-site at the origin, whereas the setting with the B-site at the origin generates the irreps Γ_3^+, X_2^+, M_2^+, and R_3^+. In this Thesis, the former setting is used throughout.

Representation analysis is valuable for the study of displacive phase transitions,

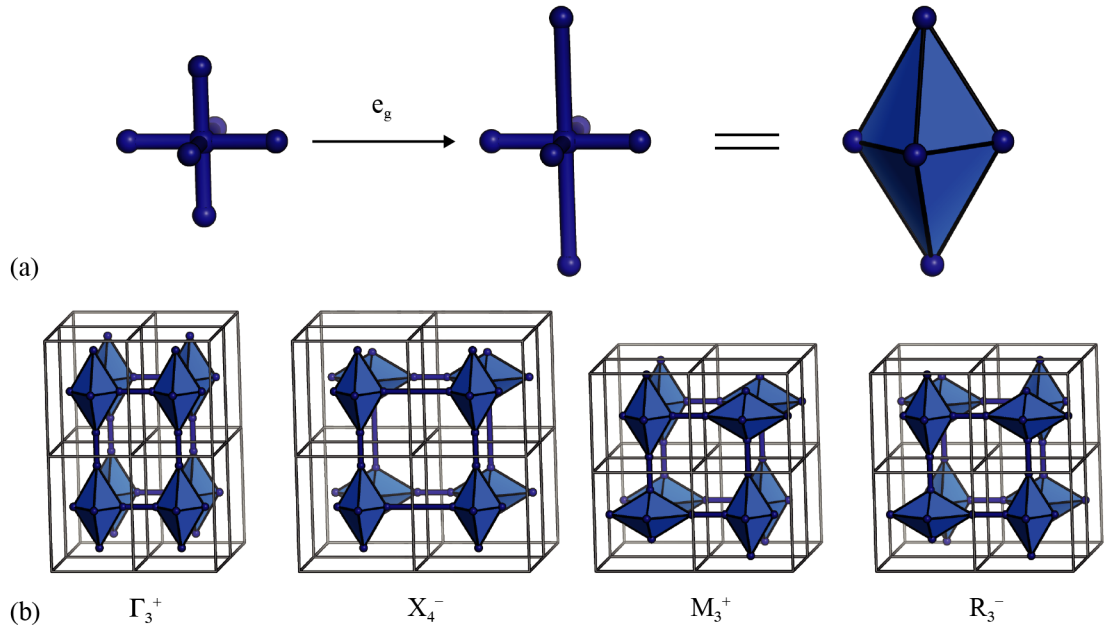


Figure 2.8: (a) One of the two degenerate modes forming a basis for the e_g representation in the octahedral point group $m\bar{3}m$ (O_h). (b) The e_g distortion with different propagation vectors in a periodic structure and the resulting irreps.

as any symmetry-breaking distortion can be represented by one or more irreps. The deformation accounting for the symmetry lowering of the aristotype is called the primary order parameter and, in general, identification of the primary order parameter cannot be carried out by inspection. Instead, group-theoretical decomposition of the hettotype relative to the aristotype is required. Sometimes, the space group symmetry of the hettotype arises from a combination of distortions, in which case there are two or more superimposed primary order parameters. The activation of a primary order parameter frequently induces the appearance of secondary order parameters, *i.e.* a distortion allowed by symmetry as a result of the primary order parameter(s). As an illustration, the $a^+b^-b^-$ tilt pattern in $GdFeO_3$ couches two superimposed primary order parameters: the in-phase and out-of-phase tilts which transform as the irreps M_2^+ and R_5^-, respectively. Neither of these distortions account fully for the observed *Pnma* symmetry on their own. An antipolar displacement of

the A-site cation belonging to the irrep X_5^- appears as a secondary order parameter and activation of this distortion does not alter the space group.

In addition to providing the relevant order parameter, the order parameter direction (OPD) also has to be specified. In essence, this is a vector stipulating the axis of polarisation for the distortion and, in the case of multiple active distortions, their relative magnitudes. For example, if the conventional out-of-phase tilt R_5^- acts along one lattice vector to drive $P4/mbm$ symmetry, the OPD is described by (a,0,0) according to the convention used by ISODISTORT.[382] Likewise, active tilts of equal amplitudes along two axes imply an order parameter direction of (a,a,0) and give rise to the space group $Imma$. For X- and M-point distortions, the situation is slightly more complex due to the ambiguity of the momentum: *e.g.* **k** = $[\frac{1}{2}, \frac{1}{2}, 0]$, $[\frac{1}{2}, 0, \frac{1}{2}]$, or $[0, \frac{1}{2}, \frac{1}{2}]$ for the M-point. These are known as different k-actives—or arms of the star of **k**—and are demarcated by semicolons in the OPD. As a result, a conventional in-phase tilt along a sole axis with only one k-active corresponds to M_2^+(a;0;0). Hence, the symmetry lowering from $Pm\bar{3}m$ to $Pnma$—as in $GdFeO_3$—is encompassed by $R_5^- \oplus M_2^+$ with OPD (a,a,0|0;b;0), indicating the different magnitudes of the two tilts. This notation uniquely defines the symmetry of $GeFeO_3$ and demonstrates how group theory provides an alternative language for convenient description of the symmetry lowering in crystal structures.

Despite the utility of representation theory, it is important to appreciate that it is a purely mathematical tool not informed by chemical rules. Consequently, it is useful in discerning between symmetry-allowed and -forbidden scenarios, *e.g.* in the study of electronic transitions, and thereby ruling out the possibility of the latter.

However, even cases allowed by symmetry may not necessarily occur, if associated with a high energy penalty. By way of example, the X-point distortion in Fig. 2.8(b) leads to unreasonable stretching of some of the molecular linker species. Therefore, although being an allowed distortion, it is unlikely to be observed in the absence of further distortions, *e.g.* tilting. In conclusion, results derived by group-theoretical methods have to be evaluated with respect to the physical sensibility using chemical intuition.

2.3 Lattice dynamics

2.3.1 Vibrational motion in crystals

Crystallography treats the motifs as static entities in a perfect infinite arrangement, but this is a very crude simplification. In reality, symmetry is constantly broken as the atoms oscillate around their mean position: the time-averaged site located by structure-determining techniques. In principle, the results obtained from the theory of vibrational motion in molecules are also applicable to the collective vibrations present in extended solids. As for molecular vibrations, quantum mechanics stipulates a quantisation of the vibrational energy levels in crystals and the fundamental quanta are known as phonons. The symmetry of the system and the number of atoms are also key considerations in lattice dynamics—as in the case of molecules. However, as crystals are periodic, the spatial frequency of the vibration must be considered [Fig. 2.9]. Since extended solids generally consist of $\sim 10^{23}$ particles, a multitude of spatial wavelengths is conceivable.

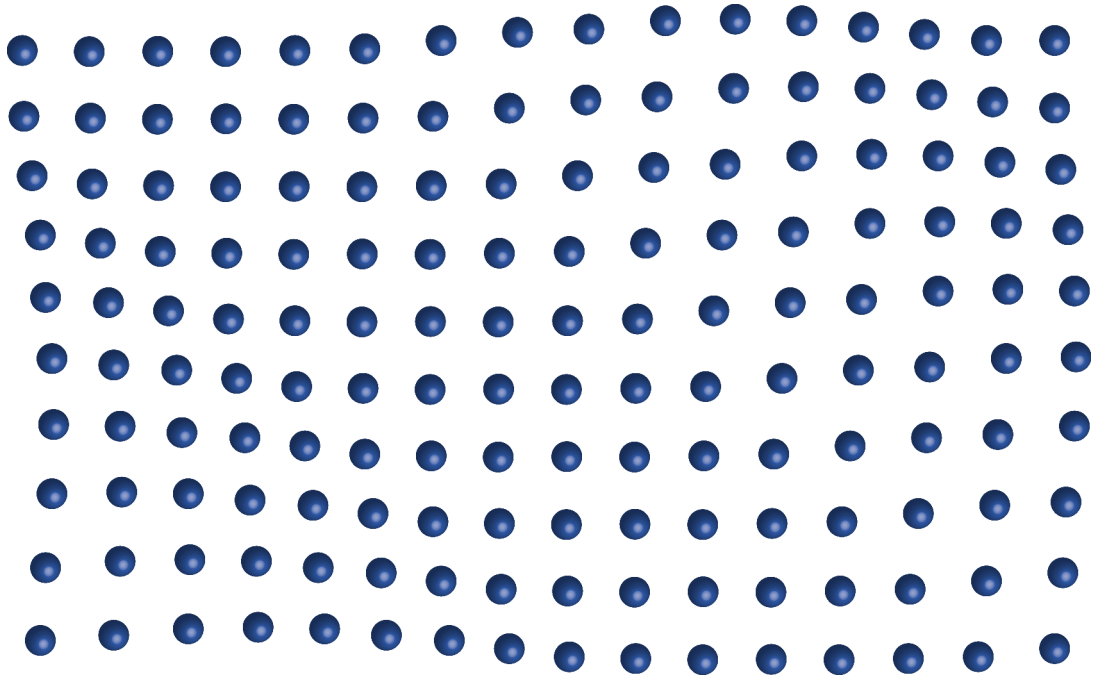


Figure 2.9: A lattice vibration propagating through a crystal structure.

The theory of lattice dynamics aims to understand how the phonon frequencies, ω, vary as a function of the spatial periodicity of the vibration, expressed by $\mathbf{k} = \frac{2\pi}{\lambda}$. For simplicity, it is instructive to consider first a monoatomic one-dimensional chain, where each atom only has one degree of freedom. In a chain of N atoms of mass m connected by bonds with a force constant J and length a, the energy of species n within the harmonic approximation is

$$E_n = \frac{1}{2}J(u_{n+1} - u_n)^2 + \frac{1}{2}J(u_n - u_{n-1})^2 \tag{2.18}$$

where u_n is the instantaneous position of atom n. The force is given by the positional derivative of Eq. 2.18 and by assuming simple harmonic motion, the k dependence of ω can be derived as:

$$\omega(k) = \sqrt{\frac{4J}{m}} \left| \sin \frac{ka}{2} \right| . \tag{2.19}$$

Note that while the propagation vector **k** is in general a vector, it reduces to a scalar quantity (k) in 1D. A plot of ω as a function of k is known as a phonon dispersion curve [Fig. 2.10(a)]. As is easily verified from Eq. 2.19, the phonon dispersion curve is a periodic function, which naturally arises from the periodicity of the underlying lattice. Consequently, all the unique information is contained within $-\frac{\pi}{a} < k < -\frac{\pi}{a}$: the Brillouin zone, as introduced in Section 2.1.2. As this simple example only features one particle with one degree of freedom, the phonon dispersion curve contains a single vibrational mode. In the limit of $k \to 0$, the vibrational frequency approaches zero—as is also clear from inspection of Eq. 2.19. This reflects the vanishing vibrational energy cost of a simple translation of the crystal [Fig. 2.10(b)]. Conversely, at the boundary of the BZ, the wavelength assumes its maximum value and the mode consequently increases in energy [Fig. 2.10(c)]. These simple considerations apply to all phonon dispersion curves, although the appearance is often complicated by the addition of higher dimensions and a larger number of atoms per unit cell.

The extension of this simple model to 3D introduces a larger number of degrees of freedom for the atoms. For a given **k**-vector, the atoms may either displace parallel or perpendicular to the direction of propagation of the wave. These two possibilities are known as longitudinal and transverse vibrations, respectively, and as they in general correspond to different energies, additional branches appear in the phonon dispersion curve [Fig. 2.10(d)]. For a given direction of **k**, there are two transverse modes; yet they are degenerate along some high-symmetry directions in reciprocal space, *i.e.* along a four-fold or three-fold rotation axis. This is apparent in Fig. 2.10(d), where the transverse branch along Γ–X splits into two separate

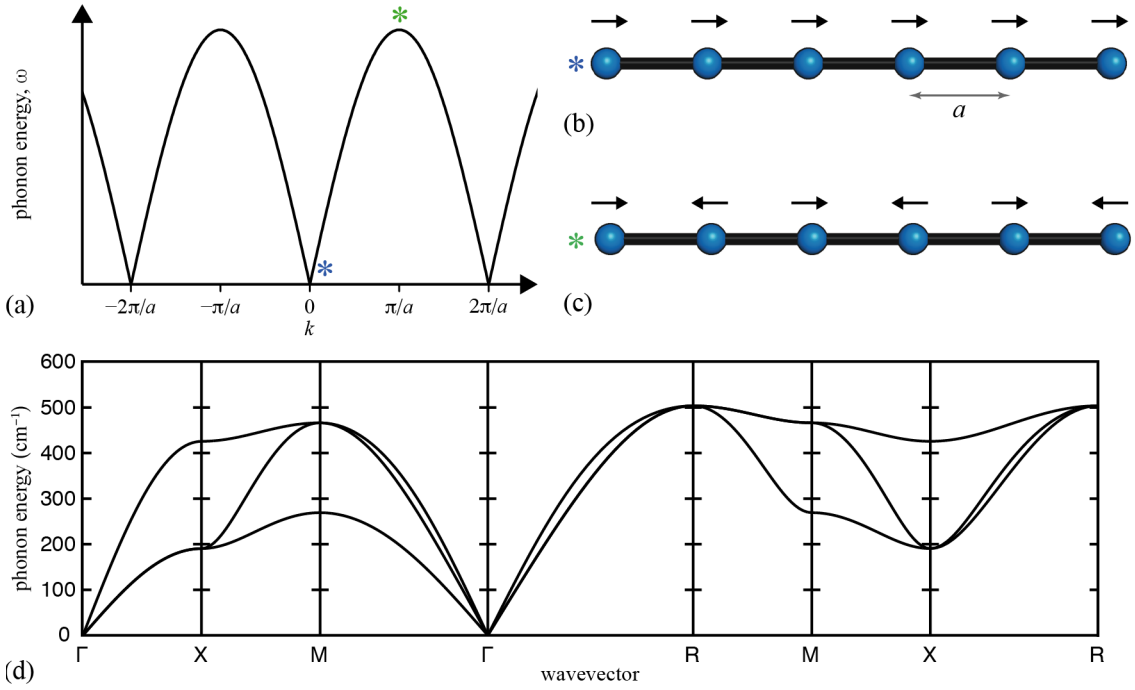


Figure 2.10: Phonon dispersion curves for monoatomic crystals. (a) A schematic phonon dispersion curve for a monoatomic linear chain of atoms with one degree of freedom. Depictions of the atomic motion (b) in the limit of $k \to 0$ and (c) at $k = \pi/a$ are also shown. (d) A calculated phonon dispersion curve for a primitive monoatomic crystal in 3D. Panel d adapted from Ref. 389.

branches along X–M.

In multiatomic crystals, further complications arise as the distinct neighbouring atoms may displace in phase or out of phase [Fig. 2.11(a)–(b)]. These two cases are referred to as acoustic and optic modes, respectively, and in a 3D crystal with N distinct atoms in the primitive unit cell, there are 3 acoustic modes and $3N-3$ optic modes. In line with the above discussion, the energies of the acoustic modes tend to 0 as $\mathbf{k} \to 0$, whereas optic modes have nonzero frequencies even at the centre of the Brillouin zone. Strictly speaking, the distinction between optic and acoustic modes is only valid in the limit of small values of $\mathbf{k}$, and these terms are no longer meaningful at the zone boundary.

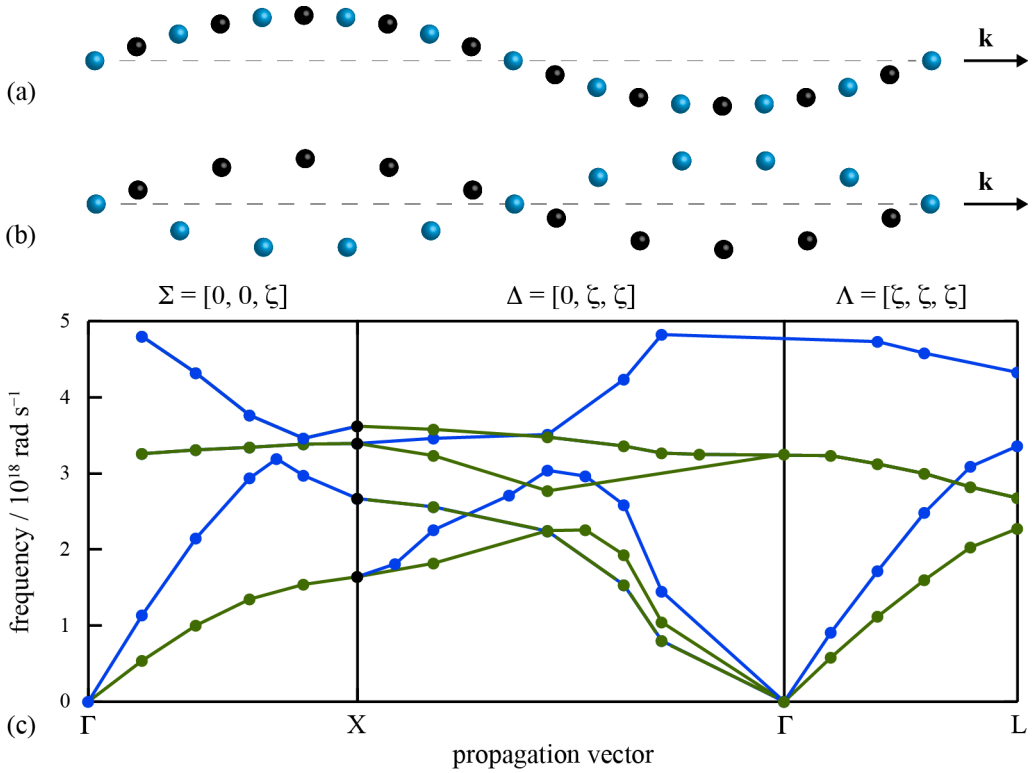


Figure 2.11: Transverse (a) acoustic and (b) optic phonon modes for a diatomic linear chain. (c) The phonon dispersion of NaCl, measured by inelastic neutron scattering (INS), where transverse modes are shown in green and longitudinal in blue. Data reproduced from Ref. 390.

To illustrate the concepts developed in this Section, the experimentally determined dispersion curve for NaCl is shown in Fig. 2.11(c),[390] with transverse modes shown in green and longitudinal in blue. As the primitive unit cell of NaCl contains two distinct atoms, the dispersion curve features 3 acoustic and 3 optic modes, which are easily identified by virtue of their divergent behaviour at the zone centre. The degeneracy of the branches is also clear; for example the transverse optic branch along Γ–L is doubly degenerate, but splits along the less symmetrical Δ path. The nontrivial shape of the acoustic branch along Γ–Δ is due to significant next-nearest neighbour interactions along this path. This illustrates how even a simple example such as NaCl can display relatively complex phonon dispersion behaviour.

2.3.2 Lattice-dynamical calculations

In more complicated crystals, calculation of dispersion relations is usually performed computationally by the dynamical matrix approach. A full derivation is not given here, but suffice to say that the dynamical matrix, $\mathbf{D}(\mathbf{k})$, may be assembled from the interatomic potential of the crystal and the masses of the constituent atoms. By defining the mode eigenvector $\mathbf{e}(\mathbf{k})$—sometimes also known as the polarisation vector—as the normalised vector along which the atoms displace, the following relation can be derived

$$\mathbf{D}(\mathbf{k}) \times \mathbf{e}(\mathbf{k}) = \omega^2(\mathbf{k}) \times \mathbf{e}(\mathbf{k}), \tag{2.20}$$

where the vibrational frequencies $\omega^2(\mathbf{k})$ are the eigenvalues of $\mathbf{D}(\mathbf{k})$. Hence, the task of finding the $\mathbf{k}$ dependence of the phonon frequencies is recast as an eigenproblem, which is readily solved by computational software. Often, the form of the dynamical matrix is greatly simplified through a knowledge of the symmetry of the crystal prior to computing.

One program capable of calculating phonon dispersion curves is the General Utility Lattice Program (GULP), developed for symmetry-adapted lattice energy minimisation and structural optimisation of solids using force field methods.[391,392] As the name suggests, this is a highly versatile piece of software capable of calculating a range of physical data, including thermal conductivity, pair distribution functions, phonons, surface phenomena, and dielectric data.[391–394] The input to GULP requires information regarding the crystal structure, ionic charges, and the interaction potentials. A large number of different standard potentials can be implemented, including

Buckingham, Morse and Lennard-Jones.[391]

The first step during a GULP simulation is structural optimisation of the given starting structure. The minimisation algorithm is based on the Taylor expansion of the lattice energy

$$E(x+dx) = E(x) + \frac{dE(x)}{dx}dx + \frac{d^2E(x)}{2dx^2}dx^2 + \frac{d^3E(x)}{3dx^3}dx^3 + ..., \qquad (2.21)$$

where x is a variable. The Taylor series is normally truncated at the first- or second-order term and a local minimum is found by the so-called Newton-Raphson method.[391] As the algorithm relies on second derivatives without any stochastic basis, it is deterministic and so the outcome is reproducible. Following the structural optimisation, the physical properties of interest are computed. Phonon frequencies can be calculated for arbitrary points in reciprocal space from the dynamical matrix and this was the main use of GULP in this Thesis.

2.3.3 Anharmonicity and thermal expansion

The above treatment has been carried out within the harmonic approximation, which involves attenuating the Taylor expansion of the free energy at the second-order terms [Eq. 2.18]. The harmonic approximation is advantageous as it can be solved exactly and, for many purposes, is sufficient. However, the omission of higher-order terms excludes from the model the creation and annihilation of phonons through collisions and spontaneous decay. These processes are key to understanding transport properties such as thermal conductivity and thermal expansion, as well as the occurrence of displacive phase transitions.[355,395,396] As the latter two are of relevance

for the research presented in subsequent Chapters, they are outlined here.

Thermal expansion

Thermal expansion refers to the thermally induced strain of a crystal and the isobaric coefficient of volume thermal expansion is defined as

$$\alpha_V = \frac{1}{V}\left(\frac{\partial V}{\partial T}\right)_p, \tag{2.22}$$

where V is the crystal volume, T is the temperature and p denotes pressure.[397] This can be recast as the sum of the expansivities of the three principal axes, α_{11}, α_{22}, and α_{33} defined by

$$\alpha_{ii} = \frac{1}{l_{ii}}\left(\frac{\partial l_{ii}}{\partial T}\right)_p, \tag{2.23}$$

where l_{ii} is the length of the principal axis ii. As with all physical properties, $\alpha_{11} = \alpha_{22} = \alpha_{33}$ for cubic materials and so $\alpha_V = 3\alpha_{11}$.

The driving force for thermal expansion stems from the volume dependence of the phonon frequencies. For a single vibrational mode, this is quantified by the mode Grüneisen parameter, γ_j,[398] defined by

$$\gamma_j = -\frac{\partial \ln \omega_j}{\partial \ln V}. \tag{2.24}$$

As a crystal contains an ensemble of phonon frequencies, it is useful to define the mean effective Grüneisen parameter as

$$\gamma = \frac{1}{C_V}\sum_j \gamma_j \hbar\omega_j \frac{\partial n(\omega_j, T)}{\partial T}, \tag{2.25}$$

where C_V is the heat capacity at constant volume, and $n(\omega_j, T)$ is the phonon number, *i.e.* the number of phonons with frequency ω_j at temperature T. Note that since $n(\omega_j, T)$ is a function of T, so is γ. The coefficient of thermal expansion may be rewritten as the simple relation

$$\alpha_V = \frac{K_T \gamma C_V}{V}, \tag{2.26}$$

where K_T is the isothermal compressibility. The magnitude of the thermal expansion correlates with the type of interatomic/intermolecular forces present in the material. Dense inorganic materials frequently exhibit relatively modest expansivities (usually $\alpha_{ii} < 50\,\mathrm{MK}^{-1}$), reflecting the high strengths of covalent and metallic bonds.[397,399] On the other hand, molecular crystals may show a more dramatic thermal expansion behaviour due to the weaker intermolecular forces. By way of example, Panda *et al.* reported a remarkably high uniaxial thermal expansion coefficient of 260 MK^{-1} for an organometallic complex that also exhibited thermosalient properties partially driven by the thermal expansion.[400]

Usually, γ assumes positive values, leading to net positive thermal expansion (PTE), but this is not a universal phenomenon. Phonon modes with negative Grüneisen parameters occur in several ostensibly different materials and if these modes are sufficiently numerous and of low energy, the bulk property of negative thermal expansion (NTE) is observed. This is often desirable, as composites of NTE and PTE compounds can be constructed to achieve net zero thermal expansion, which finds application in dentistry, high-precision optics and electronics.[7,401,402] One mechanism commonly invoked to explain the occurrence of NTE is the tension

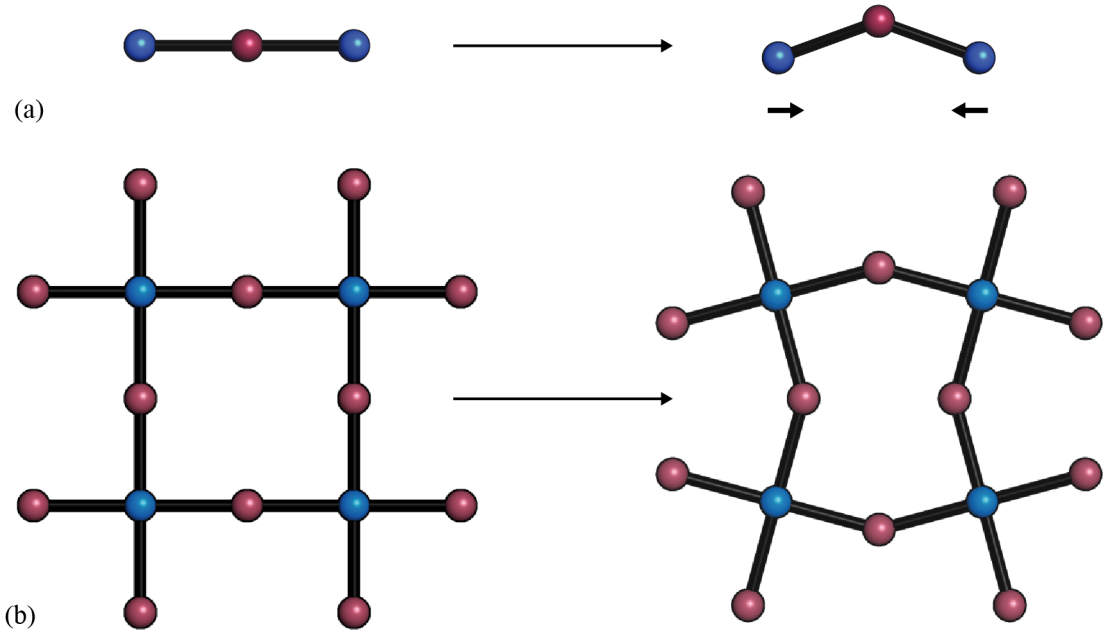


Figure 2.12: (a) The excitation of low-energy transverse vibrations induce a uniaxial contraction of the structural motif and may so engender negative thermal expansion, known as the tension effect model.[403] (b) In a framework, these transverse phonons normally propagate with the metal coordination sphere vibrating as a rigid unit: the rigid unit model.

effect [Fig. 2.12(a)].[403] The transverse vibrations of linear M–O–M linkages reduce the intermetallic distance and as this usually outweighs the longitudinal expansion of the M–O bonds, the excitation of such low-energy transverse phonons may induce macroscopic NTE.

In framework materials, the low-energy transverse modes from the tension effect are correlated throughout the structure, as described by the rigid unit mode (RUM) model.[118,404–406] The distortion of coordination polyhedra tends to incur a high energy penalty, whereas phonon modes that preserve the polyhedral geometry are often more energetically accessible. Hence, the transverse vibrations featuring in the tension model propagate as shown in Fig. 2.12(b), with retention of the local geometry of the metal. This mechanism underlies the strong NTE observed in the A-site deficient perovskite ScF_3, as well as the canonical NTE material zirconium

tungstate (ZrW_2O_8).[407–410] In certain cases, the RUM-driven NTE effect can be enhanced by using linearly bridged M–L–M moieties (where L is a polyatomic linker) as in $Ag_3[Co(CN)_6]$ and $Cd(CN)_2$: two coordination polymers with extremely strong thermal contraction.[411–413]

Displacive phase transitions

Within the anharmonic treatment of lattice dynamics, the frequencies of phonon modes are temperature dependent and usually decrease (soften) upon heating. However, phonons known as "soft modes" exhibit the opposite temperature dependence: they soften upon cooling. Therefore, the excitation energy of such modes can eventually reach zero at sufficiently low temperatures and the vibration condenses. This forms the basis of soft mode theory, which is readily applied to phase transitions of ceramic materials, frequently involving RUMs.[355] For example, the octahedral tilting in perovskites is often dynamic at elevated temperatures, but condenses below a certain temperature and gives rise to the tilted structures observed at ambient conditions. Tilting in conventional perovskites is usually a manifestation of a zone-boundary mode, but soft modes may be either acoustic or optic and can occur at any point in reciprocal space.[355]

Another prominent theory regarding phase transitions is Landau theory, where the free energy of a system is expanded in terms of the primary order parameter(s).[414] At temperatures above the phase transition, the free energy curve corresponds to a parabola centred at $\eta = 0$, reflecting the stability of the undistorted structure. Upon cooling through the transition temperature, the minimum displaces to a nonzero value of η and activation of the order parameter is energetically

favourable. The exact shape of the free energy curve depends on whether the order parameter changes continuously (second-order transition) or discontinuously (first-order transition) during the phase transition.[355] Landau theory underpins the study presented in Chapter 5 and is treated in more detail there.

2.4 Atomic absorption spectroscopy

As mentioned in the context of X-ray generation, electronic transitions within a metal—or indeed any element—are characteristic of the particular element in question. This is exploited in atomic absorption spectroscopy (AAS) to determine unknown metal concentrations of a sample by comparing its absorbance of the relevant wavelength against a calibration curve.[65]

As AAS is developed for solutions, the sample must first be digested, usually by addition of acid prior to dilution to the required volume. Subsequently, the solution is aspirated and passes into a nebulising chamber, where it is converted into an aerosol and atomised. In flame AAS—the method of relevance to this research—the atomisation is achieved by means of an open flame fuelled by a mixture of air and acetylene or nitrous oxide. Next, the atomised sample is exposed to radiation generated by a hollow cathode lamp. The wavelength is chosen such that it corresponds to a single electronic transition inherent to the metal under study, *e.g.* 327.4 nm for the $4s \rightarrow 4p$ transition in Cu.[415,416] The attenuation of the light is measured relative to a blank solution and the concentration is calculated from the Beer–Lambert law,[417,418]

$$A = \log_{10} \frac{I_0}{I} = \epsilon l c, \tag{2.27}$$

where A is the absorbance, I_0 and I are the incident and transmitted intensities of the light, ϵ is a constant, l is the path length and c is the concentration. In practise, the metal content is determined from a calibration curve, constructed from standard solutions of known concentration. As the linear relationship between A and c given by the Beer-Lambert law only is valid for low absorbances, dilute solutions are required. Nowadays, the calculations are usually performed automatically by the software controlling the spectrometer and the concentration given directly.

AAS has excellent sensitivity and is able to detect concentrations as low as $\mu\mathrm{g\,dm^{-3}}$;[65] however, there are a number of factors that may affect the accuracy.[416,419] Spectral interference arises when the absorption line of another species present in the solution overlaps with that of the analyte. Chemical interference—the alteration of the chemical nature of the analyte—results primarily in incomplete atomisation of the metal in the flame.[416] For example, alkali metals are prone to ionisation by the high temperatures and the AAS signal is therefore systematically underestimated. Moreover, refractory complexes can sometimes form between the analyte and a spectator species, which has a similar detrimental effect.[419]

2.5 Monte Carlo techniques

Monte Carlo (MC) simulations are a very broad class of computational methods used to obtain numerical results or realistic configurations from an initially random model. Within the solid-state sciences, it is a valuable tool for the study of local order within disordered materials, including ordering phenomena that remain "hidden" from conventional structure-determining techniques.[420–422]

In a direct Monte Carlo simulation, the modelling is driven by a knowledge of the local interactions dictating the energy—the Hamiltonian—of the material. A starting model is created where the relevant parameter (*i.e.* spin in the case of magnetism or Jahn-Teller phase for orbital order) at each site is allocated a random starting value. An arbitrary site is chosen and its value changed by a random amount. The associated energy change, $\Delta E = E_\mathrm{f} - E_\mathrm{i}$, is computed and evaluated based on the Metropolis algorithm,[423] *i.e.* the move is accepted on condition that

$$p < \exp \frac{-\Delta E}{kT}, \tag{2.28}$$

where p is a random number between 0 and 1 and k is Boltzmann's constant. As $\exp \frac{-\Delta E}{kT} > 1$ provided that $\Delta E < 0$, all changes leading to a net energy lowering are accepted. Additionally, a certain number of "bad" moves are accepted ($\Delta E > 0$) in order to prevent the convergence into a local minimum. By gradually decreasing the value of T—so-called simulated annealing[424]—the probability of accepting unfavourable changes is reduced as the system descends in energy and approaches the global minimum. As T is a freely variable parameter, direct Monte Carlo methods are useful in order to investigate thermally induced changes, *e.g.* phase transitions, of the system.[425] The simulation is continued for a given number of accepted moves or until a pre-defined energy value has been reached.

In any Monte Carlo simulation, the computational factors influencing the final results are the size of the configurations ("boxsize") and the equilibration time. Clearly, an infinitely large box is the most accurate representation of a real system, but the computational cost of the calculation inevitably scales with the dimensions

of the configurations. In general, periodic boundary conditions are employed and care has to be taken that the boxsize is larger than the length scale of any short-range correlations present in the model.

Chapter 3

Columnar Shifts in Molecular Perovskites

3.1 Chapter overview

This Chapter focuses on a previously unidentified degree of freedom in molecular perovskites involving concerted translations of octahedral columns, which I refer to as "columnar shifts". This degree of freedom is a rigid unit mode exclusively accessible to systems with polyatomic linkers and together with tilts (both conventional and unconventional), it constitutes a complete set of RUMs for molecular perovskites. The Chapter is arranged as follows. First, the mathematical background to RUMs in molecular perovskites is presented, followed by a discussion of the implications for dynamic columnar shifts. Second, the effect of static shifts on the symmetry is investigated in both a 2D model system and real examples from the literature. It will be shown that shifts are as crucial to molecular perovskites as tilts are to conventional perovskites. And, third, the Chapter concludes with a discussion about shift trends across different families of molecular perovskites, with a view towards rational shift design.

I am grateful to Joshua Hill for valuable discussions.

3.2 Rigid unit modes

Rigid unit modes (RUMs) are defined as phonon modes which propagate through a structure without altering the bond lengths and angles of the coordination polyhedra.[426] They are normally associated with low vibrational frequencies and therefore frequently influence the thermal expansion[406,427] and act as soft modes in displacive phase transitions.[118,404,428] Moreover, systems that sustain a range of RUMs across the entirety of reciprocal space are able to dissipate local stresses by a linear superposition of a number of modes, *i.e.* a RUM wavepacket. This is important for porous materials, such as zeolites, where the stress from absorption of a guest species can be relieved in this manner.[429,430] In the context of molecular perovskites, the main motivation for understanding the RUMs is the desire to analyse temperature-dependent behaviour and symmetry-breaking phenomena.

RUMs are most straightforwardly identified by means of a dynamical matrix approach.[426,431] As outlined in Section 2.3, the dynamical matrix, $\mathbf{D}(\mathbf{k})$, yields the square of the phonon frequencies, $\omega^2(\mathbf{k})$, as eigenvalues when acting upon the phonon eigenvectors, $\mathbf{e}$, through the formula

$$\mathbf{D}(\mathbf{k}) \times \mathbf{e}(\mathbf{k}) = \omega^2(\mathbf{k}) \times \mathbf{e}(\mathbf{k}). \tag{3.1}$$

The entries in a dynamical matrix correspond to second derivatives of the lattice energy with respect to pairwise displacements. It is possible to design a lattice potential such that RUMs emerge as the solutions to Eq. 3.1 for which $\omega = 0$. The so-constructed dynamical matrix for a 2D conventional perovskite—*i.e.* an array of

corner-sharing squares—assumes the following form:[426]

$$\mathbf{D}(\mathbf{k}) = \left[\begin{array}{cc|c} 4K(1-\sigma) & 0 & \rho K \\ 0 & 4K(1-\sigma) & -\tau K \\ \hline -\rho K & \tau K & Ka^2(1+\sigma) \end{array}\right], \tag{3.2}$$

with

$$\sigma = \frac{\cos(2\pi k_x) + \cos(2\pi k_y)}{2}, \tag{3.3}$$

$$\rho = a\mathrm{i}\sin(2\pi k_y), \tag{3.4}$$

$$\tau = a\mathrm{i}\sin(2\pi k_x), \tag{3.5}$$

where K is a fictitious force constant, a is the lattice constant, and $\mathbf{k} = k_x\mathbf{a}^* + k_y\mathbf{b}^*$ is the propagation vector [see Appendix A for a derivation]. The three columns and rows correspond to displacements along **a** and **b** and rotations in the ab-plane, with lines demarcating the translational entries from the rotational.

Now, the task at hand involves finding combinations of eigenvectors and propagation vectors that will yield zero-valued eigenvalues of Eq. 3.2; the so obtained set of eigenvectors constitutes a complete list of RUMs supported by the system. The eigenvector [1, 0, 0] is associated with translational modes along **a** and its eigenvalue is given by $4K(1-\sigma)$. The only zero-valued solution is when $\sigma = 1$, *i.e.* when $k_x = k_y = 0$. This is a zone-centre acoustic mode (lattice translation). Similar arguments hold for the translations along **b**, which are the eigenstates of the vector [0, 1, 0]. In other words, translational RUMs are only permitted if the entire crystal displaces as a collective object. The only other case where $\mathbf{D}(\mathbf{k})$ has a zero-valued

eigenvalue is for the specific wavevector $[\frac{1}{2}, \frac{1}{2}]$, for which [0, 0, 1] is the eigenvector. This case corresponds to collective rigid body rotations. As anticipated, rotational RUMs are allowed as long as the sense of the tilts alternate in the directions perpendicular to the rotation axis; *i.e.* conventional tilts. The dynamical matrix hence confirms that the only nontrivial RUM supported by 2D conventional perovskites is an octahedral tilt with propagation vector $[\frac{1}{2}, \frac{1}{2}]$.

In a molecular perovskite with polyatomic linkers, the corners of the octahedra no longer coincide and, as a result, new RUMs may be expected. The dynamical matrix for a 2D system is given by[350]

$$\mathbf{D}(\mathbf{k}) = \left[\begin{array}{cc|c} 1-\cos(2\pi k_x) & 0 & 0 \\ 0 & 1-\cos(2\pi k_y) & 0 \\ \hline 0 & 0 & 0 \end{array}\right]. \tag{3.6}$$

Since this is a diagonal matrix, the eigenvalues are simply the diagonal entries for the corresponding eigenvector. As a result, [0, 0, 1] is now an eigenvector with zero-valued eigenvalues for all propagation vectors $\mathbf{k}$, which means that rotations with arbitrary periodicities are permissible. This includes the conventional tilts discussed above and also the unconventional tilts, where $k_x \neq \frac{1}{2}$ and/or $k_y \neq \frac{1}{2}$. For the translational eigenvectors [1, 0, 0] and [0, 1, 0], the eigenvalues are given by $1-\cos(2\pi k_x)$ and $1-\cos(2\pi k_y)$, respectively, which puts restrictions on the allowed values of k_x and k_y. For a translation along $\mathbf{a}$, k_x has to equal zero for the displacement to comprise a rigid unit mode, whereas k_y may take any value. This implies that translations along $\mathbf{a}$ are only allowed if the entire column parallel to

the a-axis translates cooperatively. Analogous relationships hold for columnar shifts polarised along **b**.

When extended to 3D, the dynamical matrix for molecular perovskites assumes the form[350]

$$\mathbf{D}(\mathbf{k}) = \left[\begin{array}{ccc|c} 1-\cos(2\pi k_x) & 0 & 0 & \\ 0 & 1-\cos(2\pi k_y) & 0 & * \\ 0 & 0 & 1-\cos(2\pi k_z) & \\ \hline & * & & * \end{array}\right], \qquad (3.7)$$

where the asterisks denote zero-valued 3×3 submatrices representing the rotations. Hence, as for the 2D system, there are no restrictions on the periodicities of octahedral tilts. The top left corner consists of 9 entries pertaining to translational modes along each of the three crystallographic axis. As for the 2D case, a displacement along axis i is only a RUM if the corresponding wavevector component $k_i = 0$; whereas the components of the propagation vector in the remaining directions can take arbitrary values. Consequently, acceptable propagation vectors are [0, k_y, k_z], [0, k_y, 0], and [0, 0, 0] for a shift polarised along **a** [Fig. 3.1]. If the unrestricted variables are set to $\frac{1}{2}$,* the first solution corresponds to out-of-phase correlations along the **b** and **c** directions, giving a checkerboard-like arrangement [Fig. 3.1(a)]. The second case denotes translations of entire planes of octahedra [Fig. 3.1(b)] and, finally, the third vector describes a shear of the lattice [Fig. 3.1(c)]. Note that these columnar shifts comprise modes at the M-, X- and Γ-points of reciprocal space, some

*Zone-boundary tilts are prevalent in perovskites and—to a first approximation—the same can be expected to be true for shifts.

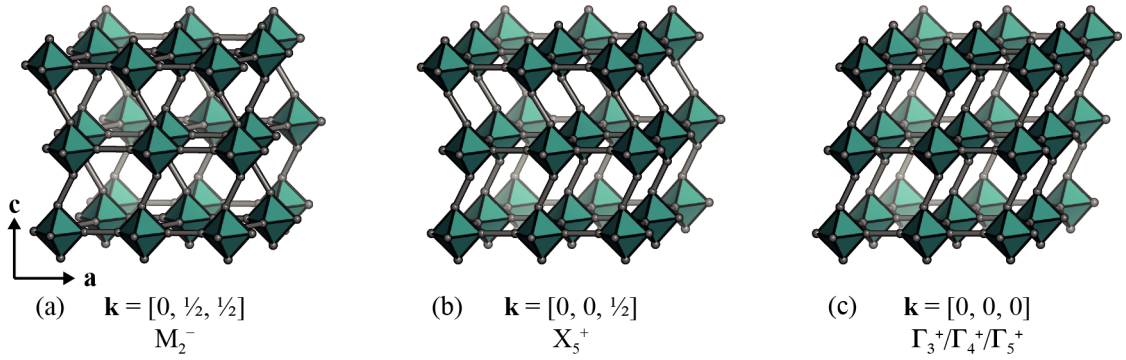


Figure 3.1: Three representative periodicities for columnar shifts polarised along **a**. (a) A checkerboard-like distortion arising from $\mathbf{k} = [0, \frac{1}{2}, \frac{1}{2}]$, (b) a planar shift where $\mathbf{k} = [0, 0, \frac{1}{2}]$, and (c) a shear shift distortion with $\mathbf{k} = [0, 0, 0]$. The corresponding irreps are also shown.

of which are inaccessible to conventional tilt distortions.

3.3 Dynamic shifts

RUMs are often low-frequency modes and potentially have a considerable effect on the dynamic behaviour of a material. Here, a simple lattice-dynamical model is used to investigate the importance of shifts as phonon modes in molecular perovskites.

3.3.1 Lattice-dynamical model

The important features of the lattice-dynamical model are (i) a perovskite topology with polyatomic linker species, (ii) rigid metal-linker and linker-linker bonds, (iii) rigid linker-metal-linker angles, and (iv) flexible metal-linker-metal angles. This was implemented in the software GULP,[391] employing a $Pm\bar{3}m$ unit cell with a B-site atom at the 1a Wyckoff position (0, 0, 0) and a diatomic X-site atom at the 6e position (0, 0, x). Thus, the molecular formula is $B(X_2)_3$ and represents the simplest possible molecular perovskite. For simplicity, and since shifts—at least at face value—only involve distortions of the framework, the A-site cation is omitted

Table 3.1: The parameter values used for the lattice-dynamical model of a hypothetical molecular perovskite, as implemented in GULP.[391]

Parameter	Value	Parameter	Value
Space group	$Pm\bar{3}m$	r_0(X–X) (Å)	1.0
a (Å)	5.0	k_{harm}(X...X) (eV/Å^2)	1.0
m_{B} (a.m.u.)	54.94	r_0(X...X) (Å)	2.828
m_{X} (a.m.u.)	16.00	k_{angle}(X–B–X) (eV/rad^2)	1.0
k_{harm}(B–X) (eV/Å^2)	1.0	θ_0(X–B–X) (°)	90.0
r_0(B–X) (Å)	2.0	k_{angle}(X–X–X) (eV/rad^2)	0.01
k_{harm}(X–X) (eV/Å^2)	1.0	θ_0(X–B–X) (°)	135.0

and both B and X are treated as uncharged. The harmonic lattice enthalpy of this model is given by

$$E_{\mathrm{latt}} = \frac{1}{2}\sum_{\mathrm{bonds}} k_{\mathrm{harm}}(r - r_0)^2 + \frac{1}{2}\sum_{\mathrm{angles}} k_{\mathrm{angle}}(\theta - \theta_0)^2, \tag{3.8}$$

where r_0 and θ_0 refer to the equilibrium bond lengths and angles, respectively. The equilibrium B–X–X angle is 180° to ensure that shifts are accounted for in the phonon spectrum instead of appearing as static distortions. Further details of the implementation of the lattice-dynamical model are given in Table 3.1. The phonon dispersion curves were calculated on a k-grid of 0.025 reciprocal lattice units [Fig. 3.2(a)]. Given the fictitious values of the parameters, the absolute energies themselves are not meaningful, but useful qualitative information can still be extracted. For example, the shallow slope of the soft acoustic transverse branch along Γ–X is indicative of a shear instability, *i.e.* a zone-centre shift distortion. Other important features are the presence of dispersionless bands and zone-boundary soft modes.

Shifts are associated with mode eigenvector $\mathbf{e}(\mathbf{k}, \nu)$ polarised along a single Cartesian axis. Therefore, the extent to which a given phonon mode ν corresponds to

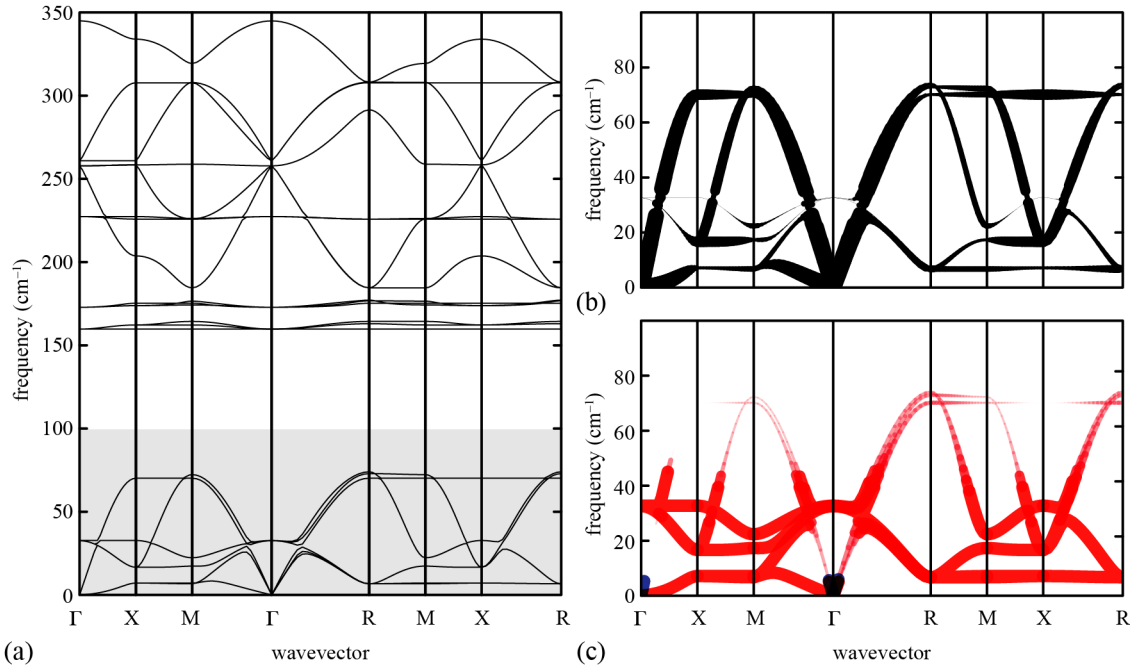


Figure 3.2: Calculated phonon dispersion curves for a hypothetical molecular perovskite model. (a) The full phonon dispersion, with the low-energy regime shaded in grey. (b) The low-energy region with the branches broadened according to their value of $\rho(\mathbf{k}, \nu)$ [Eq. 3.9], which is an effective measure of the extent to which the branch represents a columnar shift. (c) The low-energy region with the branches coloured and broadened according to their sign and absolute value of the Grüneisen parameters, where blue and red denote positive and negative values, respectively.

shift degrees of freedom at wavevector $\mathbf{k}$ can be quantified by

$$\rho(\mathbf{k}, \nu) = \sum_{\alpha} \left| \sum_{j} \frac{1}{\sqrt{m_j}} e_{j\alpha}(\mathbf{k}, \nu) \right|^2 , \tag{3.9}$$

where α labels the Cartesian axes and j indexes the atoms in the unit cell. In Fig. 3.2(b), the low-frequency region of the phonon dispersion is shown with the branches broadened according to the value of $\rho(\mathbf{k}, \nu)$. In this way, the phonon modes with a large shift character are easily identified. It becomes apparent that the low-lying phonon modes host numerous shift-like vibrations; for example, the transverse acoustic branches along Γ–X and Γ–M are almost entirely accounted for by shifts. The longitudinal acoustic branches increase significantly in energy along

the same paths, which is consistent with the requirement for shifts polarised along α to propagate with $k_\alpha = 0$.

3.3.2 Negative thermal expansion

As discussed more fully in Section 2.3.3, the sign of the thermal expansion coefficient is stipulated by the sign of the mean Grüneisen parameter, which in turn is dictated by the signs of the Grüneisen parameters, γ, of the individual phonon modes. Consequently, if a significant proportion of the low-energy phonons possesses large and negative values of γ, negative thermal expansion is likely.[7]

In order to estimate the Grüneisen parameters for the phonons calculated above, a 1% strain was applied to the model prior to recalculating the mode frequencies. In Fig. 3.2(c), the phonon branches are coloured and broadened according to their value of γ, where red denotes negative values and blue positive values. Interestingly, the majority of the low-energy modes are associated with negative Grüneisen parameters—including those modes previously identified as columnar shifts—and so capable of driving NTE. It is possible to count the number of key NTE modes at each high-symmetry reciprocal lattice point, giving 6 as $\mathbf{k} \to \Gamma$, 5 at X, 4 at M and 3 at R. At each point, three of these modes correspond to rigid body rotations and hence there are additional shift modes at Γ, X and M with $\gamma < 0$. Tilting is commonly invoked as an explanation for the occurrence of NTE in certain molecular perovskites, *e.g.* PBAs,[190,191,412] but the present analysis reveals that shifts perhaps play an as-yet underappreciated role. In fact, a shift-like distortion has been identified as a key NTE mode in MOF-5, which has a topology reminiscent of an A-site

deficient molecular perovskite.[432,433] Furthermore, this investigation suggests that shifts are strongly anharmonic and the simple harmonic model employed here may therefore not fully capture the phonon behaviour.

3.4 Static shifts

As columnar shifts constitute low-energy phonon modes, they are prone to condensation and hence a permanent symmetry lowering. This Section focuses on the symmetry breaking enforced by static shifts and develops a nomenclature for describing shifts in 2D and 3D. It will be shown that the activation of shifts has a profound effect on the symmetry of the structure, as can be expected.

3.4.1 Two-dimensional shifts

For ease of representation, it is instructive to first consider shifts in a two-dimensional perovskite. In 2D, the high-symmetry undistorted aristotype belongs to the plane group *p4mm* [Fig. 3.3(a)]. By analogy to the predominant periodicities of tilts in conventional perovskites, one might anticipate that shifts will frequently appear at the centre or boundary of the Brillouin zone. Within this assumption, there are three possibilities for each of the two axes: inactive shifts, active shifts with $\mathbf{k} = \langle 0,\, 0\rangle$; and active shifts with $\mathbf{k} = \langle \frac{1}{2},\, 0\rangle$. This yields nine permutations in total [Fig. 3.3].

The conceptually simplest examples of two-dimensional shift distortions are systems with shifts along one axis only. Yet, the activation of one zone-centre shift [Fig. 3.3(b),(d)] leads to a relatively complex situation. The plane group symmetry

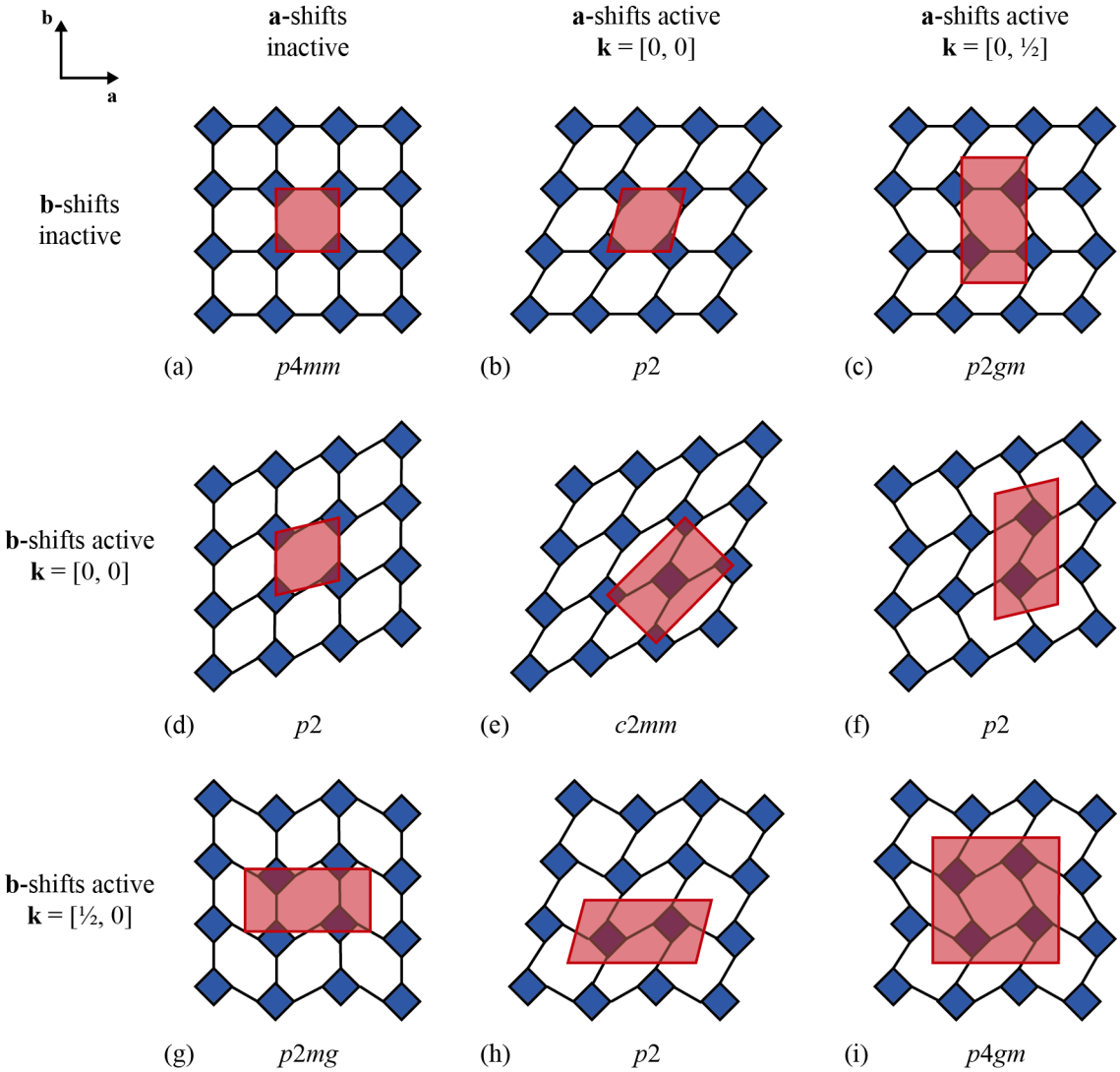


Figure 3.3: Shifts in 2D. The unit cell is drawn in red and the plane group included.

is lowered to $p2$ and the absence of mirror lines enables tilts as a secondary order parameter. The tilting is significant, as it allows for a continuous transformation between the two structures produced by shifts polarised along **a** and **b**, respectively [Fig. 3.4(a)]. As a consequence, the precise direction of the shift cannot be uniquely defined in this case as the direction can be interconverted *via* a continuous pathway. The same intricacy does not occur for shifts modulated at the zone boundary. Instead, the two resulting structures are interchangeable by rotation in 2D space and the plane group is $p2gm$ for shifts along **a** and $p2mg$ for shifts polarised along **b**

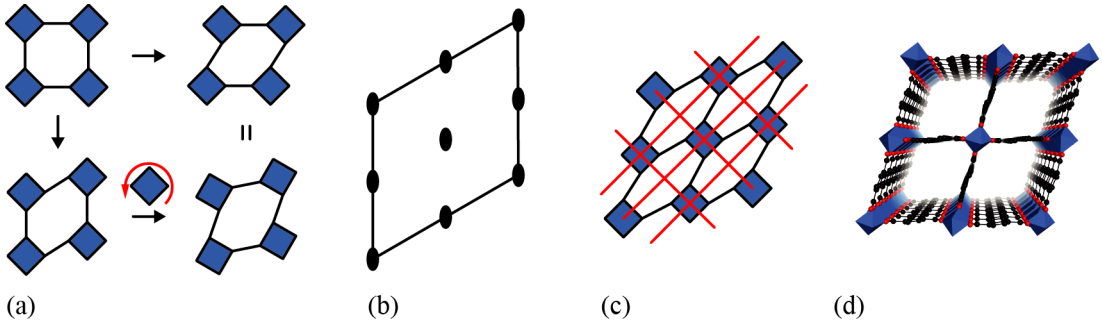


Figure 3.4: (a) The interconversion of the a^+b^0 and a^0b^+ shift patterns through tilting. (b) The two-fold rotation axes in plane group $p2$. (c) The presence of mirror planes prevents tilting in the a^+a^+ pattern. (d) The structure of MIL-53.[434]

[Fig. 3.3(c),(g)]. In essence, even uniaxial shift distortions are associated with severe and diverse symmetry-breaking properties.

For active shifts along both Cartesian axes, there are fewer complications. Two zone-centre shifts of equal magnitude yield the plane group $c2mm$ [Fig. 3.3(e)], where the mirror lines prevent tilting [Fig. 3.4(c)]. This symmetry lowering is analogous to a ferroelastic distortion of the lattice. Such states are often associated with mechanical compliance that can generate intriguing functional responses, including negative linear compressibility (NLC) and uniaxial NTE.[435–438] The 2D situation considered here is akin to a projection of a 3D wine-rack topology, which accounts for the NLC exhibited by the canonical wine-rack MOF MIL-53 [Fig. 3.4(d)].[437,439] The converse antiferroelastic state arises from zone-boundary shifts of equal magnitudes along both axes [Fig. 3.3(i)]. The unit cell is now doubled relative to the aristotype and the plane group is $p4gm$, with the mirror lines again preventing tilting. Finally, the activation of one zone-boundary and one zone-centre shift drives a severe symmetry lowering to $p2$, irrespective of the choice of axes. Tilting is allowed, but as there is no continuous pathway between the two structures, interconversion does not occur and they are in fact enantiomers.

3.4.2 Notation in 2D

Given the complexity of shifts, it is desirable to develop a notation to aid characterisation and comparison, similarly to Glazer notation for tilts in conventional perovskites [Section 1.3.4].[120] An analogous notation of the form λ^{μ} can be used for shifts, where the index μ refers to the component of the propagation vector normal to the relevant axis. For example, the ferroelastic distortion given by two equal zone-centre shifts is described by $a^{+}a^{+}$, indicating $k_x = 0$ for shifts modulating along **b** (normal to **a**) and $k_y = 0$ for shifts modulating along **a** (normal to **b**). The use of the same base ("a") denotes equal magnitude of the two shifts. Another illustrative example is the ambiguous case of one zone-centre shift, as depicted in Fig. 3.3(b) and (d). The notation is $a^{+}b^{0}/a^{0}b^{+}$ for shifts polarised along **a**/**b**, but as these two are interconvertible by tilts, the descriptions are equivalent and also indistinguishable from the intermediate scenario of $a^{+}b^{+}$. Consequently, there is not a unique notation for this shift system. Glazer-type notations for all the shift patterns in Fig. 3.3 are given in Table 3.2.

Although the Glazer-type nomenclature is successful in 2D, its extension to 3D is nontrivial and a matrix notation is more suitable. This mirrors the notation developed for unconventional tilting in molecular perovskites [Section 1.5.1].[318] The shift matrix is decorated with $\lambda_{\alpha\beta} = \epsilon_{\alpha} \exp(2\pi i k_{\beta})$, signifying a shift of columns parallel to axis α propagating along direction β, where $\epsilon_{\alpha} = 1$ for active shifts and $\epsilon_{\alpha} = 0$ for inactive shifts:

$$\begin{bmatrix} \lambda_{\alpha\alpha} & \lambda_{\alpha\beta} \\ \lambda_{\beta\alpha} & \lambda_{\beta\beta} \end{bmatrix}. \tag{3.10}$$

Table 3.2: Symmetry of the 2D shift systems.

a-shifts	**b**-shifts	"Glazer" symbol	Matrix symbol	Plane group
inactive	inactive	a^0a^0	$\begin{bmatrix} 0 & 0 \\ 0 & 0 \end{bmatrix}$	$p4mm$
in phase	inactive	a^+b^0	$\begin{bmatrix} + & + \\ 0 & 0 \end{bmatrix}$	$p2$
in phase	in phase	a^+a^+	$\begin{bmatrix} + & + \\ + & + \end{bmatrix}$	$c2mm$
out of phase	inactive	a^-b^0	$\begin{bmatrix} + & - \\ 0 & 0 \end{bmatrix}$	$p2gm$
out of phase	in phase	a^-b^+	$\begin{bmatrix} + & - \\ + & + \end{bmatrix}$	$p2$
out of phase	out of phase	a^-a^-	$\begin{bmatrix} + & - \\ - & + \end{bmatrix}$	$p4gm$

Thus, the ferroelastic distortion (a^+a^+) is described by

$$\begin{bmatrix} + & + \\ + & + \end{bmatrix}, \tag{3.11}$$

and the uniaxial zone-centre shift along **a** by

$$\begin{bmatrix} + & + \\ 0 & 0 \end{bmatrix}, \tag{3.12}$$

which is equivalent to

$$\begin{bmatrix} 0 & 0 \\ + & + \end{bmatrix}. \tag{3.13}$$

However, the matrix notation for a^+b^+ is

$$\begin{bmatrix} + & + \\ + & + \end{bmatrix}, \tag{3.14}$$

which is identical to Eq. 3.11, despite their structural incongruence. This highlights the problem with the matrix notation: information about the relative magnitudes of the two shifts is lost. For this reason, the Glazer-like notation is likely to be preferable for shifts in 2D.

3.4.3 Notation in 3D

Shifts in 3D perovskites may occur in any combination along the three crystallographic axes subject to the restriction that $k_\alpha = 0$ for shifts polarised along the α-axis. There are now two different directions of propagation, k_β and k_γ, for each shift and this renders the Glazer notation less clear. The matrix notation on the other hand is readily extended to higher dimensions and the three-dimensional version is given by

$$\begin{bmatrix} \lambda_{\alpha\alpha} & \lambda_{\alpha\beta} & \lambda_{\alpha\gamma} \\ \lambda_{\beta\alpha} & \lambda_{\beta\beta} & \lambda_{\beta\gamma} \\ \lambda_{\gamma\alpha} & \lambda_{\gamma\beta} & \lambda_{\gamma\gamma} \end{bmatrix}, \tag{3.15}$$

where $\lambda_{\alpha\beta} = \epsilon_\alpha \exp(2\pi \mathrm{i} k_\beta)$ denotes a shift of columns parallel to axis α propagating along direction β. As an illustration, consider the X-point (planar) shift depicted in Fig. 3.1(b), where the shift is polarised along the a-axis with a modulation of $\mathbf{k} = [0, 0, \frac{1}{2}]$. The matrix associated with this shift system is

$$\begin{bmatrix} + & + & - \\ 0 & 0 & 0 \\ 0 & 0 & 0 \end{bmatrix}. \tag{3.16}$$

This shows the presence of an **a**-shift, displacing in an alternating fashion along **c** and in phase along **b**. The second and third row are populated by zeros to indicate the absence of active shifts along any of these axes.

It is conceivable to exploit the Bradley-Cracknell symbols for the special points in reciprocal space as indices in the Glazer symbol.[360] The modulation vector $\mathbf{k} = [0, 0, \frac{1}{2}]$ is abbreviated to "X" and the Glazer notation for the above shift distortion thus becomes $a^{\mathrm{X}}b^0b^0$, where $\mathrm{X} = \langle 0, 0, \frac{1}{2}\rangle$. Since $k_x = 0$, the propagation wavevector may either be $[0, 0, \frac{1}{2}]$ or $[0, \frac{1}{2}, 0]$. In the absence of further symmetry-lowering distortions, these situations are equivalent. Nonetheless, molecular perovskites are prone to structural distortions and cases with only one shift are likely to be scarce. For structures with multiple distortions, the Glazer notation thus becomes ambiguous and, therefore, the matrix notation is advantageous for shifts in 3D systems.

3.5 Case studies

The discussion so far has been purely theoretical; however, there is no paucity of real structures incorporating columnar shifts and a few representative examples are presented here.

3.5.1 $[\mathbf{N(CH_3)_4}]\mathbf{Ca(N_3)_3}$

The first example is $[\mathrm{N(CH_3)_4}]\mathrm{Ca(N_3)_3}$, which constitutes one of the earliest molecular perovskites based on the azide anion.[294] At room temperature, it adopts the tetragonal space group $P4/nmm$, with cell parameters related to that of the cubic aristotype (a_0) by $a \sim \sqrt{2}a_0$ and $c \sim a_0$ [Fig. 3.5(a)]. There is an active shift along

the **c**-direction propagating with wavevector $\mathbf{k} = [\frac{1}{2}, \frac{1}{2}, 0]$. No shifts are polarised along the perpendicular axes and this single shift (irrep M_2^-) acts as the primary order parameter for the observed space group $P4/nmm$. The shorthand Glazer notation is $a^0a^0c^{\mathrm{M}}$ and the matrix may be assembled to yield

$$\begin{bmatrix} 0 & 0 & 0 \\ 0 & 0 & 0 \\ - & - & + \end{bmatrix}. \tag{3.17}$$

The 3D shift assignment is aided by considering the shift pattern in 2D planes (*bc*, *ac*, *ab*) of the structure followed by superposition of the 2D submatrices. The right-hand panel of Fig. 3.5 shows the relevant 2D planes and the shifts are easily assigned as

$$\begin{bmatrix} \cdot & \cdot & \cdot \\ \cdot & 0 & 0 \\ \cdot & - & + \end{bmatrix} \quad \begin{bmatrix} 0 & \cdot & 0 \\ \cdot & \cdot & \cdot \\ - & \cdot & + \end{bmatrix} \quad \begin{bmatrix} 0 & 0 & \cdot \\ 0 & 0 & \cdot \\ \cdot & \cdot & \cdot \end{bmatrix}. \tag{3.18}$$

The dots correspond to correlations along the direction of viewing, *e.g.* correlations along **c** when viewing the *ab*-plane. Analogous to some of the 2D examples in the preceding Section, the mirror planes prevent tilting and, therefore, there are no active tilts in $[N(CH_3)_4]Ca(N_3)_3$.

3.5.2 $[(CH_3)_2NH_2]Mn(N_3)_3$

The second example is the room-temperature phase of $[(CH_3)_2NH_2]Mn(N_3)_3$, which was first reported in Ref. 293. This azide perovskite crystallises in the orthorhombic space group *Cmce* and the unit cell is approximately doubled in all three directions

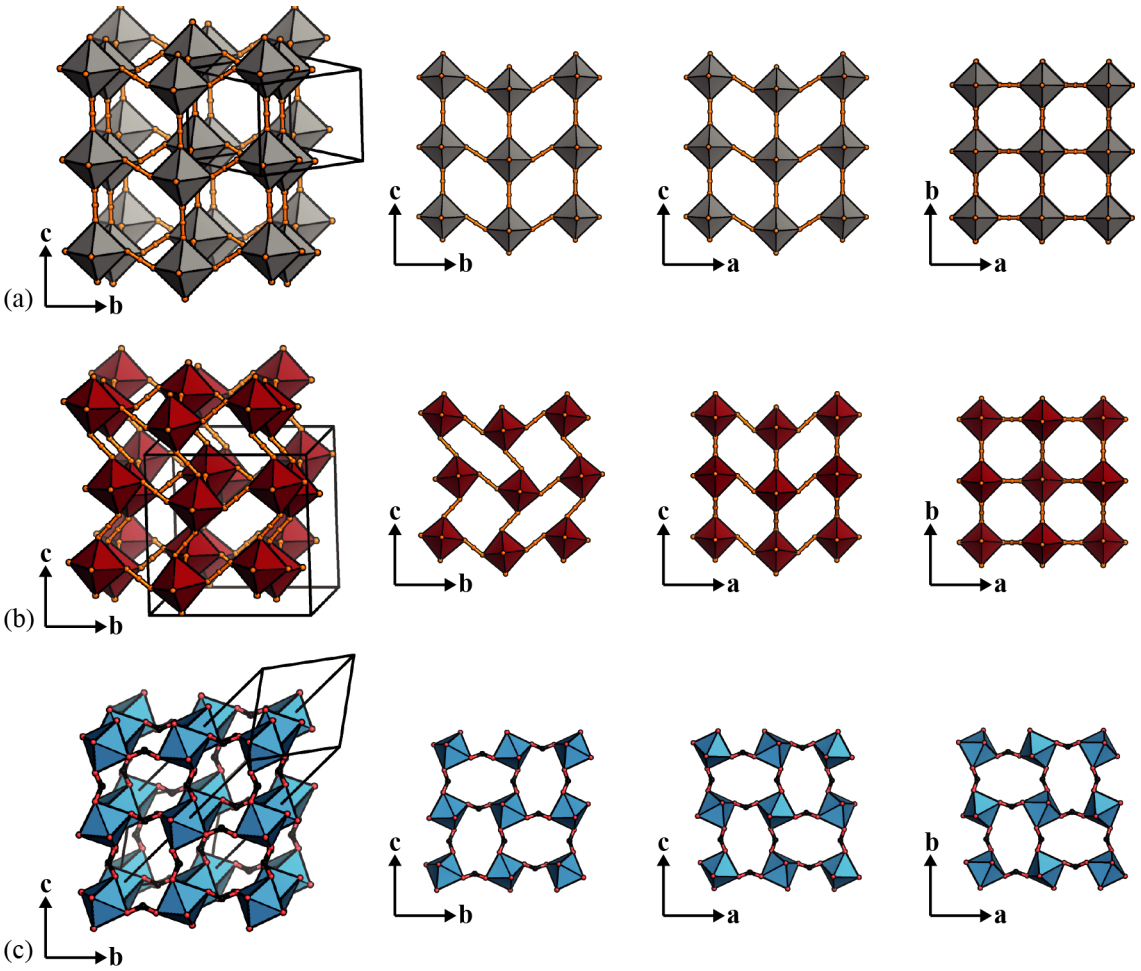


Figure 3.5: Selected examples of shifted molecular perovskites taken from literature, with the A-site cation omitted for clarity. The crystal structures are shown to the left, with the *crystallographic* unit cell indicated in black, and the 2D planes with the cell axes of the *perovskite* unit cell depicted to the right. (a) $[N(CH_3)_4]Ca(N_3)_3$,[294] (b) $[(CH_3)_2NH_2]Mn(N_3)_3$,[293] and (c) $[(CH_3)_2NH_2]Co(HCOO)_3$.[269]

relative to the aristotype [Fig. 3.5(b)]. There are active shifts polarised along two axes: firstly, a **c**-shift modulates in an out-of-phase fashion with respect to the *a*- and *b*-axes—identically to the previous system. Secondly, octahedral layers parallel to the *ab*-plane are displaced in the **b**-direction with a wavevector of $\mathbf{k} = [0, 0, \frac{1}{2}]$. Hence, the matrix notation is

$$\begin{bmatrix} 0 & 0 & 0 \\ + & + & - \\ - & - & + \end{bmatrix}. \tag{3.19}$$

As before, it is instructive to consider the shift patterns in 2D:

$$\begin{bmatrix} \cdot & \cdot & \cdot \\ \cdot & + & - \\ \cdot & - & + \end{bmatrix} \quad \begin{bmatrix} 0 & \cdot & 0 \\ \cdot & \cdot & \cdot \\ - & \cdot & + \end{bmatrix} \quad \begin{bmatrix} 0 & 0 & \cdot \\ 0 & 0 & \cdot \\ \cdot & \cdot & \cdot \end{bmatrix}. \tag{3.20}$$

The shorthand notation is $a^0b^{\mathrm{X}}c^{\mathrm{M}}$, which illustrates the afore mentioned ambiguity. It is not clear whether the X-point shift should be interpreted as $\mathbf{k} = [0,\ 0,\ \frac{1}{2}]$ or $\mathbf{k} = [\frac{1}{2},\ 0,\ 0]$ and yet, these two possibilities would give rise to distinct symmetries when combined with an M-point shift at $\mathbf{k} = [\frac{1}{2},\ \frac{1}{2},\ 0]$.

In this case, the presence of the two shifts lowers the crystal symmetry sufficiently to allow coupling to tilts. The (conventional) tilt pattern that emerges is denoted by $a^-b^0b^0$. This pattern drives $I4/mcm$ symmetry if present in isolation,[12] and so the tilts are not the primary order parameters for this compound. Representation analysis identifies the two shifts (irreps M_2^- and X_5^+) as the superimposed primary order parameters for the $Cmce$ space group symmetry in $[(\mathrm{CH_3})_2\mathrm{NH_2}]\mathrm{Mn}(\mathrm{N_3})_3$ and the tilt (irrep R_5^-) as a secondary order parameter. This demonstrates the necessity of considering shifts as well as tilts when investigating the symmetry of molecular perovskites.

3.5.3 $[(\mathrm{CH_3})_2\mathrm{NH_2}]\mathrm{Co}(\mathrm{HCOO})_3$

The final case study that is considered here concerns the formate-based perovskite $[(\mathrm{CH_3})_2\mathrm{NH_2}]\mathrm{Co}(\mathrm{HCOO})_3$,[269] which adopts $R\bar{3}c$ symmetry with $a \sim \sqrt{2}a_0$ and $c \sim 2\sqrt{3}a_0$ [Fig. 3.5(c)]. Here, zone-centre columnar shifts are present along all three

axes and can be viewed as a macroscopic shear strain polarised along the body diagonal of the pseudo-cubic perovskite unit cell. The distortion is simply given by

$$\begin{bmatrix} + & + & + \\ + & + & + \\ + & + & + \end{bmatrix} \tag{3.21}$$

or $a^{\Gamma}a^{\Gamma}a^{\Gamma}$. The shifts lower the symmetry to $R\bar{3}m$, which is a minimal supergroup of the observed space group $R\bar{3}c$. Consequently, shifts are not the primary order parameter in this case; instead it is the conventional tilt system $a^{-}a^{-}a^{-}$ that drives the observed symmetry.[12,120] The shift distortions constitute secondary order parameters, allowed by symmetry from the presence of the tilts. Thus, both shifts and tilts may act as the primary order parameter in molecular perovskites and, in general, group-theoretical analysis is required on a case-by-case basis to elucidate the precise role played by each distortion.

3.5.4 Complications

In the above examples, the shifts could be successfully assigned and analysed by inspection, but this is not universally the case. Given the inherent flexibility of molecular linker species, more complex shift situations—which do not easily lend themselves to simple identification—are to be expected. In such cases, group-theoretical software, such as ISODISTORT,[382] will be a vital tool for accurate structure descriptions.

There are numerous complications regarding the shift assignment and notation.

First, the matrix notation given here does not account for the possibility of unequal magnitudes for the different shifts. Yet, as demonstrated in Section 3.4.1, altering the relative amplitudes of two independent shift distortions sometimes changes the symmetry. Second, only zone-centre and zone-boundary shifts have been treated and although these are likely to be the most prevalent, other regions of the Brillouin zone are also accessible.[284,299,311] To illustrate this point, the crystal symmetry of the dicyanamide perovskite $[NPr_4]Ni[N(CN)_2]_3$ is described by **a**-shifts modulated by $\mathbf{k} = [0, \frac{1}{4}, \frac{1}{4}]$ [Fig. 3.6(a)].[311] This periodicity is also frequent in hypophosphite perovskites and may be represented by imaginary components in the shift matrix—as $\mathrm{i} = \exp(2\pi\mathrm{i}\frac{1}{4})$—or by the Bradley-Cracknell symbol Σ in the Glazer notation.*[283] Third, more than one active shift distortion can be polarised along the same axis [Fig. 3.6(b)]. This is a relatively common situation; for example $[Ph_3S]Mn[N(CN)_2]_3$ and the low-temperature phases of $AMn(N_3)_3$ (where $A = (CH_3)_nNH_{4-n}$ for $n = \in\{1,2,3\}$) display a combination of a shear shift and an out-of-phase shift along at least one axis.[293,312] Parallels can be drawn to the compound tilts found in some conventional perovskites.[351,440] Fourth, in systems of very low symmetry, *e.g.* the triclinic $[DAB]Mn_2(H_2POO)_6$ (DAB = dabconium), the manifold of active deformations severely complicates the unambiguous assignment and enumerations of shifts. It is debatable whether the concept of RUMs is strictly valid in such cases.

*Although it has to be remembered that Σ corresponds to a line in reciprocal space and so does not uniquely define the crystal momentum.

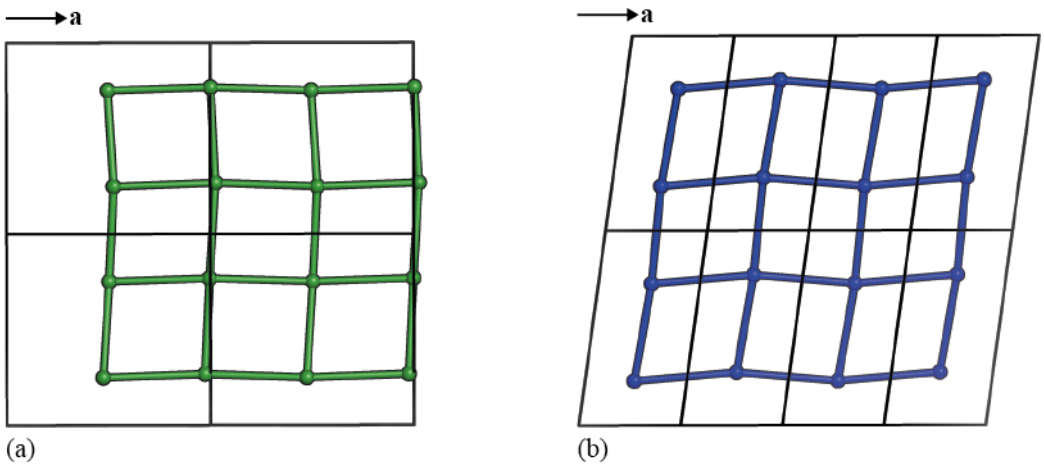


Figure 3.6: Complex shift patterns in two dicyanamide perovskites. (a) "Imaginary" shifts ($\mathbf{k} = [0, \frac{1}{4}, \frac{1}{4}]$) in $[NPr_4]Ni[N(CN)_2]_3$ and (b) two active shifts polarised along one axis in $[Ph_3S]Mn[N(CN)_2]_3$. The frameworks are shown with bonds directly joining the B-site metal cations and the unit cells are shown in black.

3.6 Shift trends

As a part of the ultimate goal of developing an framework for rational structural design of molecular perovskites, it is desirable to establish design rules for shifts. While principles for "shift engineering" are not yet available, post-rationalisation of the shift trends in the different families of molecular perovskites provides some insight into the principles governing the activation of precise shift patterns.

3.6.1 The effect of the X-site linker

The existence and nature of columnar shifts in a given family is heavily influenced by the linker. Prussian blue analogues are the only molecular perovskite without any propensity for static columnar shifts, although organic cyanoelpasolites—alkali-based PBAs with organic A-site cations—intermittently exhibit shear shifts.[223,238] Likewise, all shifts observed thus far in dicyanometallates and thiocyanate perovskites occur at the zone centre, although neither of these families display any great

compositional variation to date.[286,287,318,321] It is conceivable that systems with other shift periodicities will be synthesised in the future. In formate perovskites, the relative frequencies of the shift **k**-vectors follow the order $\mathbf{k} = \langle 0,0,0\rangle >> \langle \frac{1}{2},0,0\rangle >> \langle \frac{1}{2},\frac{1}{2},0\rangle$. Indeed, examples of entirely unsheared formates are extremely rare and M-point shifts are equally scarce. Finally, molecular perovskites comprising dicyanamide, hypophosphite or azide on the X-site typically display a rich manifold of various shifts distortions. Thermal alterations of the shift patterns often play an important role in triggering phase transitions in these families.[284,293,311,314] So when designing a system, the presence or absence of shifts may be controlled to some degree by correct choice of the anionic linker.

The natural question to ask is then "what determines the propensity for a given anion to form shifted structures?" At a basic level, the fundamental requirement for a linker to facilitate shifts is an ability to tolerate nonlinear binding modes. By way of example, the azide anion supports a wide range of M–N–N angles—from 180° in $[N(CH_3)_4]Ca(N_3)_3$ to 121° in $[N(CH_3)_4]_2KCr(N_3)_6$ [Fig. 3.7(a)]—and this flexibility likely promotes the preponderance of shifts in azide perovskites.[294,297] The extreme opposite behaviour is exhibited by cyanide, where the bonding is predominantly linear in line with predictions based on molecular orbital descriptions [Fig. 3.7(b)].[441] This is reflected in the low propensity for any condensed phonon modes in Prussian blue analogues. However, the presence of tilts in cyanoelpasolites implies that the size and/or LFSE of the B-site metals also contributes to the presence of RUMs. Another special case of bond formation is that of formate, as its geometry necessarily imposes a nonlinear binding, manifested by one of two possible conformations. As

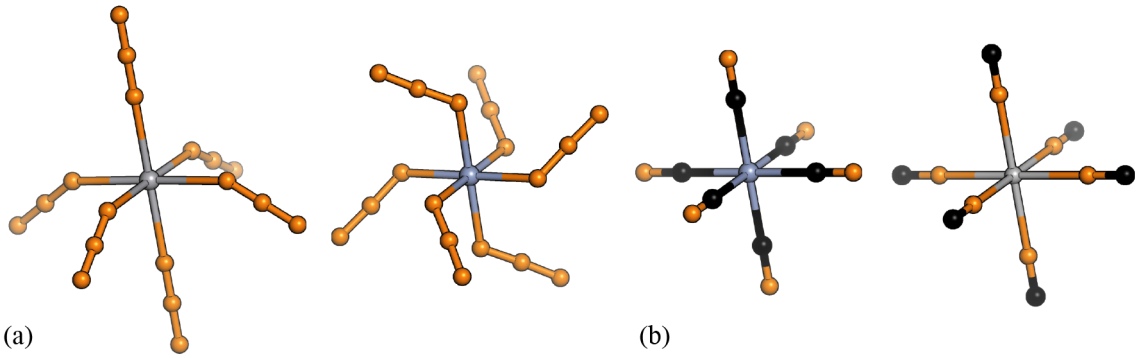


Figure 3.7: Binding angles of azide and cyanide. (a) The azide anion supports a wide range of binding modes, whereas (b) cyanide binds almost invariably linearly. Nitrogen is shown in orange, carbon in black and the metals in grey. Crystal structures taken from Ref. 294,297,442.

a result, untilted formate perovskites do not occur since the bent linker enforces tilts and similar considerations can be assumed to play a role in the activation of shifts. In order to further develop the understanding of the driving forces for shift patterns, a consideration of frontier orbitals will be valuable, albeit it is not the sole influencing factor.

3.6.2 The effect of the A-site cation

The A-site cation has a large impact on the nature of the shifts displayed by the hosting framework. Once again, formate perovskites are good model systems due to their abundance and compositional variability. In general, series of $AB(HCOO)_3$ tend to be isostructural if A is fixed and B varied, but the converse is not generally true. For example, $(CH_3NH_3)B(HCOO)_3$ adopts *Pnma* symmetry with a zone-centre uniaxial shift for any first-row metal on the B-site,[243,443–446] whereas the disordered phase of $[(CH_3)_2NH_2]B(HCOO)_3$ supports shear shifts along all three axes.[243,270,447,448] The series $[C(NH_2)_3]B(HCOO)_3$ (B^{2+} = Mg, Mn, Fe, Co, Ni, Cu, Zn) also displays triple shear shifts, in combination with a uniaxial X-point shift.[245]

All of the above crystallise in *Pnna* with the exception of the Cu analogue; the implications of which are explored in the subsequent Chapter. These examples single out the A-site cation as the main shift determinant in the formate family.

To a first approximation, the cation influence on the shift pattern can be attributed to a templating effect based on cation shape and size. In the aristotype, the site symmetry of the A-site is $m\bar{3}m$, which is higher than the point symmetry of most molecular cations. The site symmetry is reduced upon activation of shift distortions to a subgroup of $m\bar{3}m$ that frequently conforms to the point symmetry of the cation occupying the A-site. For example, tetramethylammonium possesses point symmetry $\bar{4}3m$ (T_d) and in $[N(CH_3)_4]Ca(N_3)_3$, it is situated at the $2b$ position with a site symmetry of $\bar{4}2m$—a subgroup of $\bar{4}3m$ [Section 3.5, Fig. 3.8(a)].[294] Likewise, dimethylammonium has point symmetry $mm2$, which is a supergroup of the 2 site symmetry in $[(CH_3)_2NH_2]Mn(N_3)_3$ [Section 3.5, Fig. 3.8(b)].[293] Moreover, it appears that the size of the cation affects the magnitude of a given shift. By way of illustration, $(NH_4)Cd(HCOO)_3$, $KCd(HCOO)_3$ and $RbMn(HCOO)_3$ exhibit shear shifts of considerably larger magnitude than the equivalent distortions in formate perovskites templated by larger cations.[243,250,253,448] This is unsurprising and should in fact be expected, as similar mechanisms operate for tilting in conventional perovskites. As a consequence, judicious choice of the cation may provide a future avenue for rational shift design.

Nonetheless, shift patterns can be sensitive to subtle compositional changes of the A-site cation, indicating that shape effects are not the full story. The hydrazinium cation ($NH_2NH_3^+$) strongly resembles methylammonium ($CH_3NH_3^+$); yet

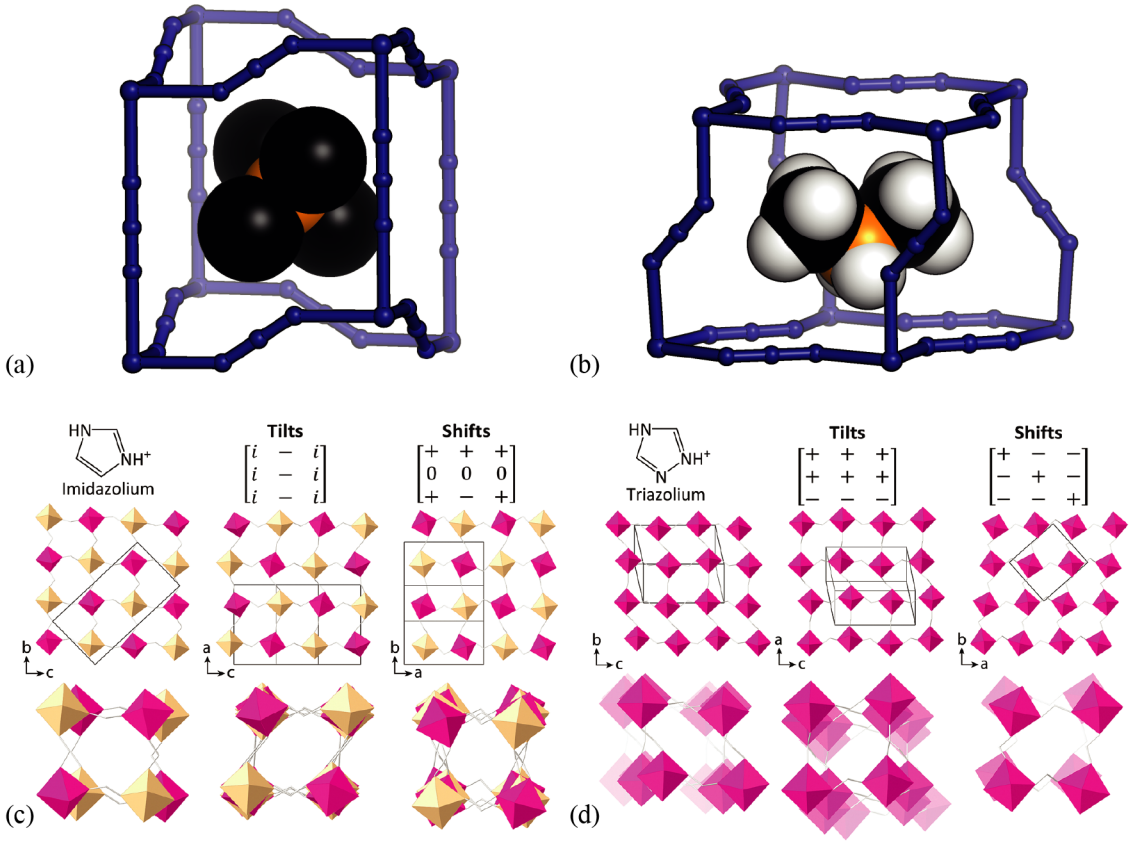


Figure 3.8: A-site cations templating different shift patterns. (a) $[N(CH_3)_4]Ca(N_3)_3$ and (b) $[(CH_3)_2NH_2]Mn(N_3)_3$. The unequal shift patterns templated by (c) imidazolium and (d) triazolium in $AMn(H_2POO)_3$, where symmetry-inequivalent octahedra are shown in different colours. Panel c and d reproduced from Ref. 283 with permission from The Royal Society of Chemistry.

the low-temperature phase of $(NH_2NH_3)Zn(HCOO)_3$ harbours a sizeable X-point shift not observed in $(CH_3NH_3)Zn(HCOO)_3$.[448,449] Likewise, replacing two atoms in imidazolium (HIm) to afford triazolium (Trz) drastically alters the shifts in the hypophosphite $[HIm]Mn(H_2POO)_3$ [Fig. 3.8(c)–(d)].[283] Although the cations in the above examples are essentially isostructural, the replacement of CH for N affects the ability to participate in hydrogen bonding. Weak interactions, *e.g.* hydrogen bonding and potentially π-π interactions, are often crucial to the chemistry of metal–organic frameworks and hence it is conceivable that they also change the shift patterns.

The above discussion reveals the vital role of the A-site cation in dictating the shift pattern of molecular perovskites. Therefore, as novel compounds with previously unexploited cations continue to emerge, additional interesting shifted structures are anticipated. Indeed, a few months before submission of this Thesis (April 2018), the recent hypophosphite perovskites were identified as a platform for intriguing shift and tilt patterns.[283] Moreover, one might expect new shift patterns for thiocyanate perovskites considering that only three structures are reported so far, all of which employ NH_4 on the A-site.[286,287] Similarly, all dicyanometallate perovskites known to date—which all only support shear shifts—host PPN as the A-site species[318,321] and it is conceivable that another cation might favour shifts propagating with different momenta. However, as the size of the framework increases, the demand for steric bulk of the cation is enhanced and so finding suitable A-site species becomes an increasingly difficult task. Consequently, extending the compositional range of the very largest molecular perovskites, such as dicyanometallates, is likely to present a challenge. It follows that the diversity of the accessible shift distortions for a given family of molecular perovskites is coupled to the substitutional scope on the A-site.

3.7 Implications

Understanding the rigid unit modes of a framework structure is crucial for a full appreciation of its structural behaviour. This Chapter has demonstrated that columnar shifts—a degree of freedom exclusive to perovskites with polyatomic linkers—play a role in molecular perovskites that is by and large comparable to that of the octahe-

dral tilting in conventional perovskites. The analogy can be extended by developing a Glazer-like nomenclature to describe the shifts, although their considerable complexity sometimes renders unique representations unfeasible. However, since the publication of this study,[352] the notation presented here has been successfully used to compare the shifts in a number of recently reported molecular perovskites.[283]

The low-energy region of the phonon dispersion for a generic molecular perovskite hosts a large number of shift-like modes, which often are characterised by negative Grüneisen parameters. Hence, dynamic shifts can be expected to drive displacive phase transitions as well as negative thermal expansion. The former is illustrated by $(NH_2NH_3)Zn(HCOO)_3$, which supports a condensed X-point shift mode in its low-temperature form that subsequently vanishes upon heating.[449] In order to further explore the latter point, system-specific molecular dynamics calculations—as carried out for $Zn(CN)_2$[450,451]—would be of interest and can likely shed some light on the role of shifts in molecular perovskites predisposed to NTE. Moreover, the prospect of finding experimental evidence for dynamic shifts in, for example, Prussian blue analogues or metal formate frameworks provides an attractive avenue for future research. Although experimental investigations of phonon dispersion in MOFs and CPs are challenging due to the large number of vibrational modes, inelastic neutron scattering (INS) studies of related systems are not without precedent.[452–454]

Given the important symmetry-breaking role of shifts, they provide highly valuable distortions from a crystal engineering viewpoint. In particular, columnar shifts give access to areas of reciprocal space not available by means of conventional tilting. This feature will be exploited in detail in the final Chapter, which will come to show

that shifts are able to couple to other distortions so as to break global inversion symmetry. Even though achieving synthetic control presents a key barrier to the targeted synthesis of acentric structures by means of shifts, framework deformations are often coupled to the A-site cation shape and chemistry, which may provide a basis for simple design rules in the future.

Chapter 4

Cooperative Jahn-Teller Effects in Molecular Perovskites

4.1 Chapter overview

This Chapter focuses on cooperative Jahn-Teller distortions in isovalently doped series of molecular perovskites, which—in contrast to columnar shifts—is a conventional degree of freedom in perovskites and has been the subject of many previous studies.[91,455–457] Three topologically distinct systems are investigated: a primitive cubic, a face-centred cubic and a defective face-centred cubic series. By incremental substitution of a Jahn-Teller inactive cation for orbitally active Cu^{2+}, the critical Cu concentration required for the onset of long-range orbital order can be determined. These compositional thresholds are analysed by experimental (PXRD) and computational (MC simulations) techniques: first for the primitive cubic formate system and, second, for the face-centred Prussian blue analogues. The Chapter concludes with a comparative evaluation of the results and a discussion regarding the potential for exploiting Jahn-Teller distortions in rational materials design.

Arkadiy Simonov helped with the implementation of the Monte Carlo simulations and provided the starting models for the vacancy configurations in Appendix B. Chloe Coates and Emily Reynolds assisted during the beamtime at I11, and Zsuzsa

Mayer and Fred Dunn aided with the collection of the AAS data. The syntheses of the formate perovskites and some characterisation were performed by Edwina Donlan, a former Part II student in the group whom I helped supervise.

4.2 Background

Many of the intriguing phenomena of perovskite oxides arise from the strong interplay between various degrees of freedom: spin, charge, lattice and orbital.[458–461] For this reason, orbital interactions have been extensively investigated in perovskites, principally in the mixed-valent manganites where they are implicated in the emergence of colossal magnetoresistance.[462] Although molecular perovskites do not exhibit these strongly correlated states due to weaker coupling, the following Chapter will nevertheless come to show that Jahn-Teller distortions* can play a key role in breaking inversion symmetry of these systems.

It is appropriate to begin with a brief overview of a few pertinent Jahn-Teller-distorted conventional perovskites. The canonical example is arguably $LaMnO_3$, where the orthorhombic Q_2 distortion of the Mn^{3+} ions is ordered in a C-type (M-point) arrangement at ambient conditions.[75,463] Upon heating above 750 K, a transition to an orbitally disordered state occurs, and obtaining a microscopic picture of this disordered phase has proven to be a challenge.[74,90,464] Ahmed *et al.* developed an anisotropic version of the 3-state Potts model where each orbital can assume one of three discrete orientations, and "head-on" correlations—*e.g.* neighbouring sites along **c** with Q_3^z states—are disfavoured.[93,94] A recent study employed neu-

*Throughout this Chapter, first-order Jahn-Teller distortions are meant unless otherwise stated.

tron and X-ray pair distribution functions to probe the disordered state in $LaMnO_3$ and although some evidence in favour of the 3-state Potts model was observed, the limitations of PDF techniques prevented a conclusive answer.[90] The exact nature of the orbital disorder thus remains an unsolved problem. Another interesting JT-active perovskite is $KCuF_3$, where the orbital order of the Q_3 distortion enforces one-dimensional $S = \frac{1}{2}$ Heisenberg antiferromagnetism.[465–468] Since $KCuF_3$ is an unusual example of an untilted perovskite with nearly pseudo-cubic symmetry, it constitutes a useful model system for the study of the interplay between orbital order and magnetic functionality.[78,461] Consequently, the orbital degrees of freedom in conventional perovskites have been, and still are, of significant interest for both fundamental and applied research.

Orbital disorder can also be induced by cation doping, as in solid solutions of formula $La_{1-x}A_xMnO_3$ where A is a divalent Group II ion.[48,58,469] In order to maintain electroneutrality, Mn^{3+} ions are replaced by JT-inactive Mn^{4+}, which has important ramifications for the e_g electrons. $La_{1-x}A_xMnO_3$ is a metallic conductor at low temperatures as the e_g electron is itinerant and so the JT distortion is quenched. At higher temperatures, the electrons localise and long-range orbital correlations persist for a sufficiently small doping level. As x increases, partial delocalisation occurs concomitant with the formation of polarons.[470] Mixed-valent manganites often exhibit rich and complex phase diagrams as the electronic degree of freedom is strongly correlated to the spin, orbital and charge degrees of freedom [Fig. 4.1].[96,98,471,472] This is not only of fundamental interest, but it is also crucial for the emergence of colossal magnetoresistance in these systems.[471,473,474] Obtaining an improved un-

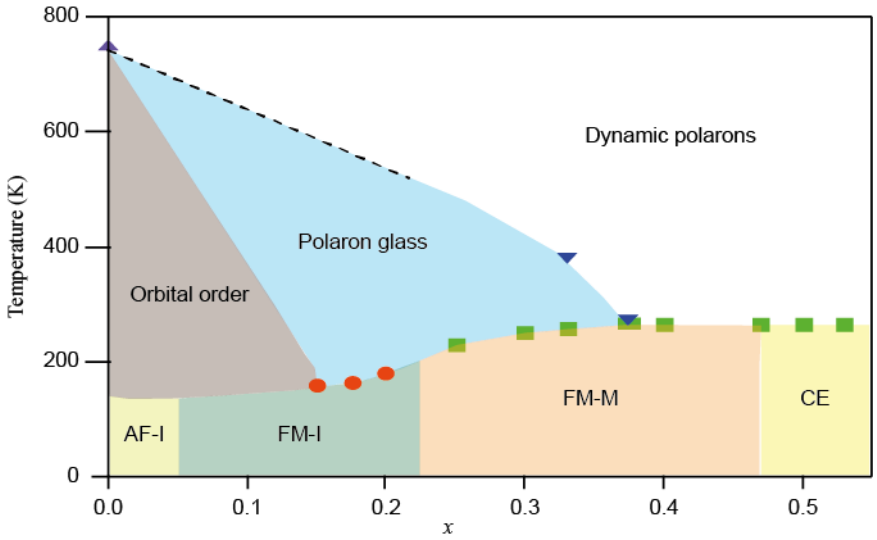


Figure 4.1: The postulated phase diagram of $La_{1-x}Ca_xMnO_3$ as a function of the Ca^{2+} content x. The low-temperature phase changes from an antiferromagnetic insulating (AF-I) state to a ferromagnetic insulator (FM-I) to a ferromagnetic metal (FM-M) and finally to a charge and orbitally ordered state (CE). Adapted with permission from J. W. Lynn *et al.*, *Phys. Rev. B*, **76**, 014437 (2007).[96] Copyright 2007 by the American Physical Society.

derstanding of the underlying chemistry of JT-active solid solutions is therefore a desirable prospect.

The B-site substituted perovskite $KZn_{1-x}Cu_xF_3$ is less complicated than the $La_{1-x}A_xMnO_3$ family and is thus valuable for the study of dilution effects on orbital order. The percolation threshold for a primitive cubic system is ~ 0.3;[475] yet the orbital order in $KZn_{1-x}Cu_xF_3$ only appears at a critical Cu^{2+} concentration, x_{oo}, of 0.5.[476] By comparison, the onset of magnetic order in diluted magnets such as $KMg_{1-x}Mn_xF_3$ is well described by percolation theory.[477] Hence, the correlation of orbitals seems more sensitive to dilution than magnetic order and cannot be fully explained based on percolative arguments alone. Seeking to rationalise these experimental observations, Tanaka *et al.* performed semi-classical Monte Carlo simulations of orbitally active sites on a cubic lattice with varying degrees of dilution.[478] They assumed a random distribution of the two metals and ignored couplings to strain.

In contrast to the 3-state Potts model developed for $LaMnO_3$,[92–94] the Jahn-Teller distortion was treated as a freely variable pseudovector within the order parameter space spanned by the Q_2 and Q_3 distortions [Section 1.3.2]. The interaction terms along a given direction involve only certain projections of the JT vector, with the precise vector component dictated by the real-space direction of the coupling. Hence, this MC simulation belongs to the vast family of compass models, of which the Kitaev model is a famous example.[479,480] A key consequence of the compass model is that a JT distortion adjacent to an inactive cation cannot be described by a simple Q_2 or Q_3 distortion (or a rotational equivalent), but as a linear combination of both. In effect, dilution not only leads to a disordered arrangement of JT-distorted cations, but the JT distortion *itself* disorders. This Hamiltonian reproduces the experimental behaviour of $KZn_{1-x}Cu_xF_3$ well and has also been extended to include magnetically active materials.[481]

Returning to molecular perovskites, their orbital order–disorder phenomena are likely to deviate from the behaviour of inorganic materials for a number of reasons. First of all, as the B-site cation is predominantly divalent, the choice of JT-active ion is restricted to Cu^{2+} or Cr^{2+}, although the latter is highly unstable. Divalent Cu has a positive reduction potential and in some cases, the molecular species—either the A-site cation or the linking anion—is sufficiently reducing to destabilise Cu^{2+} in favour of elemental Cu.[65,449] As a result, preparation of Cu-containing molecular perovskites may not always be feasible. Second, JT-active species have a low preference for octahedral coordination relative to square planar/pyramidal, which can favour adoption of alternative structure types. For instance, $[N(CH_3)_4]Cu(N_3)_3$ does not crystallise

as a perovskite;[301] likewise, attempts to prepare [PPN]Cu[Au(CN)$_2$]$_3$ have resulted in the formation of the layered, Ruddlesden-Popper-like [PPN]Cu$_2$[Au(CN)$_2$]$_5$.[318] Third, the longer linkers associated with molecular perovskites reduce the energy scale of the metal-metal correlations and should, by this argument, lead to a higher propensity for disordered states. This applies both to interactions mediated by orbital overlap (such as magnetism) and those derived from strain (such as orbital order). Assuming different distance dependencies of the spin and orbital interactions, their critical behaviour might naturally separate into distinct temperature regimes. This separation can be beneficial, as it renders orbital disorder accessible at lower temperatures without the interference of additional ordering processes, thus simplifying the study of such states. As a final point, it can be noted that molecular perovskites are usually electrical insulators and orbital disorder by electron delocalisation can therefore be ruled out. Given these observations, orbital degrees of freedom are anticipated to manifest differently in molecular perovskites relative to their inorganic congeners due to harsher compositional restrictions.

Despite the argument above, a number of Jahn-Teller active formates[245,444,482,483] and Prussian blue analogues[191,201] are known. A particularly notable example is the polar [C(NH$_2$)$_3$]Cu(HCOO)$_3$; a stark contrast to other [C(NH$_2$)$_3$]B(HCOO)$_3$ (B^{2+} = Fe, Ni, Mn, Co, Ni, Zn, Cd) compounds, which are invariably centrosymmetric.[245,281] The fact that only the Cu system is polar bears testimony to the importance of orbital order in breaking inversion symmetry; a point also highlighted by DFT calculations.[268] This system is predicted to be a room temperature ferroelectric;[268] however no experimental studies to verify this claim have been performed.

Isovalent doping of $[C(NH_2)_3]Cu(HCOO)_3$ with Cd yields the mixed-metal series $[C(NH_2)_3]Cd_{1-x}Cu_x(HCOO)_3$, which represents, to the best of my knowledge, the sole example of a JT-active complete* solid solution of molecular perovskites to date (August 2018).[485] In this system, the two endmembers differ not only by the presence of orbital order but also by the orientation of the hexapolar guanidinium A-site cation [Fig. 4.2].[245,281] The Cd endmember crystallises in $R\bar{3}c$ with the quadrupole moments of the guanidinium cations—*i.e.* the plane normal—ordered at the centre of the Brillouin zone. Long-range orbital order emerges at $x_{oo} = 0.5$, altering the symmetry to $P2_1/c$. Subsequently, the guanidinium cation reorients to adopt an X-point arrangement at $x = 0.7$, giving the final space group $Pna2_1$ observed in the Cu-rich samples. This is an example of hybrid improper ferroelectricity and will be explored in more detail in the subsequent Chapter. In order to unravel the compositional behaviour of orbital order in these systems, Monte Carlo simulations using the anisotropic 3-state Potts model developed for $LaMnO_3$ were performed.[93] The theoretical threshold concentration was determined as $x_{oo} = 0.6$ and the discrepancies with the experimental results were attributed to the existence of short-range cation correlations or orbital interactions extending beyond nearest neighbours.[485]

Another JT-active molecular perovskite is $Cu[Pt(CN)_6]$, where the alignment of the elongated octahedra reduces the symmetry from the aristotype $Fm\bar{3}m$ to the tetragonal space group $I4/mmm$. Hence, there is a strong coupling between the orbital order and strain. As all orbitally inactive compounds of formula $B[Pt(CN)_6]$ are cubic, $Cu[Pt(CN)_6]$ constitutes a unique hexacyanoplatinate. By contrast, defective PBAs of formula $Cu_3[B'(CN)_6]_2$ (B'^{3+} = Co, Fe, Ir, Rh) consistently adopt

*$[(CH_3)_2NH_2]Zn_{1-x}Cu_x(HCOO)_3$ is known, but only for $x \leq 0.1$.[484]

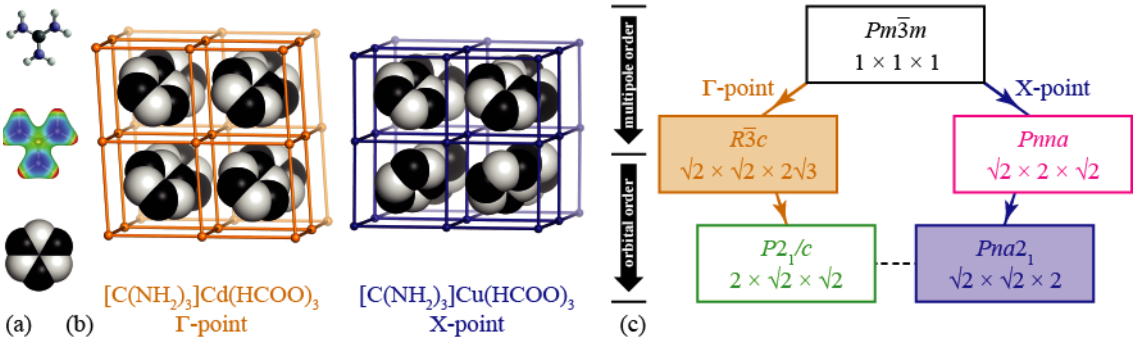


Figure 4.2: The symmetry relationships in $[C(NH_2)_3]Cd_{1-x}Cu_x(HCOO)_3$. (a) The structure of the guanidinium cation, along with its electrostatic potential and the multipole representation. (b) The Γ-point and X-point guanidinium arrangements in $[C(NH_2)_3]Cd(HCOO)_3$ and $[C(NH_2)_3]Cu(HCOO)_3$, respectively. (c) The symmetry relationships between the multipolar and orbital ordering processes. Arrows represent group–subgroup relationships and the dashed lines indicate discontinuous pathways. Adapted with permission from Evans *et al.*, *J. Am. Chem. Soc.*, 2016, **138**, 9393–9396.[485] Copyright 2016 American Chemical Society.

cubic $Fm\bar{3}m$ or $Pm\bar{3}m$ symmetry on average.[200,209] As these space groups are incompatible with any form of orbital order, these systems are necessarily disordered, implying that vacancies influence the propensity for long-range order. Collectively, these examples demonstrate that orbital order is indeed realisable in molecular perovskites with profound consequences for the structural and functional response: yet there have been few comparative studies.

The aim of this Chapter is to develop an understanding of cooperative Jahn-Teller phenomena in doped molecular perovskites, in light of the corresponding behaviour in oxide materials. The primitive $[C(NH_2)_3]Mn_{1-x}Cu_x(HCOO)_3$, the face-centred $Mn_{1-x}Cu_x[Pt(CN)_6]$, and the defective face-centred mixed-metal series $(Mn_{1-x}Cu_x)_3[Co(CN)_6]_2$ are synthesised [Fig. 4.3], then analysed with PXRD and the resulting behaviour interpreted in terms of the compass model developed for $KZn_{1-x}Cu_xF_3$. It will be shown that the coordination numbers of the Cu-containing sublattice—which range from 4 to 12 depending on the topology—play a crucial

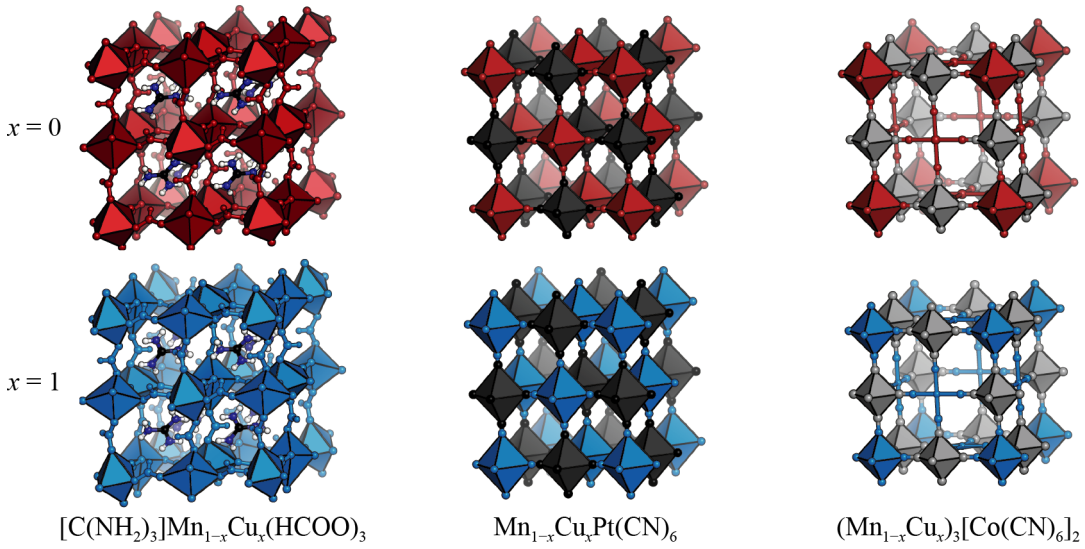


Figure 4.3: The crystal structures of the three molecular perovskites under study,[191,245,487,488] where Mn is shown in red, Cu in blue, Pt in black and Co in grey. The variation in coordination number of the Cu sublattice is easily seen. For simplicity, the disordered defects in $(Mn_{1-x}Cu_x)_3[Co(CN)_6]_2$ are portrayed as ordered at the centre of the unit cell.

role in determining the orbital order–disorder processes. Although the strongly correlated states observed in perovskites are not realisable here, orbital order is an important symmetry-breaking degree of freedom in molecular perovskites, as demonstrated by $[C(NH_2)_3]Cu(HCOO)_3$ and $Cu[Pt(CN)_6]$. In particular, the former illustrates how cooperative JT effects can couple to other distortions in such a fashion that the global inversion symmetry is lifted; a phenomenon that forms a key point in the subsequent Chapter. Ferroelectric materials with paraelectric impurities, such as $PbMg_{0.33}Nb_{0.67}O_3$, exhibit interesting relaxor-like behaviour by virtue of the existence of polar nanoregions.[486] Therefore, the local structure of mixed-metal molecular perovskites with a polar endmember is of special interest, as it may show similar structural features.

4.3 Methods

4.3.1 Synthesis

Powder samples of $[C(NH_2)_3]Mn_{1-x}Cu_x(HCOO)_3$ were synthesised by the addition of $[C(NH_2)_3]CO_3$ (3.13 mmol) dissolved in HCOOH (9.68 mmol) and MeOH (10 ml) to a methanolic solution of 0.1 M $Mn(NO_3)_2{\cdot}4H_2O$ and 0.1 M $Cu(NO_3)_2{\cdot}2.5H_2O$ (total 10 ml) in the appropriate ratio. The reaction mixture was stirred for 16 h at ambient temperature, leading to the formation of a precipitate. The product was isolated as a powder by filtration *in vacuo* prior to air-drying. Yields were in the range 77–92% and the sample colour varied from white to blue with increasing Cu^{2+} content.

$(B_{1-x}Cu_x)_3[B'(CN)_6]_2$ (B = Mn, Cd and B′ = Co, Fe) were prepared by the dropwise addition of an aqueous solution of $MnSO_4{\cdot}H_2O$ or $Cd(OAc)_2{\cdot}2H_2O$ and $CuSO_4$ in the required ratio (total of 0.5 mmol, 0.5 ml) to an aqueous solution containing $K_3B'(CN)_6$ (0.5 mmol, 0.5 ml). A precipitate instantly formed and the reaction mixture was stirred for 1 h at 60 °C and 1 h at room temperature. The product was isolated as a fine powder by filtration *in vacuo* and dried in air. Yields ranged from 34% to 70%. The hexacyanoferrates were invariably brown, whereas the colour of the hexacyanocobaltates varied from white to blue with increasing Cu^{2+} concentration [Fig. 4.4].

Hexacyanoplatinates of formula $B_{1-x}Cu_x[Pt(CN)_6]$ (B = Mn, Fe, Zn, Cd) were synthesised as outlined above using $K_2[Pt(CN)_6]$, but longer stirring times were

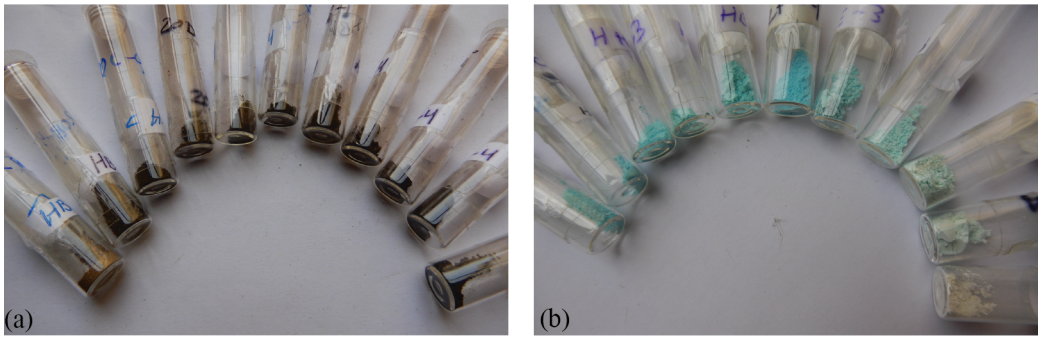


Figure 4.4: Samples of (a) $(Mn_{1-x}Cu_x)_3[Fe(CN)_6]_2$ and (b) $(Cd_{1-x}Cu_x)_3[Co(CN)_6]_2$.

employed to facilitate precipitation. Yields were typically in the range 30–67%. The sample colour varied from white to blue-green as a function of the Cu^{2+} content.

4.3.2 X-ray diffraction

The X-ray powder diffraction experiments were performed at beamline I11, Diamond Light Source, UK. The samples were finely ground prior to being packed in 0.5 mm borosilicate capillaries to a length of at least 1.5 cm. Diffraction patterns were collected using a beam energy of 15 keV and a Mythen2 PSD detector with exposure times of 2×4 s with 0.25° detector offset. Firstly, all samples were measured at ambient conditions, followed by data collections at 500 K, 400 K, 300 K, 200 K, and 100 K. Variable-temperature measurements were carried out using an Oxford Cryostream attachment and each sample was allowed to equilibrate for 60 s before data collections at non-ambient temperatures. As the compounds were prone to radiation damage, the capillaries were translated between repeated scans to ensure that each measurement was carried out on a pristine sample.

All analysis of these diffraction data was performed using TOPAS ACADEMIC v4.1[370] and intrinsic instrument parameters (wavelength, zero offset and intrinsic

peak shape) were obtained by refinement of a Si NIST 640c standard. To account for sample-dependent peak broadening, a Lorentzian strain term was employed and in the case of multiple phases, individual strain terms for distinct phases were used. Where multiple phases were present, their respective phase fractions were found from a simplistic Rietveld refinement using previously published starting models.[191,488] For simplicity and as detailed structural information was not the primary aim, the models were kept simple and no structural variables (atomic positions, occupancies or thermal parameters) were allowed to refine. This refinement protocol is denoted "constrained Rietveld refinements" henceforth to emphasise the crudeness of this approach. Despite its simplicity, it is sufficient for the qualitative purposes of this study.

4.3.3 Atomic absorption spectroscopy

In order to determine sample compositions, atomic absorption spectroscopy (AAS) was performed on all hexacyanoplatinates and formates using a Varian AA240FS spectrometer, equipped with Perkin Elmer ATOMAX hollow cathode lamps. The lamp current was 5–10 mA and the fuel a mixture of air and acetylene. The samples were dissolved in small amounts of concentrated hydrochloric acid and diluted with deionised water. The metal concentration of each sample was determined against a calibration curve prepared using at least 4 reference solutions, which had been diluted from the appropriate stock solution ($1\,\mathrm{g\,dm^{-3}}$). Each sample was measured at least 3 times per metal and the uncertainties calculated based on the standard deviation of the repeated measurements.

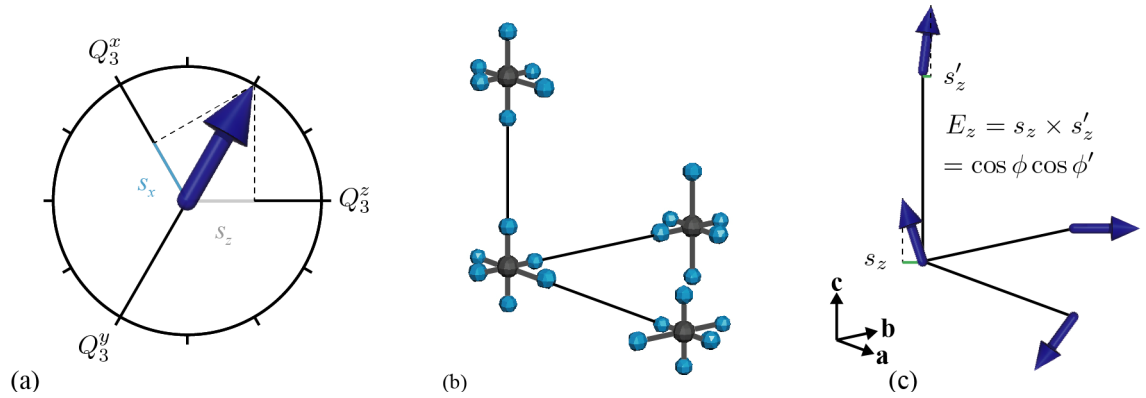


Figure 4.5: (a) The order parameter space for Jahn-Teller distortions as employed in the MC simulation in Ref. 478. A representative vector is shown, along with its projections onto the Q_3^z and Q_3^x axes (grey and blue, respectively). The projection onto Q_3^y is zero for this particular vector. (b) Jahn-Teller distortions decorated on a cubic lattice visualised in real space and (c) the mapping onto the order parameter space.

4.3.4 Monte Carlo simulations

The Monte Carlo simulations were carried out using a custom-made code implemented in FORTRAN 90. Cubic supercells of $16 \times 16 \times 16$ and $15 \times 15 \times 15$ unit cells with periodic boundary conditions were used for the primitive cubic and face-centred cubic systems, respectively. The sizes of the configurations were a compromise between obtaining a sufficiently large model and ensuring reasonable computational expense. As the primitive system exhibits an antiferro-type of order, an even number of unit cells was required. The Jahn-Teller distortion was treated as a pseudospin within the semi-classical approach, in accordance with the model developed in Ref. 478. Thus, the orbital degree of freedom was modelled by a freely variable unit vector ($\mathbf{s} = \exp \mathrm{i}\phi$) in the order parameter space spanned by the Q_2 and Q_3 distortions [Fig. 4.5(a)]. The equations

$$s_x = \cos\left(\phi - \frac{2\pi}{3}\right), \tag{4.1}$$

$$s_y = \cos\left(\phi + \frac{2\pi}{3}\right), \tag{4.2}$$

$$s_z = \cos\phi. \tag{4.3}$$

project the JT vector onto the basis vectors corresponding to Q_3^x, Q_3^y and Q_3^z, respectively [Fig. 4.5(b)]. Hence, the energy of the system is simply given by

$$H = J_x \sum_{x\text{-links}} s_x s_x' + J_y \sum_{y\text{-links}} s_y s_y' + J_z \sum_{z\text{-links}} s_z s_z', \tag{4.4}$$

where the anisotropic interaction strengths $J_x = J_y = J_z = 1$ in this implementation. The resemblance to the hexagonal Kitaev model is apparent.[480] In simple terms, the z-contribution to the energy between two JT-active cations with phase angles ϕ and ϕ' located at (0, 0, 0) and (0, 0, 1) is dictated by $\cos\phi\cos\phi'$, *i.e.* the product of the projections along the Q_3^z direction in the order parameter space [Fig. 4.5(c)]. For the face-centred systems, the directional dependence of the above equation can be modified to give

$$H = J_{xy} \sum_{xy\text{-links}} (s_x s_x' + s_y s_y') + J_{xz} \sum_{xz\text{-links}} (s_x s_x' + s_z s_z') + J_{yz} \sum_{yz\text{-links}} (s_y s_y' + s_z s_z'). \tag{4.5}$$

Hence, the correlations are now along the $\langle 110 \rangle$ directions and the projections in the order parameter space have been changed accordingly. The correlation terms along [110] vanish unless the sites at (1, 0, 0) and (0, 1, 0) are occupied, and similar relationships hold for the remaining symmetry-equivalent directions.

A specified fraction of Jahn-Teller active cations, x, was randomly decorated on the lattice and assigned random values of ϕ in the range 0–2π. In the case of

defective frameworks, the B′-sites at the centre of the face-centred cubic (FCC) unit cells were decorated with vacancies, giving a vacancy concentration of 25%. Another 8.33% randomly chosen B′-sites were allocated to be vacant to achieve the required defect concentration of 33%. Migration of defects or cations during the simulation was not considered. A simulated annealing approach was employed with an initial Monte Carlo temperature, T_i, equal to $16J$. Cooling occurred at a rate of 0.8 for 19 steps, giving a final simulation temperature of $T_f = 16 \times 0.8^{19-1} = 0.288J$. At each temperature point, a JT-active cation was chosen at random, its phase angle changed by an arbitrary amount within the range 0–2π and the conventional Metropolis-Hastings algorithm followed [Section 2.5].[423] Equilibration was carried out for 10^9 accepted MC moves. Following convergence at each temperature, the order parameter of the orbital order, η, was calculated from

$$\eta = \frac{1}{N_x} \left| \sum_j \exp \mathrm{i}\phi_j \right|, \tag{4.6}$$

where N_x denotes the number of Jahn-Teller active cations. Thus, complete orbital order gives $\eta = 1$. Orbital correlation functions were computed according to the formula

$$c(r) = \frac{1}{Z_r} \sum_{i,j} \mathbf{s}_i \cdot \mathbf{s}_j(\mathbf{r}), \tag{4.7}$$

where i and j index pairs of JT-active cations separated by r and Z_r is the total number of such pairs. In all cases, 10 independent starting configurations were employed in the simulations and the results averaged.

4.4 Primitive cubic systems

To the best of my knowledge, formate perovskites constitute the sole example of primitive cubic molecular perovskites where JT distortions have been incorporated with retention of the perovskite architecture. This Section presents the results for $[C(NH_2)_3]Mn_{1-x}Cu_x(HCOO)_3$, which is closely related to the Cd analogue mentioned in the introduction.

4.4.1 Crystallographic results

$[C(NH_2)_3]Mn(HCOO)_3$ crystallises in orthorhombic $Pnan$ ($\equiv Pnna$) as a result of the X-point orientational order of the guanidinium cation.[245] The same multipolar A-site order is present in $[C(NH_2)_3]Cu(HCOO)_3$, but the collective C-type JT distortion acts as an additional superimposed primary order parameter, lowering the symmetry to the polar space group $Pna2_1$.[245] Dissolution of Cu in the Mn compound yields a complete, single-phase solid solution, $[C(NH_2)_3]Mn_{1-x}Cu_x(HCOO)_3$, accompanied by only slight changes in the width of the reflections, as manifested by low strain values [Fig. 4.6(a)–(b)]. The Cu fractions determined by AAS are consistent with the nominal values [Fig. 4.6(c)]. Moreover, the reduced unit cell volume, $\frac{V}{Z}$, correlates linearly with x and can also be used to compute the relative metal content in good agreement with the experimental results [Fig. 4.6(c)–(d)]. Thus at face value, $[C(NH_2)_3]Mn_{1-x}Cu_x(HCOO)_3$ appears to constitute a straightforward example of a solid solution.

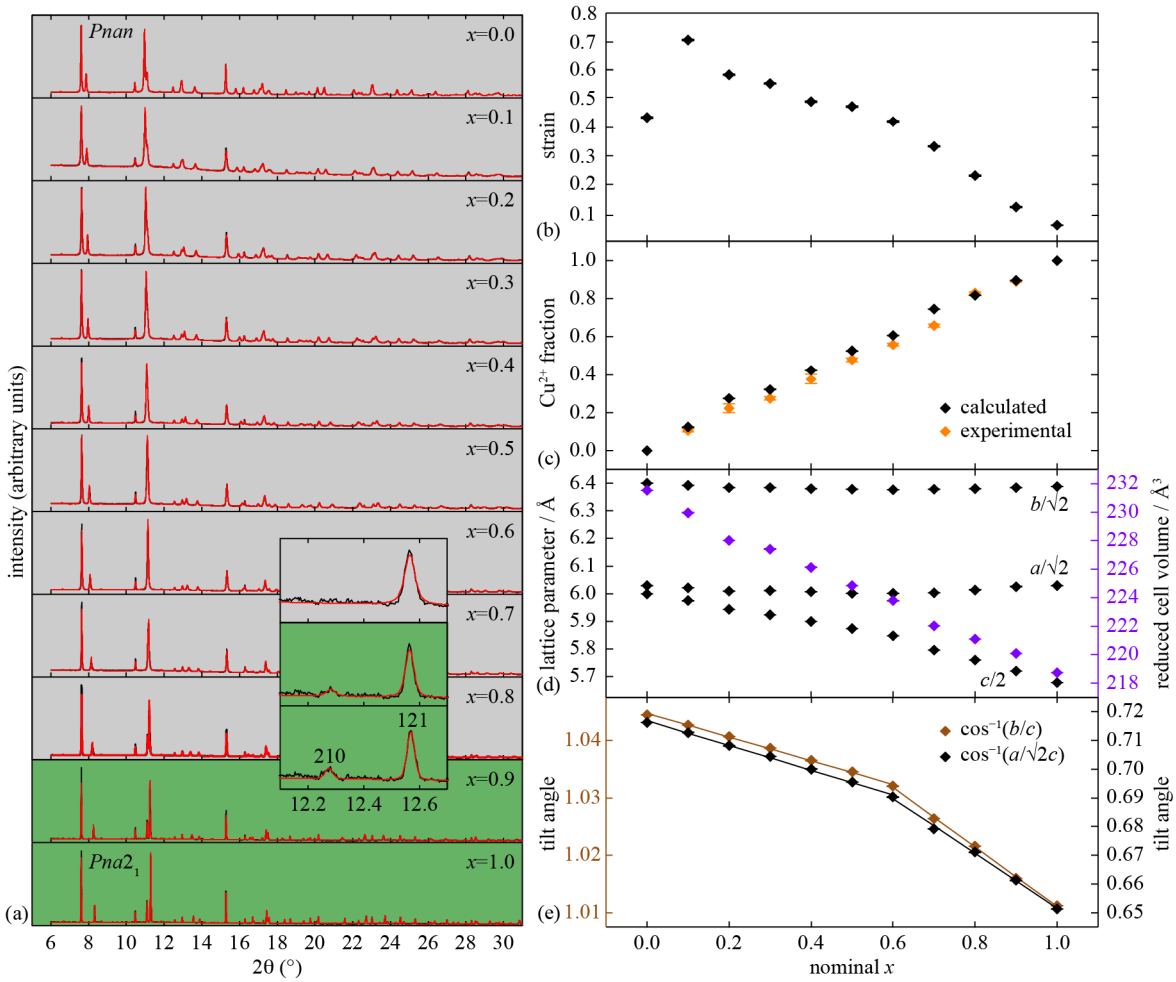


Figure 4.6: Experimental data for $[C(NH_2)_3]Mn_{1-x}Cu_x(HCOO)_3$. (a) Pawley fits of the PXRD patterns where green and grey indicate $Pna2_1$ and $Pnan$, respectively. The calculated profile is shown in red and the experimental in black. The inset shows the 210 reflection indicative of $Pna2_1$. The x dependence of (b) the Lorentzian strain, (c) the Cu^{2+} concentration as calculated from the lattice parameters (black) and as determined from AAS (yellow), (d) the lattice parameters and cell volume normalised in accordance with the perovskite unit cell and (e) the tilt angles with lines of best fit. The absolute values of the angles are arbitrary.

The point of interest is the compositional threshold for the $Pnan$–$Pna2_1$ transition, signalling the Cu fraction beyond which local Jahn-Teller correlations exhibit long-range order. As the two orthorhombic space groups differ merely by the absence/presence of an inversion centre, their diffraction patterns are very similar, rendering the precise symmetry assignment challenging. However, distinction is viable on basis of the $\{hk0\}$ reflections where $h + k = 2n$, which are allowed in $Pna2_1$ but forbidden in $Pnan$. These reflections are extremely weak and discern-

ment from the background is nontrivial; yet the critical composition can be estimated as $x_{oo} = 0.85(5)$ based on the 210 reflection [inset in Fig. 4.6(a)]. So according to these superlattice reflections, $[C(NH_2)_3]Mn_{1-x}Cu_x(HCOO)_3$ displays a remarkably high compositional threshold for the onset of long-range orbital order.

The structural information extractable from the diffraction patterns may also provide an insight into the critical behaviour of the system. The *c*-axis exhibits a higher sensitivity to substitution than the other cell parameters and this is a corollary of the orbital order pattern. The largest contribution to the difference in unit cell dimensions between the Mn and Cu endmembers is the change in metal–oxygen bond lengths. Within the *ab* plane, the *C*-type order dictates an alternation of short and long Cu–O bonds and their average length is identical to the Mn–O bond distance in $[C(NH_2)_3]Mn(HCOO)_3$. The Cu–O bonds of intermediate length in the Q_2 distortion are stacked along **c** and, hence, the length of this axis is strongly correlated with x due to the smaller ionic radius of Cu^{2+} relative to Mn^{2+}.[317] Perhaps more interestingly, the lattice parameters correlate with the magnitude of octahedral tilting: the ratios a/c and b/c are directly proportional to $\cos\theta$, where θ is the angle of the $a^-a^-b^0$ tilt system.[122] As these formulae are developed for conventional perovskites, the absolute values of the tilt angles are not meaningful when applied to molecular systems. Yet trends can be monitored and as the Cu/Mn ratio increases, the tilt angle decreases and there is also a discontinuity in the slope at $x = 0.6$ [Fig. 4.6(e)]. Abrupt changes in tilt angles and their derivatives can be indicative of phase transitions in perovskites, *e.g.* the magnetic ordering transitions in manganites.[489,490] Therefore, the tilt angles may suggest a phase transition at lower values

of x than what was implied by the superlattice reflections noted above.

It is instructive to compare the results from XRD with those from the compass model developed for $KZn_{1-x}Cu_xF_3$.[478] These simulations predict a nonzero orbital order parameter—denoted $m_O(x,T)$—even at x values as low as ~ 0.6 [Fig. 4.7(a)]; a clear contrast to the XRD-derived compositional threshold. However, the intensity of a superlattice reflection arising from orbital order is proportional to $4m_O^2(x,T)$ as $T \to 0$ and therefore decays rapidly with decreasing x. Hence, although orbital order still persists at $x = 0.6$, the superlattice reflections will be of zero intensity [Fig. 4.7(b)]. This is significant, as it suggests that ordered states may remain hidden from conventional XRD measurements in systems without a strong coupling between strain and orbital order. By computing the area of the 210 reflection relative to the 112 reflection, $I_{210}(x)$, and normalising such that $I_{210}(1) = 1$, the experimental signature of orbital order can be monitored across the compositional range [Fig. 4.7(b)]. The decrease in intensity of $I_{210}(x)$ is in agreement with the values of $4m_O^2(x,T)$ from the compass model.[478] The $[C(NH_2)_3]Mn_{1-x}Cu_x(HCOO)_3$ series may thus exhibit order at x-values lower than what was suggested by XRD. Therefore, no definite conclusion regarding the compositional threshold for orbital order can be drawn for this system and other methods are required to probe the transition. Given the polarity of $[C(NH_2)_3]Cu(HCOO)_3$, further studies involving second harmonic generation (SHG) would be beneficial.

The critical behaviour of $[C(NH_2)_3]Mn_{1-x}Cu_x(HCOO)_3$ can be contrasted with that of the $KZn_{1-x}Cu_xF_3$ solid solution.[478] $KZn_{1-x}Cu_xF_3$ with $x \geq 0.5$ undergoes thermally induced orbital order–disorder transitions and although no variable tem-

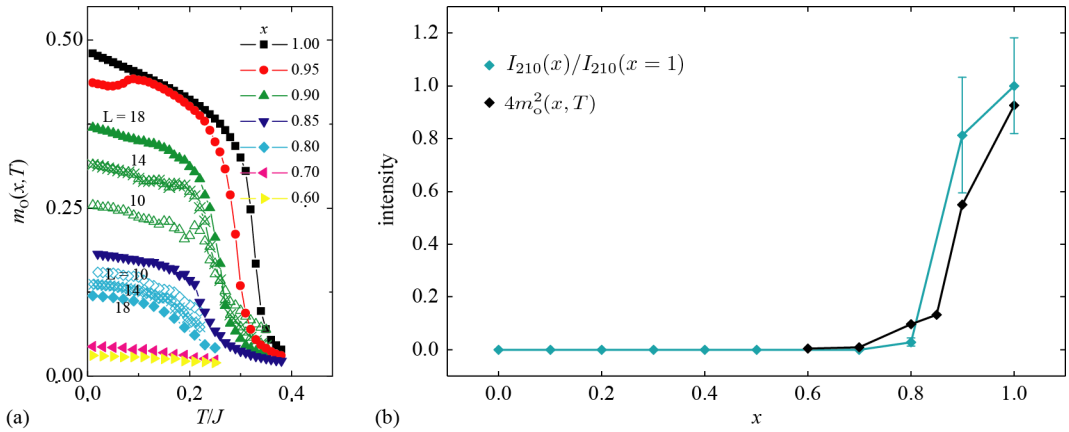


Figure 4.7: (a) The order parameter, $m_{\mathrm{O}}(x,T)$, as a function of T/J for various values of x and L, as found by Tanaka *et al.* in Ref. 478. (b) The x dependence of $4m_{\mathrm{O}}^2(x,T)$ and the normalised ratio of the intensities of the 210 and 112 reflections. Panel a adapted with permission from T. Tanaka *et al.*, *Phys. Rev. Lett.*, **95**, 267204 (2005).[478] Copyright 2005 by the American Physical Society.

perature data have been collected for this formate system, the mixed Cd-Cu analogue mentioned earlier remains in the same phase up to $\sim 400\,\mathrm{K}$.[485] Coordination polymers are less thermally stable than ceramics and so the energy required for orbital disorder may fall outside the range of thermal stability. Although the compositional threshold cannot be precisely determined, both the discontinuity in the derivative of the tilt angle and the superlattice reflections suggest a higher critical composition than for $\mathrm{KZn}_{1-x}\mathrm{Cu}_x\mathrm{F}_3$, for which $x_{\mathrm{oo}} = 0.5$. In other words, the formate system appears to favour orbitally disordered states relative to the fluoride compound. This may be a manifestation of the weaker coupling mediated by the long formate anion—possibly in tandem with the presence of octahedral tilts—leading to a destabilisation of long-range ordered phases.

4.4.2 Monte Carlo results

In order to gain a better understanding of the role of the compass model in explaining the orbital order–disorder transition, the Hamiltonian from Ref. 478 was

implemented in a custom-made Monte Carlo simulation. An accurate description of the *C*-type orbital order present in $[C(NH_2)_3]Cu(HCOO)_3$ in terms of JT phase angles is reasonably complex [Fig. 4.5], but it was approximated as an antiferrodistortive arrangement of orbitals for the purpose of the MC simulations. By analogy with other antiferro-orders, this corresponds to an alternation of the sign of the distortions, *i.e.* a periodic variation of Q_3 distortions (4 short and 2 long bonds) with its negative (4 long and 2 short bonds). Although higher-order coupling terms can be added in order to generate the correct ground state, this does not alter the behaviour of the order parameter.[478] Therefore, the simpler antiferrodistortive order was employed here. Finite size effects were investigated by varying the dimensions of the Monte Carlo supercell, L. As L decreases, the predicted onset of orbital order gradually shifts to lower values of x, consistent with previous reports [Fig. B1.1].[478] Above $L \approx 14$, it appears that the use of larger supercell dimensions does not appreciably alter the x dependence of the order parameter.

A 2D phase diagram with the order parameter for orbital order, η, as a function of x and $\frac{T}{J}$ is given in Fig. 4.8(a), where x is the fraction of JT-active cations, T is the Monte Carlo temperature and J is the coupling constant. In the ground state, orbital order is predicted to emerge at $x \approx 0.4$ and rapidly fall off with increasing $\frac{T}{J}$. This value is lower than the critical composition suggested by the superlattice reflections and the tilt angles, although the synthesised system may not necessarily correspond to the thermodynamic ground state. The orbital correlation functions at Monte Carlo temperatures above the order–disorder transition ($\frac{T}{J} = 2.68$) and at the ground state ($\frac{T}{J} = 0.288$) are shown at two distinct compositions [Fig. 4.8(b)–

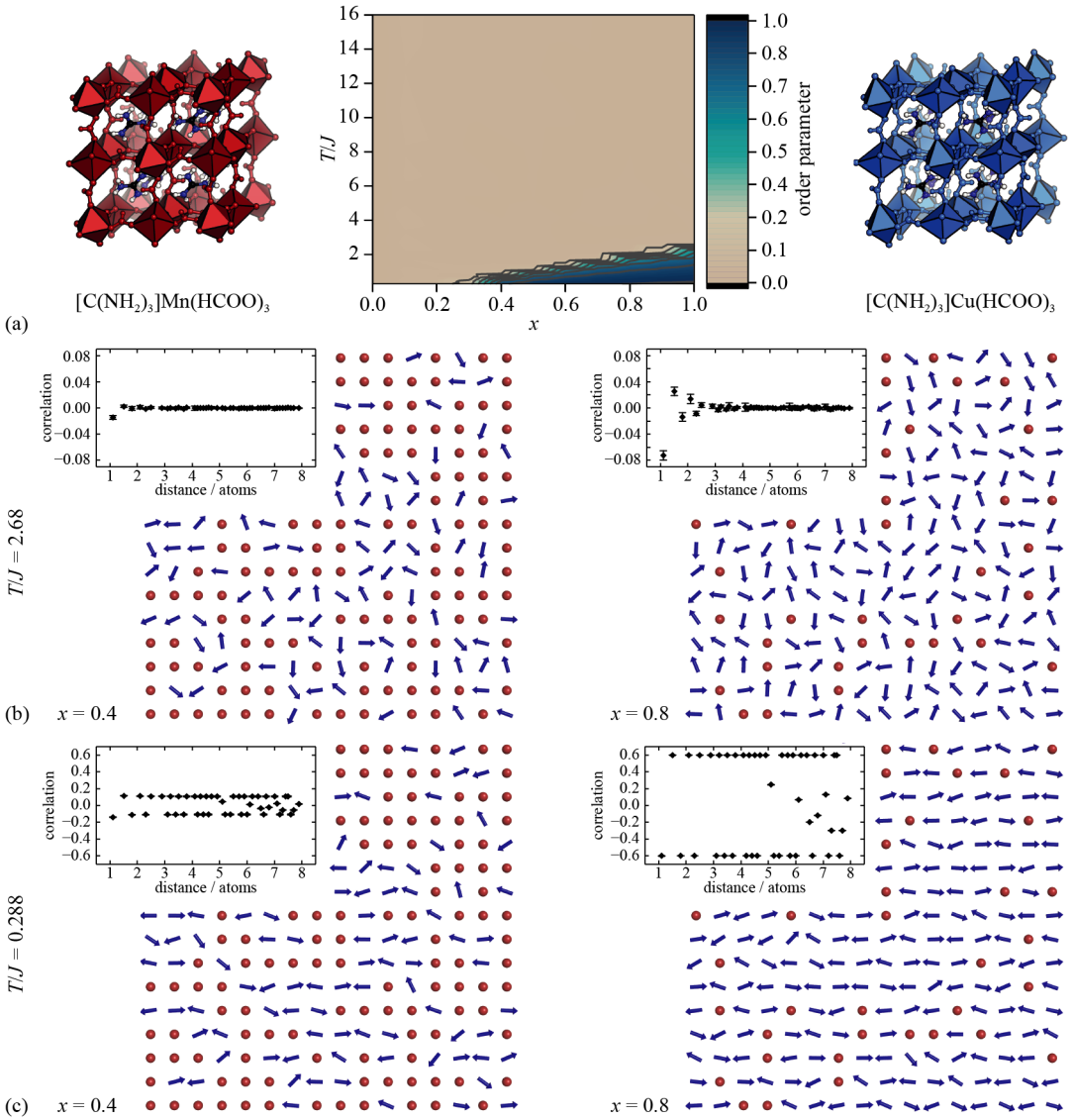


Figure 4.8: (a) The orbital order parameter, η, as a function of x and $\frac{T}{J}$ along with orbital correlation functions and MC configurations at (b) $T = 2.68J$ (disordered regime) and (c) $T = 0.288J$ (ordered regime) for $x = 0.8$ and $x = 0.4$. The Jahn-Teller distortion is represented by a blue arrow in the order parameter space in Fig. 4.5 and JT-inactive cations are shown in red. Note that the absolute direction of the JT vectors is not physically meaningful.

(c)]. Within the ordered region, the correlation length is infinite and its magnitude increases with x, as expected. In the orbitally disordered regime, short-range order persists over < 3 unit cells, suggesting the presence of locally ordered clusters of orbitals within the disordered domain.

The compass model is meaningfully different from the 3-state Potts model. The

latter only allows for three discrete states ($\phi = 0$ and $\pm\frac{2\pi}{3}$ in Fig. 4.5), whereas the former encompasses a continuously variable orbital degree of freedom. At infinitely low temperatures and $x = 1.0$, the outcome of the two models will be identical. However, the orbitally disordered states given by the compass model are characterised by a range of phase angles unfeasible for 3-state Potts [Fig. 4.8(b)]. More importantly, a fully orbitally ordered state in the presence of JT-inactive cations cannot be reached, as only certain projections of the JT vector are implicated in the energy terms in the compass model. As a consequence, the JT vectors "tilt" away from the ideal angles of 0 and π [Fig. 4.8(c)]. In other words, JT-active cations adjacent to inactive species display distortions not simply described by a Q_2 or a Q_3 mode; the local order of the orbitals is "fuzzy around the edges".

The implementation of the compass model comprises a range of assumptions regarding the local structure of the systems. Crucially, the substituting cations are presumed to be randomly distributed on the B-sites, even though deviations from randomness have an impact on the compositional dependence of the orbital order. On one hand, if like interactions (Mn–Mn and Cu–Cu) were favoured, the two cations would cluster into domains, leading to a higher threshold for percolation than in the random scenario. In the limiting case, two immiscible phases will be observable in the PXRD patterns. On the other hand, if unlike interactions (Mn–Cu) are favoured, the mixed-metal series will tend towards a state with checkerboard cation order, concomitant with a symmetry lowering to space group $P2/c$ (no orbital order) or Pc (orbital order). Assuming only nearest-neighbour interactions along the $\langle 100 \rangle$ directions as in the current model, the compositional order would yield an

orbitally disordered state even at $x = 1.0$.* Thus, any short-range cation correlations will influence the transition threshold and this is not captured by the MC model.

Interestingly, like interactions are preferred in $[C(NH_2)_3]Mn_{1-x}Cu_x(HCOO)_3$, according to a spectroscopic study.[491] By decomposing the infrared signal associated with the formate stretch *via* a non-negative matrix factorisation approach,[492] the relative contributions of formate anions bridging solely Cu, solely Mn and distinct metals could be extracted. The proportion of Mn–formate–Cu linkages is lower than expected from a statistical distribution, indicating the presence of nano-sized cation inhomogeneities, which were visualised by means of reverse Monte Carlo simulations [Fig. 4.9]. More recently, similar results have also been found by electron paramagnetic resonance (EPR) in a related system.[484] Due to the nanoregions, the MC results for the orbital order–disorder transition may slightly underestimate the critical composition for orbital order. It may prove interesting to explore the interplay between local cation order and local JT order, but such an investigation is beyond the scope of this study.

4.5 Face-centred cubic systems

By virtue of the asymmetry of the cyanide anion, Prussian blue analogues of formula $B_x[B'(CN)_6]_y$ form double perovskites with face-centred space groups. Thus, the coordination number of the Cu sublattice—12 nearest neighbours along $\langle 110 \rangle$—is doubled relative to a primitive unit cell—6 nearest neighbours along $\langle 100 \rangle$. The higher coordination of the orbitally active sublattice should result in an enhanced

*Although, as will be discussed later, even cation-ordered structures can show orbital order due to interactions along the $\langle 110 \rangle$ vectors.

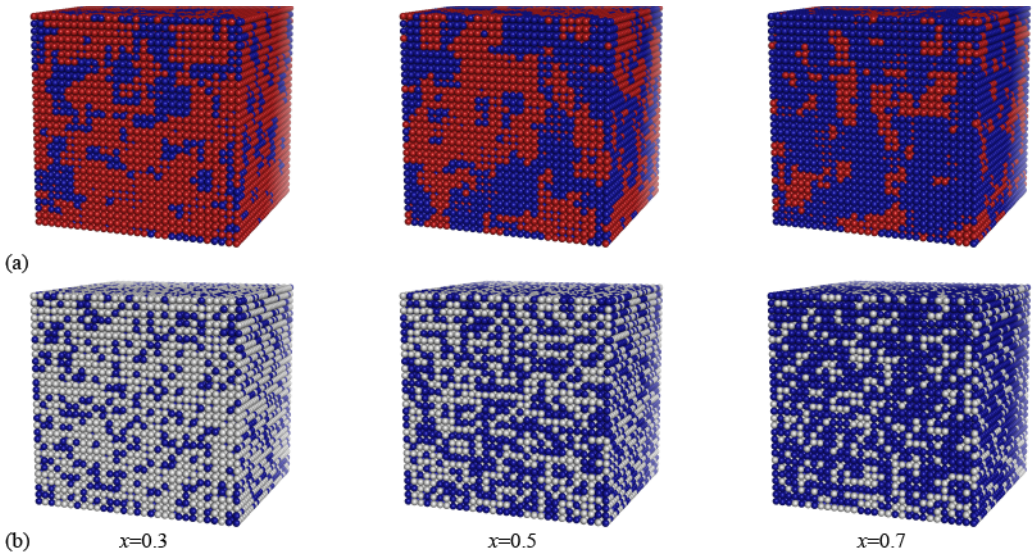


Figure 4.9: The compositional nanoregions in (a) $[C(NH_2)_3]Mn_{1-x}Cu_x(HCOO)_3$ and (b) a statistical distribution at different values of x. Cu is shown in navy, Mn in red and a generic JT-inactive cation in grey. Adapted from Ref. 491 with permission from The Royal Society of Chemistry.

stability of the orbitally ordered states with respect to dilution. Substitution with JT-distorted cations is only feasible on the nitrogen-coordinated B-site due to the relatively weak crystal field.[493] Conversely, a cation with e_g orbital degrees of freedom cannot be octahedrally coordinated by CN ions, as the strong crystal field effect favours square planar geometry, which is incompatible with a 3D perovskite.

4.5.1 Crystallographic results

$\mathbf{Mn_{1-x}Cu_x[Pt(CN)_6]}$

Metal hexacyanoplatinates of formula $B[Pt(CN)_6]$ form A-site deficient perovskites (*i.e.* double ReO_3 structure type) and the framework is fully connected. In general, these materials adopt the aristotype space group $Fm\bar{3}m$ for a wide range of divalent B-site ions. However, the orbitally ordered $Cu[Pt(CN)_6]$ crystallises in tetragonal $I4/mmm$ with a unit cell of $a \sim a_0/\sqrt{2}$ and $c \sim a_0$, where a_0 is the lattice parameter

of the aristotype.[191,198] As a consequence, the deviation from cubic symmetry is a direct measure of the magnitude of the JT distortion. Due to the strong coupling between strain and orbital order, distinguishing between ordered and disordered states by means of crystallographic methods is straightforward, in contrast to the formate system.

As expected, $Mn_{1-x}Cu_x[Pt(CN)_6]$ is cubic at low values of x, but a tetragonal phase is evident in the PXRD patterns at nominal $x \geq 0.2$ [Fig. 4.10(a)]. The fraction of the cubic phase rapidly decreases as the Cu content increases further and the tetragonal phase is predominant at $x > 0.6$. Similar to the formate system, the strain values remain low and any changes can barely be detected by eye [Fig. 4.10(b)]. If Vegard's law holds,[494] the cubic lattice parameter can be estimated by

$$a_{\mathrm{c}}(x_{\mathrm{c}}) = a_{\mathrm{c}}(0) + m_{\mathrm{c}}x_{\mathrm{c}}, \tag{4.8}$$

where $a_{\mathrm{c}}(x_{\mathrm{c}})$ is the lattice parameter as a function of the Cu^{2+} concentration of the cubic phase and m_{c} denotes the first derivative of the lattice parameter with respect to x_{c}. Likewise, by defining $a'_{\mathrm{t}} = \sqrt[3]{2a_{\mathrm{t}}^2 c_{\mathrm{t}}}$, where a_{t} and c_{t} are the dimensions of the tetragonal unit cell, the corresponding expression for the tetragonal component is

$$a'_{\mathrm{t}}(x_{\mathrm{t}}) = a'_{\mathrm{t}}(0) + m_{\mathrm{t}}x_{\mathrm{t}}. \tag{4.9}$$

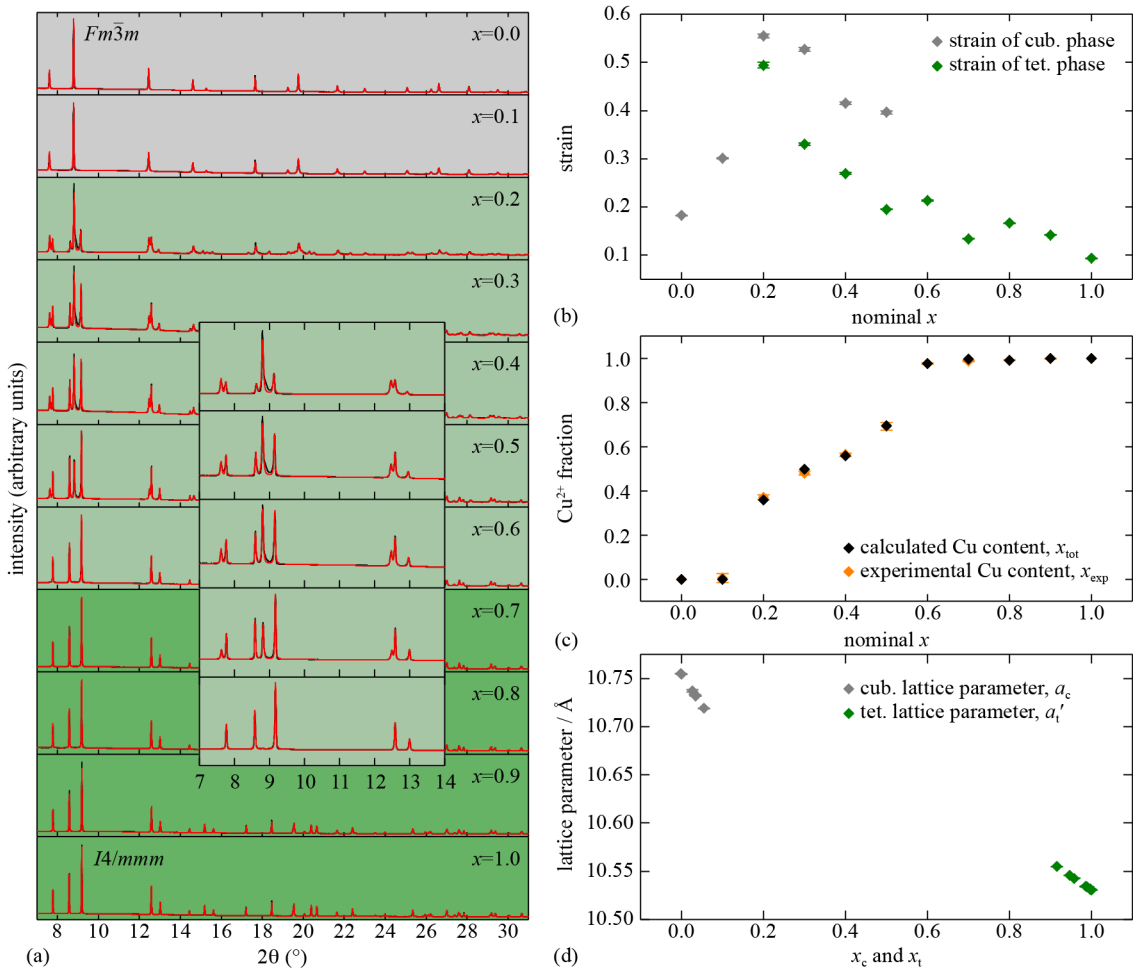


Figure 4.10: Experimental data for $Mn_{1-x}Cu_x[Pt(CN)_6]$ at ambient conditions. (a) Pawley fits of the diffraction patterns where grey and green indicate cubic and tetragonal phases, respectively, and two-phase refinements are shown in pale green. The calculated profile is shown in red and the experimental in black. The x dependence of (b) the Lorentzian strain of the cubic (grey) and tetragonal (green) phases, (c) the Cu fraction as determined by AAS (yellow) and calculated as described in the text (black), and (d) the lattice parameters as a function of the Cu concentration of the respective phase.

Therefore, if f_t denotes the fraction of tetragonal phase for a given nominal x-value, the total Cu^{2+} concentration, x_{tot}, at this nominal composition becomes

$$x_{tot} = f_t x_t + (1 - f_t)x_c = f_t \frac{a'_t(x_t) - a'_t(0)}{m_t} + (1 - f_t)\frac{a_c(x_c) - a_c(0)}{m_c}. \qquad (4.10)$$

The values of $a_c(x_c)$, $a'_t(x_t)$, $a_c(0)$, and f_t are obtainable from Pawley and Rietveld refinements [Fig. C2.1]. Recognising that $a'_t(0) = a'_t(1) - m_t$ leaves the values of m_c

and m_t as the sole unknown factors. By employing the solver function in Excel, the values of these parameters were varied to minimise

$$\chi = \sum_x (x_{tot} - x_{exp})^2, \tag{4.11}$$

where x_{exp} is the experimental Cu fraction determined by AAS [Fig. 4.10(c)] and the summation is over the nominal values of x, *i.e.* all members of the series. The values of m_c and m_t were found to be -0.64 and -0.29 and the individual values of x_c and x_t can so be computed. Plotting a_c and a'_t as a function of x_c and x_t, respectively, illustrates a key feature of this system: the substantial miscibility gap [Fig. 4.10(d)]. Only about 10 mole percent of Cu^{2+} can be dissolved in $Mn[Pt(CN)_6]$ under these conditions and *vice versa*.

$Mn_{1-x}Cu_x[Pt(CN)_6]$ can considered a cyanide analogue of Cu-containing mixed-metal double perovskites, *e.g.* $Ba_2Cu_xZn_{1-x}B'O_6$ (B'^{6+} = W, U). These perovskites are cubic at low values of x, but develop a tetragonal distortion upon increasing Cu content.[495,496] The compositional threshold for orbital order ($x_{oo} \approx 0.24$) of the perovskites is largely in agreement with the site percolation threshold on a FCC lattice (~ 0.2)[497,498] and no miscibility gaps were reported, in contrast to the present results.* Early studies proposed the space group $I4/mmm$ for the endmembers $Ba_2CuB'O_6$, but the symmetries were later reassigned as $I4/m$,[495,508–510] following the discovery of their $a^0a^0c^-$ tilt systems.[511] $Cu[Pt(CN)_6]$ does not support any static tilts, which perhaps explains the discrepancies in the solubilities of the cyanide

*Although miscibility gaps *per se* are not uncommon in minerals,[499–503] relatively few examples in perovskite systems are known.[504–507]

and oxide perovskites.* Additionally, the behaviour of $Mn_{1-x}Cu_x[Pt(CN)_6]$ reported here may not necessarily reflect the thermodynamic ground state: changes in synthesis conditions are expected to produce miscibility gaps of various sizes. Both Ba_2CuUO_6 and Ba_2CuWO_6 retain the JT distortion upon heating,[508,512] as opposed to the high-temperature orbital disorder found in $LaMnO_3$. The lack of thermal phase transitions is consistent with the hexacyanoplatinates; no order–disorder phase transitions were found in the range 100–500 K [Fig. C2.2–C2.4]. Dilution-dependent orbital correlations in oxides and cyanides thus manifest differently, although their thermal behaviour is similar.

The analogous series $B_{1-x}Cu_x[Pt(CN)_6]$ (B^{2+} = Fe, Zn, and Cd) are largely comparable to the manganese counterpart. However, the analysis proved more challenging for these systems—presumably in part due to the strong dependence of the phase fractions on the synthesis conditions—and quantitative information could not be extracted. Their diffraction patterns are shown in Sections C2.2–C2.4.

$\mathbf{(Mn_{1-x}Cu_x)_3[Co(CN)_6]_2}$

Prussian blue analogues with formula $B_3[B'(CN)_6]_2$ constitute defective double perovskites, with 33% of the $B'(CN)_6$ clusters absent relative to the fully connected hexacyanoplatinates. In general, the symmetry of these compounds is invariant to metal substitution;[200] hence, $Mn_3[Co(CN)_6]_2$ and $Cu_3[Co(CN)_6]_2$ both crystallise in $Fm\bar{3}m$ and $(Mn_{1-x}Cu_x)_3[Co(CN)_6]_2$ forms a complete solid solution without any composition-induced phase transitions [Fig. 4.11(a)]. However, the peakwidth in-

*The differentiation between $I4/mmm$ (untilted) and $I4/m$ (tilted) based on PXRD is nontrivial and, hence, the presence of tilts cannot be strictly ruled out for $Cu[Pt(CN)_6]$ here. However, tilts

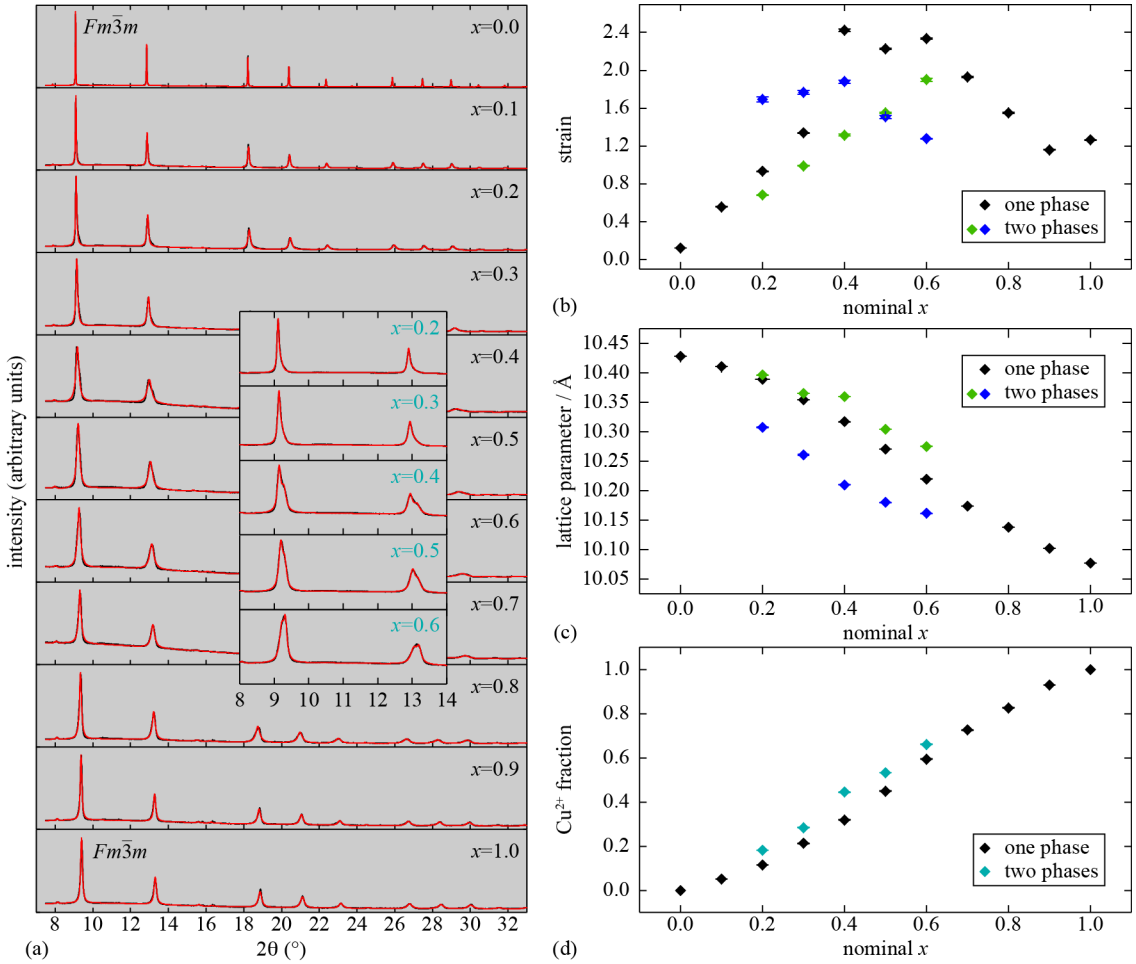


Figure 4.11: Experimental data for $(Mn_{1-x}Cu_x)_3[Co(CN)_6]_2$. (a) Pawley fits of the diffraction patterns using only one phase with the inset showing two-phase fits of the samples with intermediate x-values. The calculated profile is shown in red and the experimental in black. The x dependence of (b) the Lorentzian strain, (c) the lattice parameters, and (d) the calculated Cu fraction. The results from one-phase refinements are shown in black, whereas the two individual phases are coloured blue and green.

creases as a function of the Cu concentration and splitting of the reflections as well as significant peakshape anisotropy are evident at intermediate x-values [inset in Fig. 4.11(a)]. This is reflected by the large strain values that peak at $x = 0.4$–0.5 [Fig. 4.11(b)]. The simplest explanation for the universal peak splitting is an inhomogeneous distribution of the two B-site metals across the individual crystallites. Consequently, the refinements were carried out in duplicate, using both one and two

are infrequent in Prussian blue analogues and therefore the space group is assigned as $I4/mmm$ in agreement with a previous study.[191]

phases in the starting model, represented by black and blue/green in Fig. 4.11.

The lattice parameters correlate linearly with x in conformity with Vegard's law,[494] and the Cu fraction can be extracted by rearranging the formula $a(x) = a(0) + mx$, where $m = a(0) - a(1)$ [Fig. 4.11(c)]. When multiple phases are present, determining the overall Cu concentration also requires knowledge of the phase fractions [Eq. 4.10], which were found by constrained Rietveld refinements [Fig. C3.24]. The calculated Cu fractions are in close agreement with the nominal x-values throughout the series [Fig. 4.11(d)]. Variable-temperature measurements were carried out in the range 100 K–500 K, but no thermally induced phase transitions occurred [Fig. C3.25–C3.27]. In general, the isostructural series $(Mn_{1-x}Cu_x)_3[Fe(CN)_6]_2$ and $(Cd_{1-x}Cu_x)_3[Co(CN)_6]_2$ behave similarly to the results given here [Sections C3.2–C3.3].

As an aside, it should be mentioned that the behaviour presented for the PBAs depends on the synthesis conditions and the parameterisation of the refinements. Fig. 4.12 shows how the relative proportions of the different phases vary with synthesis conditions for a set of samples with identical nominal compositions. Therefore, the systems synthesised for this study are likely to represent kinetic phases. Systematic investigations on the effect of the reaction times on the phase fractions, so as to determine thermodynamic parameters, provide an interesting area for future research. Indeed, crystallisation of MOFs and CPs is generally poorly understood, despite being of fundamental importance. The sensitivity to subtle fluctuations in the synthesis conditions may explain the difficulty in analysing $B_{1-x}Cu_x[Pt(CN)_6]$ (B^{2+} = Fe, Zn, Cd) [Appendix C].

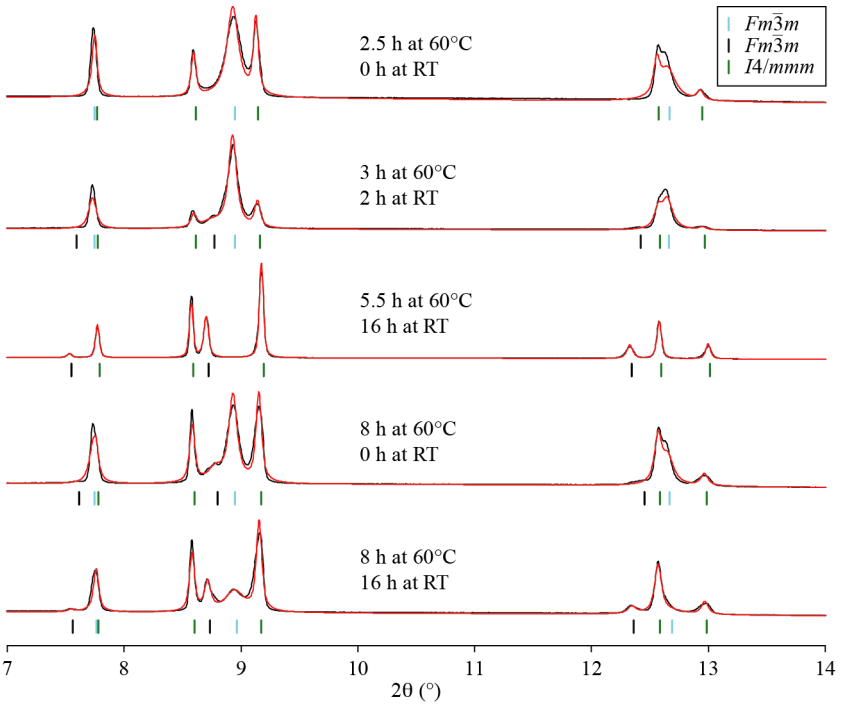


Figure 4.12: Pawley fits of the PXRD patterns for $Cd_{1-x}Cu_x[Pt(CN)_6]$ with $x = 0.8$ synthesised with various stirring times. The vertical bars indicate the allowed reflections for the tetragonal (green) and cubic phases (black and blue).

Moreover, the crystallographic analysis is complicated by the presence of multiple phases with overlapping reflections and anisotropic peak broadening. As a result, the assignment of the number of phases is sometimes nontrivial, especially for isostructural components with similar lattice parameters. The phase separation in $(Mn_{1-x}Cu_x)_3[B'(CN)_6]_2$ (B'^{3+} = Co, Fe) series is pronounced; yet on close inspection, a second cubic phase (giving three phases in total) may also be present in certain members of $Mn_{1-x}Cu_x[Pt(CN)_6]$. However, care has to be taken to avoid overparameterisation of the refinement; hence, the lowest possible number of phases was used. In essence, the refinement protocol does not capture the full complexity of these materials, which adds to the uncertainty in the obtained information. Nonetheless, quantitative results are not the primary aim of this study.

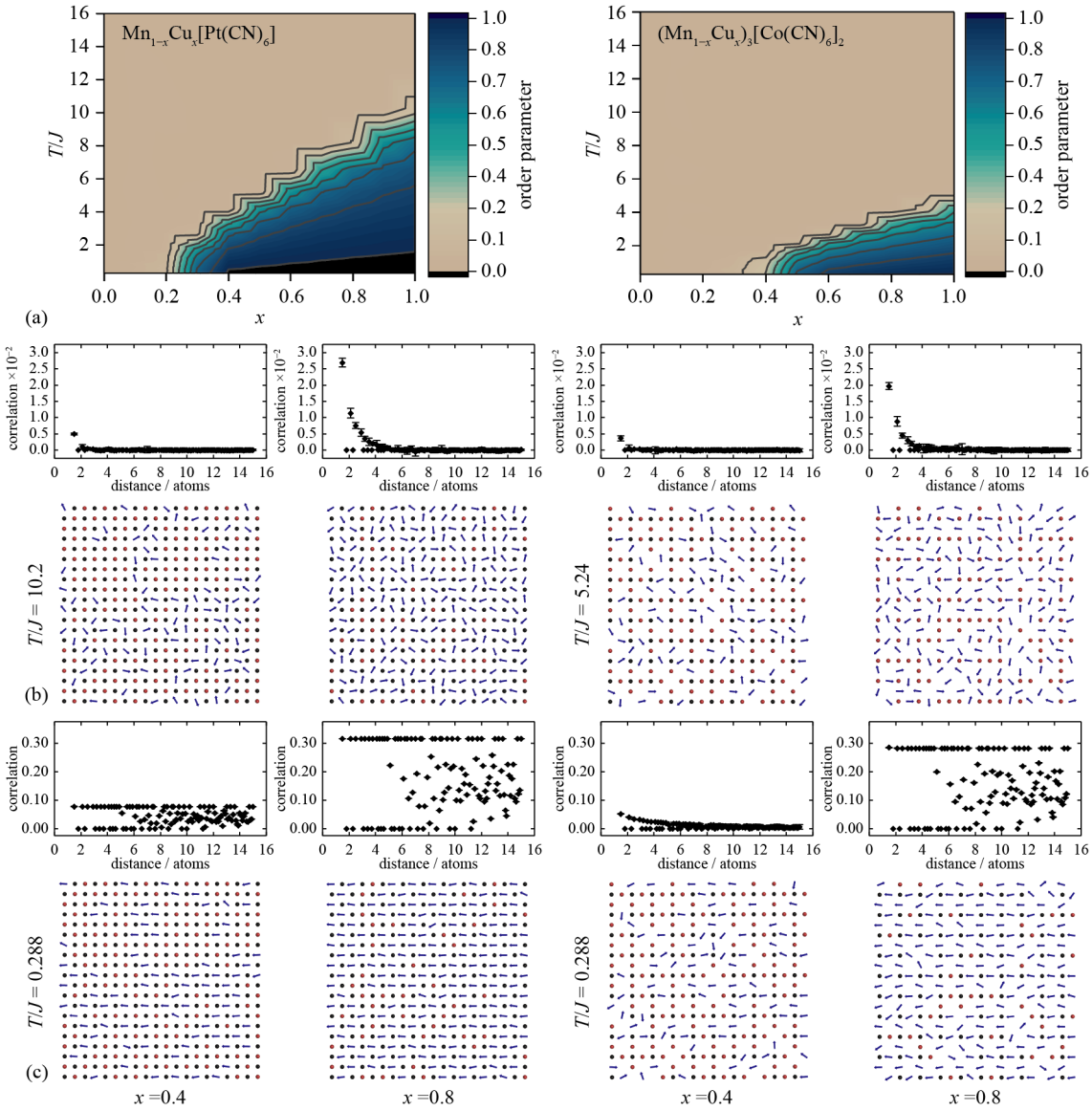


Figure 4.13: (a) The orbital order parameter, η, as a function of x and $\frac{T}{J}$, correlation functions and MC configurations in (b) the disordered and (c) the ordered regime for $x = 0.4$ and 0.8. The Jahn-Teller distortion is represented by a blue arrow as in Fig. 4.5, Mn is shown in red and the B′-site (Pt/Co) in black. The absolute direction of the JT vector is not meaningful. Note the difference in scale for the correlation functions in panels b and c.

4.5.2 Monte Carlo results

Following the satisfactory application of the compass model to the mixed-metal formates, the simulations were adapted for a face-centred unit cell. The phase diagrams of the orbital order–disorder for a fully connected—$Mn_{1-x}Cu_x[Pt(CN)_6]$—and

defective—$(Mn_{1-x}Cu_x)_3[Co(CN)_6]_2$—FCC system are shown in Fig. 4.13, along with configurations at $x = 0.4$ and $x = 0.8$ at temperatures above the phase transition and at the ground state. The areas of orbital order are considerably larger than for the primitive cubic series; a corollary of the increased coordination number of the Cu^{2+} ions in FCC unit cells. The critical composition, $x_{oo} \approx 0.3$, predicted for the hexacyanoplatinates is not inconsistent with the experimentally determined results, although the miscibility gap complicates the interpretation. It should be noted again that the MC model does not allow for coupling between orbital order and strain, despite the important role of strain in orbitally ordered PBAs. The defective PBAs display a higher critical value of x for the onset of order than the fully connected systems. When $\frac{T}{J} > 5$, orbital disorder is predicted for the defective hexacyanocobaltates, in agreement with the crystallographic data. Therefore, the experimentally determined behaviour may not represent the true thermodynamic ground state, as noted above, and different extents of orbital orders may be accessible by adjustment of the synthesis conditions. However, Prussian blue analogues are well known to precipitate rapidly from solution and control of the rate of growth is a major challenge within the field.[213]

As for the formates, information regarding the local order is available from the correlation functions [Fig. 4.13(b)–(c)]. Above the phase transition, the short-range order persists on average over a distance of 3–4 atoms for $x = 0.8$ and 1–2 atoms for $x = 0.4$. At the lowest temperature point, the correlation lengths are infinite for both the fully connected and defective PBAs for $x = 0.8$, whereas it tends to zero for the defective system for $x = 0.4$. Thus, a doping level of $x = 0.4$ likely entails

locally ordered clusters of sufficient separation to prevent percolation and long-range orbital order.

This model also encompasses a number of assumptions regarding the distribution of cations and vacancies. As discussed for the formates, the simulation presumes a random distribution of the two cations. However, $(Mn_{1-x}Cu_x)_3[Co(CN)_6]_2$—and perhaps also $Mn_{1-x}Cu_x[Pt(CN)_6]$—features an inhomogeneous cation distribution with clustering of like species. In the limit of non-percolating cation-ordered domains, the tendency for orbital order will thus be overestimated by the MC simulations. However, as even the endmember $Cu_3[Co(CN)_6]_2$ is disordered, cation correlations cannot explain the orbital disorder in $(Mn_{1-x}Cu_x)_3[Co(CN)_6]_2$. The converse non-random scenario—avoidance of like cations—is presumably less plausible, as cation-ordered triple perovskites are very rare.[513,514] Also, there are no experimental signs of further symmetry lowering.

The distribution of the $Co(CN)_6$ vacancies in the defective framework is another critical point. Vacancies reduce the coordination number of the B-sites and should therefore be able to prevent strain-mediated coupling. As already discussed, 33% of the $Co(CN)_6$ moieties is absent in hexacyanocobaltates and understanding the factors governing the vacancy order is challenging. Whilst often presumed random,[190,200,209,515] there is evidence from diffuse scattering analysis and ^{113}Cd NMR spectroscopy in favour of correlated—as opposed to random—vacancy disorder [Section 2.1.6].[204,205,207,208] Appendix B contains the results from Monte Carlo simulations employing two alternative vacancy arrangements: a random distribution and an ordering based on another Monte Carlo simulation informed by diffuse scattering.

Any differences to the present results are discussed therein.

Finally, the distribution of vacancies and cations are assumed to be uncorrelated. However, the absence of $B'(CN)_6$ moieties drastically disrupts the local symmetry of the adjacent B-site cation and consequently perturbs its local crystal field. Since crystal field effects are central to the emergence of Jahn-Teller distortions, a correlation between the vacancies and the location of the Cu^{2+} cations can be expected. Indeed, $Cu_3[Co(CN)_6]_2$ is believed to contain an extreme type of vacancy order relative to other hexacyanocobaltates [Appendix D].

4.6 Comparative discussion

Mixed-metal series of molecular perovskites evidently exhibit highly diverse solubility behaviour, possibly due to the differences in flexibility. The formate system supports a sizeable octahedral tilt, and local variations in the tilt angles presumably facilitate the accommodation of Cu cations within the Mn matrix and *vice versa*. As a result, the orbital order–disorder transition is only weakly coupled to the macroscopic lattice strain. By contrast, the rigid hexacyanoplatinates do not contain any static tilts and the orbital order transition induces a substantial macroscopic strain that lowers the symmetry from cubic to tetragonal. These differences might rationalise why miscibility gaps feature in the hexacyanoplatinates, but not in the formates. The defective Prussian blue analogues comprise a lower connectivity of the B-site sublattice and, hence, the local strains from the incorporation of a slightly smaller cation are presumably relatively minor. In spite of that, there is evidence in favour of cation clustering even in the formate and hexacyanocobaltate

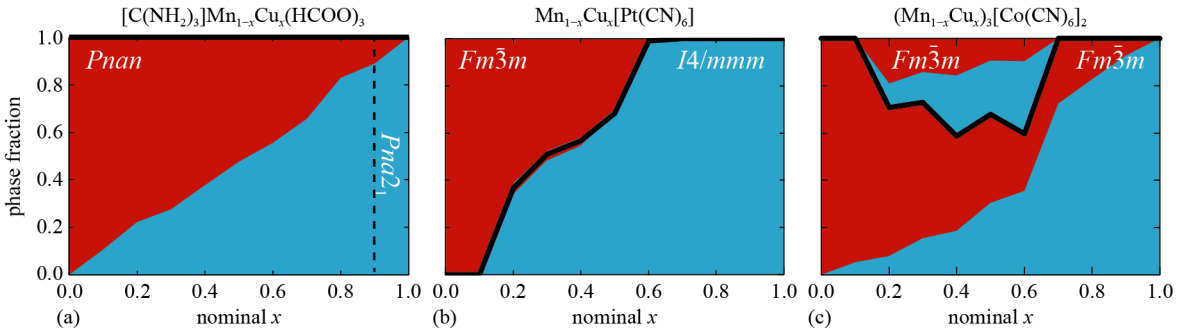


Figure 4.14: Semaphore diagrams for the three mixed-metal series under study. Phase fractions are demarcated by the bold black line and the colours show the metal ratio within each phase, with Cu represented by blue and Mn by red.

solid solutions, suggesting a nonzero energy penalty associated with the mixing of the two endmembers.

The coexistence of multiple phases with distinct metal ratios can be summarised in what I call a "semaphore diagram" [Fig. 4.14]. Here, the bold black line demarcates the phase fractions and the relative sizes of the coloured areas—with Cu represented by blue and Mn by red—give the ratio of the two metals within a given phase. For example, in $[C(NH_2)_3]Mn_{1-x}Cu_x(HCOO)_3$, the bold black line appears horizontally at the top of the diagram, reflecting that this system only forms one phase. Consequently, the line demarcating the two colours simply corresponds to the experimental Cu fraction as presented in Fig. 4.6(c). The phase transition, if present, is indicated by a dashed vertical line. Although semaphore diagrams are trivial for one-phase systems; they provide a concise illustration of phase separation and solubility readily extended to more complicated scenarios.

Indeed, semaphore diagrams are more complex for the two-phase series—and arguably also more useful. The phase line in $Mn_{1-x}Cu_x[Pt(CN)_6]$ is coincident with the x dependence of the tetragonal phase fraction [Fig. 4.10(b)]. In the region $0.2 \leq x \leq 0.6$, a thin red area below the phase line represents the small amount of

Mn within the tetragonal phase. Likewise, the blue region above the black line is virtually vanishing, indicative of a very low Cu content in the cubic phase at those compositions. At Cu fractions above 0.6, the tetragonal phase dominates and it is devoid of Mn, as indicated by the lack of red colour. The semaphore diagram of $(Mn_{1-x}Cu_x)_3[Co(CN)_6]_2$ shows a second phase when $0.2 \leq x \leq 0.6$ [Fig. 4.10(c)]. The minority component (top) has a larger blue proportion than the main phase so as to highlight its higher Cu fraction. In essence, the closer the proximity between the partitioning of the colours and the phase line, the lower the solubility of the system. Semaphore diagrams thus provide a simple visualisation of the phase behaviour of mixed-metal series, although the diagrams drawn here are not unique. In addition, the behaviour described in Fig. 4.10 should not be interpreted as the thermodynamic ground state.

Returning to the orbital order–disorder transitions, the topology is a crucial factor as it dictates the connectivity of the JT-active sublattice, which in turn affects the compositional threshold for orbital order. The average nearest-neighbour coordination number in the systems under study ranges from 4 (hexacyanocobaltates) to 6 (formates) to 12 (hexacyanoplatinates). The MC simulations highlight the strong effect of the coordination number on the relative size of the orbitally ordered regime in the phase diagrams. As the three molecular perovskites are topologically inequivalent,* this study effectively serves to establish topology-order relationships for Jahn-Teller distortions in cubically connected materials. Importantly, a comparison of the defective $(Mn_{1-x}Cu_x)_3[Co(CN)_6]_2$ and the fully connected $Mn_{1-x}Cu_x[Pt(CN)_6]$

*Despite both the hexacyanoplatinates and the hexacyanocobaltates possessing face-centred cubic structures, the presence of defects in the latter render these two systems topologically distinct.

reveals the key role of structural vacancies in the stabilisation of disordered states. Missing cluster defects are emerging as ubiquitous and functionally relevant features in many metal–organic frameworks, with UiO-66 as the canonical example.[346–349] In consequence, the results obtained here are potentially applicable to ordering processes in other framework compounds with analogous structures.

The orbitally disordered states are conceptually related to quadrupolar spin glasses, also known as orientational glasses.[516–518] These are topical materials, as they share the anomalous low-temperature thermodynamic behaviour with classical glasses; yet their crystalline states are well understood—in contrast to classical glasses.[516] For these reasons, they constitute valuable model systems for amorphous states of condensed matter and have been widely studied. The defining feature of quadrupolar spin glasses is the existence of anisotropic quadrupolar interactions in combination with site disorder, generating a frustrated state. A canonical example is the mixed cyanide-halide crystals, such as $KBr_{1-x}CN_x$.[519–521] Pure KCN crystallises with $Fm\bar{3}m$ space group symmetry and shows four-fold reorientational disorder of the cyanide anions. Upon cooling, a phase transition into a cyanide-ordered orthorhombic phase occurs, analogous to a orbital disorder–order transition.[522–524] Halide substitution suppresses the low-temperature quadrupolar order in the mixed crystals with $x < 0.6$ through a dilution effect.[525] Recognising the quadrupolar nature of FOJT distortions, the homologous nature of orientational glasses and the orbitally disordered states presented here should be obvious. However, no evidence for dynamic orbital fluctuations at elevated temperatures was observed in the orbital systems, in contrast to the dynamical nature of quadrupolar spin glasses. Hence,

the orbitally disordered compounds present examples of quadrupolar spin glasses with significantly higher energy scales relative to the conventional cyanide–halide solutions.

4.7 Implications

A diverse range of orbital order–disorder processes can be found in mixed-metal series of molecular perovskites, dictated by a combination of topology and framework flexibility. In the absence of a coupling to macroscopic lattice strain, detecting the orbital order–disorder transitions by crystallographic techniques can be challenging. Yet orbitally disordered states appear to be more prevalent in molecular perovskites relative to the inorganic congeners [Fig. 4.15]. As coordination polymers are typically synthesised under mild conditions, the prevalence of disorder may arise from the trapping of kinetic products. In addition, the Cu-rich endmembers ($x = 1.0$) in defect-free frameworks are invariably orbitally ordered and disorder can only be induced by dilution—through vacancies or inactive cations—and not thermally accessed, in contrast to most oxide systems. The compass model developed for $KZn_{1-x}Cu_xF_3$ can be applied to molecular perovskites and gives a reasonable reproduction of the experimental results. This demonstrates how similar principles may underpin ostensibly different behaviour in both molecular and inorganic materials.

Developing an understanding of the key features implicated in orbital order is an important step towards rational materials design based on JT distortions. From a synthetic viewpoint, orbital degrees of freedom are more amenable to strategic control than condensed phonon modes, such as shifts and tilts. As exempli-

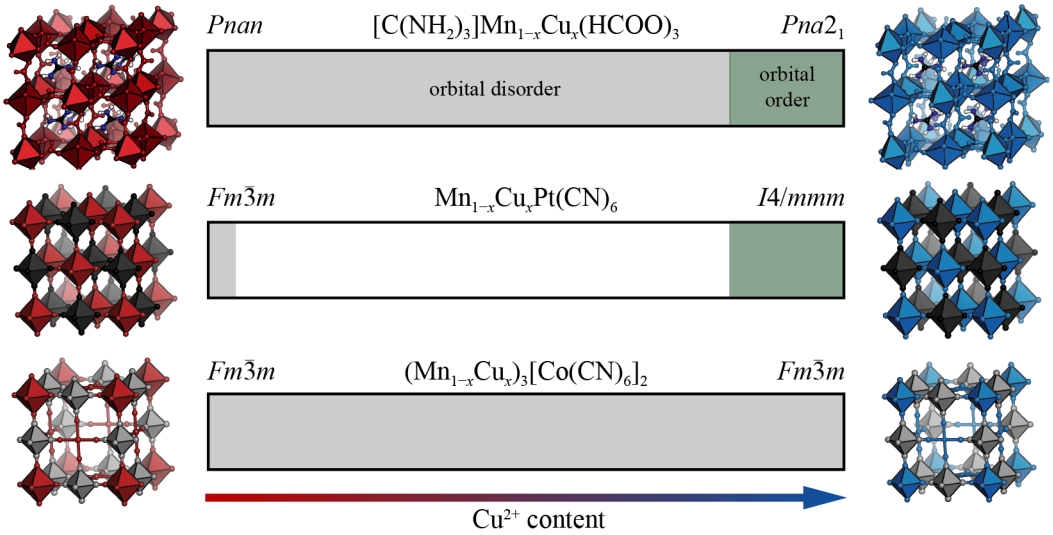


Figure 4.15: A summary of the orbital order–disorder behaviour as found by XRD in the three systems studied. The Mn/Cu endmembers are shown on the left/right and the colours indicate regions of orbital disorder (grey) or order (green).

fied by the formate and hexacyanoplatinate series, cooperative Jahn-Teller distortions can have a drastic effect on the symmetry and, thus, the functional response. $[C(NH_2)_3]Cu(HCOO)_3$ is the only polar member of the $[C(NH_2)_3]B(HCOO)_3$ family and $Cu[Pt(CN)_6]$ exhibits anisotropic thermal expansion, which are direct consequences of the orbital order.[191,245] The 2D phase diagrams from the Monte Carlo simulations are produced using only topological information, whilst both the synthetic details and the nature of the chemical system determine $\frac{T}{J}$, *i.e.* the horizontal location of the experimental systems in the phase diagram. Hence, by investigating topologically identical systems and either varying the synthesis conditions or the coupling pathway—for example by employing linkers of varying length and flexibility—further tuneability of the orbital order–disorder transition may be achieved.

As noted, the energy landscape of a JT distortion is described by a Mexican hat potential with local minima at integer multiples of $\phi = \frac{\pi}{6}$, *i.e.* a "crimped" Mexican hat.[70] However, the compass model assumes a continuously variable Jahn-

Teller distortion, analogous to a magnet with planar (XY) spin degrees of freedom. Hence, bonding environments with both Q_2 and Q_3 character ($\phi \neq \frac{n\pi}{6}$ for integer n) are predicted for JT-active species adjacent to inactive cations. In order to experimentally probe the existence of such deformations, techniques sensitive to local metal environments—*e.g.* NMR, PDF or XAS—are required, although resolution may present a problem. Systems with continuously variable degrees of freedom can harbour topological defects unfeasible in Ising/Potts states, such as skyrmions and hedgehog defects.[526–528] By analogy, similar phenomena may perhaps be anticipated in orbitally disordered materials, although it will depend on the exact shape of the energy landscape. Interestingly, the Mexican hat potential for the JT distortions has been extended to explain the symmetry-breaking phenomena in the cooling universe after the Big Bang,[64] as also explored for ferroelectric manganites.[529,530] Consequently, the possibility of continuously variable Jahn-Teller distortions in these systems may be a potential source of intriguing physics.

The formate system is particularly interesting in light of the existence of nanoregions and the polar nature of the orbitally ordered endmember. Polar nanoregions due to compositional inhomogeneities are characteristic ingredients of relaxor ferroelectrics, of which $PbMg_{0.33}Nb_{0.67}O_3$ is a particularly prominent example.[486,531] Relaxor ferroelectrics are characterised by a broad and strong dielectric response with a considerable frequency dispersion, which render them technologically relevant as capacitors.[532–534] Thus, it is anticipated that the mixed-metal formates can behave analogously, as they appear to support polar nanoregions. Based on the results presented here, the range $0.5 < x < 0.8$ should be of the greatest interest for further ex-

ploration of relaxor-like dielectric behaviour in $[C(NH_2)_3]Mn_{1-x}Cu_x(HCOO)_3$. However, as the MC simulations suggest a more disordered orbital arrangement at the edges of the local orbitally ordered Cu clusters, the polarisation of the compositional domains may be lower than expected. Future studies using *e.g.* dielectric and SHG measurements will be invaluable in this regard.

Chapter 5

Hybrid Improper Ferroelectricity in Molecular Perovskites

5.1 Chapter overview

The preceding discussion investigated selected degrees of freedom accessible to molecular perovskites and this Chapter highlights how individual distortions can couple to lift the global inversion symmetry, so-called hybrid improper ferroelectricity.[137] Ferroelectricity—the presence of a switchable electronic polarisation—is an attractive property of relevance for capacitors and components within computer memories.[138] The Chapter commences by giving a brief account of the necessary background and group-theoretical methods, followed by an enumeration of the coupling schemes of the five degrees of freedom pertinent to molecular perovskites. This explicitly identifies combinations of distortion modes resulting in acentric structures and it will be shown that columnar shifts and multipole moments are particularly significant for the emergence of polarity. Next, this type of analysis is used to rationalise the symmetry of a number of noncentrosymmetric systems from the literature and the Chapter concludes by discussing the utility of the group-theoretical protocol in the development of new polar molecular perovskites. Besides providing general guidelines, a few as-yet unrealised compositions anticipated to adopt acentric space

groups are suggested.

This study was carried out in collaboration with Mark Senn (University of Warwick).

5.2 Background

It is clear from the previous Chapters that molecular substitution enhances the number of structural degrees of freedom of a perovskite. The question then follows: how can the expanded toolbox of distortions be exploited for the development of desirable functionality? An answer is provided by the formate perovskite $[C(NH_2)_3]Cu(HCOO)_3$. It is polar (space group $Pna2_1$) on account of the collective Jahn-Teller order and the arrangement of the multipolar guanidinium cation—an unconventional degree of freedom. However, neither distortion mode can break inversion symmetry on its own and so it follows that the unconventional degree of freedom—the orientational cation order—is necessary for the polarisation to emerge.

Several studies have been devoted to understanding the potential for ferroelectricity and multiferroicity in $[C(NH_2)_3]Cu(HCOO)_3$.[245,268,535] By defining an order parameter, λ, as the linear interpolation of atomic positions between a virtual nonpolar $Pnan$ structure and the experimental $Pna2_1$—the difference being a Jahn-Teller distortion—the structure dependence of computable properties can be studied [Fig. 5.1(a)–(c)].[268] There is indeed a strong coupling between the polarisation and the direction of the Jahn-Teller distortion, which presumably induces a ferroelectric state. In addition to computational approaches, experimental studies have found evidence for a weak magnetoelectric coupling, in agreement with the theoretical

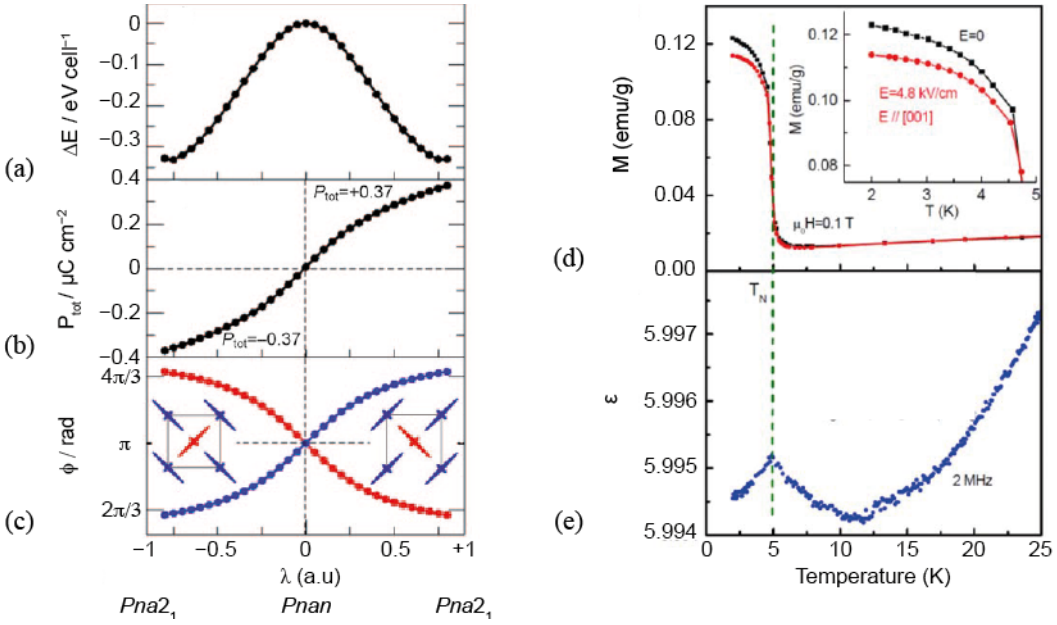


Figure 5.1: The relation between structure, polarisation and magnetisation in $[C(NH_2)_3]Cu(HCOO)_3$. The calculated λ dependence of (a) the energy, (b) the polarisation and (c) the Jahn-Teller phases, where λ is the order parameter between the virtual $Pnan$ parent and the experimental $Pna2_1$ structure. (d) The temperature dependence of the magnetisation in the ab plane along the [110] direction, in the absence (black) and presence (red) of an applied electric field ($E = 4.8\,\mathrm{kV\,m^{-1}}$). The inset shows a magnification of the low-temperature region. (e) The relative permittivity as a function of temperature along the [110] direction. Dielectric anomalies at the magnetic transition temperature are normally considered as evidence for magnetoelectric coupling.[536,537] Panels a–c are adapted from Ref. 268 and d–e from Ref. 535.

predictions of multiferroicity [Fig. 5.1(d)–(e)].[268,535]

The coupling of multiple nonpolar distortions to achieve a macroscopic polarisation is known as hybrid improper ferroelectricity (HIF). The term was first coined by Benedek *et al.* in a study of Ruddlesden-Popper phases,[137] although related phenomena had been explored previously.[538,539] In the prototypical HIF material $Ca_3Mn_2O_7$, two tilt modes along perpendicular axes collectively lift the inversion symmetry and reduce the space group symmetry from the aristotype $I4/mmm$ to the polar space group $A2_1am$ ($\equiv Cmc2_1$).[137] As the direction of the polarisation arises from the sense of the tilting, it can be switched by reversal of one of the tilting modes. Besides, as the octahedral rotations are coupled to the magnetic order,

magnetoelectric coupling can be anticipated, which has also been experimentally confirmed.[540] Indeed, the relative ease by which multiferroicity may be generated in HIF materials represents one of the key advantages of this mechanism. In contrast, conventional mechanisms for inversion symmetry breaking often rely on the absence of *d*-electrons in order to facilitate a second-order Jahn-Teller distortion [Section 1.3.3].[115,116] Moreover, the principles governing the activation of octahedral tilts are well understood and, hence, these degrees of freedom lend themselves to rational design more easily than SOJT off-centring. This is illustrated by the so-called "tilt engineering" approaches, which have been successfully exploited to strategically synthesise multiferroic Ruddlesden-Popper oxides based on hybrid improper ferroelectricity.[6,124]

It is no coincidence that the original research on hybrid improper ferroelectricity has been carried out on Ruddlesden-Popper oxides, which in effect constitute layered perovskites.[137,540,541] The two structural degrees of freedom available to simple unlayered conventional perovskites—tilting and Jahn-Teller distortions—always preserve the inversion centre on the B-site and, as a consequence, cannot generate acentric symmetries.[17,542] As a result, layering in the form of compositional A-site cation order or by the use of Ruddlesden-Popper oxides is necessary for HIF in conventional perovskites.[17,541,543] However, this Chapter will come to show how the unconventional degrees of freedom arising from molecular substitution enable the emergence of polarity in molecular perovskites in the absence of layered order, as in $[C(NH_2)_3]Cu(HCOO)_3$.

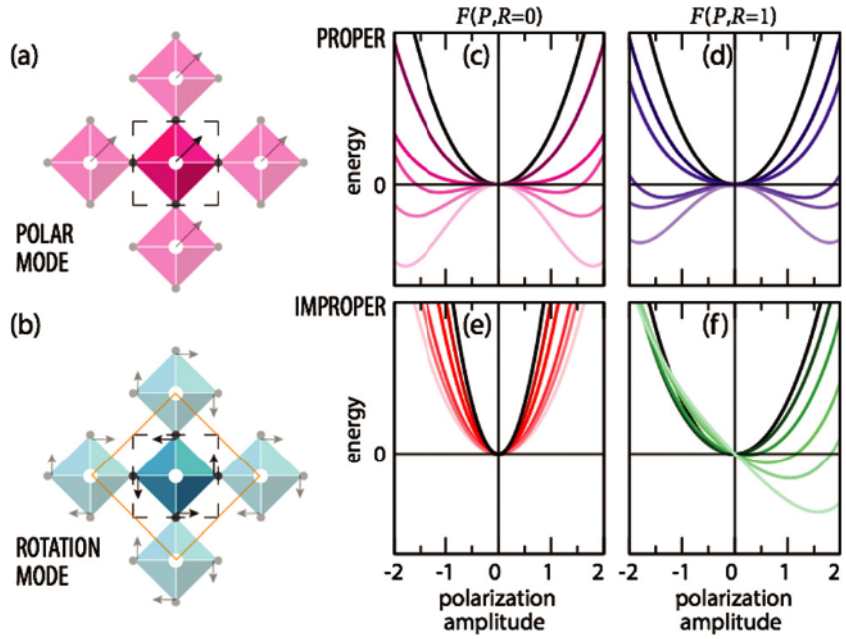


Figure 5.2: Landau energy expansion for proper and improper ferroelectrics. (a) A polar and (b) a nonpolar distortion mode in a hypothetical system. In proper ferroelectrics, the free energy exhibits the classical double-well potential both in (c) the presence and (d) absence of the activation of the nonpolar rotation mode. For the improper ferroelectric, the nonzero polarisation amplitude does not lower the free energy in (e) the absence of the distortion, R. However, if (f) R is activated, the minimum of the free energy shifts to a nonzero value of the polarisation. As the direction of R switches, the free energy curve reflects in the vertical axis. Lighter colours of the graphs correspond to lower temperatures. Reproduced from Ref. 544 with permission from The Royal Society of Chemistry.

A more formal treatment of the coupling schemes in hybrid improper ferroelectrics can be obtained by invoking Landau theory. Consider a system with a polar and a nonpolar distortion mode [Fig. 5.2(a)–(b)]. In a proper ferroelectric coupling, where the primary order parameter is the polar mode (P), the free energy can be written as a Taylor expansion—here truncated at the fourth order—in terms of the polar mode:[544]

$$E = E_0 + \alpha P^2 + \beta P^4, \tag{5.1}$$

where Greek letters denote constants. Below the ferroelectric ordering temperature, $\alpha < 0$ irrespective of whether the nonpolar mode is active and so the classical double-well potential associated with ferroelectric states results [Fig. 5.2(c)–(d)].

In improper ferroelectrics, on the other hand, the primary order parameter is the nonpolar mode (R), which is coupled at linear order to the polar distortion:[544]

$$E = E_0 + \alpha_1 R^2 + \alpha_2 P^2 + \beta_1 R^4 + \beta_2 P^4 + \beta_3 R^3 P + \beta_4 R^2 P^2. \tag{5.2}$$

Accordingly, there is always a choice of sign for P such that the term $\beta_3 R^3 P$ leads to a lowering of the free energy, *irrespective* of the sign of β_3 [Fig. 5.2(e)–(f)]. Note that Eq. 5.1 can be obtained from Eq. 5.2 by setting the appropriate constants to zero. Examples of improper ferroelectrics include the hexagonal manganites, *e.g.* $YMnO_3$, where the polarisation emerges in response to the tilting of the corner-sharing trigonal pyramidal MnO_6.[538] Finally, in *hybrid* improper ferroelectricity, the polarisation is coupled to *two* superimposed order parameters through a trilinear coupling term $E = \gamma R_1 R_2 P$. Like for improper ferroelectrics, there is always a nonzero value of P that will stabilise the structure when R_1 and R_2 are condensed.

All polynomials in a Landau expansion are required to be invariant under the symmetry operations of the high-symmetry space group.[545] As a consequence, the trilinear term $R_1 R_2 P$ has to span the totally symmetric representation of the aristotype $Pm\bar{3}m$ space group (Γ_1^+). Since P transforms as Γ^-, the direct product $R_1 R_2$ must also form a basis for Γ^- in order for a polar* coupling to appear—as $\Gamma^- \oplus \Gamma^- = \Gamma^+$. Irreps for periodic structures are labelled by $K_n^{+/-}$, where the superscript contains information about the parity and the Bradley-Cracknell symbol indicates the crystal momentum [Section 2.2].[360,388] Conservation of both parity and

*Strictly speaking, the method outlined here only requires P to be an acentric distortion mode, but not necessarily polar. However, in practice, these rules very often yield polar couplings, although this is not a stringent mathematical consequence.

momentum is necessary in order for R_1R_2 to transform as Γ^- and, as a result, the two distortions must transform as irreps with opposite signs, but identical periodicities. For R-point distortions, this equates to irreps with opposite signs and identical Bradley-Cracknell symbols, *e.g.* R_5^+ and R_5^-. However, due to the multiplicity of high-symmetry points in the Brillouin zone, this is not always a sufficient condition. By way of example, the coupling of X_5^+ and X_5^- drives an improper polarisation (space group $Cmc2_1$) when the crystal momenta both are [0, $\frac{1}{2}$, 0]; however, if the momenta are [0, $\frac{1}{2}$, 0] and [$\frac{1}{2}$, 0, 0], the resulting isotropy subgroup is the centrosymmetric space group $Pmmn$. Consequently, combining irreps with opposite sign and same periodicity will often—but not always—induce an improper acentric distortion mode. Nevertheless, these rules enable suitable candidate irreps for trilinear couplings to be identified by inspection without the requirement for explicit Landau theory and invariants analysis.[545]

In addition to trilinear couplings, fourth–order terms—as well as even higher orders—are also possible, although as before a term linear in P is required for improper ferroelectric couplings. As a consequence of the above-mentioned requirements, three irreps at distinct points in reciprocal space, where only one has a positive superscript, are now necessary. To illustrate, the three distortions transforming as the irreps X_5^+ [0, $\frac{1}{2}$, 0], M_2^+ [$\frac{1}{2}$, 0, $\frac{1}{2}$], and R_5^- [$\frac{1}{2}$, $\frac{1}{2}$, $\frac{1}{2}$] can act as superimposed primary order parameters for the polar space group $Pmc2_1$. It is easily verified that this coupling scheme conserves both the crystal momentum and parity.

The aim of this Chapter is to use the above method to investigate the propensity for global inversion symmetry breaking in molecular perovskites by a hybrid

improper mechanism. As molecular perovskites support a wider range of structural distortions relative to their inorganic counterparts, a larger prevalence of polar space groups can be expected. Indeed, the polarity of $[C(NH_2)_3]Cu(HCOO)_3$ already reveals that hybrid improper ferroelectricity is attainable in molecular perovskites even in the absence of layering.

5.3 Methods

5.3.1 Irrep identification

Prior to the application of group-theoretical methods to molecular perovskites, it is necessary to determine the irreps associated with each distortion mode. There are five degrees of freedom to consider: conventional tilting, unconventional tilting, columnar shifts, Jahn-Teller distortions and orientational ordering of polyatomic cations—here described as ordering of multipole moments. To investigate the framework distortions, a hypothetical aristotype molecular perovskite was used as a model system, with the space group $Pm\bar{3}m$ and a monoatomic A-site cation at Wyckoff site $1a$ (0, 0, 0), B-site cation at $2a$ ($\frac{1}{2}$, $\frac{1}{2}$, $\frac{1}{2}$), and X-site anion at $6f$ ($\frac{1}{2}$, $\frac{1}{2}$, z). The formula is thus $AB(X_2)_3$, which represents the simplest possible molecular perovskite. Hettotype structures with tilts, shifts and Jahn-Teller distortions were created manually and decomposed relative to the aristotype in ISODISTORT,[382] allowing for the rigid unit modes and orbital ordering patterns to be identified by inspection.

Orientational cation order requires a more formal approach, making use of their inherent multipolar charge distribution, as discussed for guanidinium in the pre-

vious Chapter. Hence, determining whether a particular irrep allows for ordered multipole moments at a given site provides information regarding whether this irrep can drive orientational cation ordering at that site. Mathematically, multipoles are defined as the irreps of the rotational group SO(3): the group of all rotations in 3D space. This infinite list of irreps may be enumerated by the index $l \in \mathbb{N}$ and the dimensionality—and, therefore, the degeneracy—of each irrep is given by $2l+1$. A visual representation of multipole moments is provided by the spherical harmonics and the first four moments are denoted the monopole ($l = 0$), dipole ($l = 1$), quadrupole ($l = 2$), and hexapole ($l = 3$) moments according to the number of nodes [Fig. 5.3(a)]. The similarity between the multipoles and the atomic orbitals, where l is the angular orbital quantum number, is evident.

Now, the objective involves determining which irreps of the aristotype $Pm\bar{3}m$ space group that induce multipolar ordering* at the A-site. When the symmetry of SO(3) is lowered to that of a crystallographic point group, the multipole moments will enter into one or more of the irreps of the crystallographic point group in question. If this irrep is the totally symmetric representation, this multipole moment is considered to order. Information regarding the transformation of irreps during such a descent of symmetry is readily available in subduction tables.[383–385] To take a familiar example, when the point symmetry is lowered from SO(3) to $m\bar{3}m$, the dipole moments enter the t_{1u} representation and the quadrupole moments transform as e_g and t_{2g}—like the p and d orbitals. Therefore, quadrupole and dipoles cannot order at the A-site of an aristotype perovskite. By determining the A-site symmetry

*Only dipolar and quadrupolar moments were considered here, but multipoles of higher dimensionality are often ordered even in the aristotype.

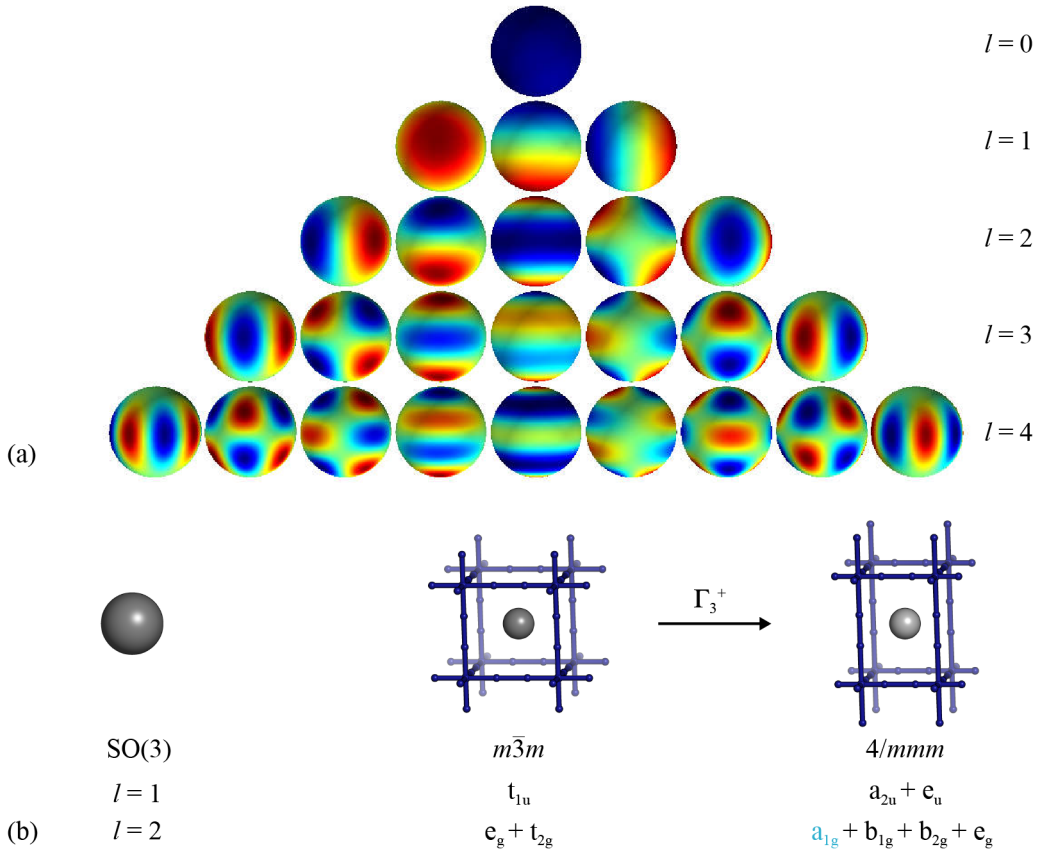


Figure 5.3: (a) The spherical harmonics for the five first values of l, where the colour spectrum visualises the charge distribution. Reproduced from Ref. 546. (b) The descent of symmetry from SO(3) to $m\bar{3}m$ and finally to $4/mmm$ along with the transformation of the irreps corresponding to dipole ($l = 1$) and quadrupole ($l = 2$) moments. In the aristotype perovskite, the A-site has site symmetry $m\bar{3}m$ and since neither the dipoles nor quadrupoles form a basis for the totally symmetric irrep, the A-site cation exhibits dipolar and quadrupolar disorder. However, the irrep Γ_3^+ reduces the A-site symmetry to $4/mmm$ and the irreps associated with the quadrupole moments now span the totally symmetric representation (highlighted in blue). Consequently, Γ_3^+ induces quadrupolar order at the A-site of a perovskite.

following the action of all the irreps of $Pm\bar{3}m$, the subduction tables may be used to identify the number of ordered multipoles. As an illustration, the action of Γ_3^+—tetragonal strain—with order parameter direction (a,0) lowers the site symmetry of the A-site to $4/mmm$ and, in this point group, the dipole moment transforms as a_{2u} and e_u and the quadrupole moment as a_{1g}, b_{1g}, b_{2g}, and e_g [Fig. 5.3(b)]. Since the quadrupole moment spans the totally symmetric a_{1g}, it can be concluded that the action of irrep Γ_3^+ as a primary order parameter leads to some quadrupolar—but

not dipolar—order at the A-site of a perovskite.

If the primary order parameter under consideration activates secondary order parameters, it is necessary to ascertain which mode is responsible for any observed multipolar order. Indeed, several zone-boundary distortions imply a lattice strain, which drive quadrupolar order at the A-site, but this order does not directly follow from the zone-boundary mode itself and should not be considered as such. Whenever possible, this ambiguity was avoided by choosing order parameter directions such that no secondary parameters were generated, but this is not always feasible. In those cases, any multipolar order originating from the secondary modes were subtracted. For example, the irrep R_5^-—conventional a^- tilts—with OPD (a,0,0) lowers the site symmetry of the A-site to $\bar{4}2m$, which implies an ordering of quadrupolar moments. However, the secondary modes are Γ_1^+ and Γ_3^+ and, as seen, it is the latter that drives quadrupolar order. Therefore, the action of R_5^- by itself does not engender orientational order of a quadrupolar A-site cation. This elimination method was performed for all irreps associated with secondary order parameters and, hence, a complete set of irreps associated with quadrupolar and dipolar A-site order could be determined.

The irreps of the various degrees of freedom of molecular perovskites are enumerated in Table 5.1 and visually depicted in Appendix E. The analysis here is restricted to zone-boundary distortions, although tilts and shifts—as noted in Chapter 3—can also occur at less symmetrical points in the Brillouin zone. Yet, inclusion of these different periodicities does not change the main argument developed here. As a note of caution, it should be remembered that zone-boundary irreps are not invariant with

Table 5.1: The degrees of freedom of molecular perovskites and the irreps for which they form a basis. Distortions available to conventional perovskites (*i.e.* conventional distortions) are highlighted in grey.

Distortion	Irreps			
Conventional tilting			M_2^+	R_5^-
Unconventional tilting	Γ_4^+	$X_{1,5}^-$	M_5^+	
Columnar shifts	$\Gamma_3^+/\Gamma_4^+/\Gamma_5^+$	X_5^+	M_2^-	
Jahn-Teller distortions	Γ_3^+		M_3^+	R_3^-
Dipolar A-site order	Γ_4^-	$X_{3,5}^-$	$M_{3,,5}^-$	R_4^-
Quadrupolar A-site order	$\Gamma_{3,5}^+$	$X_{2,5}^+$	$M_{1,2,4,5}^+$	R_5^+

respect to an origin shift of the unit cell. In this study, the A-site is located at the origin and, hence, the irreps given here are not directly comparable to those found in *e.g.* Refs. 12,81,123. The conversion of irreps between the two origin choices is presented in Appendix E.

5.3.2 Coupling and crystal structure decomposition

Following the recasting of the degrees of freedom as irreps, analysis of the symmetry-lowering properties of multiple, coexisting distortions is straightforward by modern software. In ISODISTORT,[382] two or more irreps were applied to the hypothetical aristotype and if a polar space group resulted for any order parameter direction, the coupling scheme results in improper occurrence of polarisation.

When decomposing crystal structures from the literature, an aristotype was created as above, but some modifications were necessary to avoid orientational disorder as its treatment in ISODISTORT is nontrivial. Consequently, A-site cations with an atom at the centre of mass were approximated by the central atom (*e.g.* $C(NH_2)_3$ and NH_4 were reduced to C and N, respectively) and other A-site cations were neglected altogether. All linker atoms were positioned at $6f$ ($\frac{1}{2}$, $\frac{1}{2}$, z) and any pendant

hydrogen atoms ignored, in order to create a system with a monoatomic cation at the A-site and linear linker. The crystal structure files taken from literature were used as the hettotypes, following appropriate omission of relevant moieties to ensure an atomic one-to-one mapping from the aristotype to the hettotype. To confirm that the preclusion of parts of the structure did not alter the symmetry, the space groups of the modified hettotype structures were verified using FINDSYM,[547] prior to the decomposition in ISODISTORT. In this manner, a list of possible primary order parameters was obtained. Note that the choice of primary order parameters is rarely unique, as there may be many equivalent sets of distortions generating the same symmetry, especially for hettotypes comprising a manifold of distortions. Moreover, sometimes when an order parameter induces another as a secondary order parameter, the converse is also valid such that only one has to be specified for both to be active. For the purposes of this study, a set of order parameters explainable in terms of physically sensible distortions was chosen as the coupling scheme.

5.4 Results

The irreps in Table 5.1 illustrate the difficulty of generating polarity in simple, conventional perovskites *via* a hybrid improper mechanism. Recalling the requirement for distortion modes with the same periodicity but opposite signs, it is clear that the two distortions accessible to conventional perovskites (conventional tilting and Jahn-Teller distortions) cannot break inversion symmetry as they both transform as M^+ and R^-. However, the conventional *and* unconventional degrees of freedom span irreps at all high-symmetry points in the Brillouin zone with both positive

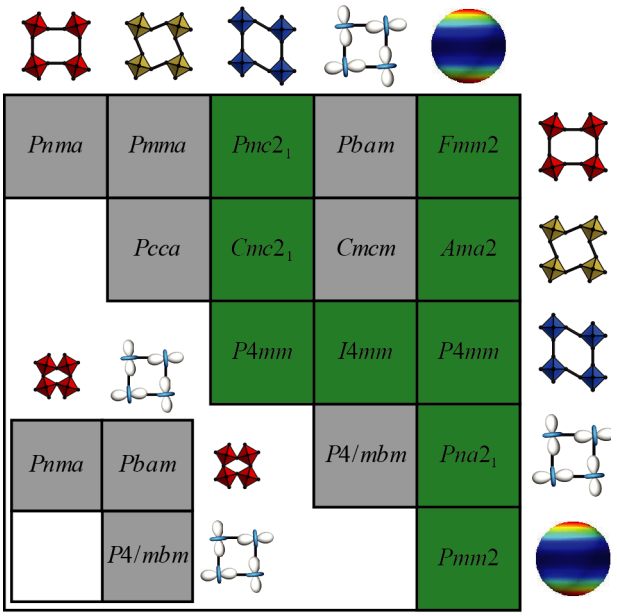


Figure 5.4: Coupling schemes of the distortions accessible to molecular perovskites: conventional tilts, unconventional tilts, columnar shifts, Jahn-Teller distortions, and multipolar order. A representative space group from each coupling scheme is shown and the colour indicates whether a polar distortion is attainable (green) or not (grey). The inset gives the corresponding table for simple conventional perovskites.

and negative signs and, therefore, molecular perovskites can be expected to show a greater propensity for adopting acentric structures. This is confirmed by the coupling schemes depicted graphically in Fig. 5.4, where potentially polar outcomes are highlighted in green. For instance, the green entry at the top right indicates the existence of at least one combination of multipolar order and conventional tilting capable of driving a polarisation. The inset in Fig. 5.4 shows the corresponding couplings for conventional perovskites, and so the importance of the molecular substitution is obvious. For hybrid improper coupling schemes in terms of irreps, see Tables E0.2–E0.3.

Interestingly, either multipolar order on the A-site or a columnar shift—accessible through molecular substitution on the A- and X-site, respectively—is sufficient to remove the centres of symmetry when correctly coupled to any other order parame-

Table 5.2: A summary of known acentric molecular perovskites, their crystal symmetries, and the corresponding distortion mode irreps.

Compound	Space group	Irreps			Ref.
$NH_4Cd(HCOO)_3$	$Pna2_1$	X_5^+	X_5^-		250
$[C(NH_2)_3]Cu(HCOO)_3$	$Pna2_1$	X_5^+	M_3^+	R_5^-	245
$[C(NH_2)_3]Cr(HCOO)_3$	$Pna2_1$	X_5^+	M_3^+	R_5^-	548
$[NH_3NH_2]Mn(HCOO)_3$	$Pna2_1$	X_5^+	M_2^+	R_5^-	449
$[NH_3NH_2]Zn(HCOO)_3$	$Pna2_1$	X_5^+	M_2^+	R_5^-	449
$[EtNH_3]Mn(HCOO)_3$	$Pna2_1$	X_5^+	M_2^+	R_5^-	243
$[(CH_2)_2NH_2]Mn(N_3)_3$	$P2_1$	M_5^+	M_2^-		293
$[PrPEt_3]Mn[N(CN)_2]_3$	$P2_12_12_1$	X_5^-	M_2^-	R_5^-	313
$[MeOCH_2PEt_3]Mn[N(CN)_2]_3$	$P2_12_12_1$	X_5^-	M_2^-	R_5^-	313

ter. This is unsurprising, as multipolar order is a very wide term and covers a large range of distortions and columnar shifts provide useful X- and M-point modes. Consequently, molecular substitution on one site (A or X) is sufficient to increase the number of polar coupling schemes and both purely A-site substituted perovskites (*e.g.* the organic halide perovskites) and purely X-site substituted ones (*e.g.* Prussian blue analogues) may theoretically exhibit polar ground states.

This type of analysis can be used to rationalise the emergence of polarisation in a number of acentric molecular perovskites reported in literature. Table 5.2 lists molecular perovskites known to adopt noncentrosymmetric structures along with the irreps responsible for the inversion symmetry breaking. The first two systems are now discussed in detail. To aid visualisation, 2D versions of the distortion modes are given in Fig. 5.5, where the loss of two-fold rotation points equates to the loss of inversion centres in 3D.

The first example is the formate perovskite $NH_4Cd(HCOO)_3$, which was synthesised several decades ago, and recently revisited for its electric properties.[250,254]

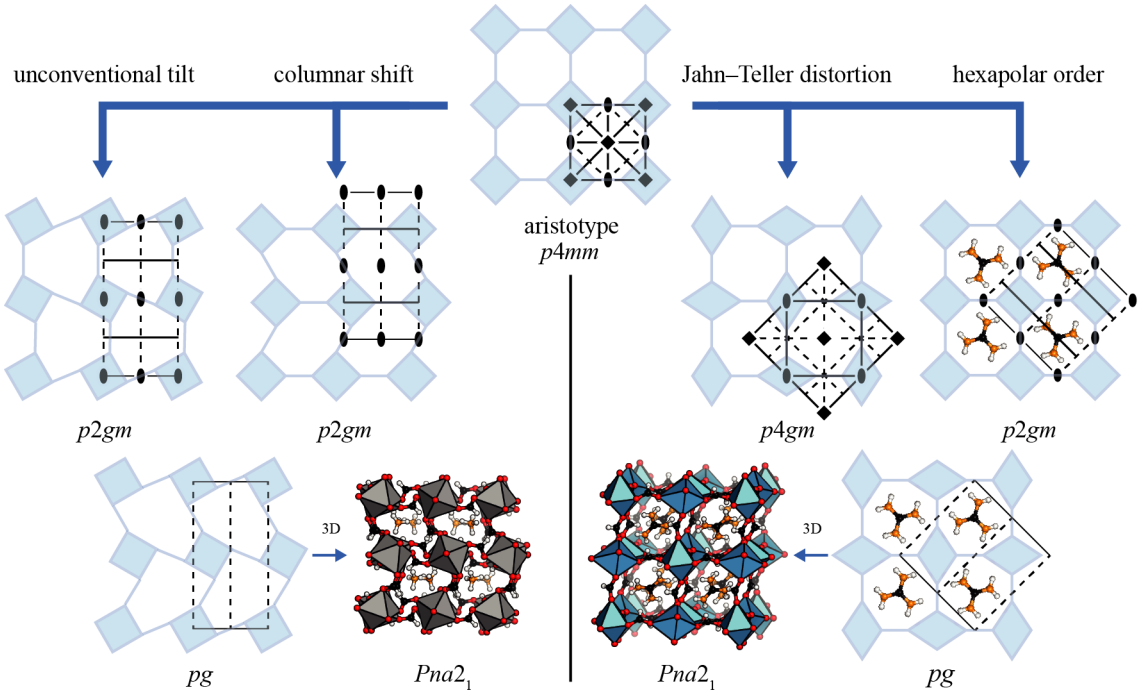


Figure 5.5: Inversion symmetry breaking in 2D molecular perovskites. Left: both unconventional tilting and columnar shifts yield the plane group $p2gm$, but with distinct origins. If combined as superimposed primary order parameters, the resulting plane group is pg, which lacks two-fold rotation points (2D analogue of centres of symmetry) and can therefore be considered to be polar. This scenario corresponds to a 2D projection of $NH_4Cd(HCOO)_3$, which crystallises in $Pna2_1$. Right: a zone-boundary Jahn-Teller distortion lowers the symmetry to $p4gm$, whereas the antiferrohexapolar order leads to $p2gm$. As before, the two distortions may couple to generate the polar plane group pg. This is a 2D version of the acentric symmetry of $[C(NH_2)_3]Cu(HCOO)_3$.

It is a rare example of a formate perovskite with a *syn–anti* binding mode and contains a considerable planar shift alternating along **c**, transforming as the irrep X_5^+. The structure also supports an unconventional tilt that forms a basis for X_5^-. The superimposition of these two distortions conserves parity and for appropriate choices of the crystal momenta, the polar space group $Cmc2_1$ ensues. Addition of the conventional in-phase tilting (M_2^+) also present in $NH_4Cd(HCOO)_3$ yields the correct space group $Pna2_1$. Despite the fact that three order parameters are needed to fully account for the observed symmetry, the shift (X_5^+) and unconventional tilt (X_5^-) are sufficient to drive the polarity.

The second example is $[C(NH_2)_3]Cu(HCOO)_3$, which also crystallises in $Pna2_1$. As has already been discussed, the polarity is a corollary of the C-type Jahn-Teller distortion and the orientation of the hexapolar guanidinium cation.[268,485] The JT distortion transforms as M_3^+, whereas the multipole moment couches two order parameters: the quadrupolar order (orientation of the plane normal), forming a basis for the X_5^+ irrep, and the hexapolar order (orientation around the three-fold axis), transforming as a R_4^- or R_5^-. The precise R-point primary order parameter considered in the coupling scheme is arbitrary,* but since the large a^- tilt also present in $[C(NH_2)_3]Cu(HCOO)_3$ is represented by R_5^-, it is a sensible choice. Hence, the fourth-order coupling of M_3^+, X_5^+ and R_5^- accounts for the polar $Pna2_1$ symmetry.

5.5 Propolar perovskites

The ultimate goal of distortion–symmetry relationships is the ability to identify as-yet unrealised compounds with the desired symmetry and thereby potential functionality. The analysis of the pre-existing polar molecular perovskites revealed the utility of Jahn-Teller distortions and multipolar A-site order as ingredients within a hybrid improper coupling scheme. Importantly, these degrees of freedom are more amenable to synthetic control than framework distortions and so may be of practical use as design elements in the search for new ferroelectrics. Indeed, the previous Chapter aimed to develop an understanding of how to control JT distortions in molecular perovskites. This Section explores "propolar" materials, *i.e.* compounds where the addition of either orbital order or a multipole moment is sufficient to

*The decomposition indicated that either R_4^- or R_5^- can act as a primary order parameter and it was verified that whichever is chosen, the other will appear as a secondary order parameter.

break the macroscopic inversion symmetry.

C-type orbital order appears to be the predominant arrangement adopted by JT-distorted molecular perovskites,[245,444,549] and since it forms a basis for the M_3^+ irrep, propolar perovskites must provide required distortions at the R- and X-points in reciprocal space. The ubiquitous conventional a^- tilts transform as R_5^-, whereas planar columnar shifts transform as X_5^+, so systems exhibiting these two distortion modes would be suitable propolar candidates. As a^- tilting is highly prevalent, the problem is effectively reduced to identifying appropriately shifted perovskites that may be able to support a Jahn-Teller distortion. At least two molecular perovskites satisfying this criterion can be found. Firstly, the recently reported hypophosphite perovskite [Trz]Mn(H_2PO_2)$_3$ (Trz = 1,2,4-triazolium)[284] contains the required tilt and shift and consequently adopts the space group $P2_1/c$. Addition of the *C*-type orbital order with the appropriate order parameter direction would lower the symmetry to the polar subgroup $P2_1$. Secondly, the formate-based [HIm]Mn(HCOO)$_3$ (HIm = imidazole, $C_3N_2H_4$) harbours the same distortion modes as above and the addition of a JT distortion is likely to yield polarity.[246] In both cases, substitution of Mn^{2+} for Cu^{2+} might reasonably be expected to drive hybrid improper ferroelectricity—a prediction that can be tested experimentally.

The choice of A-site cations with suitable multipole moments is another degree of freedom over which the synthetic chemist has considerable control. Zone-boundary dipolar and quadrupolar orderings transform as irreps with opposite signs with respect to the inversion parity [Table 5.1] and therefore, incorporating a cation with both a dipole and quadrupole moment—*e.g.* hydrazinium, imidazolium, or

methylammonium—substantially enhances the number of improper polar couplings. Steric considerations reduce the temperatures required for ordering of large cations and design rules for quadrupolar order are starting to emerge.[485] Hence, judicious choice of a molecular cation with the correct type of multipole moment may be another useful design element when engineering hybrid improper ferroelectricity.

The strategy for predicting polar systems driven by multipolar order can be illustrated by considering a conventional perovskite with the space group *Pnma* as a model system. This represents the most prevalent symmetry of conventional perovskites,[122] and while it is not yet clear what crystal symmetry—if any—is especially prominent amongst molecular perovskites, the argument developed here can be adapted to other structures. The *Pnma* space group symmetry in conventional perovskites is driven by the $a^+b^-b^-$ tilt pattern, which comprises the irreps M_2^+ and R_5^-. In addition, an antiferroelectric A-site cation displacement (X_5^-) appears as a secondary order parameter. Therefore, quadrupolar A-site order transforming as either of the R_5^+ or X_5^+ irreps may provide the required coupling with the octahedral rotations (R_5^-) or anti-polar distortions (X_5^-) present in the *Pnma* structure. Alternatively, dipolar order belonging to M_3^- or M_5^- could couple to the octahedral rotations at the M-point (M_2^+). Consequently, a molecular cation with both a dipole and quadrupole moment, enclosed in a *Pnma* perovskite, is likely to drive hybrid improper ferroelectricity provided that the dipole moment orders at the M-point (or, trivially, Γ) or the quadrupole moment orders at the X- or R-point. Similar arguments can easily be constructed for any other crystal symmetry.

5.6 Implications

This study has used representation theory to demonstrate a profound augmentation of the number of polar coupling schemes in molecular perovskites relative to the corresponding oxide materials. Notably, global lifting of the inversion symmetry cannot be achieved by a hybrid improper mechanism in simple conventional perovskites, whereas it is perfectly feasible in the molecular analogues. The underlying rationale for this discrepancy is the unconventional degrees of freedom in molecular perovskites enabled by the introduction of polyatomic species. In particular, the possibilities of ordered multipole moments from aspherical cations and columnar shifts are conducive to the emergence of polarisation. The general rules developed here also enable the identification of several propolar perovskites, where the addition of a Jahn-Teller distortion is highly likely to break the inversion symmetry.

However, the elucidation of distortion–symmetry relationships is only one step in the process of rational materials design. As highlighted throughout the Thesis, there is a need for synthetic control over the accessible distortions and this presents one of the greatest challenges in the informed development of ferroelectrics. As HIF relies on the presence of several distortion modes with particular order parameter directions, simply adding the correct distortions is not necessarily sufficient. Naturally, these problems also arise within the conventional tilt engineering research; for example, the attempt to prepare a polar Ruddlesden-Popper oxyfluoride indeed resulted in local polarisation, but with antiferroelectric alignment.[550] Nevertheless, one might anticipate that the results presented here will provide a valuable start-

ing point for theoretical predictions of stable structures with acentric space groups, which may subsequently serve as sensible synthetic targets. It should also be emphasised that polarity does not necessarily imply ferroelectricity, as the latter requires the polarisation to be switchable by reversal of an external electric field; a feature that in general has to be tested experimentally.

A further point that should be addressed is the attainable values of the polarisation in molecular materials relative to inorganic oxides. Polarisation (or, more correctly, polarisation *density*) is defined as

$$\mathbf{P} = \frac{q \times \mathbf{d}}{V}, \tag{5.3}$$

where q is the magnitude of the charges, $\mathbf{d}$ is their separation and V is the volume element. Therefore, the substantially lower charges in molecular perovskites—usually $A^{+}B^{2+}X_3^{-}$—relative to those possible in ceramic materials—where B^{6+} is realisable[33]—inevitably reduce the accessible dipole moments. The larger dimensions of molecular frameworks present a further disadvantage in the search for materials with high values of polarisation. As an illustration, the calculated magnitude of the polarisation in $[C(NH_2)_3]Cu(HCOO)_3$ is $0.37\,\mu C\,cm^{-2}$, which can be compared to $\sim 20\,\mu C\,cm^{-2}$ in $BaTiO_3$.[268,551] However, the spacious nature of coordination polymers allows larger ion displacements than in dense ceramics, which enhances the magnitude of the dipole moment and thus the polarisation. By way of example, the diamondoid framework $Cd(CN)_2$ exhibits an off-centring of the Cd^{2+} cation of nearly 1 Å, creating a local dipole larger than that of $BaTiO_3$.[551,552] If this tendency for large cation displacements can be exploited, it may provide a mechanism to

enhance the polarisation of molecular frameworks. Furthermore, the application of external pressure can augment the polarisation of metal formate perovskites by up to more than 300% relative to ambient values.[254,262,553]

In addition, the versatility of coordination polymers and their potential for functionalisation mean that molecular perovskites can harbour combinations of properties intractable in inorganic compounds. For instance, the magnetic coupling in Prussian blue analogues, in combination with their permanent porosity, has enabled the creation of materials with humidity-induced magnetic pole inversions.[554] In theory, the creation of similar couplings to ferroelectric functionality is not outside the realms of possibility. Furthermore, the merit of multipolar ordering patterns in the generation of polarity may be used to devise ferroelectric materials susceptible to the effect of external strain fields. To summarise, the diverse chemistry of molecular perovskites results in considerable potential for the design of multifunctional ferroelectric materials.

Chapter 6

Outlook

As expected, many of the concepts developed for conventional perovskites can be translated onto molecular perovskites. Yet in doing so, it is necessary to include the additional structural degrees of freedom enabled by the presence of molecular species. This is illustrated by columnar shifts; these phonon modes are intractable in ceramic materials and—by virtue of their RUM character—play a role very similar to that of tilting in conventional perovskites [Chapter 3]. Notably, they frequently constitute soft modes and so may drive phase transitions by condensation and are also predicted to enhance the propensity for NTE behaviour. Furthermore, molecular substitution of the perovskite structure can alter the nature of pre-existing (conventional) degrees of freedom. Indeed, Jahn-Teller distortions are realisable in both inorganic and molecular perovskites, yet manifest very differently in the two materials [Chapter 4]. For example, molecular perovskites show a higher propensity for dilution-induced orbital disorder than their inorganic counterparts. Conversely, disordered states cannot be thermally accessed in contrast to the canonical orbitally active ceramic perovskites. Here, the primary interest in both columnar shifts and orbital order stems from their effect on symmetry. The expanded toolbox of symmetry-breaking distortions in molecular perovskites facilitates global inversion symmetry breaking of the aristotype structure [Chapter 5]. It is hoped that this Thesis has contributed to an enhanced understanding of the fundamental chemistry of molecular perovskites by identifying the structural consequences of unconventional degrees of freedom.

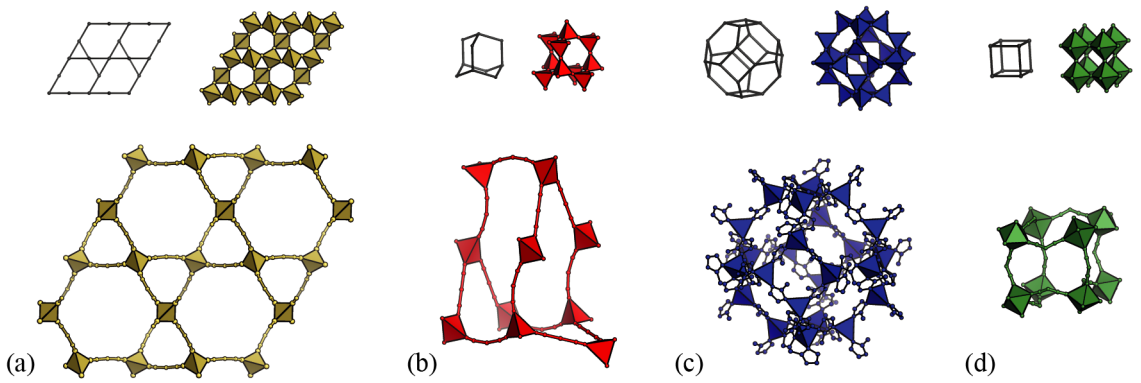


Figure 6.1: Some mineralomimetic systems. (a) β-quartz and $Zn[Au(CN)_2]_2$,[555,556] (b) cristobalite and $[NEt_4]Ag_3(CN)_4$,[557,558] (c) sodalite and ZIF-8,[559,560] and (d) perovskite and a dicyanamide perovskite.[309,561] All systems are depicted to scale and any extra-framework cations have been omitted.

However, molecular perovskites are far from the sole class of coordination polymers with mineral topologies. In fact, they represent only a subclass of so-called "mineralomimetic" systems, which encompasses a wide range of diverse compounds [Fig. 6.1].[354] Another obvious example is the family of zeolitic imidazolate frameworks (ZIFs), where the similar binding geometries of the imidazolate and oxide anions are exploited to generate large metal–organic frameworks with zeolite topologies.[560,562] Moreover, numerous molecular analogues of SiO_2 exist, often—but not necessarily—featuring some extent of interpenetration.[563,564] By way of illustration, the isostructural $Zn(CN)_2$ and $Cd(CN)_2$ are stoichiometrically identical to silica and crystallise as doubly interpenetrated cristobalite networks (diamondoid topology).[354,563–565] Single frameworks of the latter can be synthesised *via* the inclusion of guest molecules and this gives access to a wider range of mineral-like crystal structures, including α-cristobalite, β-cristobalite and α-tridymite (Lonsdaleite topology).[566,567] Substantially larger silica analogues also exist and, here, the dicyanometallate anion has established itself as a particularly versatile ligand.[318,568,569]

The α-polymorph of $Zn[Au(CN)_2]_2$ crystallises as a six-fold interpenetrated β-quartz network, whereas the β-polymorph is homologous to cristobalite with five-fold interpenetration.[570] These families of molecular minerals also exhibit unconventional degrees of freedom that are instrumental to the structural and functional responses. This concluding Chapter aims to place the results developed throughout the Thesis in the context of mineralomimetic structures more generally.

Columnar shifts and unconventional tilting constitute rigid unit modes, which are supported by many inorganic materials besides perovskites. Indeed, these phonon modes were first studied in silicate frameworks and it is unsurprising that many molecular silicate analogues exhibit their own version of unconventional RUMs. By way of example, analysis of the dynamical matrix allowed for identification of translational RUMs in the cristobalite-like $Zn(CN)_2$, similarly to the study undertaken in Chapter 3.[350] Phonon modes corresponding to unconventional tilts are also present in $Zn(CN)_2$ and due to their negative Grüneisen parameters, they are likely a contributing factor to the observed negative thermal expansion, in conjunction with conventional tilting modes.[450,451] This is again analogous to the results regarding shifts in molecular perovskites. These examples bear testimony to the observation that the introduction of polyatomic species in a framework structure enhances the number of RUMs.

Rotational degrees of freedom of low-symmetry moieties are another very important and diverse class of distortion modes. Cooperative Jahn-Teller effects correspond to orientational order on the B-site and so can be considered a subclass of this degree of freedom. Rotational modes are generally more prominent in molecu-

lar frameworks, as inorganic motifs tend to be spherically symmetric. Orientational order of polyatomic A-site cations plays a vital role for the functional response of numerous molecular minerals and has already been mentioned briefly. For example, the rotational motion of methylammonium in $(CH_3NH_3)PbI_3$ influences the charge carrier lifetime; a crucial aspect of the photovoltaic performance of perovskite solar cells.[178–182] Moreover, the presence of polar rotors in cyanoelpasolites such as $(HIm)_2K[Fe(CN)_6]$ imparts thermally switchable dielectric properties, since the rotational motion of the A-site cation progressively freezes upon cooling.[223,571–573]

Additionally, the decoration of the X-site with cylindrically asymmetric anions opens up for anion reorientational motion. This is of particular currency for ZIFs and has been extensively studied in the topical ZIF-8; a porous material with the **SOD** topology.[560] Counterintuitively, it absorbs larger molecules than what was deemed possible due to the ability of the imidazolate to rotate and thereby increase the pore window ("the swing effect").[574–577] Judicious functionalisation of the imidazolate anion allows for control over the extent of linker rotation and hence the dimensions of the pore window, which is strongly relevant for applications within gas storage, separation and catalysis.[578] Imidazolate also features as an anion in cristobalite-like $Cd(Im)_2$ and the linker reorientation is responsible for the anisotropic and nonlinear thermal response.[579] Another dipolar ligand is dicyanamide and its order–disorder processes likely contribute to the dielectric anomaly observed on heating in the perovskite $[Pr_4N]Mn[N(CN)_2]_3$.[315] In part, the interest in orientational degrees of freedom stems from the exciting prospect of controlling and tuning of the properties by means of electric fields.[580]

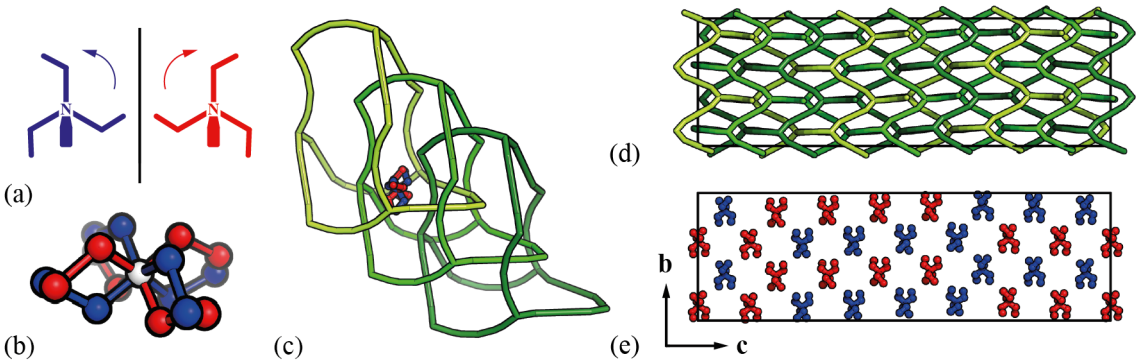


Figure 6.2: Chiral density waves in $[NEt_4]Ag_3(CN)_4$. (a)–(b) The two enantiomeric forms of NEt_4 shown in red and blue, with hydrogen atoms omitted. (c) The position of NEt_4^+ within the triply-interpenetrated $Ag_3(CN)_4^-$ framework, where different shades of green are used for distinct frameworks. The incommensurate modulation of (d) the framework and (e) the chiral guest cations. Figure adapted with permission from J. A. Hill, C. E. Kristensen, and A. L. Goodwin, *Phys. Rev. Lett.*, **119**, 115501 (2017).[558] Copyright 2017 by the American Physical Society.

The continuously variable Jahn-Teller distortions—specified by phase angles—are conceptually related to conformational changes of a molecule upon enclosure—specified by torsion angles. For instance, the torsion angle of methylammonium has been proposed to deviate from the ideal value of 180°,[183] which is reminiscent of the unusual phase angles of JT distortions emerging from the MC models developed in Chapter 4. Another example of confinement-induced conformational changes is $[PPN]B[Au(CN)_2]_3$ (B^{2+} = Mn or Cd), where a phase transition is driven by a change in the tilt system and a reorganisation of the phenyl rings in PPN [Fig. 1.17].[322] Furthermore, enclosure into a framework hinders the free rotation of sizeable molecules, which may prevent interconversion between enantiomeric forms and therefore cause permanent chirality.[581,582] In the cristobalite-like framework $[NEt_4]Ag_3(CN)_4$, this mechanism leads to an incommensurate chiral density wave of the confined NEt_4^+ cation anharmonically coupled to a distortion of the framework [Fig. 6.2].[558] Given the vast range of available molecular guest species, more intriguing examples of conformational and configurational flexibility can be anticipated in the future.

The focus throughout this Thesis has been on degrees of freedom available to discrete topologies; however, interconversion between different structure types is sometimes feasible and is worth mentioning. The formate-bridged molecular perovskite $[EtNH_3]Cu(HCOO)_3$ crystallises in $Pna2_1$ at ambient conditions, but undergoes a thermal reconstructive phase transition to the diamondoid topology with the space group $P2_12_12_1$.[483] The diamondoid phase is retained on cooling, but reverts to perovskite upon application of external pressure. It can be noted that reconstructive phase transitions are comparatively scarce in coordination polymers, with only a few known examples.[583–586] However, one may speculate whether such topological interconversions are more common in metal–molecular frameworks, as a result of the weaker coordination bonds relative to the strong M–O bonds in minerals.

To conclude, mineralomimetic coordination polymers sustain a diverse range of intriguing degrees of freedom inaccessible to conventional ceramics and these distortions influence both the structural chemistry and the functional response. As a result, an understanding of the degrees of freedom and their consequences is imperative for the ultimate aim of controlling properties through synthetic materials design—whether polarity or absorption capacity or photovoltaic performance. The greatest challenge for the field of targeted materials design is likely to be the control of the distortions and further research aimed towards the development of clear design rules would be highly beneficial. The focus here has been on structural degrees of freedom and their interdependence; yet these structural deformations are also likely to be coupled to the magnetic interactions.

Bibliography

[1] U. Scherf and E. J. W. List, *Adv. Mater.*, 2002, **14**, 477–487.

[2] Y. Jiao, F. Zhang, M. Grätzel and S. Meng, *Adv. Funct. Mater.*, 2013, **23**, 424–429.

[3] C. B. Aakeröy and A. S. Borovik, *Coord. Chem. Rev.*, 1999, **183**, 1.

[4] N. W. Thomas, *Acta Crystallogr. B Struct. Sci.*, 1989, **45**, 337–344.

[5] M. T. Dove, M. Gambhir, K. D. Hammonds, V. Heine and A. K. A. Pryde, *Phase Transitions*, 1996, **58**, 121–143.

[6] M. J. Pitcher, P. Mandal, M. S. Dyer, J. Alaria, P. Borisov, H. Niu, J. B. Claridge and M. J. Rosseinsky, *Science*, 2015, **347**, 420–424.

[7] J. S. O. Evans, *J. Chem. Soc. Dalton Trans.*, 1999, 3317–3326.

[8] M. De Graef and M. E. McHenry, *Structure of materials: an introduction to crystallography, diffraction and symmetry*, Cambridge University Press, Cambridge, 2012.

[9] V. M. Goldschmidt, *Naturwissenschaften*, 1926, **14**, 477–485.

[10] T. F. W. Barth and E. Posnjak, *Z. Kristallogr.*, 1934, **88**, 265–270.

[11] P. M. Woodward, *Acta Crystallogr. B Struct. Sci.*, 1997, **53**, 32–43.

[12] C. J. Howard and H. T. Stokes, *Acta Crystallogr. B Struct. Sci.*, 1998, **54**, 782–789.

[13] R. H. Buttner and E. N. Maslen, *Acta Crystallogr. B Struct. Sci.*, 1992, **48**, 644–649.

[14] R. Comes, M. Lambert and A. Guinier, *Solid State Commun.*, 1968, **6**, 715–719.

[15] S. N. Ruddlesden and P. Popper, *Acta Crystallogr.*, 1957, **10**, 538–540.

[16] R. E. Cohen, *Nature*, 1992, **358**, 136–138.

[17] J. M. Rondinelli and C. J. Fennie, *Adv. Mater.*, 2012, **24**, 1961–1968.

[18] J. G. Bednorz and K. A. Müller, *Rev. Mod. Phys.*, 1988, **60**, 585–600.

[19] Y. Maeno, H. Hashimoto, K. Yoshida, S. Nishizaki, T. Fujita, J. G. Bednorz and F. Lichtenberg, *Nature*, 1994, **372**, 532–534.

[20] K.-I. Kobayashi, T. Kimura, H. Sawada, K. Terakura and Y. Tokura, *Nature*, 1998, **395**, 677–680.

[21] C. N. R. Rao and A. K. Cheetham, *Science*, 1996, **272**, 369–370.

[22] A. A. Bokov, N. P. Protsenko and Z.-G. Ye, *J. Phys. Chem. Solids*, 2000, **61**, 1519–1527.

[23] J. B. Goodenough, *Phys. Rev.*, 1955, **100**, 564–573.

[24] S. Yano, D. Louca, J. C. Neuefeind, J.-Q. Yan, J.-S. Zhou and J. B. Goodenough, *Phys. Rev. B*, 2014, **90**, 214111.

[25] M. Azuma, K. Oka and K. Nabetani, *Sci. Technol. Adv. Mater.*, 2015, **16**, 034904.

[26] M. Jansen and H. P. Letschert, *Nature*, 2000, **404**, 980–982.

[27] U. Robels, R. Herbiet and G. Arlt, *Ferroelectrics*, 1989, **93**, 95–103.

[28] G. Shirane, K. Suzuki and A. Takeda, *J. Phys. Soc. Jpn.*, 1952, **7**, 12–18.

[29] M. T. Anderson, K. B. Greenwood, G. A. Taylor and K. R. Poeppelmeier, *Prog. Solid St. Chem.*, 1993, **22**, 197–233.

[30] G. M. McNally, Á. M. Arévalo-López, P. Kearins, F. Orlandi, P. Manuel and J. P. Attfield, *Chem. Mater.*, 2017, **29**, 8870–8874.

[31] P. D. Battle, M. A. Green, N. S. Laskey, J. E. Millburn, L. Murphy, M. J. Rosseinsky, S. P. Sullivan and J. F. Vente, *Chem. Mater.*, 1997, **9**, 552–559.

[32] M. S. Senn, W.-t. Chen, T. Saito, S. García-Martín, J. P. Attfield and Y. Shimakawa, *Chem. Mater.*, 2014, **26**, 4832–4837.

[33] M. C. Knapp and P. M. Woodward, *J. Solid State Chem.*, 2006, **179**, 1076–1085.

[34] G. King and P. M. Woodward, *J. Mater. Chem.*, 2010, **20**, 5785–5796.

[35] S. Vasala and M. Karppinen, *Prog. Solid St. Chem.*, 2015, **43**, 1–36.

[36] E. Solana-Madruga, Á. M. Arévalo-López, A. J. Dos Santos-García, E. Urones-Garrote, D. Ávila-Brande, R. Sáez-Puche and J. P. Attfield, *Angew. Chem. Int. Ed.*, 2016, **55**, 9340–9344.

[37] S. G. Ebbinghaus, H.-P. Abicht, R. Dronskowski, T. Müller, A. Reller and A. Weidenkaff, *Prog. Solid St. Chem.*, 2009, **37**, 173–205.

[38] H. Kermoun and L. Benziada-Taïbi, *J. Flourine Chem.*, 1999, **99**, 119–122.

[39] M. Yang, J. Oró-Solé, J. A. Rodgers, A. Belén Jorge, A. Fuertes and J. P. Attfield, *Nat. Chem.*, 2011, **3**, 47–52.

[40] M. Retuero, C. de la Calle, M. J. Martínez-Lope, F. Porcher, K. Krezhov, N. Menéndez and J. A. Alonso, *J. Solid State Chem.*, 2012, **185**, 18–24.

[41] J. P. Attfield, *Solid State Sci.*, 2006, **8**, 861–867.

[42] T. Terai, T. Murata and T. Kakeshita, *J. Magn. Magn. Mater.*, 2007, **310**, 768–770.

[43] F. Millange, V. Caignaert, B. Domengès, B. Raveau and E. Suard, *Chem. Mater.*, 1998, **10**, 1974–1983.

[44] B. Raveau and M. Motin Seikh, *Z. Anorg. Allg. Chem.*, 2015, **641**, 1385–1394.

[45] D. E. Cox and A. W. Sleight, *Acta Crystallogr. B Struct. Cryst. Cryst. Chem.*, 1979, **35**, 1–10.

[46] I. Yamada, K. Takata, N. Hayashi, S. Shinohara, M. Azuma, S. Mori, S. Muranaka, Y. Shimakawa and M. Takano, *Angew. Chem. Int. Ed.*, 2008, **47**, 7032–7035.

[47] M. S. Senn, J. P. Wright and J. P. Attfield, *Nature*, 2012, **481**, 173–176.

[48] R. Kajimoto, H. Yoshizawa, Y. Tomioka and Y. Tokura, *Phys. Rev. B*, 2001, **63**, 212407.

[49] P. Karen, P. M. Woodward, J. Lindén, T. Vogt, A. Studer and P. Fischer, *Phys. Rev. B*, 2001, **64**, 214405.

[50] M. Hervieu, S. Malo, O. Perez, P. Beràn, C. Martin, G. Baldinozzi and B. Raveau, *Chem. Mater.*, 2003, **15**, 523–527.

[51] A. J. Williams and J. P. Attfield, *Phys. Rev. B*, 2005, **72**, 024436.

[52] S. Larochelle, A. Mehta, N. Kaneko, P. K. Mang, A. F. Panchula, L. Zhou, J. Arthur and M. Greven, *Phys. Rev. Lett.*, 2001, **87**, 095502.

[53] J. van den Brink and D. I. Khomskii, *J. Phys.: Condens. Matter*, 2008, **20**, 434217.

[54] A. A. Taskin and Y. Ando, *Phys. Rev. Lett.*, 2007, **98**, 207201.

[55] N. C. Bristowe, J. Varignon, D. Fontaine, E. Bousquet and P. Ghosez, *Nat. Commun.*, 2015, **6**, 6677.

[56] A. Chroneos, R. V. Vovk, I. L. Goulatis and L. I. Goulatis, *J. Alloys Compd.*, 2010, **494**, 190–195.

[57] T. Whittle, W. R. Brant, J. R. Hester, Q. Gu and S. Schmid, *Dalton Trans.*, 2017, **46**, 7253–7260.

[58] F. W. Poulsen, *Solid State Ionics*, 2000, **129**, 145–162.

[59] F. Beech, S. Miraglia, A. Santoro and R. S. Roth, *Phys. Rev. B*, 1987, **35**, 8778–8781.

[60] B. A. Richert and R. E. Allen, *J. Phys.: Condens. Matter*, 1989, **1**, 9451–9455.

[61] D. M. Smyth, *Annu. Rev. Mater. Sci.*, 1985, **15**, 329–357.

[62] S. Stølen, E. Bakken and C. E. Mohn, *Phys. Chem. Chem. Phys.*, 2006, **8**, 429–447.

[63] H. A. Jahn and E. Teller, *Proc. R. Soc. A.*, 1937, **161**, 220–235.

[64] I. B. Bersuker, *Chem. Rev.*, 2001, **101**, 1067–1114.

[65] C. E. Housecroft and A. G. Sharpe, *Inorganic Chemistry*, Pearson, Harlow, 2012.

[66] H. A. Bethe, *Ann. Phys.*, 1929, **3**, 133–206.

[67] F. Hund, *Z. Phys.*, 1925, **33**, 855–859.

[68] J. Hemberger, H.-A. Krug von Nidda, V. Fritsch, J. Deisenhofer, S. Lobina, T. Rudolf, P. Lunkenheimer, F. Lichtenberg, A. Loidl, D. Bruns and B. Büchner, *Phys. Rev. Lett.*, 2003, **91**, 066403.

[69] G. R. Blake, T. T. M. Palstra, Y. Ren, A. A. Nugroho and A. A. Menovsky, *Phys. Rev. Lett.*, 2001, **87**, 245501.

[70] J. K. Burdett, *Inorg. Chem.*, 1981, **20**, 1959–1962.

[71] J. H. Van Vleck, *J. Chem. Phys.*, 1939, **7**, 72–84.

[72] J. B. Goodenough, *Annu. Rev. Mater. Sci.*, 1998, **28**, 1–27.

[73] M. A. Halcrow, *Chem. Soc. Rev.*, 2013, **42**, 1784–1795.

[74] J. Rodríguez-Carvajal, M. Hennion, F. Moussa, A. H. Moudden, L. Pinsard and A. Revcolevschi, *Phys. Rev. B*, 1998, **57**, R3189–3192.

[75] T. A. Mellan, F. Corà, R. Grau-Crespo and S. Ismail-Beigi, *Phys. Rev. B*, 2015, **92**, 085151.

[76] J. Kanamori, *J. Appl. Phys.*, 1960, **31**, 14–23.

[77] G. A. Gehring and K. A. Gehring, *Rep. Prog. Phys.*, 1975, **38**, 1–89.

[78] M. D. Towler and R. Dovesi, *Phys. Rev. B*, 1995, **52**, 10150–10159.

[79] E. O. Wollan and W. C. Koehler, *Phys. Rev.*, 1955, **100**, 545–563.

[80] F. Fauth, E. Suard, V. Caignaert, B. Domengès, I. Mirebeau and L. Keller, *Eur. Phys. J. B*, 2001, **21**, 163–174.

[81] M. A. Carpenter and C. J. Howard, *Acta Crystallogr. B Struct. Sci.*, 2009, **65**, 134–146.

[82] J. Kanamori, *J. Phys. Chem. Solids*, 1959, **10**, 87–98.

[83] P. W. Anderson, *Phys. Rev.*, 1959, **115**, 2–13.

[84] A. M. dos Santos, A. K. Cheetham, T. Atou, Y. Syono, Y. Yamaguchi, K. Ohoyama, H. Chiba and C. N. R. Rao, *Phys. Rev. B*, 2002, **68**, 064425.

[85] B. Raveau, A. Maignan, C. Martin and M. Hervieu, *Chem. Mater.*, 1998, **10**, 2641–2652.

[86] A. R. Bishop and H. Röder, *Curr. Opin. Solid State Mater. Sci.*, 1997, **2**, 244–251.

[87] A. J. Millis, R. Mueller and B. I. Shraiman, *Phys. Rev. B*, 1996, **54**, 5406–5417.

[88] A. J. Millis, P. B. Littlewood and B. I. Shraiman, *Phys. Rev. Lett.*, 1995, **74**, 5144–5147.

[89] O. S. Wenger and H. U. Güdel, *J. Chem. Phys.*, 2001, **114**, 5832–5841.

[90] P. M. M. Thygesen, C. A. Young, E. O. R. Beake, F. D. Romero, L. D. Connor, T. E. Proffen, A. E. Phillips, M. G. Tucker, M. A. Hayward, D. A. Keen and A. L. Goodwin, *Phys. Rev. B*, 2017, **95**, 174107.

[91] T. Chatterji, F. Fauth, B. Ouladdiaf, P. Mandal and B. Ghosh, *Phys. Rev. B*, 2003, **68**, 052406.

[92] M. R. Ahmed and G. A. Gehring, *J. Phys. A.: Math. Gen.*, 2005, **38**, 4047–4067.

[93] M. R. Ahmed and G. A. Gehring, *Phys. Rev. B*, 2006, **74**, 014420.

[94] M. R. Ahmed and G. A. Gehring, *Phys. Rev. B*, 2009, **79**, 174106.

[95] F. Y. Wu, *Rev. Mod. Phys.*, 1982, **54**, 235–268.

[96] J. W. Lynn, D. N. Argyriou, Y. Ren, Y. Chen, Y. M. Mukovskii and D. A. Shulyatev, *Phys. Rev. B*, 2007, **76**, 014437.

[97] S. Okamoto, S. Ishihara and S. Maekawa, *Phys. Rev. B*, 2000, **61**, 14647–14655.

[98] A. Mellergård, R. L. McGreevy and S. G. Eriksson, *J. Phys.: Condens. Matter*, 2000, **12**, 4975–4991.

[99] U. Öpik and M. H. L. Pryce, *Proc. R. Soc. A.*, 1957, **238**, 425–447.

[100] H. C. Longuet-Higgins, U. Öpik, M. H. L. Pryce and R. A. Sack, *Proc. R. Soc. A.*, 1958, **244**, 1–16.

[101] R. G. Pearson, *Proc. Natl. Acad. Sci. U.S.A*, 1975, **72**, 2104–2106.

[102] R. G. Pearson, *J. Mol. Struct.*, 1983, **103**, 25–34.

[103] L. Salem, *Chem. Phys. Lett.*, 1969, **3**, 99–101.

[104] P. S. Halasyamani, *Chem. Mater.*, 2004, **16**, 3586–3592.

[105] A. von Hippel, R. G. Breckenridge, F. G. Chesley and L. Tisza, *Ind. Eng. Chem.*, 1946, **38**, 1097–1109.

[106] M. S. Senn, D. A. Keen, T. C. A. Lucas, J. A. Hriljac and A. L. Goodwin, *Phys. Rev. Lett.*, 2016, **116**, 207602.

[107] M. M. Vijatović, J. D. Bobić and B. D. Stojanović, *Sci. Sintering*, 2008, **40**, 155–165.

[108] G. W. Watson and S. C. Parker, *J. Phys. Chem. B*, 1999, **103**, 1258–1262.

[109] I. Lefebvre, M. A. Szymanski, J. Olivier-Fourcade and J. C. Jumas, *Phys. Rev. B*, 1998, **58**, 1896–1906.

[110] L. E. Orgel, *J. Chem. Soc.*, 1959, 3815–3819.

[111] A. Walsh, D. J. Payne, R. G. Egdell and G. W. Watson, *Chem. Soc. Rev.*, 2011, **40**, 4455–4463.

[112] G. Catalan and J. F. Scott, *Adv. Mater.*, 2009, **21**, 2463–2485.

[113] P. S. Halasyamani and K. R. Poeppelmeier, *Chem. Mater.*, 1998, **10**, 2753–2769.

[114] N. A. Benedek and C. J. Fennie, *J. Phys. Chem. C*, 2013, **117**, 13339–13349.

[115] N. A. Hill, *J. Phys. Chem. B*, 2000, **104**, 6694–6709.

[116] N. A. Hill and A. Filippetti, *J. Magn. Magn. Mater.*, 2002, **242-245**, 976–979.

[117] P. M. Woodward, *Acta Crystallogr. B Struct. Sci.*, 1997, **53**, 44–66.

[118] M. T. Dove, V. Heine and K. D. Hammonds, *Mineral. Mag.*, 1995, **59**, 629–639.

[119] G. Burns and A. M. Glazer, *Space Groups for Solid State Scientists*, Academic Press, Oxford, 2013.

[120] A. M. Glazer, *Acta Crystallogr. B Struct. Cryst. Cryst. Chem.*, 1972, **28**, 3384–3392.

[121] S. Geller, *J. Chem. Phys.*, 1956, **24**, 1236–1239.

[122] M. W. Lufaso and P. M. Woodward, *Acta Crystallogr. B Struct. Sci.*, 2001, **57**, 725–738.

[123] C. J. Howard, B. J. Kennedy and P. M. Woodward, *Acta Crystallogr. B Struct. Sci.*, 2003, **59**, 463–471.

[124] F. Li, C. Song, Y. Y. Wang, B. Cui, J. Mao, J. J. Peng, S. N. Li, G. Y. Wang and F. Pan, *Sci. Rep.*, 2015, **5**, 16187.

[125] J. Chang, K. Lee, M. H. Jung, J.-H. Kwon, M. Kim and S.-K. Kim, *Chem. Mater.*, 2011, **23**, 2693–2696.

[126] D. Serrate, J. M. De Teresa and M. R. Ibarra, *J. Phys.: Condens. Matter*, 2007, **19**, 023201.

[127] M. Fiebig, T. Lottermoser, D. Meier and M. Trassin, *Nat. Rev. Mater.*, 2016, **1**, 16046.

[128] T. Mizokawa, D. I. Khomskii and G. A. Sawatzky, *Phys. Rev. B*, 1999, **60**, 7309–7313.

[129] M. v. Zimmermann, J. P. Hill, D. Gibbs, M. Blume, D. Casa, B. Keimer, Y. Murakami, Y. Tomioka and Y. Tokura, *Phys. Rev. Lett.*, 1999, **83**, 4872–4875.

[130] C. N. R. Rao and A. K. Cheetham, *Science*, 1997, **276**, 911–912.

[131] M. Kataoka, *Phys. Rev. B*, 1988, **37**, 143–149.

[132] R. Cortés-Gil, M. L. Ruiz-González, J. M. Alonso, M. García-Hernández, A. Hernando and J. M. González-Calbet, *Chem. Mater.*, 2013, **25**, 2100–2108.

[133] M. M. Vopson, *Crit. Rev. Solid State Mater. Sci.*, 2015, **40**, 223–250.

[134] S. Fusil, V. Garcia, A. Barthélémy and M. Bibes, *Annu. Rev. Mater. Res.*, 2014, **44**, 91–116.

[135] S. Dong and J.-M. Liu, *Mod. Phys. Lett. B*, 2012, **26**, 1230004.

[136] D. I. Khomskii, *Physics*, 2009, **2**, 20.

[137] N. A. Benedek and C. J. Fennie, *Phys. Rev. Lett.*, 2011, **106**, 107204.

[138] J. F. Scott, *Science*, 2007, **315**, 954–959.

[139] S. R. Batten, N. R. Champness, X.-M. Chen, J. Garcia-Martinez, S. Kitagawa, L. Öhrström, M. O'Keeffe, M. Paik Suh and J. Reedijk, *Pure & Appl. Chem.*, 2013, **85**, 1715–1724.

[140] G. Kieslich, S. Sun and A. K. Cheetham, *Chem. Sci.*, 2014, **5**, 4712–4715.

[141] G. Kieslich, S. Sun and A. K. Cheetham, *Chem. Sci.*, 2015, **6**, 3430–3433.

[142] G. Kieslich, S. Kumagai, K. T. Butler, T. Okamura, C. H. Hendon, S. Sun, M. Yamashita, A. Walsh and A. K. Cheetham, *Chem. Commun.*, 2015, **51**, 15538–15541.

[143] W. Travis, E. N. K. Glover, H. Bronstein, D. O. Scanlon and R. G. Palgrave, *Chem. Sci.*, 2016, **7**, 4548–4556.

[144] M. Becker, T. Klüner and M. Wark, *Dalton Trans.*, 2017, **46**, 3500–3509.

[145] J.-H. Lee, N. C. Bristowe, P. D. Bristowe and A. K. Cheetham, *Chem. Commun.*, 2015, **51**, 6434–6437.

[146] J. Mizusaki, K. Arai and K. Fueki, *Solid State Ionics*, 1983, **11**, 203–211.

[147] D. Sabba, H. Kumur Mulmudi, R. Ramanujam Prabhakar, T. Krishnamoorty, T. Baikie, P. P. Boix, S. Mhaisalkar and N. Mathews, *J. Phys. Chem. C*, 2015, **119**, 1763–1767.

[148] A. García-Fernández, J. M. Bermúdez-García, S. Castro-García, A. L. Llamas-Saiz, R. Artiaga, J. López-Beceiro, S. Hu, W. Ren, A. Stroppa, M. Sánchez-Andújar and M. A. Señarís-Rodríguez, *Inorg. Chem.*, 2017, **56**, 4918–4927.

[149] C. C. Stoumpos, C. D. Malliakas and M. G. Kanatzidis, *Inorg. Chem.*, 2013, **52**, 9019–9038.

[150] C. C. Stoumpos, L. Frazer, D. J. Clark, Y. S. Kim, S. H. Rhim, A. J. Freeman, J. B. Ketterson, J. I. Jang and M. G. Kanatzidis, *J. Am. Chem. Soc.*, 2015, **137**, 6804–6819.

[151] D. B. Mitzi, *J. Chem. Soc. Dalton Trans.*, 2001, 1–12.

[152] W. Ke, C. C. Stoumpos, I. Spanopoulos, L. Mao, M. Chen, M. R. Wasielewski and M. G. Kanatzidis, *J. Am. Chem. Soc.*, 2017, **139**, 14800–14806.

[153] I. Spanopoulos, W. Ke, C. C. Stoumpos, E. C. Schueller, O. Y. Kontsevoi, R. Seshadri and M. G. Kanatzidis, *J. Am. Chem. Soc.*, 2018, **140**, 5728–5742.

[154] D. Cortecchia, H. A. Dewi, J. Yin, A. Bruno, S. Chen, T. Baikie, P. P. Boix, M. Grätzel, S. Mhaisalkar, C. Soci and N. Mathews, *Inorg. Chem.*, 2016, **55**, 1044–1052.

[155] S. T. Williams, A. Rajagopal, S. B. Jo, C.-C. Chueh, T. F. L. Tang, A. Kraeger and A. K.-Y. Jen, *J. Mater. Chem. A*, 2017, **5**, 10640–10650.

[156] M. Kong, K. Liu, J. Ning, J. Zhou and H. Song, *J. Mater. Chem. A*, 2017, **5**, 19280–19288.

[157] D. Weber, *Z. Naturforsch.*, 1978, **33b**, 862–865.

[158] G. Chapius, R. Kind and H. Arend, *Phys. Status Solidi A*, 1976, **36**, 285–295.

[159] N. Lehner, K. Strobel, R. Geick and G. Heger, *J. Phys. C: Solid State Phys.*, 1975, **8**, 4096–4106.

[160] A. Kojima, K. Teshima, Y. Shirai and T. Miyasaka, *J. Am. Chem. Soc.*, 2009, **131**, 6050–6051.

[161] P. Gao, M. Grätzel and M. K. Nazeruddin, *Energy Environ. Sci.*, 2014, **7**, 2448–2463.

[162] Best Research-Cell Efficiencies, https://www.nrel.gov/pv/assets/images/efficiency-chart.png, (last accessed 2018-08-14).

[163] G. Giorgi, J.-I. Fujisawa, H. Segawa and K. Yamashita, *J. Phys. Chem. Lett.*, 2013, **4**, 4213–4216.

[164] Z. Shi, J. Guo, Y. Chen, Q. Li, Y. Pan, H. Zhang, Y. Xia and W. Huang, *Adv. Mater.*, 2017, **29**, 1605005.

[165] M. Szafrański and K. Ståhl, *J. Solid State Chem.*, 2007, **180**, 2209–2215.

[166] W.-J. Yin, T. Shi and Y. Yan, *J. Phys. Chem. C*, 2015, **119**, 5253–5264.

[167] D. Li, G. Wang, H.-C. Cheng, C.-Y. Chen, H. Wu, Y. Liu, Y. Huang and X. Duan, *Nat. Commun.*, 2016, **7**, 11330.

[168] J. Dhar, S. Sil, A. Dey, D. Sanyal and P. Pratim Ray, *J. Phys. Chem. C*, 2017, **121**, 5515–5522.

[169] H.-S. Kim, C.-R. Lee, J.-H. Im, K.-B. Lee, T. Moehl, A. Marchioro, S.-J. Moon, R. Humphry-Baker, J.-H. Yum, J. E. Moser, M. Grätzel and N.-G. Park, *Sci. Rep.*, 2012, **2**, 591.

[170] A. D. Wright, C. Verdi, R. L. Milot, G. E. Eperon, M. A. Pérez-Osorio, H. J. Snaith, F. Giustino, M. B. Johnston and L. M. Herz, *Nat. Commun.*, 2016, **7**, 11755.

[171] K. P. Ong, T. W. Goh, Q. Xu and A. Huan, *J. Phys. Chem. Lett.*, 2015, **6**, 681–685.

[172] O. J. Weber, K. L. Marshall, L. M. Dyson and M. T. Weller, *Acta Crystallogr., Sect. B: Struct. Sci., Cryst. Eng. Mater.*, 2015, **71**, 668–678.

[173] C. Eames, J. M. Frost, P. R. F. Barnes, B. C. O'Regan, A. Walsh and M. S. Islam, *Nat. Commun.*, 2015, **6**, 7497.

[174] J. Even, M. Carignano and C. Katan, *Nanoscale*, 2016, **8**, 6222–6236.

[175] M. T. Weller, O. J. Weber, P. F. Henry, A. M. Di Pumpo and T. C. Hansen, *Chem. Commun.*, 2015, **51**, 4180–4183.

[176] J.-H. Lee, N. C. Bristowe, J. H. Lee, S.-H. Lee, P. D. Bristowe, A. K. Cheetham and H. M. Jang, *Chem. Mater.*, 2016, **28**, 4259–4266.

[177] F. Brivio, J. M. Frost, J. M. Skelton, A. J. Jackson, O. J. Weber, M. T. Weller, A. R. Goñi, A. M. A. Leguy, P. R. F. Barnes and A. Walsh, *Phys. Rev. B*, 2015, **92**, 144308.

[178] B. Kang and K. Biswas, *J. Phys. Chem. C*, 2017, **121**, 8319–8326.

[179] A. M. A. Leguy, J. M. Frost, A. P. McMahon, V. Garcia Sakai, W. Kockelmann, C. Law, X. Li, F. Foglia, A. Walsh, B. C. O'Regan, J. Nelson, J. T. Cabral and P. R. F. Barnes, *Nat. Commun.*, 2015, **6**, 7124.

[180] C. Motta, F. El-Mellouhi and S. Sanvito, *Phys. Rev. B*, 2016, **93**, 235412.

[181] K. Drużbicki, R. S. Pinna, S. Rudić, M. Jura, G. Gorini and F. Fernandez-Alonso, *J. Phys. Chem. Lett.*, 2016, **7**, 4701–4709.

[182] J. S. Bechtel, R. Seshadri and A. Van der Ven, *J. Phys. Chem. C*, 2016, **120**, 12403–12410.

[183] P. S. Whitfield, N. Herron, W. E. Guise, K. Page, Y. Q. Cheng, I. Milas and M. K. Crawford, *Sci. Rep.*, 2016, **6**, 35685.

[184] E. J. M. Vertelman, T. T. A. Lummen, A. Meetsma, M. W. Bouwkamp, G. Molnar, P. H. M. van Loosdrecht and P. J. van Konigsbruggen, *Chem. Mater.*, 2008, **20**, 1236–1238.

[185] M. Verdaguer, A. Bleuzen, V. Marvaud, J. Vaissermann, M. Seuleiman, C. Desplanches, A. Scuiller, C. Train, R. Garde, G. Gelly, C. Lomenech, I. Rosenman, P. Veillet, C. Cartier and F. Villain, *Coord. Chem. Rev.*, 1999, **190-192**, 1023–1047.

[186] F. Grandjean, L. Samain and G. J. Long, *Dalton Trans.*, 2016, **45**, 18018–18044.

[187] J. F. Keggin and F. D. Miles, *Nature*, 1936, **137**, 577–578.

[188] H. J. Buser, D. Schwarzenbach, W. Petter and A. Ludi, *Inorg. Chem.*, 1977, **16**, 2704–2710.

[189] S. Ganguli and M. Bhattacharya, *J. Chem. Soc. Faraday Trans.*, 1983, **79**, 1513–1522.

[190] S. Adak, L. L. Daemen, M. Hartl, D. Williams, J. Summerhill and H. Nakotte, *J. Solid State Chem.*, 2011, **184**, 2854–2861.

[191] K. W. Chapman, P. J. Chupas and C. J. Kepert, *J. Am. Chem. Soc.*, 2006, **128**, 7009–7014.

[192] A. Peeters, P. Valvekens, R. Ameloot, G. Sankar, C. E. A. Kirschhock and D. E. De Vos, *ACS Catal.*, 2013, **3**, 597–607.

[193] D. Aguilà, Y. Prado, E. S. Koumousi, C. Mathonière and R. Clérac, *Chem. Soc. Rev.*, 2016, **45**, 203–224.

[194] O. Sato, T. Iyoda, A. Fujishima and K. Hashimoto, *Science*, 1996, **272**, 704–705.

[195] A. A. Karyakin, *Electroanalysis*, 2001, **13**, 813–819.

[196] J. Long, Y. Guari, C. Guérin and J. Larionova, *Dalton Trans.*, 2016, **45**, 17581–17587.

[197] S. Mukherjee, B. R. Rao, B. Sreedhar, P. Paik and C. R. Patra, *Chem. Commun.*, 2015, **51**, 7325–7328.

[198] H.-J. Buser, G. Ron and A. Ludi, *J. Chem. Soc. Faraday Trans.*, 1974, 2473–2474.

[199] T. Krah, N. Suaud, A. Zanchet, V. Robert and N. Ben Amor, *Eur. J. Inorg. Chem.*, 2012, 5777–5783.

[200] J. Roque, E. Reguera, J. Balmaseda, J. Rodríguez-Hernández, L. Reguera and L. F. del Castillo, *Micropor. Mesopor. Mater.*, 2007, **103**, 57–71.

[201] L. Reguera, C. P. Krap, J. Balmaseda and E. Reguera, *J. Phys. Chem. C*, 2008, **112**, 15893–15899.

[202] H. Tokoro and S.-i. Ohkoshi, *Dalton Trans.*, 2011, **40**, 6825–6833.

[203] A. Bleuzen, C. Lomenech, V. Escax, F. Villain, F. Varret, C. Cartier dit Moulin and M. Verdaguer, *J. Am. Chem. Soc.*, 2000, **122**, 6648–6652.

[204] D. Chernyshov and A. Bosak, *Phase Transitions*, 2010, **83**, 115–122.

[205] P. Franz, C. Ambrus, A. Hauser, D. Chernyshov, M. Hostettler, J. Hauser, L. Keller, K. Krämer, H. Stoeckli-Evans, P. Pattison, H.-B. Bürgi and S. Decurtins, *J. Am. Chem. Soc.*, 2004, **126**, 16472–16477.

[206] P. Bhatt, N. Thakur, M. D. Mukadam, S. Singh Meena and S. M. Yusuf, *J. Phys. Chem. C*, 2013, **117**, 2676–2687.

[207] A. Flambard, F. H. Köhler and R. Lescouëzec, *Angew. Chem. Int. Ed.*, 2009, **48**, 1673–1676.

[208] A. Flambard, F. H. Köhler, R. Lescouëzec and B. Revel, *Chem. Eur. J.*, 2011, **17**, 11567–11575.

[209] J. Balmaseda, E. Reguera, J. Rodríguez-Hernández, L. Reguera and M. Autie, *Micropor. Mesopor. Mater.*, 2006, **96**, 222–236.

[210] Y. Moritomo, K. Igarashi, J. Kim and H. Tanaka, *Appl. Phys. Express*, 2009, **2**, 085001.

[211] N. Shimamoto, S.-i. Ohkoshi, O. Sato and K. Hashimoto, *Inorg. Chem.*, 2002, **41**, 678–684.

[212] Y. Moritomo, T. Matsuda, Y. Kurihara and J. Kim, *J. Phys. Soc. Jpn.*, 2011, **80**, 074608.

[213] D. O. Ojwang, J. Grins, D. Wardecki, M. Valvo, V. Renman, L. Häggström, T. Ericsson, T. Gustafsson, A. Mahmoud, R. P. Hermann and G. Svensson, *Inorg. Chem.*, 2016, **55**, 5924–5934.

[214] D. Wardecki, D. O. Ojwang, J. Grins and G. Svensson, *Cryst. Growth Des.*, 2017, **17**, 1285–1292.

[215] K. Kato, Y. Moritomo, M. Takata, M. Sakata, M. Umekawa, N. Hamada, S. Ohkoshi, H. Tokoro and K. Hashimoto, *Phys. Rev. Lett.*, 2003, **91**, 255502.

[216] T. Matsuda, J. Kim and Y. Moritomo, *Dalton Trans.*, 2012, **41**, 7620–7623.

[217] C. D. Wessells, R. A. Huggins and Y. Cui, *Nat. Commun.*, 2011, **2**, 550.

[218] H.-W. Lee, R. Y. Wang, M. Pasta, S. W. Lee, N. Liu and Y. Cui, *Nat. Commun.*, 2014, **5**, 5280.

[219] L. Reguera, J. Balmaseda, L. F. del Castillo and E. Reguera, *J. Phys. Chem. C*, 2008, **112**, 5589–5597.

[220] J. C. Wojdeł and S. T. Bromley, *J. Phys. Chem. B*, 2006, **110**, 24294–24298.

[221] J. Rodríguez-Hernández, E. Reguera, E. Lima, J. Balmaseda, R. Martínez-Garcia and H. Yee-Madeira, *J. Phys. Chem. Solids*, 2007, **68**, 1630–1642.

[222] M. P. Shores, L. G. Beauvais and J. R. Long, *J. Am. Chem. Soc.*, 1999, **121**, 775–779.

[223] W. Zhang, Y. Cai, R.-G. Xiong, H. Yoshikawa and K. Awaga, *Angew. Chem. Int. Ed.*, 2010, **49**, 6608–6610.

[224] K. W. Chapman, K. A. Beyer, H. Zhao and P. J. Chupas, *CrystEngComm*, 2013, **15**, 9377–9381.

[225] C. Avendano, F. Karadas, M. Hilfiger, M. Shatruk and K. R. Dunbar, *Inorg. Chem.*, 2010, **49**, 583–594.

[226] E. Coronado, M. C. Giménez-López, T. Korzeniak, G. Levchenko, F. M. Romero, A. Segura, V. García-Baonza, J. C. Cezar, F. M. F. de Groot, A. Milner and M. Paz-Pasternak, *J. Am. Chem. Soc.*, 2008, **130**, 15519–15532.

[227] M. F. Dumont, O. N. Risset, E. S. Knowles, T. Yamamoto, D. M. Pajerowski, M. W. Meisel and D. R. Talham, *Inorg. Chem.*, 2013, **52**, 4494–4501.

[228] E. Coronado, M. C. Giménez-López, G. Levchenko, F. M. Romero, V. García-Baonza, A. Milner and M. Paz-Pasternak, *J. Am. Chem. Soc.*, 2005, **127**, 4580–4581.

[229] M. V. Bennett, L. G. Beauvais, M. P. Shores and J. R. Long, *J. Am. Chem. Soc.*, 2001, **123**, 8022–8032.

[230] W. E. Buschmann and J. S. Miller, *Inorg. Chem. Commun.*, 1998, **1**, 174–176.

[231] C. Sabelli, *Neues Jahrb. Mineral., Monatsh.*, 1987, 481–487.

[232] M. Schwarten and D. Babel, *Z. Anorg. Allg. Chem.*, 2000, **626**, 1921–1928.

[233] D. Babel, *Z. Naturforsch.*, 1982, **37b**, 1534–1539.

[234] B. Ziegler, M. Witzel and D. Babel, *Z. Anorg. Allg. Chem.*, 1991, **600**, 239–248.

[235] M. Schwarten, M. Witzel and D. Babel, *Z. Naturforsch.*, 2000, **55b**, 487–494.

[236] S. Peschel and D. Babel, *Z. Naturforsch.*, 1994, **49b**, 1373–1380.

[237] K. Qian, F. Shao, Z. Yan, J. Pang, X. Chen and C. Yang, *CrystEngComm*, 2016, **18**, 7671–7674.

[238] C. Shi, C.-H. Yu and W. Zhang, *Angew. Chem. Int. Ed.*, 2016, **55**, 5798–5802.

[239] M. Rok, J. K. Prytys, V. Kinzhybalo and G. Bator, *Dalton Trans.*, 2017, **46**, 2322–2331.

[240] W.-J. Xu, P.-F. Li, Y.-Y. Tang, W.-X. Zhang, R.-G. Xiong and X.-M. Chen, *J. Am. Chem. Soc.*, 2017, **139**, 6369–6375.

[241] C. J. Jones, *D and f Block Chemistry*, Royal Society of Chemistry, Cambridge, 2001.

[242] E. Reguera, J. Rodríguez-Hernández, A. Champi, J. G. Duque, E. Granado and C. Rettori, *Z. Phys. Chem.*, 2006, **220**, 1609–1619.

[243] Z. Wang, B. Zhang, T. Otsuka, K. Inoue, H. Kobayashi and M. Kurmoo, *Dalton Trans.*, 2004, 2209–2216.

[244] W. Li, Z. Wang, F. Deschler, S. Gao, R. H. Friend and A. K. Cheetham, *Nat. Rev. Mater.*, 2017, **2**, 16099.

[245] K.-L. Hu, M. Kurmoo, Z. Wang and S. Gao, *Chem. Eur. J.*, 2009, **15**, 12050–12064.

[246] B.-Q. Wang, H.-B. Yan, Z.-Q. Huang and Z. Zhang, *Acta Crystallogr., Sect. C: Cryst. Struct. Commun.*, 2013, **69**, 616–619.

[247] A. Cornia, A. Caneshi, P. Dapporto, A. C. Fabretti, D. Getteschi, W. Malavasi, C. Sangregorio and R. Sessoli, *Angew. Chem.*, 1999, **111**, 1897–1899.

[248] Y.-Q. Tian, Y.-M. Zhao, H.-J. Xu and C.-Y. Chi, *Inorg. Chem.*, 2007, **46**, 1612–1616.

[249] V. Paredes-García, I. Rojas, R. Madrid, A. Vega, E. Navarro-Moratalla, W. Cañón-Mancisidor, E. Spodine and D. Venegas-Yazigi, *New. J. Chem.*, 2013, **37**, 2120–2127.

[250] A. S. Antsyshkina, M. A. Porai Koshits, V. N. Ostrikova and G. G. Sadikov, *Koord. Khim.*, 1983, **9**, 855–858.

[251] M. Mączka, N. L. Marinho Costa, A. Gągor, W. Paraguassu, A. Sieradzki and J. Hanuza, *Phys. Chem. Chem. Phys.*, 2016, **18**, 13993–14000.

[252] Y. Yu, R. Shang, S. Chen, B.-W. Wang, Z.-M. Wang and S. Gao, *Chem. Eur. J.*, 2017, **23**, 9857–9871.

[253] S. M. Bovill and P. J. Saines, *CrystEngComm*, 2015, **17**, 8319–8326.

[254] L. C. Gómez-Aguirre, B. Pato-Doldán, A. Stroppa, S. Yáñez-Vilar, L. Bayarjargal, B. Winkler, S. Castro-García, J. Mira, M. Sánchez-Andújar and M. A. Señarís-Rodríguez, *Inorg. Chem.*, 2015, **54**, 2109–2116.

[255] G.-C. Xu, X.-M. Ma, L. Zhang, Z.-M. Wang and S. Gao, *J. Am. Chem. Soc.*, 2010, **132**, 9588–9590.

[256] B. Liu, R. Shang, K.-L. Hu, Z.-M. Wang and S. Gao, *Inorg. Chem.*, 2012, **51**, 13363–13372.

[257] R. Shang, G.-C. Xu, Z.-M. Wang and S. Gao, *Chem. Eur. J.*, 2014, **20**, 1146–1158.

[258] S. Chen, R. Shang, B.-W. Wang, Z.-M. Wang and S. Gao, *Angew. Chem.*, 2015, **127**, 11245–11248.

[259] P. Jain, N. S. Dalal, B. H. Toby, H. W. Kroto and A. K. Cheetham, *J. Am. Chem. Soc.*, 2008, **130**, 10450–10451.

[260] M. Sánchez-Andújar, S. Presedo, S. Yáñez-Vilar, S. Castro-García, J. Shamir and M. A. Señarís-Rodríguez, *Inorg. Chem.*, 2010, **49**, 1510–1516.

[261] D.-W. Fu, W. Zhang, H.-L. Cai, Y. Zhang, J.-Z. Ge, R.-G. Xiong, S. D. Huang and T. Nakamura, *Angew. Chem. Int. Ed.*, 2011, **50**, 11947–11951.

[262] M. Sánchez-Andújar, L. C. Gómez-Aguirre, B. Pato Doldán, S. Yáñez-Vilar, R. Artiaga, A. L. Llamas-Saiz, R. S. Manna, F. Schnelle, M. Lang, F. Ritter, A. A. Haghighirad and M. A. Señarís-Rodríguez, *CrystEngComm*, 2014, **16**, 3558–3566.

[263] W. Zhang and R.-G. Xiong, *Chem. Rev.*, 2012, **112**, 1163–1195.

[264] M. Mączka, A. Gągor, B. Macalik, A. Pikul, M. Ptak and J. Hanuza, *Inorg. Chem.*, 2014, **53**, 457–467.

[265] G.-C. Xu, W. Zhang, X.-M. Ma, Y.-H. Chen, L. Zhang, H.-L. Cai, Z.-M. Wang, R.-G. Xiong and S. Gao, *J. Am. Chem. Soc.*, 2011, **133**, 14948–14951.

[266] B. Pato-Doldán, M. Sánchez-Andújar, L. C. Gómez-Aguirre, S. Yáñez-Vilar, J. López-Beceiro, C. Gracia-Fernández, A. A. Haghighirad, F. Ritter, S. Castro-García and M. A. Señarís-Rodríguez, *Phys. Chem. Chem. Phys.*, 2012, **14**, 8498–8501.

[267] N. Abhyankar, J. Jung Kweon, M. Orio, S. Bertaina, M. Lee, E. S. Choi, R. Fu and N. S. Dalal, *J. Phys. Chem. C*, 2017, **121**, 6314–6322.

[268] A. Stroppa, P. Jain, P. Barone, M. Marsman, J. M. Perez-Mato, A. K. Cheetham, H. W. Kroto and S. Picozzi, *Angew. Chem. Int. Ed.*, 2011, **50**, 5847–5850.

[269] X.-Y. Wang, L. Gan, S.-W. Zhang and S. Gao, *Inorg. Chem.*, 2004, **43**, 4615–4625.

[270] P. Jain, V. Ramachandran, R. J. Clark, H. D. Zhou, B. H. Toby, N. S. Dalal, H. W. Kroto and A. K. Cheetham, *J. Am. Chem. Soc.*, 2009, **131**, 13625–13627.

[271] M. Melník, *Coord. Chem. Rev.*, 1982, **42**, 259–293.

[272] M. Kato, *Coord. Chem. Rev.*, 1988, **92**, 45–83.

[273] W. Eerenstein, N. D. Mathur and J. F. Scott, *Nature*, 2006, **442**, 759–765.

[274] L. C. Gómez-Aguirre, B. Pato-Doldán, J. Mira, S. Castro-García, M. A. Señarís-Rodríguez, M. Sánchez-Andújar, J. Singleton and V. S. Zapf, *J. Am. Chem. Soc.*, 2016, **138**, 1122–1125.

[275] Y. Tian, A. Stroppa, Y. Chai, L. Yan, S. Wang, P. Barone, S. Picozzi and Y. Sun, *Sci. Rep.*, 2014, **4**, 6062.

[276] Y. Tian, J. Cong, S. Shen, Y. Chai, L. Yan, S. Wang and Y. Sun, *Phys. Status Solidi RRL*, 2014, **8**, 91–94.

[277] Y. Tian, S. Shen, J. Cong, L. Yan, S. Wang and Y. Sun, *J. Am. Chem. Soc.*, 2016, **138**, 782–785.

[278] N. Abhyankar, S. Bertaina and N. S. Dalal, *J. Phys. Chem. C*, 2015, **119**, 28143–28147.

[279] W. Wang, L.-Q. Yan, J.-Z. Cong, Y.-L. Zhao, F. Wang, S.-P. Shen, T. Zou, D. Zhang, S.-G. Wang, X.-F. Han and Y. Sun, *Sci. Rep.*, 2013, **3**, 2024.

[280] D. Di Sante, A. Stroppa, P. Jain and S. Picozzi, *J. Am. Chem. Soc.*, 2013, **135**, 18126–18130.

[281] I. E. Collings, J. A. Hill, A. B. Cairns, R. I. Cooper, A. L. Thompson, J. E. Parker, C. C. Tang and A. L. Goodwin, *Dalton Trans.*, 2016, **45**, 4169–4178.

[282] W. Li, A. Thirumurugan, P. T. Barton, Z. Lin, S. Henke, H. H.-M. Yeung, M. T. Wharmby, E. G. Bithell, C. J. Howard and A. K. Cheetham, *J. Am. Chem. Soc.*, 2014, **136**, 7801–7804.

[283] Y. Wu, T. Binford, J. A. Hill, S. Shaker, J. Wang and A. K. Cheetham, *Chem. Commun.*, 2018, **54**, 3751–3754.

[284] Y. Wu, S. Shaker, F. Brivio, R. Murugavel, P. D. Bristowe and A. K. Cheetham, *J. Am. Chem. Soc.*, 2017, **139**, 16999–17002.

[285] Y. Wu, D. M. Halat, F. Wei, T. Binford, I. D. Seymour, M. W. Gaultois, S. Shaker, J. Wang, C. P. Grey and A. K. Cheetham, *Chem. Eur. J.*, 2018, **24**, 11309–11313.

[286] K.-P. Xie, W.-J. Xu, C.-T. He, B. Huang, Z.-Y. Du, Y.-J. Su, W.-X. Zhang and X.-M. Chen, *CrystEngComm*, 2016, **18**, 4495–4498.

[287] G. Thiele and D. Messer, *Z. Anorg. Allg. Chem.*, 1980, **464**, 255–267.

[288] A. Halder, R. Chulliyil, A. S. Subbiah, T. Khan, S. Chattoraj, A. Chowdhury and S. K. Sarkar, *J. Phys. Chem. Lett.*, 2015, **6**, 3483–3489.

[289] Y.-H. Chiang, M.-H. Li, H.-M. Chen, P.-S. Shen and P. Chen, *ACS Appl. Mater. Interfaces*, 2017, **9**, 2403–2409.

[290] Q. Jiang, D. Rebollar, J. Gong, E. L. Piacentino, C. Zheng and T. Xu, *Angew. Chem. Int. Ed.*, 2015, **54**, 7617–7620.

[291] L. Birckenbach and K. Kellermann, *Chem. Ber.*, 1925, **58**, 2377–2386.

[292] M. J. Cliffe, J. Lee, J. A. M. Paddison, S. Schott, P. Mukherjee, M. W. Gaultois, P. Manuel, H. Sirringhaus, S. E. Dutton and C. P. Grey, *Phys. Rev. B*, 2018, **97**, 144421.

[293] X.-H. Zhao, X.-C. Huang, S.-L. Zhang, D. Shao, H.-Y. Wei and X.-Y. Wang, *J. Am. Chem. Soc.*, 2013, **135**, 16006–16009.

[294] F. A. Mautner, H. Krischner and C. Kratky, *Monat. Chem.*, 1988, **119**, 1245–1249.

[295] F. A. Mautner, R. Cortés, L. Lezama and T. Rojo, *Angew. Chem. Int. Ed. Engl.*, 1996, **35**, 78–80.

[296] Z.-Y. Du, Y.-P. Zhao, W.-X. Zhang, H.-L. Zhou, C.-T. He, W. Xue, B.-Y. Wang and X.-M. Chen, *Chem. Commun.*, 2014, **50**, 1989–1991.

[297] Z.-Y. Du, Y.-P. Zhao, C.-T. He, B.-Y. Wang, W. Xue, H.-L. Zhou, J. Bai, B. Huang, W.-X. Zhang and X.-M. Chen, *Cryst. Growth Des.*, 2014, **14**, 3903–3909.

[298] F. A. Mautner, H. Krischner and C. Kratky, *Z. Kristallogr.*, 1986, **175**, 105–110.

[299] K. Qian, Y. Xu, Z. Wang and J. Yang, *Z. Naturforsch.*, 2017, **72b**, 409–413.

[300] Z.-Y. Du, T.-T. Xu, B. Huang, Y.-J. Su, W. Xue, C.-T. He, W.-X. Zhang and X.-M. Chen, *Angew. Chem. Int. Ed.*, 2015, **54**, 914–918.

[301] F. A. Mautner, S. Hanna, R. Cortés, L. Lezama, M. Gotzone Barandika and T. Rojo, *Inorg. Chem.*, 1999, **38**, 4647–4652.

[302] Z.-Y. Du, Y.-S. Sun, S.-L. Chen, B. Huang, Y.-J. Su, T.-T. Xu, W.-X. Zhang and X.-M. Chen, *Chem. Commun.*, 2015, **51**, 15641–15644.

[303] J. Ribas, A. Escuer, M. Monfort, R. Vicente, R. Cortés, L. Lezama and T. Rojo, *Coord. Chem. Rev.*, 1999, **193-195**, 1027–1068.

[304] A. Escuer, R. Vicente, M. A. S. Goher and F. A. Mautner, *Inorg. Chem.*, 1995, **34**, 5707–5708.

[305] L. K. Thompson, S. S. Tandon and M. E. Manuel, *Inorg. Chem.*, 1995, **34**, 2356–2366.

[306] L. C. Gómez-Aguirre, B. Pato-Doldán, A. Stroppa, L.-M. Yang, T. Frauenheim, J. Mira, S. Yáñez-Vilar, R. Artiaga, S. Castro-García, M. Sánchez-Andújar and M. A. Señarís-Rodríguez, *Chem. Eur. J.*, 2016, **22**, 7863–7870.

[307] V. R. P. Verneker and L. Avrami, *J. Phys. Chem.*, 1968, **72**, 778–783.

[308] D. M. Badgujar, M. B. Talawar, S. N. Asthana and P. P. Mahulikar, *J. Hazard. Mater.*, 2008, **151**, 289–305.

[309] M.-L. Tong, J. Ru, Y.-M. Wu, X.-M. Chen, H.-C. Chang, K. Mochizuki and S. Kitagawa, *New. J. Chem.*, 2003, **27**, 779–782.

[310] L. Zhou, X. Zheng, P.-P. Shi, Z. Zafar, H.-Y. Ye, D.-W. Fu and Q. Ye, *Inorg. Chem.*, 2017, **56**, 3238–3244.

[311] J. A. Schlueter, J. L. Manson and U. Geiser, *Inorg. Chem.*, 2005, **44**, 3194–3202.

[312] J. A. Schlueter, J. L. Manson, K. A. Hyzer and U. Geiser, *Inorg. Chem.*, 2004, **43**, 4100–4102.

[313] F.-J. Geng, L. Zhou, P.-P. Shi, X.-L. Wang, X. Zheng, Y. Zhang, D.-W. Fu and Q. Ye, *J. Mater. Chem. C*, 2017, **5**, 1529–1536.

[314] J. M. Bermúdez-García, M. Sánchez-Andújar, S. Yáñez-Vilar, S. Castro-García, R. Artiaga, J. López-Beceiro, L. Botana, A. Alegría and M. A. Señarís-Rodríguez, *J. Mater. Chem. C*, 2016, **4**, 4889–4898.

[315] J. M. Bermúdez-García, M. Sánchez-Andújar, S. Yáñez-Vilar, S. Castro-García, R. Artiaga, J. López-Beceiro, L. Botana, Á. Alegría and M. A. Señarís-Rodríguez, *Inorg. Chem.*, 2015, **54**, 11680–11687.

[316] J. M. Bermúdez-García, M. Sánchez-Andújar, S. Castro-García, J. López-Beceiro, R. Artiaga and M. A. Señarís-Rodríguez, *Nat. Commun.*, 2017, **8**, 15715.

[317] R. D. Shannon, *Acta Crystallogr., Sect. A: Cryst. Phys., Diffr., Theor. Gen. Crystallogr.*, 1976, **32**, 751–767.

[318] J. A. Hill, A. L. Thompson and A. L. Goodwin, *J. Am. Chem. Soc.*, 2016, **138**, 5886–5896.

[319] D. B. Leznoff and J. Lefebvre, *Gold Bull.*, 2005, **38**, 47–54.

[320] E. V. Alexandrov, A. V. Virovets, V. A. Blatov and E. V. Peresypkina, *Chem. Rev.*, 2015, **115**, 12286–12319.

[321] J. Lefebvre, D. Chartrand and D. B. Leznoff, *Polyhedron*, 2007, **26**, 2189–2199.

[322] J. A. Hill, *D.Phil. Thesis*, University of Oxford, 2016.

[323] P. Schouwink, F. Morelle, Y. Sadikin, Y. Filinchuk and R. Černý, *Energies*, 2015, **8**, 8286–8299.

[324] Y.-L. Sun, X.-B. Han and W. Zhang, *Chem. Eur. J.*, 2017, **23**, 11126–11132.

[325] K. T. Møller, M. B. Ley, P. Schouwink, R. Černý and T. R. Jensen, *Dalton Trans.*, 2016, **45**, 831–840.

[326] P. Schouwink, M. B. Ley, A. Tissot, H. Hagemann, T. R. Jensen, Ľ. Smrčok and R. Černý, *Nat. Commun.*, 2014, **5**, 5706.

[327] M. Paskevicius, L. H. Jepsen, P. Schouwink, R. Černý, D. B. Ravnsbæk, Y. Filinchuk, M. Dornheim, F. Besenbacher and T. R. Jensen, *Chem. Soc. Rev.*, 2017, **46**, 1565–1634.

[328] P. Schouwink, A. Ramel, E. Giannini and R. Černý, *CrystEngComm*, 2015, **17**, 2682–2689.

[329] G. Feng, X. Jiang, W. Wei, P. Gong, L. Kang, Z. Li, Y. Li, X. Li, X. Wu, Z. Lin, W. Li and P. Lu, *Dalton Trans.*, 2016, **45**, 4303–4308.

[330] H.-Y. Ye, Y.-Y. Tang, P.-F. Li, W.-Q. Liao, J.-X. Gao, X.-N. Hua, H. Cai, P.-P. Shi, Y.-M. You and R.-G. Xiong, *Science*, 2018, **361**, 151–155.

[331] E. E. Gordon, K. Xu, H. Xiang, A. Bussmann-Holder, R. K. Kremer, A. Simon, J. Köhler and M.-H. Whangbo, *Angew. Chem. Int. Ed.*, 2016, **55**, 3682–3684.

[332] A. J. Blake, R. O. Gould, S. Parsons, C. Radek and M. Schröder, *Angew. Chem. Int. Ed. Engl.*, 1995, **34**, 2374–2376.

[333] P. Curie, *J. Phys. Theor. Appl.*, 1894, **3**, 393–415.

[334] B. Guigue, A. Marizy and P. Loubeyre, *Phys. Rev. B*, 2017, **95**, 020104(R).

[335] A. P. Drozdov, M. I. Eremets, I. A. Troyan, V. Ksenofontov and S. I. Shylin, *Nature*, 2015, **525**, 73–76.

[336] E. Schrödinger, *Naturwissenschaften*, 1935, **23**, 807–812.

[337] M. Ptak, M. Mączka, A. Gągor, A. Sieradzki, A. Stroppa, D. Di Sante, J. M. Perez-Mato and L. Macalik, *Dalton Trans.*, 2016, **45**, 2574–2583.

[338] G. Kieslich, S. Kumagai, A. C. Forse, S. Sun, S. Henke, M. Yamashita, C. P. Grey and A. K. Cheetham, *Chem. Sci.*, 2016, **7**, 5108–5112.

[339] R. Shang, X. Sun, Z.-M. Wang and S. Gao, *Chem. Asian J.*, 2012, **7**, 1697–1707.

[340] S. Ferlay, T. Mallah, R. Ouahès, P. Veillet and M. Verdaguer, *Nature*, 1995, **378**, 701–703.

[341] D. M. Pajerowski, T. Watanabe, T. Yamamoto and Y. Einaga, *Phys. Rev. B*, 2011, **83**, 153202.

[342] S. P. Gabuda, S. G. Kozlova, V. A. Drebuschak, D. N. Dybtsev and V. P. Fedin, *J. Phys. Chem. C*, 2008, **112**, 5074–5077.

[343] I. Swainson, L. Chi, J.-H. Her, L. Cranswick, P. Stephens, B. Winkler, D. J. Wilson and V. Milman, *Acta Crystallogr. B Struct. Sci.*, 2010, **66**, 422–429.

[344] S. G. Duyker, J. A. Hill, C. J. Howard and A. L. Goodwin, *J. Am. Chem. Soc.*, 2016, **138**, 11121–11123.

[345] M. A. Pena and J. L. G. Fierro, *Chem. Rev.*, 2001, **101**, 1981–2017.

[346] M. J. Cliffe, W. Wan, X. Zou, P. A. Chater, A. K. Kleppe, M. G. Tucker, H. Wilhelm, N. P. Funnell, F.-X. Coudert and A. L. Goodwin, *Nat. Commun.*, 2014, **5**, 4176.

[347] S. Dissegna, K. Epp, W. R. Heinz, G. Kieslich and R. A. Fischer, *Adv. Mater.*, 2018, 1704501.

[348] Z. Fang, B. Bueken, D. E. De Vos and R. A. Fischer, *Angew. Chem. Int. Ed.*, 2015, **54**, 7234–7254.

[349] A. K. Cheetham, T. D. Bennett, F.-X. Coudert and A. L. Goodwin, *Dalton Trans.*, 2016, **45**, 4113–4126.

[350] A. L. Goodwin, *Phys. Rev. B*, 2006, **74**, 134302.

[351] M. D. Peel, S. P. Thompson, A. Daoud-Aladine, S. E. Ashbrook and P. Lightfoot, *Inorg. Chem.*, 2012, **51**, 6876–6889.

[352] H. L. B. Boström, J. A. Hill and A. L. Goodwin, *Phys. Chem. Chem. Phys.*, 2016, **18**, 31881–31894.

[353] T. Iwamoto, S.-i. Nishikori and T. Kitazawa, *Supramol. Chem.*, 1995, **6**, 179–186.

[354] T. Iwamoto, S.-i. Nishikori, T. Kitazawa and H. Yuge, *J. Chem. Soc. Dalton Trans.*, 1997, 4127–4136.

[355] M. T. Dove, *Introduction to Lattice Dynamics*, Cambridge University Press, Cambridge, 1993.

[356] J. Pickworth Glusker and K. N. Trueblood, *Crystal Structure Analysis: A Primer*, Oxford University Press, Oxford, 2010.

[357] A. J. Blake, W. Clegg, J. M. Cole, J. S. O. Evans, P. Main, S. Parsons and D. J. Watkin, *Crystal Structure Analysis: Principles and Practice*, Oxford University Press, Oxford, 2009.

[358] *International Tables for Crystallography, Volume A*, ed. M. I. Aroyo, International Union of Crystallography, Chester, 2016.

[359] The Nobel Prize in Chemistry, https://www.nobelprize.org/nobel_prizes/themes/chemistry/malmstrom/index.html, (last accessed 2018-08-14).

[360] G. J. Bradley and A. P. Cracknell, *The Mathematical Theory of Symmetry in Solids*, Clarendon Press, Oxford, 1972.

[361] W. Setyawan and S. Curtarolo, *Comput. Mater. Sci.*, 2010, **49**, 299–312.

[362] A. L. Patterson, *Z. Kristallogr.*, 1935, **90**, 517–542.

[363] D. Sayre, *Acta Crystallogr.*, 1952, **5**, 60–65.

[364] J. Karle and H. Hauptman, *Acta Crystallogr.*, 1950, **3**, 181–187.

[365] L. Palatinus and G. Chapius, *J. Appl. Cryst.*, 2007, **40**, 786–790.

[366] H. M. Rietveld, *Acta Crystallogr.*, 1967, **22**, 151–152.

[367] B. H. Toby, *Powder Diffr.*, 2006, **21**, 67–70.

[368] G. S. Pawley, *J. Appl. Cryst.*, 1981, **14**, 357–361.

[369] A. Le Bail, H. Duroy and J. L. Fourquet, *Mater. Res. Bull.*, 1988, **23**, 447–452.

[370] A. A. Coelho, *TOPAS-Academic, version 4.1 (computer software)*, Coelho Software, Brisbane.

[371] A. C. Larson and R. B. von Dreele, *General Structure Analysis System (GSAS)*, Los Alamos National Laboratory Report LAUR 86-748, 1994.

[372] J. Rodríguez-Carvajal, *Physica B*, 1993, **192**, 55–69.

[373] R. Jenkins, R. Manne, R. Robin and C. Senemaud, *Pure & Appl. Chem.*, 1991, **63**, 735–746.

[374] *International Tables for Crystallography, Volume C*, ed. E. Prince, International Union of Crystallography, Chester, 2006.

[375] Diamond Instruments, http://www.diamond.ac.uk/Beamlines.html, (last accessed 2018-08-14).

[376] I11: High Resolution Powder Diffraction, https://www.diamond.ac.uk/Instruments/Crystallography/I11.html, (last accessed 2018-08-08).

[377] X. Zou, S. Hovmöller and P. Oleynikov, *Electron Crystallography: Electron Microscopy and Electron Diffraction*, Oxford University Press, Oxford, 2011.

[378] H. Ihee, V. A. Lobastov, U. M. Gomez, B. M. Goodson, R. Srinivasan, C.-Y. Ruan and A. H. Zewail, *Science*, 2001, **291**, 458–462.

[379] D. A. Keen and A. L. Goodwin, *Nature*, 2015, **521**, 303–309.

[380] T. R. Welberry and T. Weber, *Cryst. Rev.*, 2016, **22**, 2–78.

[381] A. R. Kolatkar, J. B. Clarage and G. N. Phillips, *Acta Crystallogr., Sect. D: Biol. Crystallogr.*, 1994, **50**, 210–218.

[382] B. J. Campbell, H. T. Stokes, D. E. Tanner and D. M. Hatch, *J. Appl. Cryst.*, 2006, **39**, 607–614.

[383] M. I. Aroyo, A. Kirov, C. Capillas, J. M. Perez-Mato and H. Wondratschek, *Acta Crystallogr., Sect. A: Found. Crystallogr.*, 2006, **62**, 115–128.

[384] M. I. Aroyo, J. M. Perez-Mato, D. Orobengoa, E. Tasci, G. de la Flor and A. Kirov, *Bulg. Chem. Commun.*, 2011, **43**, 183–197.

[385] M. I. Aroyo, J. M. Perez-Mato, C. Capillas, E. Kroumova, S. Ivantchev, G. Madariaga, A. Kirov and H. Wondratschek, *Z. Kristallogr.*, 2006, **221**, 15–27.

[386] F. A. Cotton, *Chemical Applications of Group Theory*, John Wiley & Sons Ltd, New York, 1990.

[387] E. Kroumova, M. I. Aroyo, J. M. Perez-Mato, A. Kirov, C. Capillas, S. Ivantchev and H. Wondratschek, *Phase Transitions*, 2003, **76**, 155–170.

[388] S. C. Miller and W. F. Love, *Tables of Irreducible Representations of Space Groups and Co-Representations of Magnetic Space Groups*, Pruett Press, Boulder, Colorado, 1967.

[389] A. R. Overy, A. Simonov, P. A. Chater, M. G. Tucker and A. L. Goodwin, *Phys. Status Solidi B*, 2017, **254**, 1600586.

[390] G. Raunio, L. Almqvist and R. Stedman, *Phys. Rev.*, 1969, **178**, 1496–1501.

[391] J. D. Gale, *J. Chem. Soc. Faraday Trans.*, 1997, **93**, 629–637.

[392] J. D. Gale and A. L. Rohl, *Mol. Simul.*, 2003, **29**, 291–341.

[393] J. M. Larkin and A. J. H. McGaughey, *Phys. Rev. B*, 2014, **89**, 144303.

[394] E. R. Cope and M. T. Dove, *J. Appl. Cryst.*, 2007, **40**, 589–594.

[395] S. Alexander, O. Entin-Wohlman and R. Orbach, *Phys. Rev. B*, 1986, **34**, 2726–2734.

[396] A. D. Bruce and R. A. Cowley, *J. Phys. C: Solid State Phys.*, 1973, **6**, 2422–2240.

[397] R. E. Newnham, *Properties of Materials: Anisotropy, Symmetry, Structure*, Oxford University Press, Oxford, 2005.

[398] F. Grüneisen, *Ann. Phys.*, 1912, **344**, 257–306.

[399] H. D. Megaw, *Mater. Res. Bull.*, 1971, **6**, 1007–1018.

[400] M. K. Panda, T. Runčevski, S. Chandra Sahoo, A. A. Belik, N. K. Nath, R. E. Dinnebier and P. Naumov, *Nat. Commun.*, 2014, **5**, 4811.

[401] K. Takenaka, *Sci. Technol. Adv. Mater.*, 2012, **13**, 013001.

[402] J. S. O. Evans, T. A. Mary and A. W. Sleight, *Physica B*, 1998, **241-243**, 311–316.

[403] M. T. Dove and H. Fang, *Rep. Prog. Phys.*, 2016, **79**, 066503.

[404] K. D. Hammonds, M. T. Dove, A. P. Giddy, V. Heine and B. Winkler, *Am. Mineral.*, 1996, **81**, 1057–1079.

[405] M. J. Conterio, A. L. Goodwin, M. G. Tucker, D. A. Keen, M. T. Dove, L. Peters and J. S. O. Evans, *J. Phys.: Condens. Matter*, 2008, **20**, 255225.

[406] J. Z. Tao and A. W. Sleight, *J. Solid State Chem.*, 2003, **173**, 442–448.

[407] B. K. Greve, K. L. Martin, P. L. Lee, P. J. Chupas, K. W. Chapman and A. P. Wilkinson, *J. Am. Chem. Soc.*, 2010, **132**, 15496–15498.

[408] L. Hu, J. Chen, A. Sanson, H. Wu, C. Guglieri Rodriguez, L. Olivi, Y. Ren, L. Fan, J. Deng and X. Xiang, *J. Am. Chem. Soc.*, 2016, **138**, 8320–8323.

[409] J. S. O. Evans, T. A. Mary, T. Vogt, M. A. Subramanian and A. W. Sleight, *Chem. Mater.*, 1996, **8**, 2809–2823.

[410] T. A. Mary, J. S. O. Evans, T. Vogt and A. W. Sleight, *Science*, 1996, **272**, 90–92.

[411] A. L. Goodwin, M. Calleja, M. J. Conterio, M. T. Dove, J. S. O. Evans, D. A. Keen, L. Peters and M. G. Tucker, *Science*, 2008, **319**, 794–797.

[412] A. L. Goodwin and C. J. Kepert, *Phys. Rev. B*, 2005, **71**, 140301(R).

[413] A. L. Goodwin, *Z. Kristallogr. Suppl.*, 2009, **30**, 1–11.

[414] R. A. Cowley, *Adv. Phys.*, 1980, **29**, 1–110.

[415] I. S. Aleksakhin, A. A. Borovik, V. P. Starodub and I. I. Shafranjosh, *Zh. Prikl. Spektrosk.*, 1978, **30**, 236–239.

[416] Flame Atomic Absorption Spectrometry User Manual, https://www.agilent.com/cs/library/usermanuals/Public/0009.pdf, (last accessed 2018-08-14).

[417] A. Beer, *Ann. Phys. Chem.*, 1852, **86**, 78–88.

[418] J. H. Lambert, *Photometria Sive de Mensura et Gradibus Luminis, Colorum et Umbrae*, Eberhardt Klett, Augsburg, 1760.

[419] A. Sanz-Medel and R. Pereiro, *Atomic Absorption Spectrometry: an Introduction*, Momentum Press, New York, 2014.

[420] J. A. M. Paddison, J. R. Stewart and A. L. Goodwin, *J. Phys.: Condens. Matter*, 2013, **25**, 454220.

[421] C. Tealdi, M. Y. Lavrentiev, C. E. Mohn and N. L. Allan, *J. Struct. Chem.*, 2016, **57**, 257–266.

[422] M. J. Cliffe and A. L. Goodwin, *Phys. Status Solidi B*, 2013, **250**, 949–956.

[423] N. Metropolis and S. Ulam, *J. Am. Stat. Assoc.*, 1949, **44**, 335–341.

[424] S. Fitzpatrick, C. D. Gelatt Jr. and M. P. Vecchi, *Science*, 1983, **220**, 671–680.

[425] A. M. Ferrenberg and R. H. Swendsen, *Phys. Rev. Lett.*, 1988, **61**, 2635–2638.

[426] A. P. Giddy, M. T. Dove, G. S. Pawley and V. Heine, *Acta Crystallogr., Sect. A: Found. Crystallogr.*, 1993, **49**, 697–703.

[427] M. S. Senn, C. A. Murray, X. Luo, L. Wang, F.-T. Huang, S.-W. Cheong, A. Bombardi, C. Ablitt, A. A. Mostofi and N. C. Bristowe, *J. Am. Chem. Soc.*, 2016, **138**, 5479–5482.

[428] M. T. Dove, *Am. Mineral.*, 1997, **82**, 213–244.

[429] K. D. Hammonds, H. Deng, V. Heine and M. T. Dove, *Phys. Rev. Lett.*, 1997, **78**, 3701–3704.

[430] K. D. Hammonds, V. Heine and M. T. Dove, *J. Phys. Chem. B*, 1998, **102**, 1759–1767.

[431] G. S. Pawley, *Phys. Status Solidi B*, 1972, **49**, 475–488.

[432] H. Li, M. Eddaoudi, M. O'Keeffe and O. M. Yaghi, *Nature*, 1999, **402**, 276–279.

[433] L. H. N. Rimmer, M. T. Dove, A. L. Goodwin and D. C. Palmer, *Phys. Chem. Chem. Phys.*, 2014, **16**, 21144–21152.

[434] C. Serre, F. Millange, C. Thouvenot, M. Noguès, G. Marsolier, D. Louër and G. Férey, *J. Am. Chem. Soc.*, 2002, **124**, 13519–13526.

[435] A. U. Ortiz, A. Boutin, A. H. Fuchs and F.-X. Coudert, *Phys. Rev. Lett.*, 2012, **109**, 195502.

[436] F.-X. Coudert, *Chem. Mater.*, 2015, **27**, 1905–1916.

[437] A. B. Cairns and A. L. Goodwin, *Phys. Chem. Chem. Phys.*, 2015, **17**, 20449–20465.

[438] S. A. T. Redfern and E. K. H. Salje, *J. Phys. C: Solid State Phys.*, 1988, **21**, 277–285.

[439] P. Serra-Crespo, A. Dikhtiarenko, E. Stavitski, J. Juan-Alcañiz, F. Kapteijn, F.-X. Coudert and J. Gascon, *CrystEngComm*, 2015, **17**, 276–280.

[440] C. J. Howard, R. L. Withers, K. S. Knight and Z. Zhang, *J. Phys.: Condens. Matter*, 2008, **20**, 135202.

[441] I. Escorihuela, L. R. Falvello and M. Tomás, *Inorg. Chem.*, 2001, **40**, 636–640.

[442] H. U. Guedel, *Acta Chem. Scand.*, 1972, **26**, 2169–2176.

[443] M. Boča, I. Svoboda, F. Renz and H. Fuess, *Acta Crystallogr., Sect. C: Cryst. Struct. Commun.*, 2004, **60**, m631–m633.

[444] G. A. Nifontova, O. S. Filipenko, A. S. Astakhova, I. P. Lavrent'ev and L. O. Atovmyan, *Koord. Khim.*, 1990, **16**, 218–224.

[445] C.-X. Wang, X.-M. Zhou and W.-Y. Shi, *Acta Crystallogr., Sect. E: Struct. Rep. Online*, 2007, **63**, m411–m412.

[446] B. Pato-Doldán, L. C. Gómez-Aguirre, A. P. Hansen, J. Mira, S. Castro-García, M. Sánchez-Andújar, M. A. Señarís-Rodríguez, V. S. Zapf and J. Singleton, *J. Mater. Chem. C*, 2016, **4**, 11164–11172.

[447] Y. Wang, R. Cao, W. Bi, X. Li, D. Yuan and D. Sun, *J. Micropor. Mesopor. Mater.*, 2006, **91**, 215–220.

[448] H. F. Clausen, R. Damgaard Poulsen, A. B. Bond, M.-A. S. Chevallier and B. Brummerstedt Iversen, *J. Solid State Chem.*, 2005, **178**, 3342–3351.

[449] S. Chen, R. Shang, K.-L. Hu, Z.-M. Wang and S. Gao, *Inorg. Chem. Front.*, 2014, **1**, 83–98.

[450] H. Fang, M. T. Dove, L. H. N. Rimmer and A. J. Misquitta, *Phys. Rev. B*, 2013, **88**, 104306.

[451] F. Trousselet, A. Boutin and F.-X. Coudert, *Chem. Mater.*, 2015, **27**, 4422–4430.

[452] M. R. Ryder, B. Van de Voorde, B. Civalleri, T. D. Bennett, S. Mukhopadhyay, G. Cinque, F. Fernandez-Alonso, D. De Vos, S. Rudić and J.-C. Tan, *Phys. Rev. Lett.*, 2017, **118**, 255502.

[453] M. R. Ryder, B. Civalleri, T. D. Bennett, S. Henke, S. Rudić, G. Cinque, F. Fernandez-Alonso and J.-C. Tan, *Phys. Rev. Lett.*, 2014, **113**, 215502.

[454] X. Zhang, I. da Silva, H. G. W. Godfrey, S. K. Callear, S. A. Sapchenko, Y. Cheng, I. Vitórica-Yrezábal, M. D. Frogley, G. Cinque, C. C. Tang, C. Giacobbe, C. Dejoie, S. Rudić, A. J. Ramirez-Cuesta, M. A. Denecke, S. Yang and M. Schröder, *J. Am. Chem. Soc.*, 2017, **139**, 16289–16296.

[455] G. Song and W. Zhang, *Phys. Rev. B*, 2016, **94**, 064409.

[456] K. Liu, W. Yin, S. Chen, X. G. Gong, S.-H. Wei and H. J. Xiang, *Phys. Rev. B*, 2016, **93**, 205207.

[457] N. Drichko, C. Broholm, K. Kimura, R. Ishii and S. Nakasutji, *Phys. Rev. B*, 2016, **93**, 184425.

[458] Z. Li, Y. Zhou, H. Qi, Q. Pan, Z. Zhang, N. Nan Shi, M. Lu, A. Stein, C. Y. Li, S. Ramanathan and N. Yu, *Adv. Mater.*, 2016, **28**, 9117–9125.

[459] A. P. Ramirez, G. Lawes, D. Li and M. A. Subramanian, *Solid State Commun.*, 2004, **131**, 251–255.

[460] R. J. Radwanski and Z. Ropka, *J. Magn. Magn. Mater.*, 2004, **272-276**, e259–e261.

[461] K. Bieniasz, M. Berciu and A. M. Olés, *Phys. Rev. B*, 2017, **95**, 235153.

[462] B. Raveau, *Angew. Chem. Int. Ed.*, 2013, **52**, 167–175.

[463] J. H. Van Santen and G. H. Jonker, *Physica*, 1950, **16**, 599–600.

[464] L. Martín-Carrón and A. de Andrés, *Eur. Phys. J. B*, 2001, **22**, 11–16.

[465] S. E. Nagler, D. A. Tennant, R. A. Cowley, T. G. Perring and S. K. Satija, *Phys. Rev. B*, 1991, **44**, 12361–12368.

[466] M. T. Hutchings, E. J. Samuelsen, G. Shirane and K. Hirakawa, *Phys. Rev.*, 1969, **188**, 919–923.

[467] S. Kadota, I. Yamada, S. Yoneyama and K. Hirakawa, *J. Phys. Soc. Jpn.*, 1967, **23**, 751–756.

[468] A. Okazaki and Y. Suemune, *J. Phys. Soc. Jpn.*, 1961, **16**, 671–675.

[469] C. N. R. Rao, *J. Phys. Chem. B*, 2000, **104**, 5877–5889.

[470] M. Daghofer, A. M. Oleś and W. von der Linden, *Phys. Rev. B*, 2004, **70**, 184430.

[471] E. Dagotto, T. Hotta and A. Moreo, *Phys. Rep.*, 2001, **344**, 1–153.

[472] S. Kumar, A. P. Kampf and P. Majumdar, *Phys. Rev. Lett.*, 2006, **97**, 176403.

[473] R. von Helmolt, J. Wecker, B. Holzapfel, L. Schultz and K. Samwer, *Phys. Rev. Lett.*, 1993, **71**, 2331–2333.

[474] Y. Tokura and Y. Tomioka, *J. Magn. Magn. Mater.*, 1999, **200**, 1–23.

[475] M. F. Sykes and J. W. Essam, *Phys. Rev.*, 1964, **133**, 310–315.

[476] N. Tatami, Y. Ando, S. Niioka, H. Kira, M. Onodera, H. Nakao, K. Iwasa, Y. Murakami, T. Kakiuchi, Y. Wakabayashi, H. Sawa and S. Itoh, *J. Magn. Magn. Mater.*, 2007, **310**, 787–789.

[477] D. J. Breed, K. Gilijamse, J. W. E. Sterkenburg and A. R. Miedema, *J. Appl. Phys.*, 1970, **41**, 1267–1268.

[478] T. Tanaka, M. Matsumoto and S. Ishihara, *Phys. Rev. Lett.*, 2005, **95**, 267204.

[479] Z. Nussinov and J. van den Brink, *Rev. Mod. Phys.*, 2015, **87**, 1–59.

[480] A. Kitaev, *Ann. Phys.*, 2006, **321**, 2–111.

[481] T. Tanaka and S. Ishihara, *Phys. Rev. B*, 2009, **79**, 035109.

[482] E. Sletten and L. H. Jensen, *Acta Crystallogr. B Struct. Cryst. Cryst. Chem.*, 1973, **29**, 1752–1756.

[483] R. Shang, S. Chen, B.-W. Wang, Z.-M. Wang and S. Gao, *Angew. Chem. Int. Ed.*, 2016, **55**, 2097–2100.

[484] M. Šimėnas, A. Ciupa, G. Usevičius, K. Aidas, D. Klose, G. Jeschke, M. Mączka, G. Völkel, A. Pöppl and J. Banys, *Phys. Chem. Chem. Phys.*, 2018, **20**, 12097–12105.

[485] N. L. Evans, P. M. M. Thygesen, H. L. B. Boström, E. M. Reynolds, I. E. Collings, A. E. Phillips and A. L. Goodwin, *J. Am. Chem. Soc.*, 2016, **138**, 9393–9396.

[486] M. Paściak, T. R. Welberry, J. Kulda, M. Kempa and J. Hlinka, *Phys. Rev. B*, 2012, **85**, 224109.

[487] A. Ludi, H.-U. Güdel and M. Rüegg, *Inorg. Chem.*, 1970, **9**, 2224–2227.

[488] M. R. Hartman, C. K. Peterson and L. Yun, *Chem. Mater.*, 2006, **18**, 3221–3224.

[489] T.-Y. Tan, B. J. Kennedy, Q. Zhou, C. D. Ling, W. Miiller, C. J. Howard, M. A. Carpenter and K. S. Knight, *Phys. Rev. B*, 2012, **85**, 104107.

[490] M. V. Lobanov, A. M. Balagurov, V. J. Pomjakushin, P. Fischer, M. Gutmann, A. M. Abakumov, O. G. D'yachenko, E. V. Antipov, O. I. Lebedev and G. Van Tendeloo, *Phys. Rev. B*, 2000, **61**, 8941–8949.

[491] E. A. Donlan, H. L. B. Boström, H. S. Geddes, E. M. Reynolds and A. L. Goodwin, *Chem. Commun.*, 2017, **53**, 11233–11236.

[492] D. D. Lee and H. S. Seung, *Nature*, 1999, **401**, 788–791.

[493] D. F. Shriver, S. A. Shriver and S. E. Anderson, *Inorg. Chem.*, 1965, **4**, 725–730.

[494] L. Vegard, *Z. Phys.*, 1921, **5**, 17–26.

[495] S. Kemmler-Sack and H.-J. Rother, *Z. Anorg. Allg. Chem.*, 1979, **448**, 143–155.

[496] D. Reinen, *J. Solid State Chem.*, 1979, **27**, 71–85.

[497] M. F. Sykes, D. S. Gaunt and J. W. Essam, *J. Phys. A.: Math. Gen.*, 1976, **9**, L43–L46.

[498] X. Xu, J. Wang, J.-P. Lv and Y. Deng, *Front. Phys.*, 2014, **9**, 113–119.

[499] J. M. D. Coey, M. Viret and S. von Molnár, *Adv. Phys.*, 1999, **48**, 167–293.

[500] X. Liu, X. Lu, X. Liu and H. Zhou, *Am. Mineral.*, 2015, **100**, 172–180.

[501] S.-W. Cheong, H. Y. Hwang, B. Batlogg and L. W. Rupp Jr., *Solid State Commun.*, 1996, **98**, 163–166.

[502] S. Schott, Z. Jua, A. K. Schaper, V. Thangadurai, W. Weppner and P. Schmid-Beurmann, *Phys. Status Solidi A*, 2005, **12**, 2330–2335.

[503] E. Pollert, P. Holba, M. Nevřiva and J. Novák, *J. Phys. Chem. Solids*, 1977, **38**, 1145–1147.

[504] M. Wyss, A. Reller and H. R. Oswald, *Solid State Ionics*, 1997, **101-103**, 547–554.

[505] H. A. Hopper, J. Le, J. Cheng, T. Weller, R. Marschall, J. Z. Bloh, D. E. Macphee, A. Folli and A. C. Mclaughlin, *J. Solid State Chem.*, 2016, **234**, 87–92.

[506] A. D. Lozano-Gorrin, J. E. Greedan, P. Núñez, C. González-Silgo, G. A. Botton and G. Radtke, *J. Solid State Chem.*, 2007, **180**, 1209–1217.

[507] J. Blasco, J. Stankiewicz and J. García, *J. Solid State Chem.*, 2006, **179**, 898–908.

[508] Q. Zhou and B. J. Kennedy, *J. Phys. Chem. Solids*, 2007, **68**, 1643–1647.

[509] D. Reinen and H. Weitzel, *Z. Anorg. Allg. Chem.*, 1976, **424**, 31–38.

[510] X. Bokhimi, *Powder Diffr.*, 1992, **7**, 228–230.

[511] C. J. Howard and M. A. Carpenter, *Acta Crystallogr. B Struct. Sci.*, 2010, **66**, 40–50.

[512] D. Reinen, H. O. Wellern and J. Wegwerth, *Z. Phys. B*, 1997, **104**, 595–600.

[513] L. Jiao, J. Xu, Z. Li, J.-F. Wang, J. Zhou, Z.-B. Gu and S.-T. Zhang, *J. Mater. Sci: Mater. Electron.*, 2013, **24**, 4970–4973.

[514] J.-F. Wang, B. Hu, J. Zhang, Z.-B. Gu and S.-T. Zhang, *Ceram. Int.*, 2014, **40**, 8753–8759.

[515] F. Herren, P. Fischer, A. Ludi and W. Hälg, *Inorg. Chem.*, 1980, **19**, 956–959.

[516] A. Loidl, *Annu. Rev. Phys. Chem.*, 1989, **40**, 29–60.

[517] K. Binder, in *Spin glasses and random fields*, ed. A. P. Young, World Scientific, London, 1998, 4, 99–118.

[518] U. T. Höchli, K. Knorr and A. Loidl, *Adv. Phys.*, 1990, **39**, 405–615.

[519] J. M. Rowe, J. J. Rush, D. G. Hinks and S. Susman, *Phys. Rev. Lett.*, 1979, **43**, 1158–1161.

[520] J. J. De Yoreo, W. Knaak, M. Meissner and R. O. Pohl, *Phys. Rev. B*, 1986, **34**, 8828–8842.

[521] K. H. Michel and J. M. Rowe, *Phys. Rev. B*, 1980, **22**, 1417–1428.

[522] D. L. Price, J. M. Rowe, J. J. Rush, E. Prince, D. G. Hinks and S. Susman, *J. Chem. Phys.*, 1972, **56**, 3697–3702.

[523] J. J. Rowe, J. J. Rush and E. Prince, *J. Chem. Phys.*, 1977, **66**, 5147–5149.

[524] J. M. Rowe, J. J. Rush, N. J. Chesser, K. H. Michel and J. Naudts, *Phys. Rev. Lett.*, 1978, **40**, 455–458.

[525] A. Loidl, T. Schräder, K. Knorr, R. Böhmer, B. Mertz, G. J. McIntyre, T. Vogt, H. Mutka, M. Müller, H. Jex and S. Haussühl, *Z. Phys. B*, 1989, **75**, 81–99.

[526] X. Z. Yu, Y. Onose, N. Kanazawa, J. H. Park, J. H. Han, Y. Matsui, N. Nagaosa and Y. Tokura, *Nature*, 2010, **465**, 901–904.

[527] S. Mühlbauer, B. Binz, F. Jonietz, C. Pfleiderer, A. Rosch, A. Neubauer, R. Georgii and P. Böni, *Science*, 2009, **323**, 915–919.

[528] T. Jonsson, *Commun. Math. Phys.*, 1983, **90**, 175–186.

[529] N. A. Spaldin, *Nat. Rev. Mater.*, 2017, **2**, 17017.

[530] S. M. Griffin, M. Lilienblum, K. T. Delaney, Y. Kumagai, M. Fiebig and N. A. Spaldin, *Phys. Rev. X*, 2012, **2**, 041022.

[531] G. Smolensky, V. A. Isupov, A. I. Agranovskaya and S. N. Popov, *Sov. Phys. Solid State*, 1961, **2**, 2584–2594.

[532] C. W. Ahn, C.-H. Hong, B.-Y. Choi, H.-P. Kim, H.-S. Han, Y. Hwang, W. Jo, K. Wang, J.-F. Li, J.-S. Lee and I. W. Kim, *J. Korean Phys. Soc.*, 2016, **68**, 1481–1494.

[533] L. E. Cross, *Ferroelectrics*, 1987, **76**, 241–267.

[534] I.-W. Chen, P. Li and Y. Wang, *J. Phys. Chem. Solids*, 1996, **57**, 1525–1536.

[535] Y. Tian, A. Stroppa, Y.-S. Chai, P. Barone, M. Perez-Mato, S. Picozzi and Y. Sun, *Phys. Status Solidi RRL*, 2015, **9**, 62–67.

[536] T. Kimura, T. Goto, H. Shintani, K. Ishizaka, T. Arima and Y. Tokura, *Nature*, 2003, **426**, 55–58.

[537] N. Hur, S. Park, P. A. Sharma, J. S. Ahn, S. Guha and S.-W. Cheong, *Nature*, 2004, **429**, 392–395.

[538] B. B. Van Aken, T. T. M. Palstra, A. Filippetti and N. A. Spaldin, *Nat. Mater.*, 2004, **3**, 164–170.

[539] E. Bousquet, M. Dawber, N. Stucki, C. Lichtensteiger, P. Hermet, S. Gariglio, J.-M. Triscone and P. Ghosez, *Nature*, 2008, **452**, 732–737.

[540] X. Q. Liu, J. W. Wu, X. X. Shi, H. J. Zhao, H. Y. Zhou, R. H. Qiu, W. Q. Zhang and X. M. Chen, *Appl. Phys. Lett.*, 2015, **106**, 202903.

[541] Y. S. Oh, X. Luo, F.-T. Huang, Y. Wang and S.-W. Cheong, *Nat. Mater.*, 2015, **14**, 407–413.

[542] Z. Jirák, *Phys. Rev. B*, 1987, **35**, 5437–5445.

[543] H. J. Zhao, J. Íñiguez, X. M. Chen and L. Bellaiche, *Phys. Rev. B*, 2014, **89**, 174101.

[544] N. A. Benedek, J. M. Rondinelli, H. Djani, P. Ghosez and P. Lightfoot, *Dalton Trans.*, 2015, **44**, 10543–10558.

[545] D. M. Hatch and H. T. Stokes, *J. Appl. Cryst.*, 2003, **36**, 951–952.

[546] Spherical harmonics, http://www.csc.kth.se/∼fpokorny/static/codeanddata/harmonicregression/harmonics.jpg, (last accessed 2018-04-28).

[547] H. T. Stokes and D. M. Hatch, *J. Appl. Cryst.*, 2005, **38**, 237–238.

[548] A. Stroppa, P. Barone, P. Jain, J. M. Perez-Mato and S. Picozzi, *Adv. Mater.*, 2013, **25**, 2284–2290.

[549] R. Shang, S. Chen, Z.-M. Wang and S. Gao, *Chem. Eur. J.*, 2014, **20**, 15872–15883.

[550] R. Zhang, M. S. Senn and M. A. Hayward, *Chem. Mater.*, 2016, **28**, 8399–8406.

[551] G.-H. Kwei, A. C. Lawson, S. J. L. Billinge and S.-W. Cheong, *J. Phys. Chem.*, 1993, **97**, 2368–2377.

[552] V. E. Fairbank, A. L. Thompson, R. I. Cooper and A. L. Goodwin, *Phys. Rev. B*, 2012, **86**, 104113.

[553] S. Ghosh, D. Di Sante and A. Stroppa, *J. Phys. Chem. Lett.*, 2015, **6**, 4553–4559.

[554] S.-i. Ohkoshi, K.-I. Arai, Y. Sato and K. Hashimoto, *Nat. Mater.*, 2004, **3**, 857–861.

[555] M. G. Tucker, D. A. Keen and M. T. Dove, *Mineral. Mag.*, 2001, **65**, 489–507.

[556] A. B. Cairns, J. Catafesta, C. Levelut, J. Rouquette, A. van der Lee, L. Peters, A. L. Thompson, V. Dmitriev, J. Haines and A. L. Goodwin, *Nat. Mater.*, 2013, **12**, 212–216.

[557] D. R. Peacor, *Z. Kristallogr.*, 1973, **138**, 274–298.

[558] J. A. Hill, K. E. Christensen and A. L. Goodwin, *Phys. Rev. Lett.*, 2017, **119**, 115501.

[559] Sodalite, http://europe.iza-structure.org/IZA-SC/framework.php?STC=SOD, (last accessed 2018-08-29).

[560] K. S. Park, Z. Ni, A. P. Côté, J. Y. Choi, R. Huang, F. J. Uribe-Romo, H. K. Chae, M. O'Keeffe and O. M. Yaghi, *Proc. Natl. Acad. Sci. U.S.A*, 2006, **103**, 10186–10191.

[561] T. F. W. Barth, *Nor. Geol. Tidsskr.*, 1925, **8**, 201–216.

[562] A. Phan, C. J. Doonan, F. J. Uribe-Romo, C. B. Knobler, M. O'Keeffe and O. M. Yaghi, *Acc. Chem. Res.*, 2010, **43**, 58–67.

[563] B. F. Hoskins and R. Robson, *J. Am. Chem. Soc.*, 1990, **112**, 1546–1554.

[564] R. Robson, *J. Chem. Soc. Dalton Trans.*, 2000, 3735–3744.

[565] E. Shugam and H. Zhdanov, *Acta Physicochim. URSS*, 1945, **20**, 247–252.

[566] T. Kitazawa, T. Kikuyama, M. Takeda and T. Iwamoto, *J. Chem. Soc. Dalton Trans.*, 1995, 3715–3720.

[567] T. Kitazawa, S.-i. Nishikori, R. Kuroda and T. Iwamoto, *J. Chem. Soc. Dalton Trans.*, 1994, 1029–1036.

[568] S. C. Abrahams, L. E. Zyontz and J. L. Bernstein, *J. Chem. Phys.*, 1982, **76**, 5458–5462.

[569] B. F. Hoskins, R. Robson and N. V. Y. Scarlett, *Angew. Chem. Int. Ed. Engl.*, 1995, **34**, 1203–1204.

[570] M. J. Katz, T. Ramnial, H.-Z. Yu and D. B. Leznoff, *J. Am. Chem. Soc.*, 2008, **130**, 10662–10673.

[571] W.-J. Xu, K.-P. Xie, Z.-F. Xiao, W.-X. Zhang and X.-M. Chen, *Cryst. Growth Des.*, 2016, **16**, 7212–7217.

[572] H. D. Duncan, E. O. R. Beake, H. Y. Playford, M. T. Dove and A. E. Phillips, *CrystEngComm*, 2017, **19**, 7316–7321.

[573] W. Zhang, H.-Y. Ye, R. Graf, H. W. Spiess, Y.-F. Yao, R.-Q. Zhu and R.-G. Xiong, *J. Am. Chem. Soc.*, 2013, **135**, 5230–5233.

[574] K. Li, D. H. Olson, J. Seidel, T. J. Emge, H. Gong, H. Zeng and J. Li, *J. Am. Chem. Soc.*, 2009, **131**, 10368–10369.

[575] A. Demessence, C. Boissière, D. Grosso, P. Horcajada, C. Serre, G. Férey, G. J. A. A. Soler-Illia and C. Sanchez, *J. Mater. Chem.*, 2010, **20**, 7676–7681.

[576] S. A. Moggach, T. D. Bennett and A. K. Cheetham, *Angew. Chem. Int. Ed.*, 2009, **48**, 7087–7089.

[577] D. Fairen-Jimenez, S. A. Moggach, M. T. Wharmby, P. A. Wright, S. Parsons and T. Düren, *J. Am. Chem. Soc.*, 2011, **133**, 8900–8902.

[578] C. L. Hobday, T. D. Bennett, D. Fairen-Jimenez, A. J. Graham, C. A. Morrison, D. R. Allan, T. Düren and S. A. Moggach, *J. Am. Chem. Soc.*, 2018, **140**, 382–387.

[579] I. E. Collings, A. B. Cairns, A. L. Thompson, J. E. Parker, C. C. Tang, M. G. Tucker, J. Catafesta, C. Levelut, J. Haines, V. Dmitriev, P. Pattison and A. L. Goodwin, *J. Am. Chem. Soc.*, 2013, **135**, 7610–7620.

[580] A. Knebel, B. Geppert, K. Volgmann, D. I. Kolokolov, A. G. Stepanov, J. Twiefel, P. Heitjans, D. Volkmer and J. Caro, *Science*, 2017, **358**, 347–351.

[581] S. P. Gabuda and S. G. Kozlova, *J. Chem. Phys.*, 2014, **141**, 044701.

[582] S. P. Gabuda, S. G. Kozlova, D. G. Samsonenko, D. N. Dybtsev and V. P. Fedin, *J. Phys. Chem. C*, 2011, **115**, 20460–20465.

[583] X. Jiang and H.-Z. Kou, *Chem. Commun.*, 2016, **52**, 2952–2955.

[584] S. J. Hunt, M. J. Cliffe, J. A. Hill, A. B. Cairns, N. P. Funnell and A. L. Goodwin, *CrystEngComm*, 2015, **17**, 361–369.

[585] L. Longley, N. Li, F. Wei and T. D. Bennett, *R. Soc. Open Sci.*, 2017, **4**, 171355.

[586] E. C. Spencer, M. S. R. N. Kiran, W. Li, U. Ramamurty, N. L. Ross and A. K. Cheetham, *Angew. Chem. Int. Ed.*, 2014, **53**, 5583–5586.

Appendix A

This Appendix contains derivations of the dynamical matrices used to identify RUMs in Chapter 3. I am grateful to Emma Wolpert for helping me understand the derivation of Δr.

As noted, the dynamical matrix approach is a convenient method for expressing and calculating phonon frequencies in the form of an eigenvector problem:

$$\mathbf{D}(\mathbf{k}) \times \mathbf{e}(\mathbf{k}) = \omega^2(\mathbf{k}) \times \mathbf{e}(\mathbf{k}), \tag{A0.1}$$

where $\mathbf{D}(\mathbf{k})$ represents the dynamical matrix, $\mathbf{e}(\mathbf{k})$ is the mode eigenvector and $\omega(\mathbf{k})$ is the phonon frequency. The elements of $\mathbf{D}(\mathbf{k})$ are derived from the lattice potential and explicitly given by[355]

$$D_{\alpha,\beta} = \frac{1}{\sqrt{m_j m_{j'}}} \sum_l \Phi_{\alpha,\beta} \begin{pmatrix} jj' \\ 0l \end{pmatrix} \exp[\mathrm{i}\mathbf{k} \cdot (\mathbf{r}(j'l) - \mathbf{r}(j0)], \tag{A0.2}$$

where m_j and $m_{j'}$ denote the masses of distinct atoms j and j', l indexes the unit cells along which the interactions take place, and the matrix $\Phi_{\alpha,\beta}$ comprises the

force constants through

$$\Phi_{\alpha,\beta}\begin{pmatrix} jj' \\ ll' \end{pmatrix} = \frac{\partial^2 H}{\partial u_\alpha(jl)\partial u_\beta(j'l')}, \tag{A0.3}$$

where H is the Hamiltonian of the system.

For the purpose of finding RUMs, a lattice potential can be designed such that any modes corresponding to RUMs are necessarily zero valued. This process is termed the split-atom approach and involves treating each polyhedron as a unit with three translational and three rotational degrees of freedom.[426] Each rigid polyhedron is joined to its neighbours by harmonic springs with zero equilibrium length and fictitious nonzero force constants. Hence, the lattice energy is equal to zero for modes where the individual polyhedra remain corner sharing. As absolute values of the frequencies are not the objective, the values of masses can be set to unity such that the mass factor vanishes. Furthermore, as the models implemented here only involve one rigid unit, j, per cell, Eq. A0.2 can be simplified to

$$D_{\alpha,\beta} = \sum_l \Phi_{\alpha,\beta}\begin{pmatrix} jj \\ 0l \end{pmatrix} \exp[\mathrm{i}\mathbf{k}\cdot(\mathbf{r}(jl) - \mathbf{r}(j0)]. \tag{A0.4}$$

A1 Conventional perovskites

The energy of a conventional inorganic perovskite in the split-atom approach is given by

$$E(r) = \frac{1}{2}Kr^2 \tag{A1.5}$$

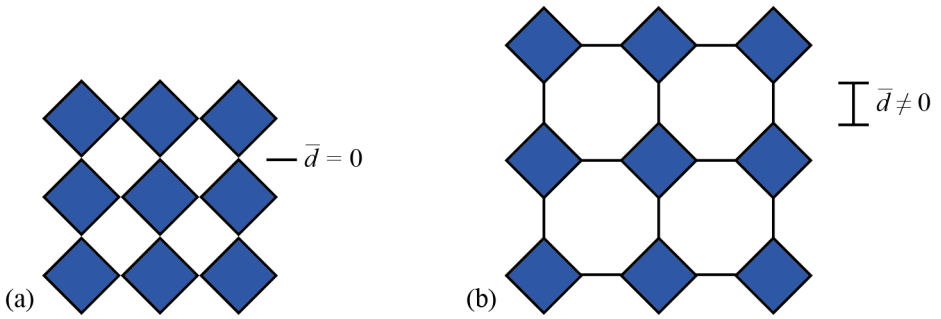


Figure A1.1: A 2D (a) inorganic and (b) molecular perovskite with the equilibrium separation of the rigid units indicated.

where r is the separation between adjacent units and K is the force constant. In a 2D scenario [Fig. A1.1(a)], the Hamiltonian is[426]

$$H = \frac{1}{2}\sum_{m,n}(\dot{u}_{m,n} + \dot{v}_{m,n} + a^2\dot{\theta}^2_{m,n}) + \frac{K}{2}\sum_{m,n}[(u_{m,n} - u_{m+1,n})^2 + (u_{m,n} - u_{m,n+1})^2$$
$$+ (v_{m,n} - v_{m+1,n})^2 + (v_{m,n} - v_{m,n+1})^2 + a^2(\theta_{m,n} - \theta_{m+1,n})^2 + a^2(\theta_{m,n} - \theta_{m,n+1})^2$$
$$+ 2a(u_{m,n} - u_{m,n+1})(\theta_{m,n} + \theta_{m,n+1}) + 2a(v_{m,n} - v_{m+1,n})(\theta_{m,n} + \theta_{m+1,n})], \quad \text{(A1.6)}$$

where m and n index the rigid units and u, v, and θ correspond to translations along $\mathbf{a}$, $\mathbf{b}$ and rigid body rotations within the plane, respectively. Restricting the analysis to nearest neighbours, there are five values of l to consider, namely (0, 0), (1, 0), (−1, 0), (0, 1) and (0, −1) in real space. Since $\mathbf{k} = [k_x\mathbf{a}^* + k_y\mathbf{b}^*]$, the exponential arguments $\mathbf{k}\cdot[\mathbf{r}(jl) - \mathbf{r}(j0)]$ from Eq. A0.4 become 0, $2\pi k_x$, $-2\pi k_x$, $2\pi k_y$, and $-2\pi k_y$.

The top left entry of the 3×3 matrix $\mathbf{D}(\mathbf{k})$ corresponds to $\alpha = \beta = u$ in Eq. A0.3. It is readily computed from Eq. A0.4:

$$\Phi_{\alpha,\beta}\begin{pmatrix} 11 \\ 0l \end{pmatrix} = \frac{\partial^2 H}{\partial u_n(10)\partial u_n(1l)} = \frac{\partial}{\partial u_n(1l)} K[4u_{0,0} - u_{1,0} - u_{0,1} - u_{-1,0} - u_{0,-1}] \tag{A1.7}$$

Substituting these values into Eq. A0.4 gives

$$D_{uu}(\mathbf{k}) = 4K\exp(\mathrm{i}0) - K[\exp(2\pi \mathrm{i}k_x) + \exp(-2\pi \mathrm{i}k_x) + \exp(2\pi \mathrm{i}k_y) + \exp(-2\pi \mathrm{i}k_y)] = 4K(1-\sigma) \tag{A1.8}$$

where

$$\sigma = \frac{\cos(2\pi k_x) - \cos(2\pi k_y)}{2}. \tag{A1.9}$$

A similar procedure can be applied to generate the remaining eight matrix elements and so the full dynamical matrix

$$\mathbf{D}(\mathbf{k}) = \left[\begin{array}{cc|c} 4K(1-\sigma) & 0 & \rho K \\ 0 & 4K(1-\sigma) & -\tau K \\ \hline -\rho K & \tau K & Ka^2(1+\sigma) \end{array}\right]. \tag{A1.10}$$

where

$$\rho = a\mathrm{i}\sin(2\pi k_y) \tag{A1.11}$$

$$\tau = a\mathrm{i}\sin(2\pi k_x) \tag{A1.12}$$

for an inorganic perovskite can be assembled. The RUMs can now be identified as the zero-valued phonon modes, in line with the analysis in Section 3.2.

A2 Molecular perovskites

For a molecular perovskite, the same method applies, but the rigid units are now joined by springs of finite, nonzero length r [Fig. A1.1(b)].[350] As a result, the lattice potential becomes

$$E(r) = \frac{1}{2}K(r - \bar{r})^2 = \frac{1}{2}K(\Delta r)^2, \tag{A2.13}$$

where $\bar{r}$ is the equilibrium bond length between the neighbouring units. Whereas RUMs for inorganic perovskites constitute modes where the polyhedra remain corner sharing, the process for molecular perovskites entails identifying vibrations where the separation between adjacent vertices is preserved. Prior to assembling the dynamical matrix, an expression for Δr has to be derived. For simplicity, a 2D situation is initially considered which may subsequently be generalised to higher dimensions.

A molecular perovskite can be parametrised by vectors from the origin to the corners of the 2D octahedra (squares) denoted $\mathbf{e}$ and inter-unit vectors $\mathbf{r}$ [Fig. A2.2]. Following the application of rotation matrix R and displacement $\mathbf{u}$, the following relationship holds in the limit of small displacements

$$\mathbf{e}_1 + \mathbf{r} - \mathbf{e}_2 = \mathbf{u}_1 + R_1 \cdot \mathbf{e}_1 + \mathbf{r}' - R_2 \cdot \mathbf{e}_2 - \mathbf{u}_2 \tag{A2.14}$$

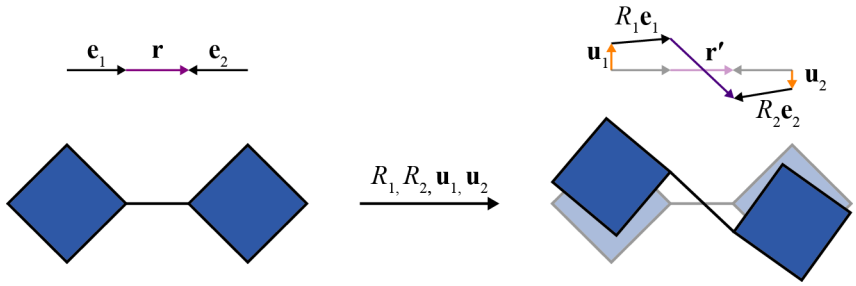


Figure A2.2: Vectorisation of a 2D molecular perovskite. Two rigid units of the aristotype are depicted to the left along with the $\mathbf{e}$ and $\mathbf{r}$ vectors. Following a transformation of rotations, R, and translations, $\mathbf{u}$, a new set of vectors emerges related to the previous set.

Thus, the distance between rigid units following transformation, $\mathbf{r}'$, is

$$\mathbf{r}' = \mathbf{r} + \mathbf{e}_1 - \mathbf{e}_2 - R_1 \cdot \mathbf{e}_1 - \mathbf{u}_1 + R_2 \cdot \mathbf{e}_2 + \mathbf{u}_2 \tag{A2.15}$$

which, for small distortions, can be written in full to yield

$$\begin{bmatrix} r'_x \\ r'_y \end{bmatrix} = \begin{bmatrix} r_x + \theta_1 e_{1y} - u_{1x} - \theta_2 e_{2y} + u_{2x} \\ r_y - \theta_1 e_{1x} - u_{1y} + \theta_2 e_{2x} + u_{2y} \end{bmatrix}, \tag{A2.16}$$

where θ is the angle of rotation. In the limit of $\theta, u << |\mathbf{r}|$, the absolute value of $\mathbf{r}'$ is given by

$$|\mathbf{r}'| \simeq \sqrt{r_x^2 + r_y^2}[1 + \frac{r_x}{r_x^2 + r_y^2}(\theta_1 e_{1y} - u_{1x} - \theta_2 e_{2y} + u_{2x}) + \frac{r_y}{r_x^2 + r_y^2}(-\theta_1 e_{1x} - u_{1y} + \theta_2 e_{2x} + u_{2y})], \tag{A2.17}$$

making use of the approximation $\sqrt{1+x} \simeq 1 + \frac{1}{2}x$. Now, by defining the unit vector $\boldsymbol{\rho}$ in the direction $\mathbf{r}$, *i.e.*

$$\begin{bmatrix} \rho_x \\ \rho_y \end{bmatrix} \simeq \frac{1}{\sqrt{r_x^2 + r_y^2}} \begin{bmatrix} r_x \\ r_y \end{bmatrix}, \tag{A2.18}$$

the equation for $|\mathbf{r}|$ can be rewritten as ρ_x

$$|\mathbf{r}'| \simeq |\mathbf{r}| + \rho_x(\theta_1 e_{1y} - u_{1x} - \theta_2 e_{2y} + u_{2x}) + \rho_y(-\theta_1 e_{1x} - u_{1y} + \theta_2 e_{2x} + u_{2y}) \quad \text{(A2.19)}$$

and so generalised to

$$\Delta r = |\mathbf{r}'| - |\mathbf{r}| \simeq \boldsymbol{\rho} \cdot [(\mathbf{e}_1 - R_1\mathbf{e}_1 - \mathbf{u}_1) - (\mathbf{e}_2 - R_2\mathbf{e}_2 - \mathbf{u}_2)], \quad \text{(A2.20)}$$

thus giving an expression for Δr applicable to higher dimensions. This expression can now be used to find the force constant matrix

$$\Phi = \frac{\partial E^2}{\partial g, \partial h} \quad \text{(A2.21)}$$

for $g, h \in \{u_x, u_v, \theta\}$. When applied to Δr, this simplifies to

$$\phi_{gh} = K \frac{\partial \Delta r}{\partial h} \frac{\partial \Delta r}{\partial g} \quad \text{(A2.22)}$$

as any second derivatives vanish and the full force constant matrix, Φ, becomes

$$\Phi = K \begin{bmatrix} -\rho_x^2 & -\rho_x\rho_y & \rho_x^2 e_{2y} + \rho_x\rho_y e_{2x} \\ -\rho_x\rho_y & -\rho_y^2 & \rho_x\rho_y e_{2y} - \rho_y^2 e_{2x} \\ \rho_x^2 e_{1y} - \rho_x\rho_y e_{1x} & \rho_x\rho_y e_{1y} - \rho_y^2 e_{1x} & (\rho_x e_{1y} - \rho_y e_{1x})(-\rho_x e_{2y} + \rho_y e_{2x}) \end{bmatrix} \quad \text{(A2.23)}$$

From here, the final result is obtained as

$$\mathbf{D}(\mathbf{k}) = \left[\begin{array}{cc|c} 1-\cos(2\pi k_x) & 0 & 0 \\ 0 & 1-\cos(2\pi k_y) & 0 \\ \hline 0 & 0 & 0 \end{array}\right]. \tag{A2.24}$$

Appendix B

This Appendix explores the Monte Carlo model presented in Chapter 4 in more detail, by considering finite size effects and the impact of alternative vacancy order patterns in the defective Prussian blue analogues.

B1 Finite size effects

Finite size effects were investigated for the primitive system by varying the dimensions of the supercell from 4 to 20 unit cells and scaling the convergence criterion accordingly. Simulated annealing was performed as described in Chapter 4, but the MC loop exited after the eleventh cooling step, *i.e.* when $T \approx 1.72J$. 10 independent simulations were conducted and the outcomes averaged. The results are presented in Fig. B1.1 and it is clear that increasing the boxsize above 16—the value used in the simulations in the main Chapter—does not appreciably alter the critical behaviour.

B2 Alternative vacancy distributions

To explore any dependence of the orbital order on the vacancy order for the defective Prussian blue analogues, two additional vacancy distributions were considered

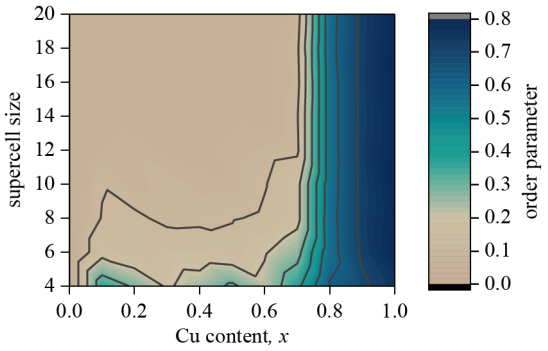


Figure B1.1: Finite size effects of the orbital order simulation for primitive systems. The order parameter is shown as a function of the size of the supercell and the Cu concentration for $T \approx 1.72J$.

and compared to the results from the vacancy arrangement in the main Chapter, hereafter referred to as the semi-ordered distribution.

Firstly, a random vacancy arrangement was modelled. The Monte Carlo simulations were carried out analogously to previous descriptions [Section 4.3.4], except that the vacancies were allocated randomly across the available B′-sites. Although this model easily leads to unphysical distributions of defects, it serves as an interesting comparison to the semi-ordered vacancy arrangements [Chapter 4]. By and large, the orbitally ordered region in the phase diagram is of similar size as in the semi-ordered model [Fig. B2.2(a) and 4.13]. However, the difference map given by $\eta_{\mathrm{so}} - \eta_{\mathrm{rdm}}$—where η_{so} and η_{rdm} represent the magnitudes of the order parameters for the semi-ordered and random model, respectively—highlights the differences [Fig. B2.2(b)]. The orbital order in a system with randomly allocated vacancies persists to higher values of $\frac{T}{J}$ than in the semi-ordered model, yet falls off more quickly with decreasing x. However, the discrepancies are relatively minor and are unlikely to be detectable experimentally—at least by XRD.

Secondly, a vacancy order derived from experimental data was considered. In

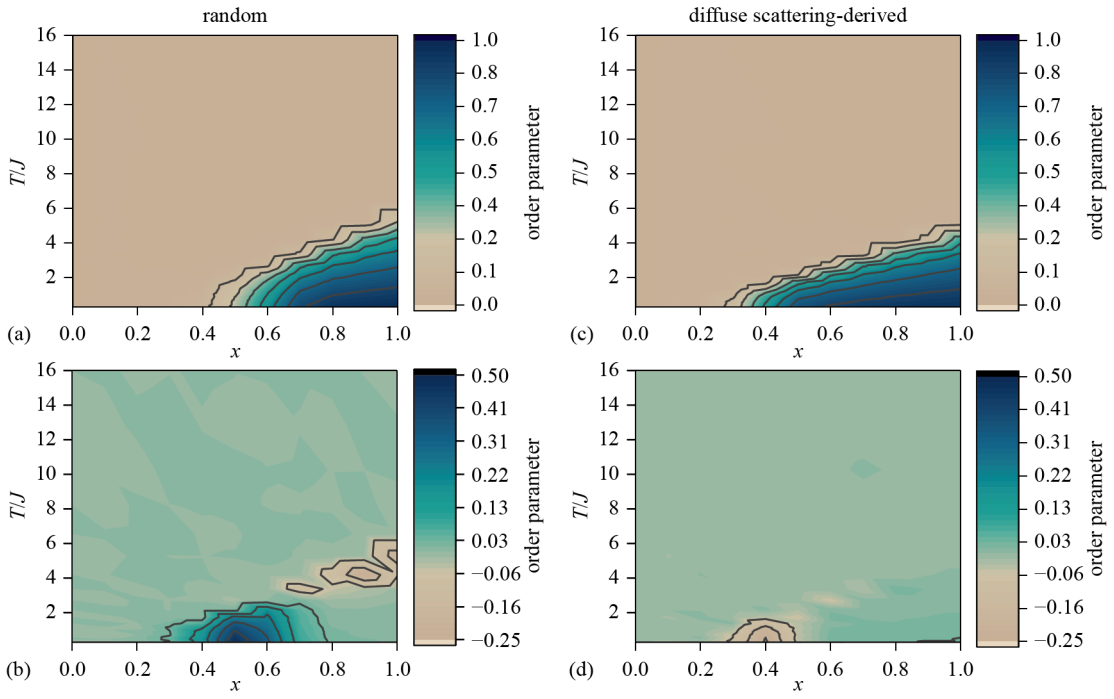


Figure B2.2: (a) The 2D orbital order phase diagrams for Prussian blue analogues with randomly allocated defects and (b) a difference map relative to the semi-ordered vacancy distribution. (c)–(d) The corresponding diagrams for the diffuse scattering-derived defect arrangements.

an as-yet unpublished study, Simonov *et al.* extracted information regarding the vacancy order in Prussian blue analogues on the basis of diffuse scattering of single crystal samples [Appendix D]. In their model, the arrangements of the defects are dictated by the (arbitrary) temperature and the ratio J_1/J_2, where the force constants J_1 and J_2 stipulate the preference for electroneutrality (homogenous distribution of vacancies across the crystallite) and centrosymmetry (*trans*-configuration of vacancies on the octahedra), respectively. Inspired by these results, the orbital order MC simulations were repeated employing 5 different vacancy distributions with $J_1/J_2 = 1$ and $\log T = 2.05$–2.55 provided by Arkadiy Simonov. These parameter values are similar to those found for $Mn_3[Mn(CN)_6]_2$ and $Mn_3[Fe(CN)_6]_2$. Except for a slightly smaller supercell size ($12 \times 12 \times 12$), the simulations were carried out as previously discussed. The calculations were repeated twice per distribution;

amounting to the usual 10 independent runs prior to averaging. The resulting 2D phase diagram for this diffuse-scattering derived vacancy arrangement bears a strong resemblance to the results for the semi-ordered distribution [Fig. B2.2(c)–(d)].

Consequently, it can be tentatively concluded that orbital order–disorder phenomena in defective Prussian blue analogues are not strongly sensitive to the arrangement of vacancies within the Prussian blue framework. However, exploration of other diffuse-scattering derived vacancy ordering patterns may be worthwhile.

Appendix C

C1 $[C(NH_2)_3]Mn_{1-x}Cu_x(HCOO)_3$

Table C1.1: Crystallographic data for $[C(NH_2)_3]Mn_{1-x}Cu_x(HCOO)_3$ at ambient conditions.

x_{nom}	a/Å	b/Å	c/Å	Strain	x_{AAS}
0	8.52581(11)	9.05134(14)	12.00074(15)	0.4331(14)	0
0.1	8.51500(19)	9.0401(2)	11.9496(2)	0.705(23)	0.105(8)
0.2	8.49991(17)	9.0281(2)	11.88590(19)	0.584(21)	0.22(2)
0.3	8.50206(13)	9.02937(16)	11.84943(15)	0.5533(17)	0.274(8)
0.4	8.49672(15)	9.02330(17)	11.79824(17)	0.4883(18)	0.38(3)
0.5	8.48846(16)	9.01912(18)	11.7477(2)	0.4707(19)	0.476(10)
0.6	8.48657(18)	9.01850(18)	11.6960(3)	0.4196(17)	0.556(7)
0.7	8.49151(15)	9.02091(17)	11.5939(3)	0.332(2)	0.656(9)
0.8	8.50590(13)	9.02368(16)	11.52219(19)	0.2306(18)	0.828(6)
0.9	8.52271(11)	9.02909(13)	11.44052(16)	0.1198(13)	0.889(5)
1	8.52734(6)	9.03341(7)	11.35840(8)	0.0559(7)	1

C2 $B_{1-x}Cu_x[Pt(CN)_6]$

C2.1 $Mn_{1-x}Cu_x[Pt(CN)_6]$

Table C2.2: Crystallographic data for $Mn_{1-x}Cu_x[Pt(CN)_6]$ at ambient conditions. Green entries were fixed during the refinement.

x_{nom}	a_{c}/Å	Strain	a_{t}/Å	c_t/Å	Strain	Tet. fraction	x_{AAS}
0	10.75416(3)	0.1825(8)				0	0
0.1	10.75507(4)	0.3007(12)				0	0.005(19)
0.2	10.73307(13)	0.555(4)	7.32612(18)	10.9541(5)	0.494(6)	0.3679	0.371(10)
0.3	10.73298(12)	0.526(4)	7.31026(9)	10.9738(2)	0.33(3)	0.5088	0.480(8)
0.4	10.73204(9)	0.415(3)	7.30231(5)	10.98807(13)	0.2698(18)	0.5674	0.563(8)
0.5	10.71892(10)	0.396(3)	7.28931(3)	10.99939(8)	0.1954(11)	0.6833	0.691(18)
0.6	10.7371(15)	0.4(5)	7.28680(2)	11.00952(6)	0.2134(7)	0.9894	0.976(2)
0.7			7.28232(2)	11.01364(4)	0.1340(5)	1	0.988(3)
0.8			7.28190(2)	11.02104(4)	0.1666(5)	1	0.991(2)
0.9			7.27853(2)	11.02413(5)	0.1422(6)	1	0.997(2)
1			7.276160(10)	11.02891(3)	0.0935(4)	1	1

Table C2.3: Crystallographic data for $Mn_{1-x}Cu_x[Pt(CN)_6]$ at 100 K. Green entries were fixed during the refinement.

x_{nom}	a_{c}/Å	Strain	a_{t}/Å	c_t/Å	Strain	Tet. fraction	x_{AAS}
0	10.76755(3)	0.2026(10)				0	0
0.1	10.76702(4)	0.2698(12)				0	0.005(19)
0.2	10.74541(13)	0.537(4)	7.3332(2)	10.9420(6)	0.565(7)	0.3617	0.371(10)
0.3	10.74463(14)	0.663(5)	7.32253(14)	10.9340(5)	0.629(5)	0.4809	0.480(8)
0.4	10.74267(9)	0.441(3)	7.30796(6)	10.96197(16)	0.348(2)	0.5596	0.563(8)
0.5	10.73119(10)	0.419(3)	7.29458(4)	10.98306(9)	0.2577(13)	0.6777	0.691(18)
0.6	10.7523(4)	0.4(3)	7.29294(3)	10.99274(7)	0.2776(9)	0.9899	0.976(2)
0.7			7.28831(2)	10.99531(6)	0.2118(8)	1	0.988(3)
0.8			7.28798(2)	11.00562(4)	0.1718(5)	1	0.991(2)
0.9			7.28521(2)	11.01379(6)	0.1444(7)	1	0.997(2)
1			7.28212(3)	11.01200(7)	0.1541(8)	1	1

Table C2.4: Crystallographic data for $Mn_{1-x}Cu_x[Pt(CN)_6]$ at 500 K. Green entries were fixed during the refinement.

x_{nom}	a_{c}/Å	Strain	a_{t}/Å	c_t/Å	Strain	Tet. fraction	x_{AAS}
0	10.74269(3)	0.1910(9)				0	0
0.1	10.73989(4)	0.2763(11)				0	0.005(19)
0.2	10.71983(13)	0.597(5)	7.3571(4)	10.8168(12)	1.65(2)	0.4154	0.371(10)
0.3	10.71949(17)	0.712(7)	7.3506(4)	10.8117(19)	1.538(15)	0.5771	0.480(8)
0.4	10.71891(10)	0.513(3)	7.30758(10)	10.9121(3)	0.574(4)	0.5366	0.563(8)
0.5	10.70582(12)	0.524(4)	7.29367(7)	10.9109(2)	0.505(3)	0.6404	0.691(18)
0.6	10.7350(13)	0.09(13)	7.28758(7)	10.9580(2)	0.468(2)	0.9894	0.976(2)
0.7			7.28162(6)	10.96414(19)	0.353(2)	1	0.988(3)
0.8			7.27727(5)	10.98202(16)	0.2905(17)	1	0.991(2)
0.9			7.28221(6)	11.00966(18)	0.480(2)	1	0.997(2)
1			7.26998(4)	11.01636(14)	0.1849(14)	1	1

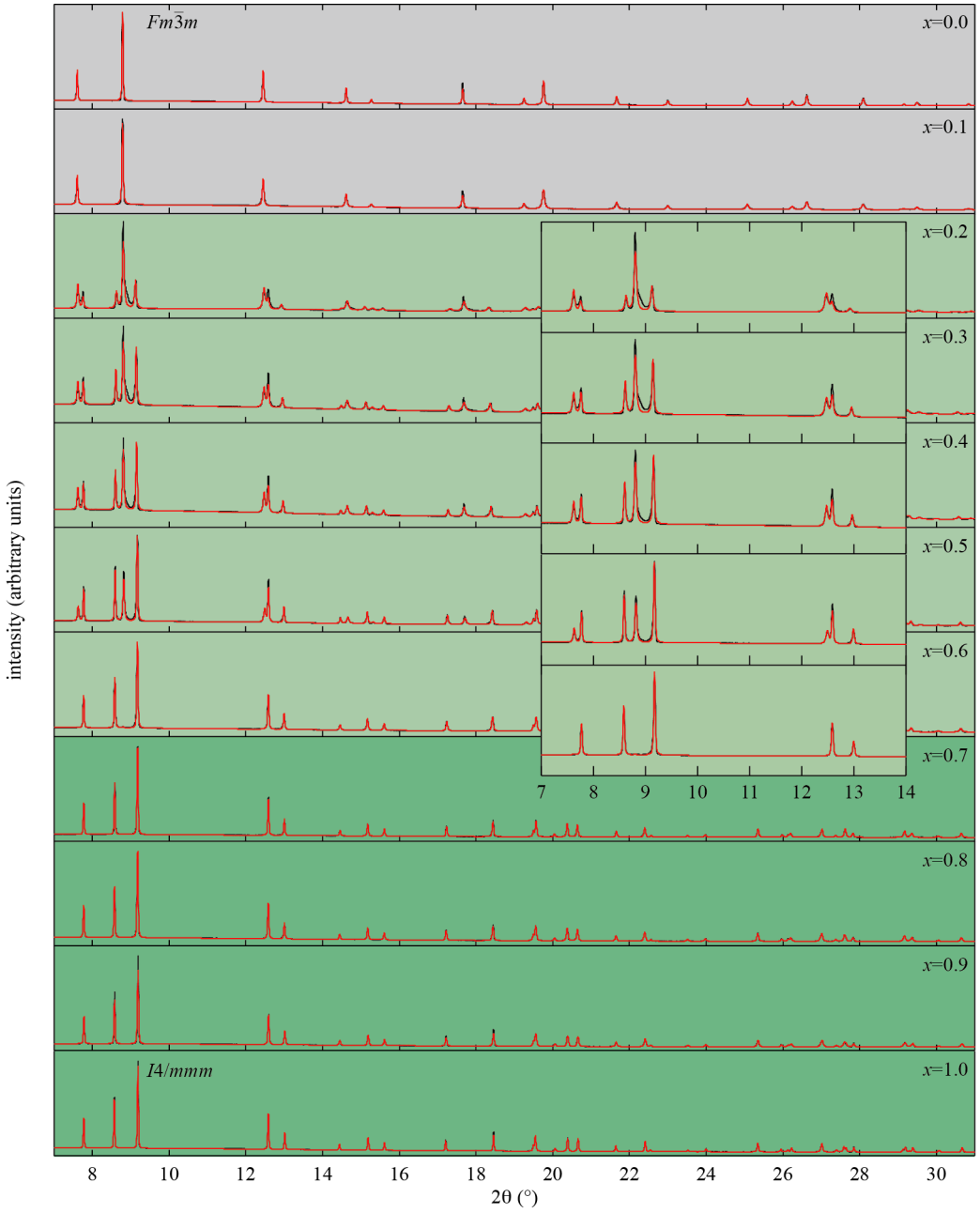


Figure C2.1: Constrained Rietveld fits of $(Mn_{1-x}Cu_x)[Pt(CN)_6]$ at ambient conditions. Grey and green indicate cubic and tetragonal phases, respectively, and pale green represents two-phase refinements. The calculated diffraction pattern is shown in red and the experimental in black.

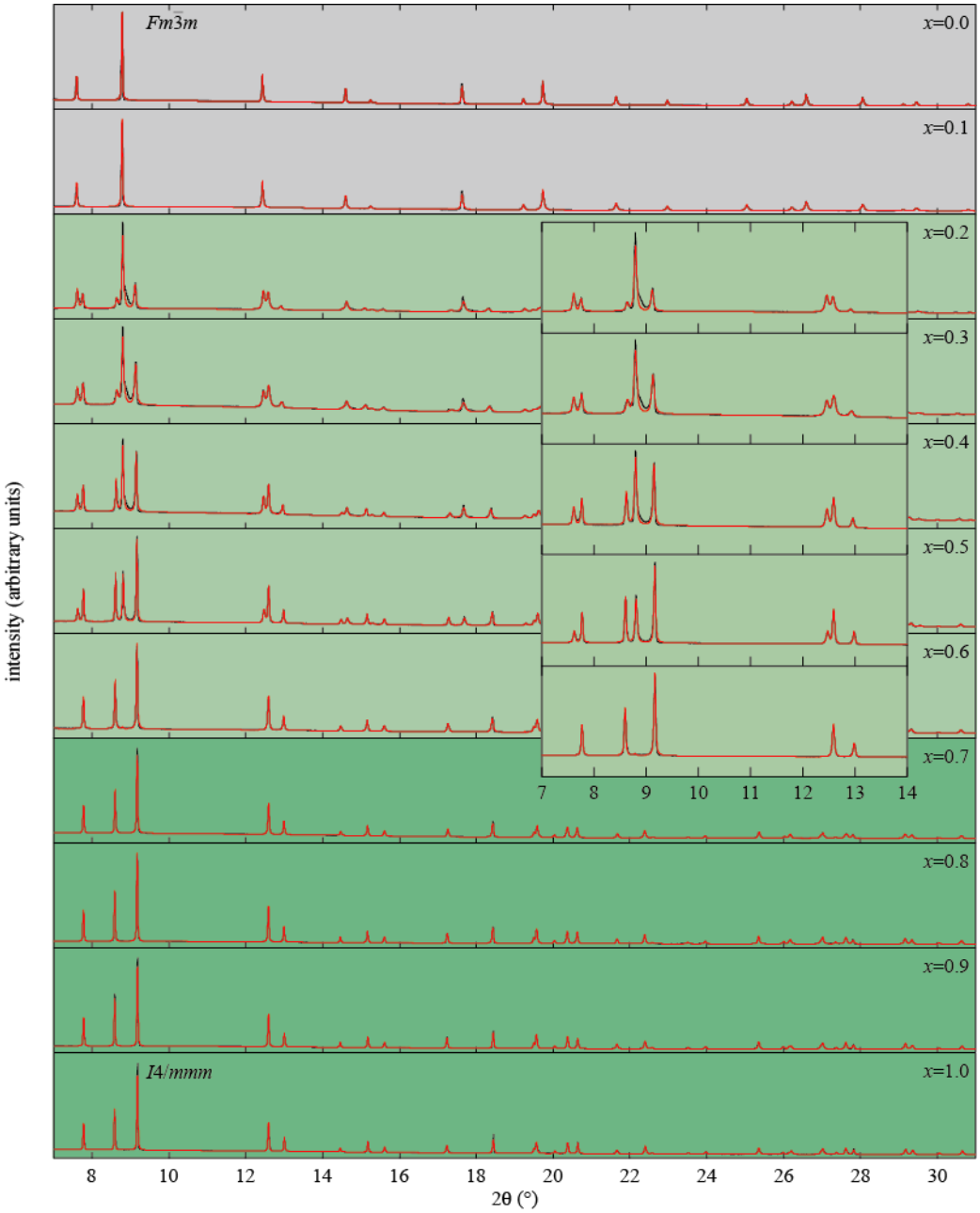


Figure C2.2: Pawley fits of the PXRD patterns of $(Mn_{1-x}Cu_x)[Pt(CN)_6]$ at 100 K. Grey and green indicate cubic and tetragonal phases, respectively, and pale green represents two-phase refinements. The calculated diffraction pattern is shown in red and the experimental in black.

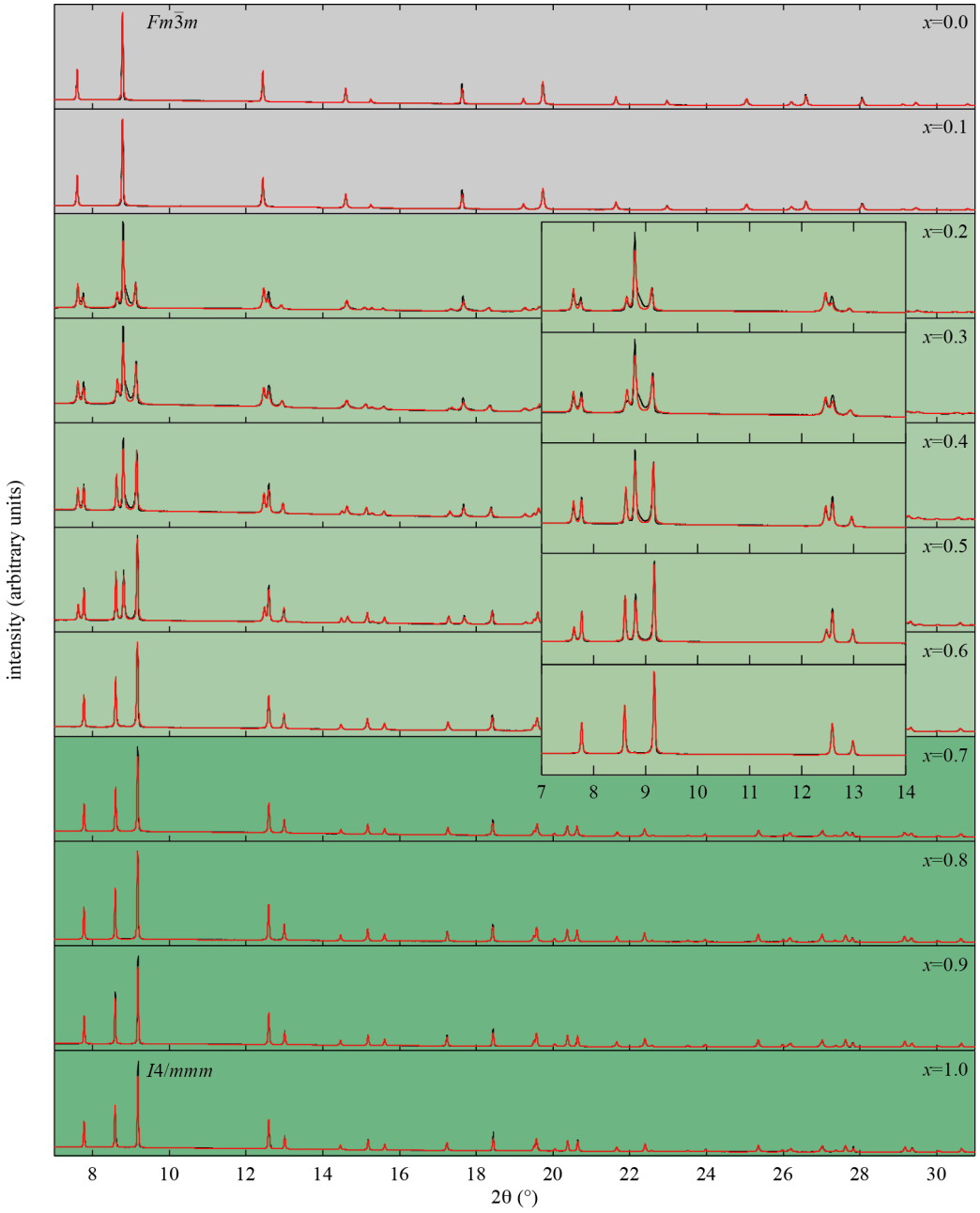


Figure C2.3: Constrained Rietveld fits of the PXRD patterns of $(Mn_{1-x}Cu_x)[Pt(CN)_6]$ at 100 K. Grey and green indicate cubic and tetragonal phases, respectively, and pale green represents two-phase refinements. The calculated diffraction pattern is shown in red and the experimental in black.

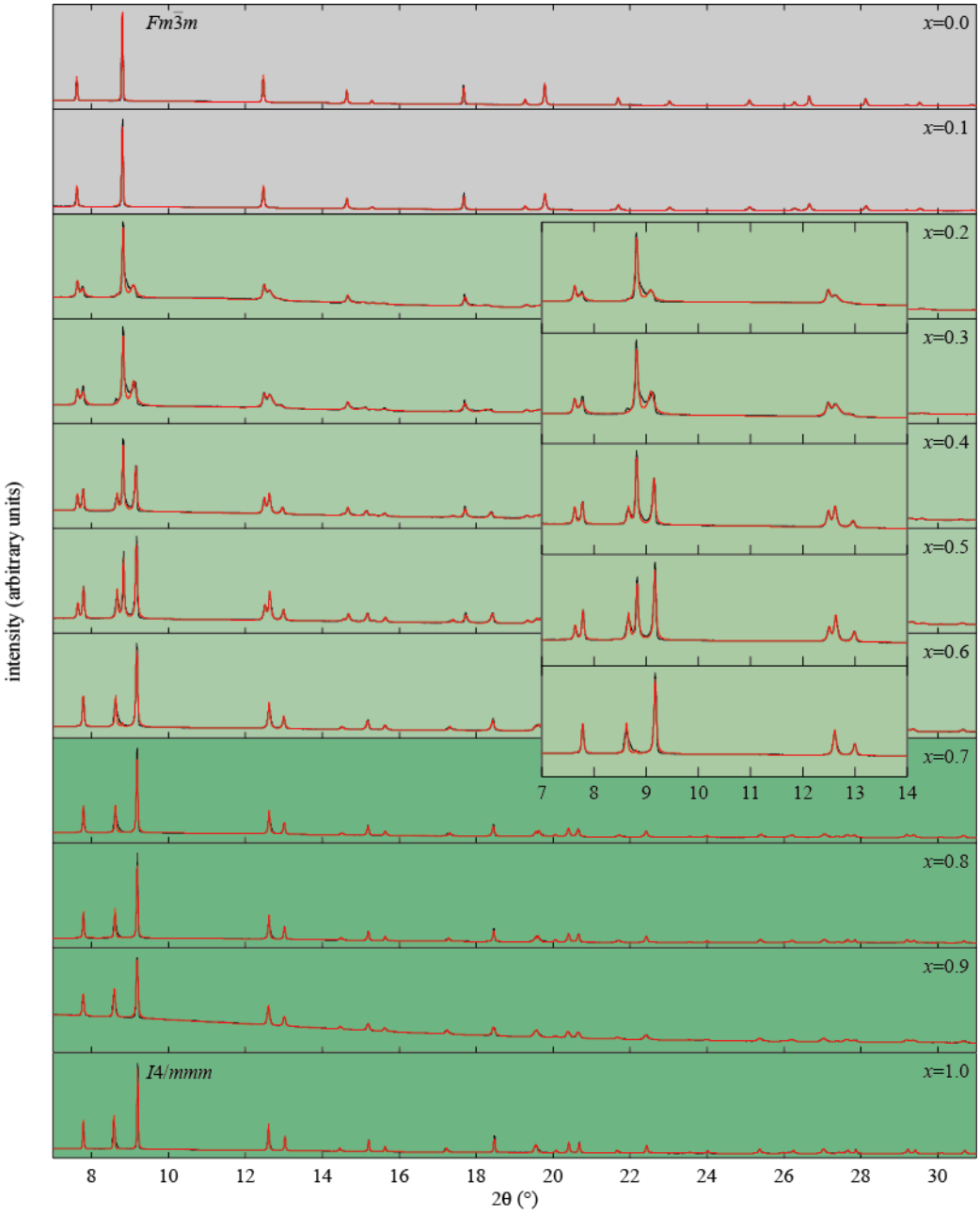


Figure C2.4: Pawley fits of the PXRD patterns of $(Mn_{1-x}Cu_x)[Pt(CN)_6]$ at 500 K. Grey and green indicate cubic and tetragonal phases, respectively, and pale green represents two-phase refinements. The calculated diffraction pattern is shown in red and the experimental in black.

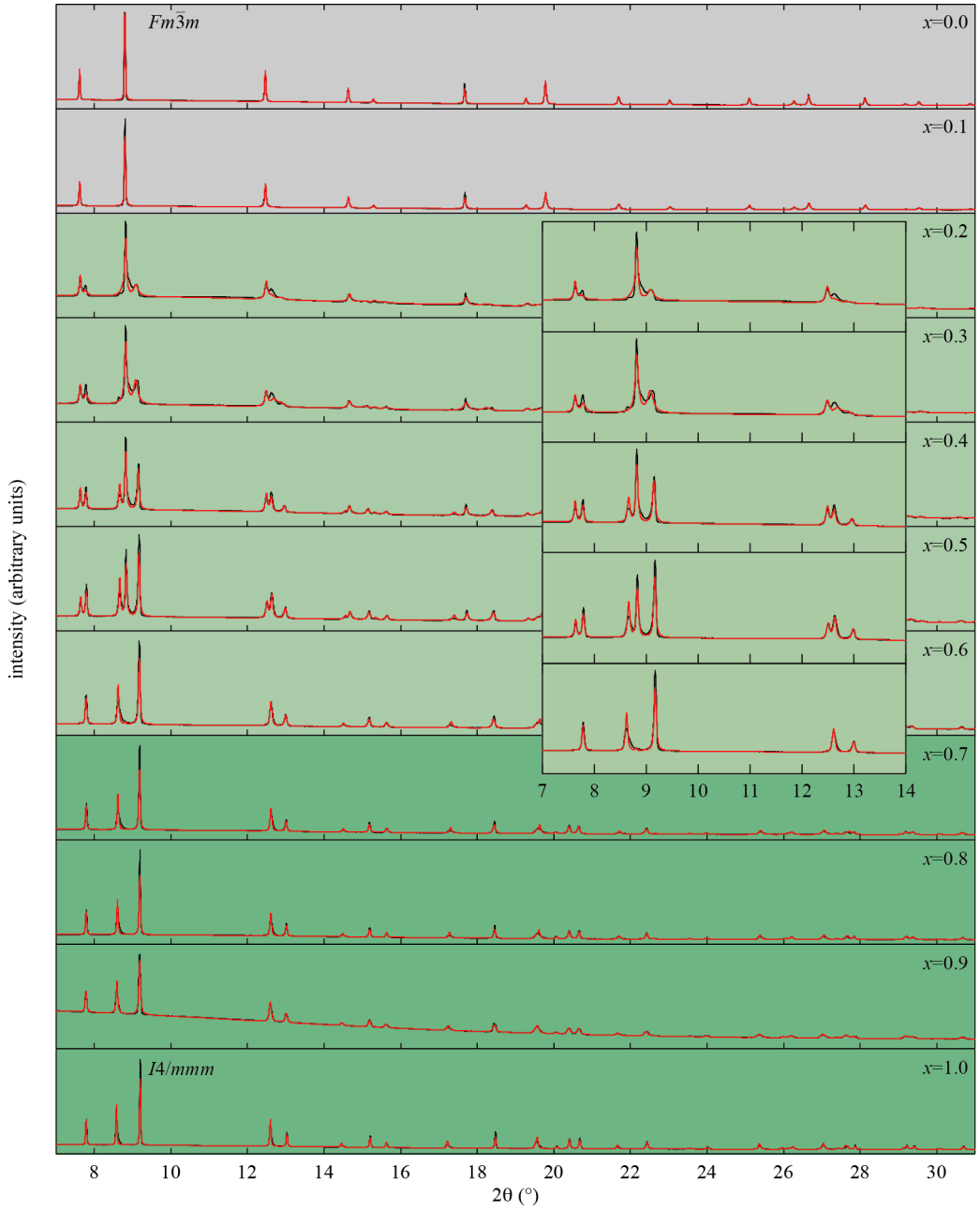


Figure C2.5: Constrained Rietveld fits of the PXRD patterns of $(Mn_{1-x}Cu_x)[Pt(CN)_6]$ at 500 K. Grey and green indicate cubic and tetragonal phases, respectively, and pale green represents two-phase refinements. The calculated diffraction pattern is shown in red and the experimental in black.

C2.2 $\mathbf{Fe_{1-x}Cu_x[Pt(CN)_6]}$

The series $Fe_{1-x}Cu_x[Pt(CN)_6]$ exhibits similar behaviour to $Mn_{1-x}Cu_x[Pt(CN)_6]$ insofar as it contains a cubic phase transitioning into a tetragonal phase upon increasing x [Fig. C2.6–C2.7 and Table C2.5]. However, the onset of the tetragonal phase occurs at higher nominal values of x (0.5) relative to the B = Mn system. Moreover, a series of reflections not predicted by the cubic $Fm\bar{3}m$ or tetragonal $I4/mmm$ phases were sometimes observed, mainly in the region 2θ = 10–12° (d = 4.74–3.95 Å). These peaks only appear in mixed-metal phases and are strongly dependent on synthesis conditions in a nontrivial manner. They may originate from a minority polymorph, an undesired side-product, or comprise diffuse scattering indicative of correlated disorder within either of the main phases. There is no phase transition upon heating or cooling [Fig. C2.8–C2.11 and Tables C2.6–C2.7].

Table C2.5: Crystallographic data for $Fe_{1-x}Cu_x[Pt(CN)_6]$ at ambient conditions.

x_{nom}	a_{c}/Å	Strain	a_{t}/Å	c_t/Å	Strain	Tet. fraction	x_{AAS}
0	10.61172(2)	0.0873(5)				0	0
0.1	10.61285(3)	0.1593(8)				0	0.157(12)
0.2	10.60599(2)	0.1236(7)				0	0.02(3)
0.3	10.60332(4)	0.1674(14)				0	0.256(12)
0.4	10.58514(6)	0.4442(17)				0	0.491(13)
0.5	10.57281(9)	0.728(3)	7.3179(2)	10.9009(8)	0.772(9)	0.2580	0.73(7)
0.6	10.56867(14)	0.965(4)	7.29463(6)	10.95841(17)	0.382(2)	0.5976	0.772(12)
0.7	10.55206(13)	1.041(4)	7.29247(7)	10.97881(17)	0.390(3)	0.4307	0.865(15)
0.8			7.28252(3)	10.9944(7)	0.1937(9)	1	0.960(8)
0.9			7.280040(10)	11.01268(4)	0.1515(5)	1	1.028(10)
1			7.276160(10)	11.02891(3)	0.0935(4)	1	1

Table C2.6: Crystallographic data for $Fe_{1-x}Cu_x[Pt(CN)_6]$ at 100 K.

x_{nom}	a_{c}/Å	Strain	a_{t}/Å	c_t/Å	Strain	Tet. fraction	x_{AAS}
0	10.61548(2)	0.0922(5)				0	0
0.1	10.61618(3)	0.1845(8)				0	0.157(12)
0.2	10.61685(3)	0.1689(7)				0	0.02(3)
0.3	10.62982(2)	0.1200(5)				0	0.256(12)
0.4	10.58826(5)	0.4326(15)				0	0.491(13)
0.5	10.58237(11)	0.779(4)	7.3268(3)	10.903(1)	0.860(12)	0.2521	0.73(7)
0.6	10.5713(15)	1.008(5)	7.30215(6)	10.9155(2)	0.424(3)	0.4433	0.772(12)
0.7	10.5552(5)	2.43(2)	7.30560(9)	10.9239(3)	0.659(4)	0.4740	0.865(15)
0.8			7.29229(4)	10.99777(10)	0.2697(13)	1	0.960(8)
0.9			7.28488(3)	10.98501(9)	0.2290(11)	1	1.028(10)
1			7.28212(3)	11.01200(7)	0.1541(8)	1	1

Table C2.7: Crystallographic data for $Fe_{1-x}Cu_x[Pt(CN)_6]$ at 500 K.

x_{nom}	a_{c}/Å	Strain	a_{t}/Å	c_t/Å	Strain	Tet. fraction	x_{AAS}
0	10.58923(2)	0.2045(7)				0	0
0.1	10.59337(4)	0.3154(11)				0	0.157(12)
0.2	10.59949(2)	0.1436(7)				0	0.02(3)
0.3	10.58890(6)	0.2079(18)				0	0.256(12)
0.4	10.56269(6)	0.4592(19)				0	0.491(13)
0.5	10.55581(11)	0.786(4)	7.3314(3)	10.8088(13)	0.937(14)	0.2469	0.73(7)
0.6	10.55252(14)	1.048(5)	7.31458(11)	10.7998(4)	0.650(5)	0.4132	0.772(12)
0.7	10.54329(8)	0.790(3)	7.30164(11)	10.8620(4)	0.683(5)	0.3611	0.865(15)
0.8			7.30537(15)	10.8284(6)	0.941(6)	1	0.960(8)
0.9			7.27734(7)	10.9613(3)	0.389(3)	1	1.028(10)
1			7.26998(4)	11.01636(14)	0.1849(14)	1	1

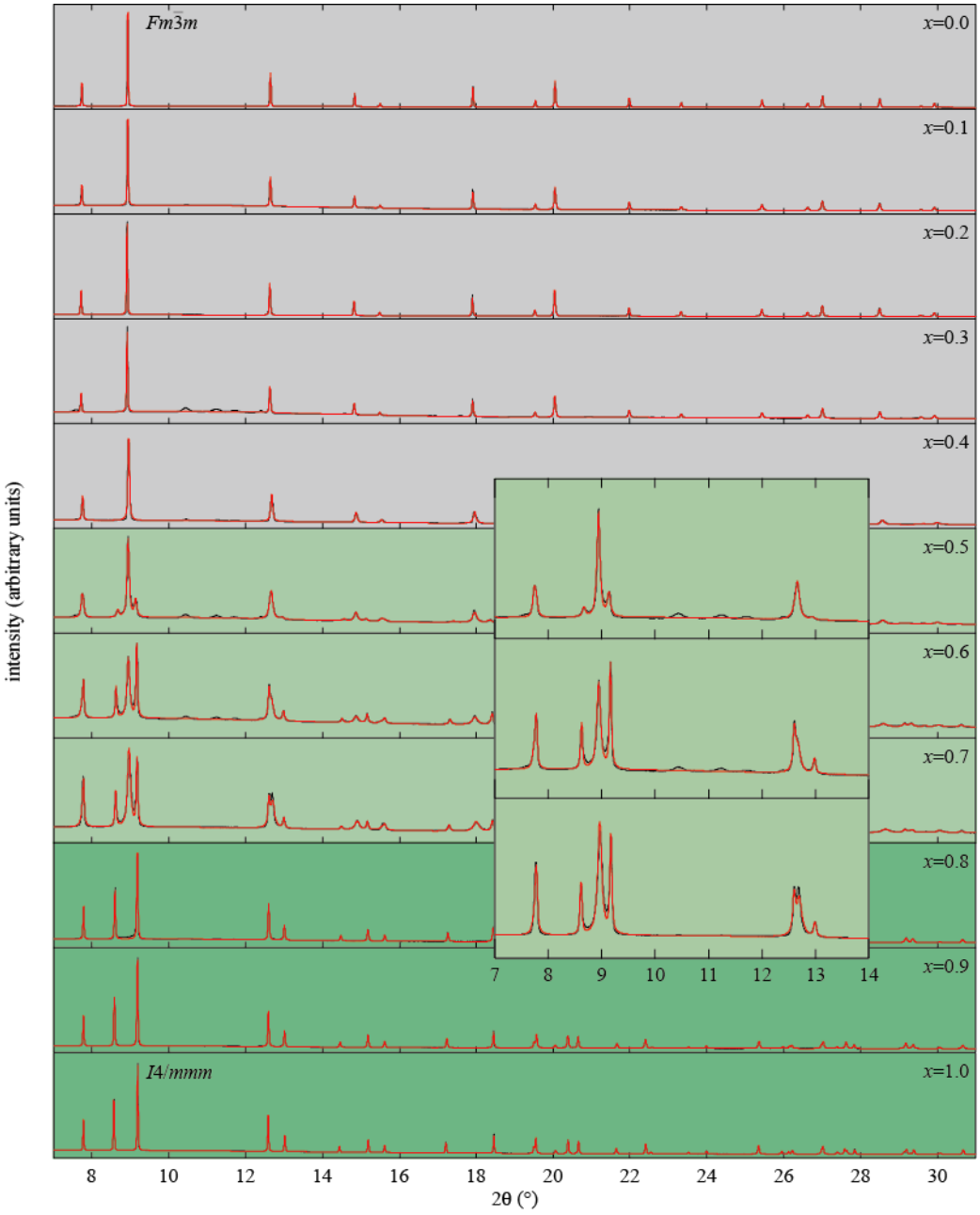


Figure C2.6: Pawley fits of the PXRD patterns of $Fe_{1-x}Cu_x[Pt(CN)_6]$ at ambient conditions. Grey and green indicate cubic and tetragonal phases, respectively, and pale green represents two-phase refinements. The calculated diffraction pattern is shown in red and the experimental in black.

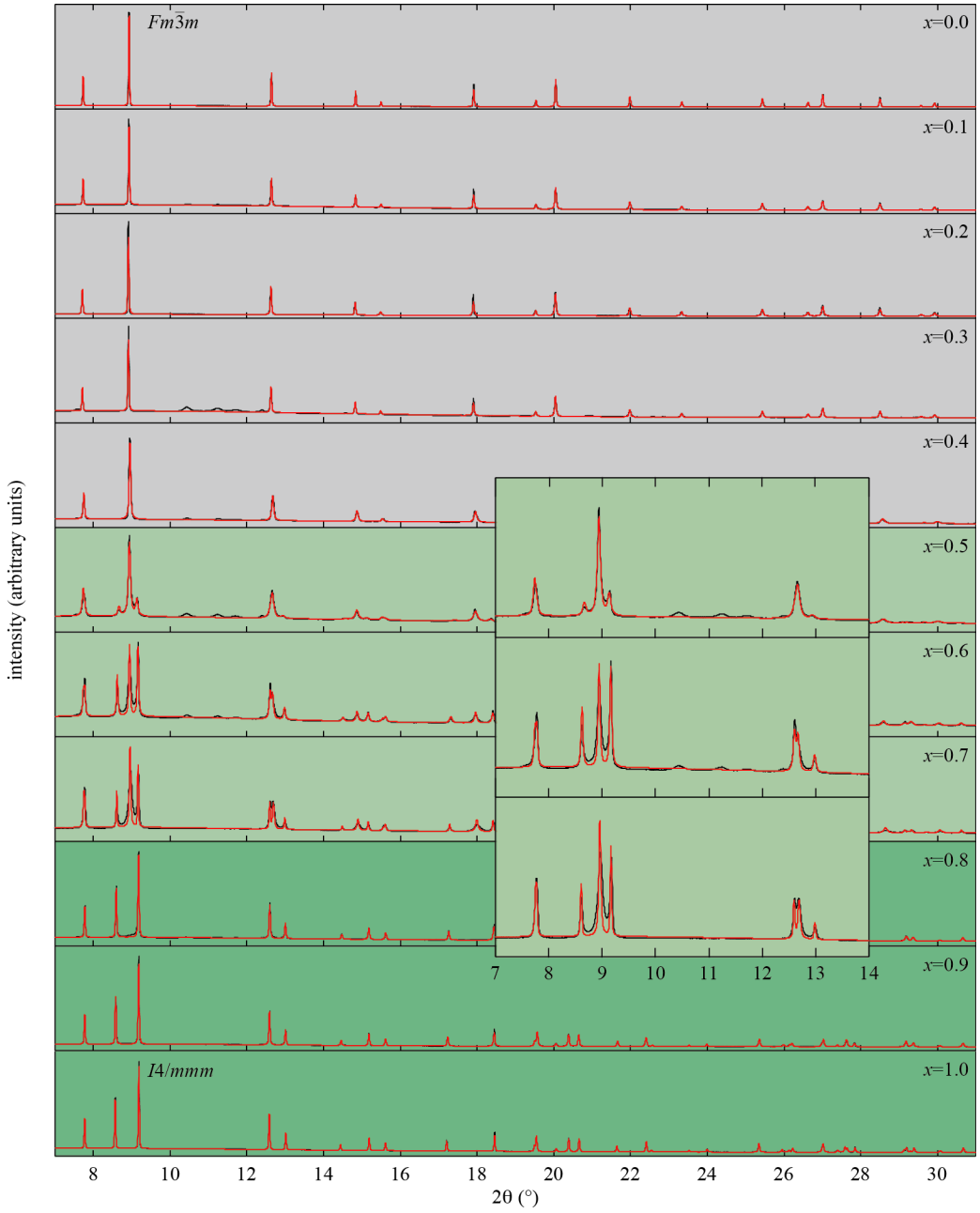


Figure C2.7: Constrained Rietveld fits of the PXRD patterns of $Fe_{1-x}Cu_x[Pt(CN)_6]$ at ambient conditions. Grey and green indicate cubic and tetragonal phases, respectively, and pale green represents two-phase refinements. The calculated diffraction pattern is shown in red and the experimental in black.

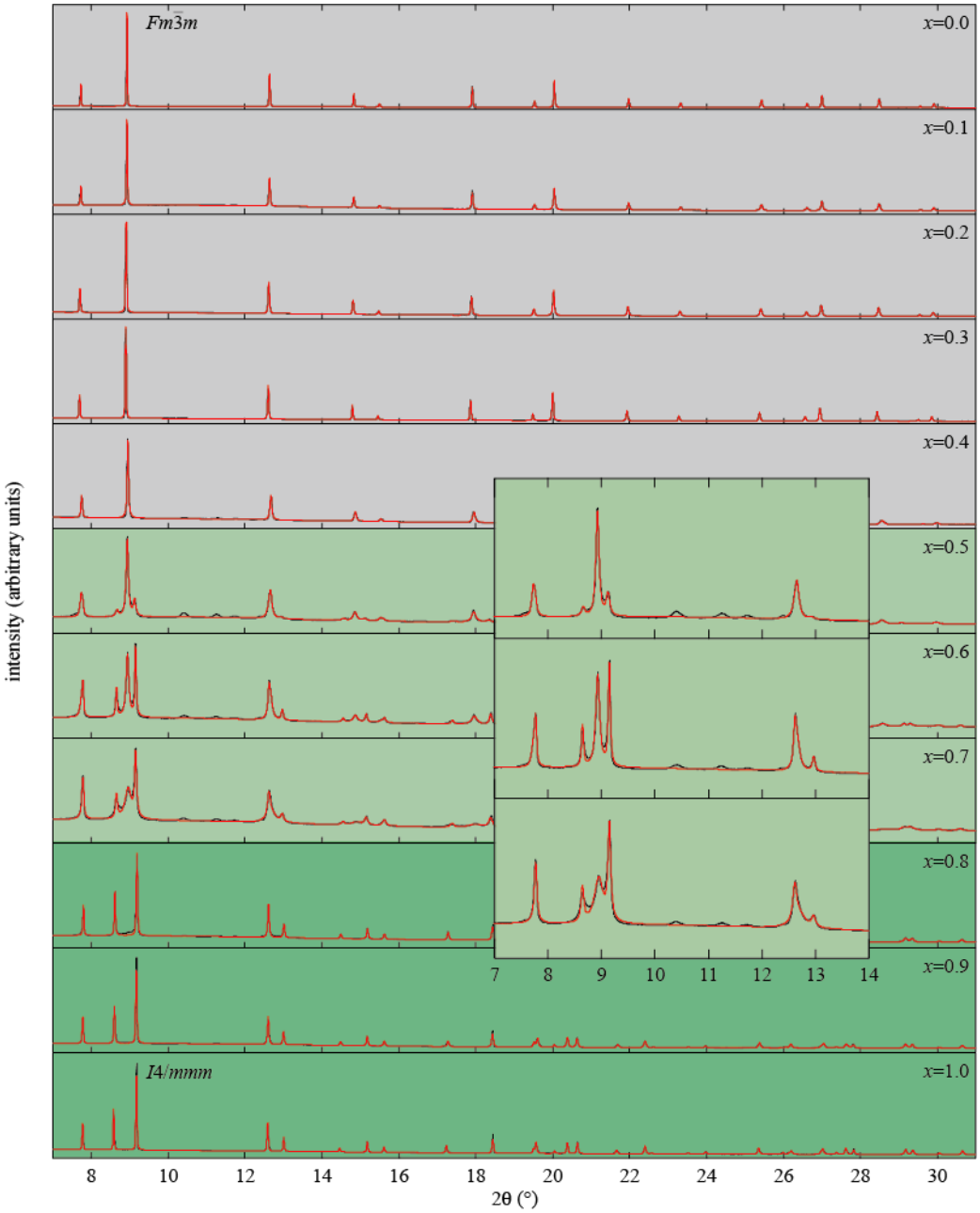


Figure C2.8: Pawley fits of the PXRD patterns of $Fe_{1-x}Cu_x[Pt(CN)_6]$ at 100 K. Grey and green indicate cubic and tetragonal phases, respectively, and pale green represents two-phase refinements. The calculated diffraction pattern is shown in red and the experimental in black.

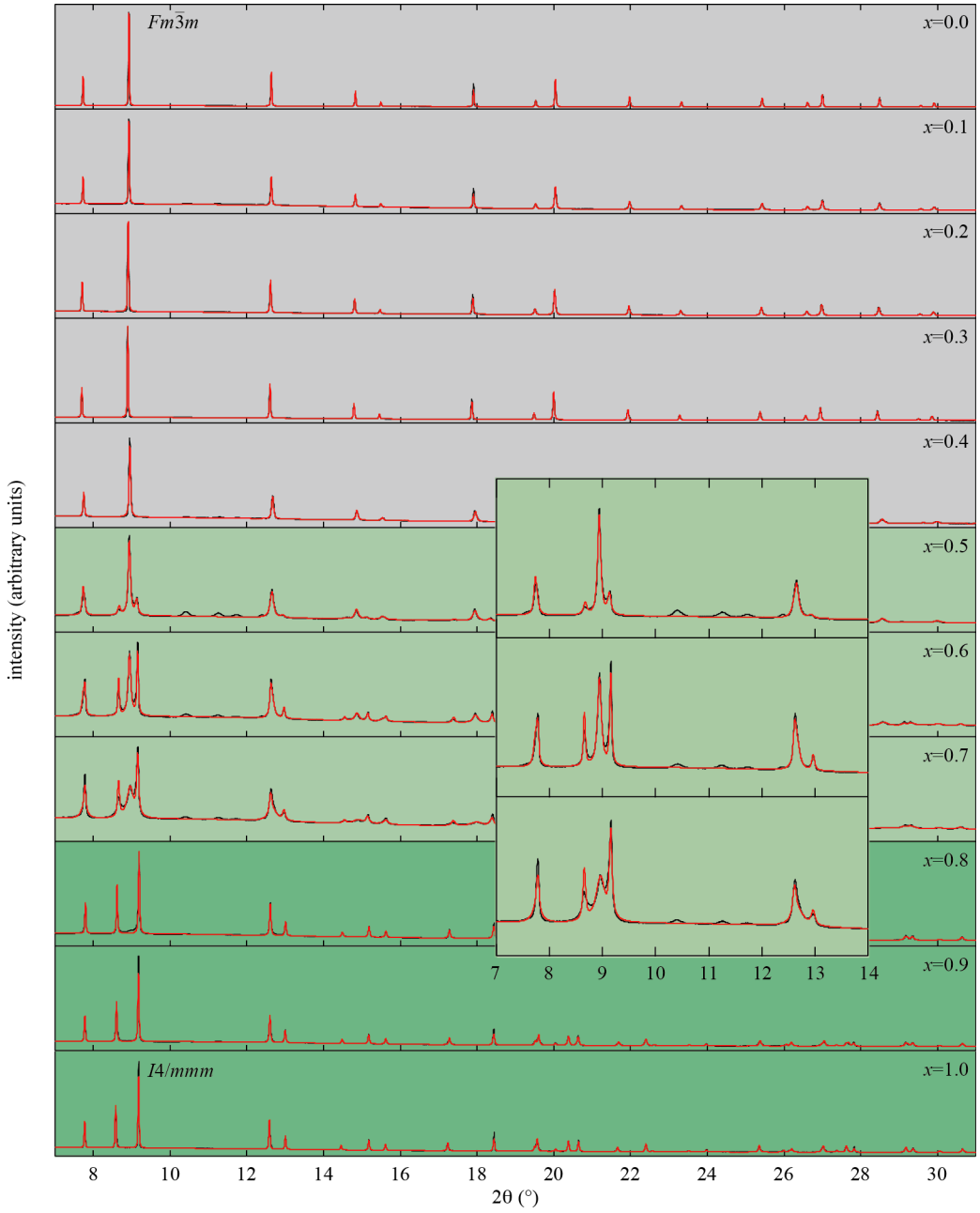


Figure C2.9: Constrained Rietveld fits of the PXRD patterns of $Fe_{1-x}Cu_x[Pt(CN)_6]$ at 100 K. Grey and green indicate cubic and tetragonal phases, respectively, and pale green represents two-phase refinements. The calculated diffraction pattern is shown in red and the experimental in black.

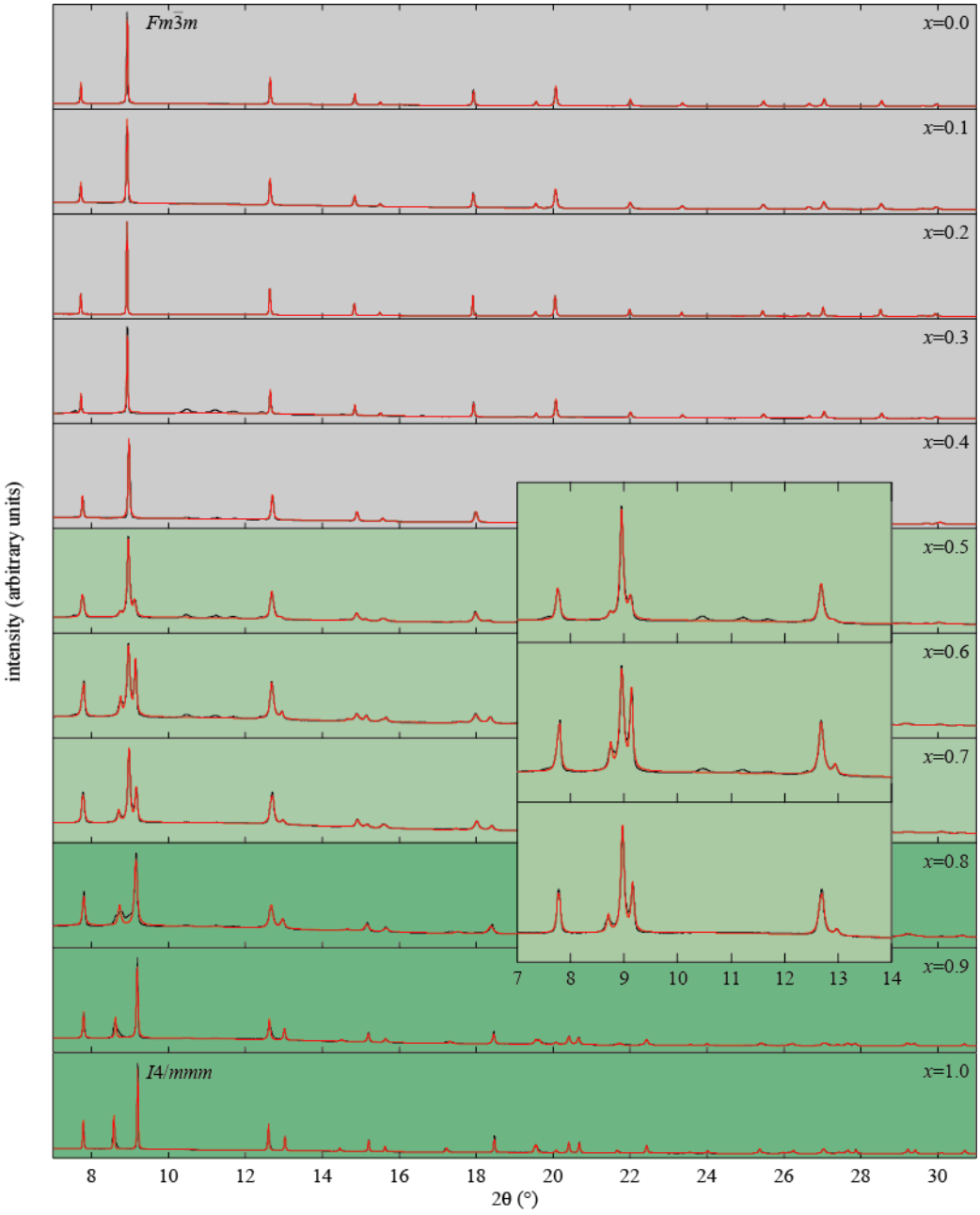


Figure C2.10: Pawley fits of the PXRD patterns of $Fe_{1-x}Cu_x[Pt(CN)_6]$ at 500 K. Grey and green indicate cubic and tetragonal phases, respectively, and pale green represents two-phase refinements. The calculated diffraction pattern is shown in red and the experimental in black.

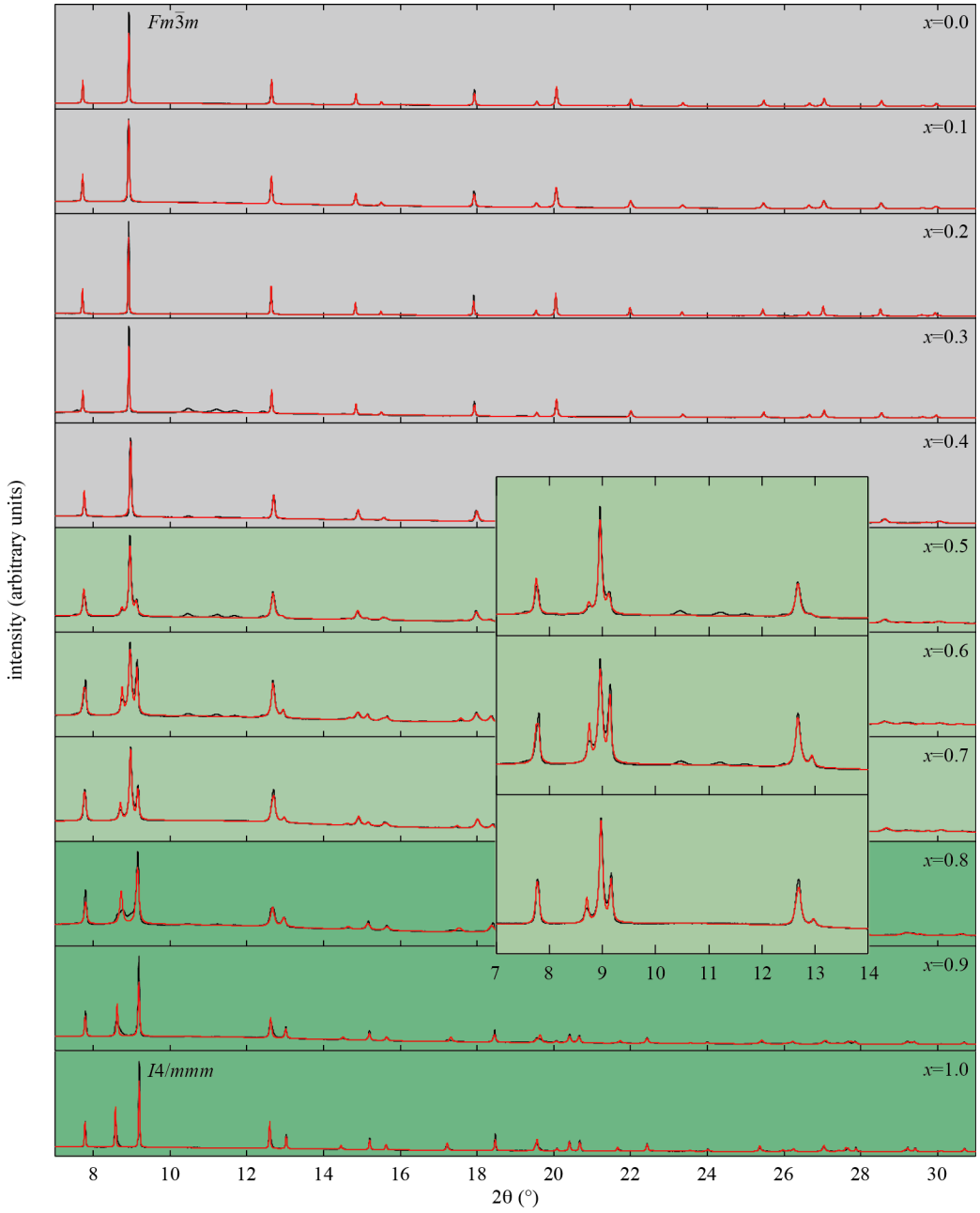


Figure C2.11: Constrained Rietveld fits of the PXRD patterns of $Fe_{1-x}Cu_x[Pt(CN)_6]$ at 500 K. Grey and green indicate cubic and tetragonal phases, respectively, and pale green represents two-phase refinements. The calculated diffraction pattern is shown in red and the experimental in black.

C2.3 $\mathbf{Zn_{1-x}Cu_x[Pt(CN)_6]}$

In $Zn_{1-x}Cu_x[Pt(CN)_6]$, the tetragonal phase emerges at nominal $x = 0.4$, which gives a small region of coexisting phases, prior to the tetragonal phase becoming predominant at $x \geq 0.7$ [Fig. C2.12–C2.13 and Table C2.8]. As with the previous systems, there are no thermal phase transitions [Fig. C2.14–C2.17 and Tables C2.9–C2.10].

Table C2.8: Crystallographic data for $Zn_{1-x}Cu_x[Pt(CN)_6]$ at ambient conditions. Green entries were fixed during the refinement.

x_{nom}	a_c/Å	Strain	a_t/Å	c_t/Å	Strain	Tet. fraction	x_{AAS}
0	10.57257(2)	0.1325(6)				0	0
0.1	10.56209(1)	0.1225(4)				0	0.17(9)
0.2	10.56325(2)	0.1781(4)				0	0.30(4)
0.3	10.56730(4)	0.3882(12)				0	0.36(2)
0.4	10.55901(4)	0.3837(13)	7.32783(11)	10.9099(4)	0.464(4)	0.2869	0.54(6)
0.5	10.55734(8)	0.411(2)	7.30173(6)	10.96788(19)	0.303(2)	0.5064	0.642(16)
0.6	10.53023(9)	0.52(5)	7.29498(8)	10.9874(2)	0.294(3)	0.8713	0.76(7)
0.7			7.28966(6)	11.00375(15)	0.2889(19)	1	0.84(8)
0.8			7.28556(3)	11.01480(9)	0.1900(10)	1	0.912(17)
0.9			7.28908(2)	11.01644(6)	0.1404(7)	1	0.96(2)
1			7.276160(10)	11.02891(3)	0.0935(4)	1	1

Table C2.9: Crystallographic data for $Zn_{1-x}Cu_x[Pt(CN)_6]$ at 100 K. Green entries were fixed during the refinement.

x_{nom}	a_c/Å	Strain	a_t/Å	c_t/Å	Strain	Tet. fraction	x_{AAS}
0	10.57814(2)	0.1497(7)				0	0
0.1	10.56762(1)	0.1313(4)				0	0.17(9)
0.2	10.56848(2)	0.1838(4)				0	0.30(4)
0.3	10.57303(4)	0.4361(12)				0	0.36(2)
0.4	10.56603(5)	0.4337(14)	7.33306(11)	10.9142(3)	0.449(4)	0.2790	0.54(6)
0.5	10.56331(8)	0.422(2)	7.30786(6)	10.95861(17)	0.303(2)	0.5124	0.642(16)
0.6	10.5305(6)	0.42(7)	7.30254(8)	10.9785(2)	0.326(3)	0.8999	0.76(7)
0.7			7.29583(6)	10.99182(15)	0.3065(19)	1	0.84(8)
0.8			7.29264(3)	11.00417(8)	0.2113(11)	1	0.912(17)
0.9			7.28908(2)	11.01644(6)	0.1404(7)	1	0.96(2)
1			7.28212(3)	11.01200(7)	0.1541(8)	1	1

Table C2.10: Crystallographic data for $Zn_{1-x}Cu_x[Pt(CN)_6]$ at 500 K. Green entries were fixed during the refinement.

x_{nom}	a_c/Å	Strain	a_t/Å	c_t/Å	Strain	Tet. fraction	x_{AAS}
0	10.56655(2)	0.1544(6)				0	0
0.1	10.55462(1)	0.1406(4)				0	0.17(9)
0.2	10.55264(2)	0.1789(5)				0	0.30(4)
0.3	10.55539(4)	0.3930(11)				0	0.36(2)
0.4	10.55261(4)	0.3825(13)	7.33335(14)	10.8658(5)	0.566(6)	0.2653	0.54(6)
0.5	10.54738(7)	0.398(2)	7.30521(7)	10.9003(2)	0.391(3)	0.4966	0.642(16)
0.6	10.5241(4)	0.398(2)	7.29717(11)	10.930(3)	0.478(4)	0.8715	0.76(7)
0.7			7.29282(8)	10.9346(2)	0.432(3)	1	0.84(8)
0.8			7.28597(6)	10.96542(17)	0.2922(19)	1	0.912(17)
0.9			7.28046(6)	10.9889(2)	0.265(2)	1	0.96(2)
1			7.26998(4)	11.01636(14)	0.1849(14)	1	1

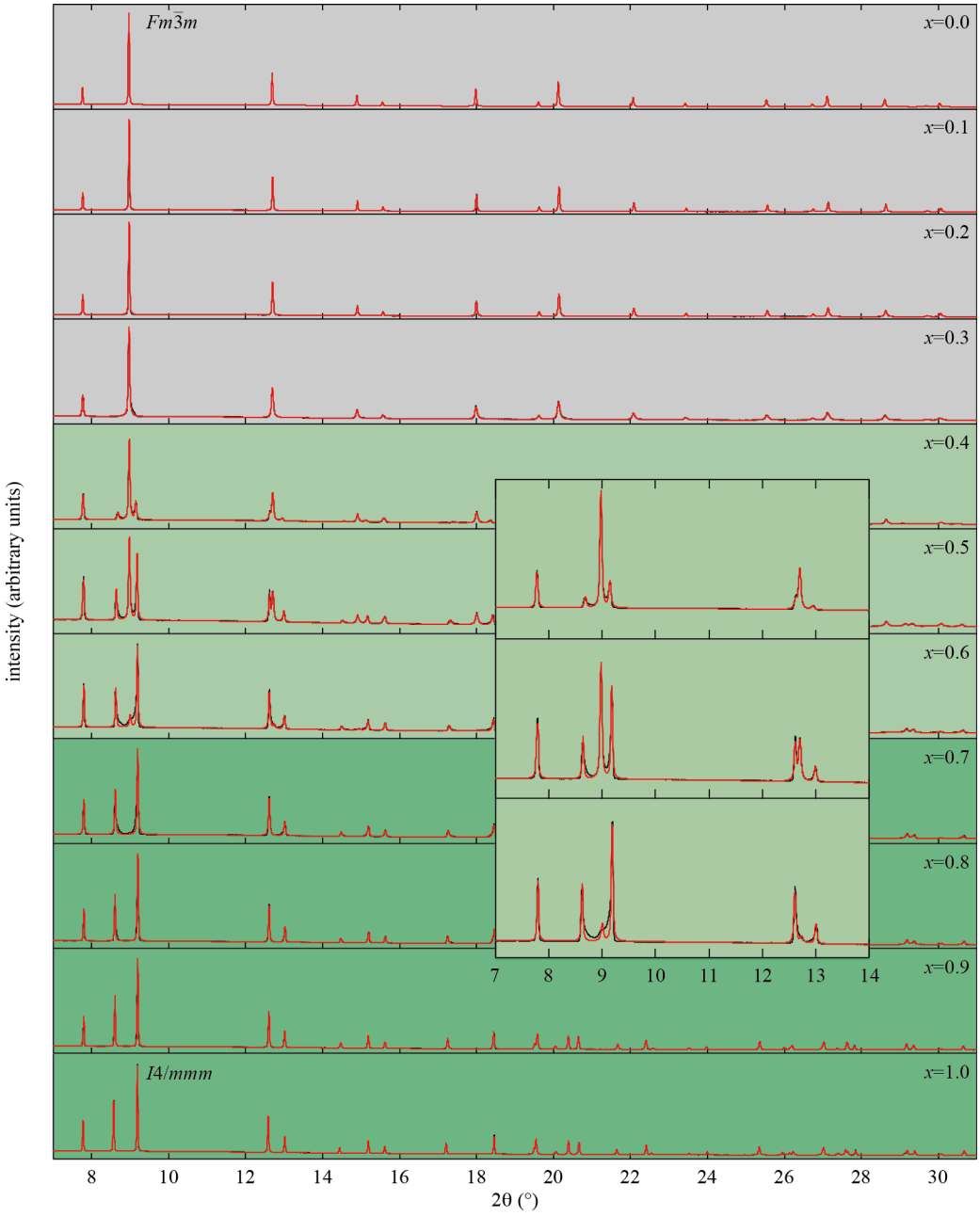


Figure C2.12: Pawley fits of the PXRD patterns of $Zn_{1-x}Cu_x[Pt(CN)_6]$ at ambient conditions. Grey and green indicate cubic and tetragonal phases, respectively, and pale green represents two-phase refinements. The calculated diffraction pattern is shown in red and the experimental in black.

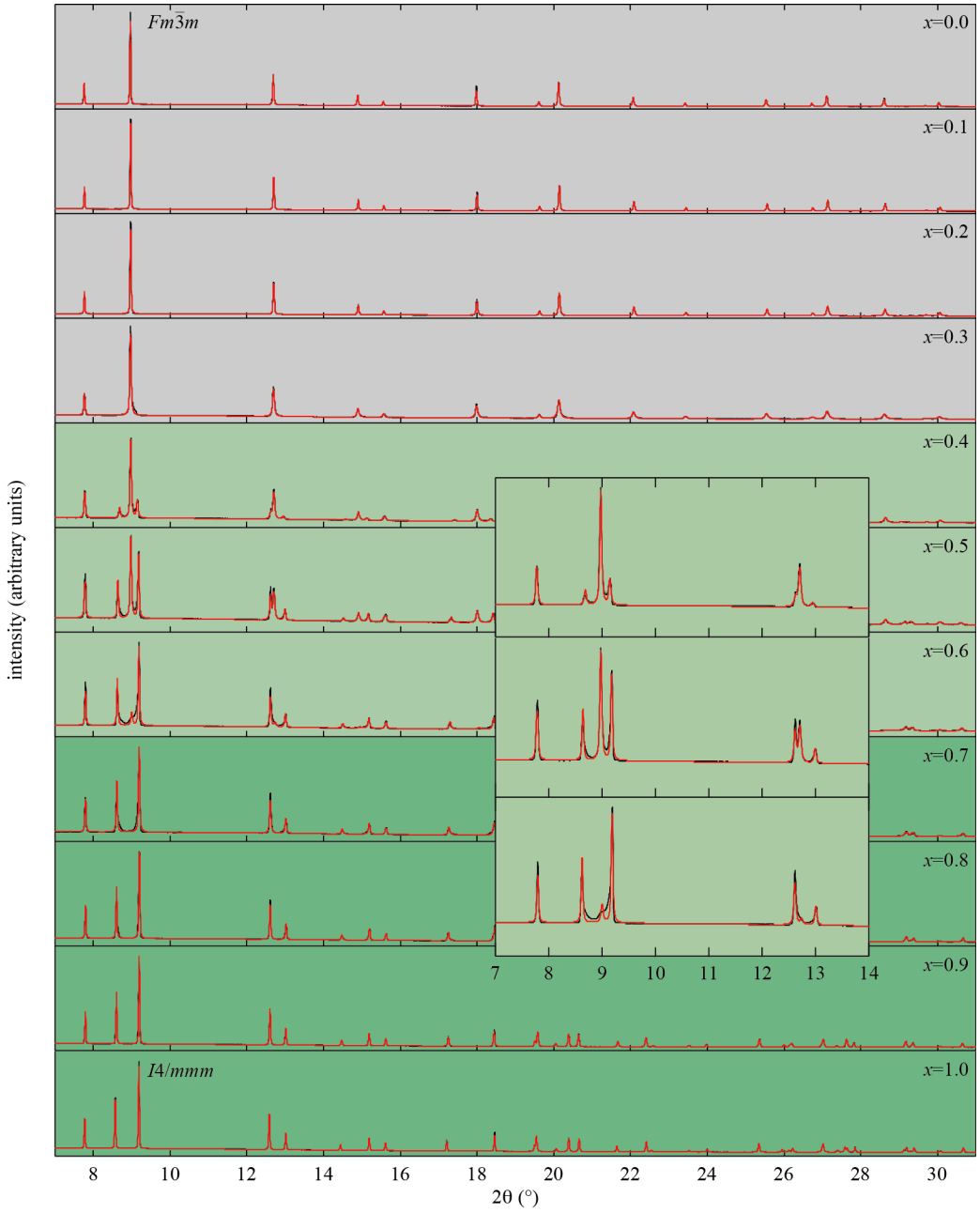


Figure C2.13: Constrained Rietveld fits of the PXRD patterns of $Zn_{1-x}Cu_x[Pt(CN)_6]$ at ambient conditions. Grey and green indicate cubic and tetragonal phases, respectively, and pale green represents two-phase refinements. The calculated diffraction pattern is shown in red and the experimental in black.

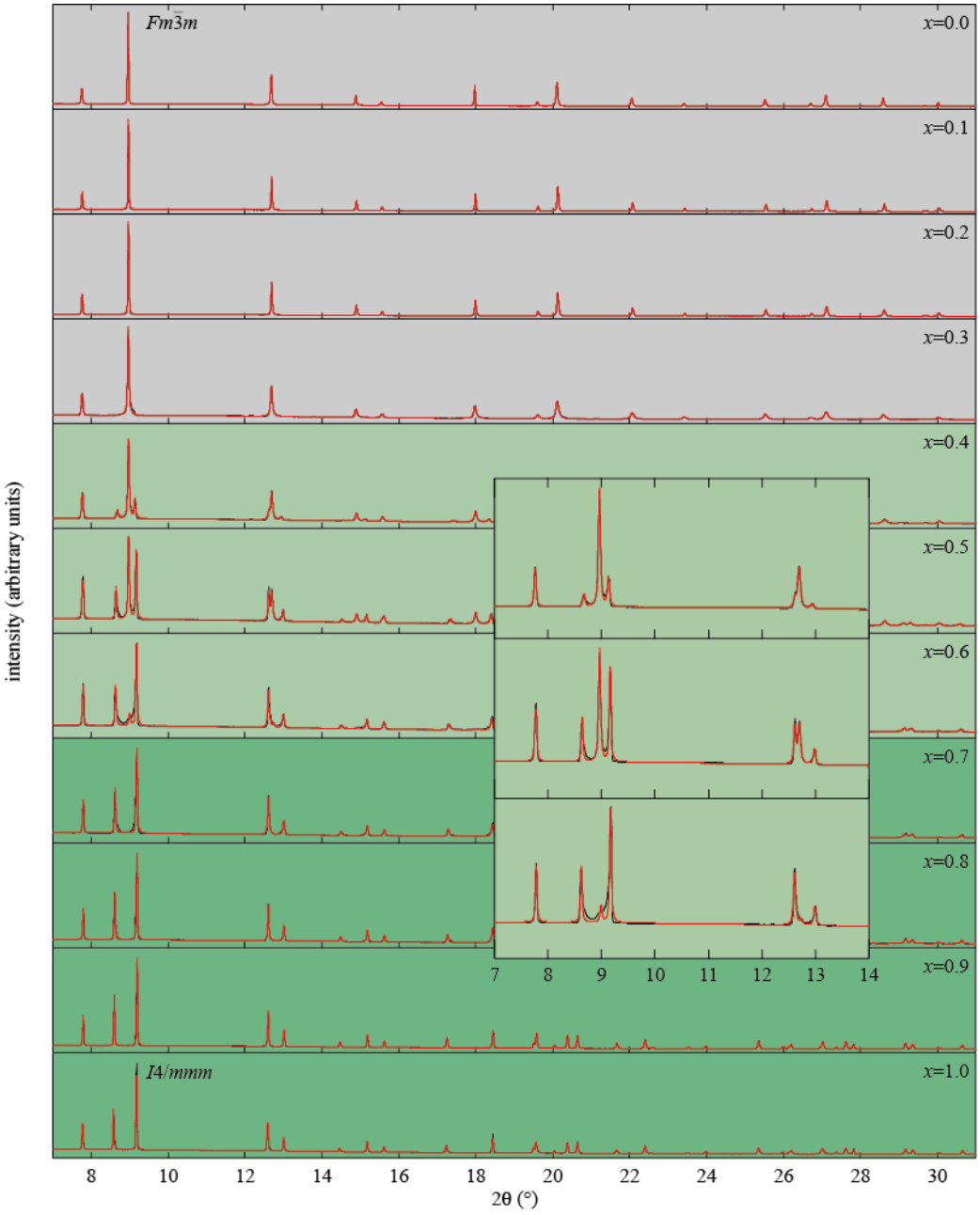


Figure C2.14: Pawley fits of the PXRD patterns of $Zn_{1-x}Cu_x[Pt(CN)_6]$ at 100 K. Grey and green indicate cubic and tetragonal phases, respectively, and pale green represents two-phase refinements. The calculated diffraction pattern is shown in red and the experimental in black.

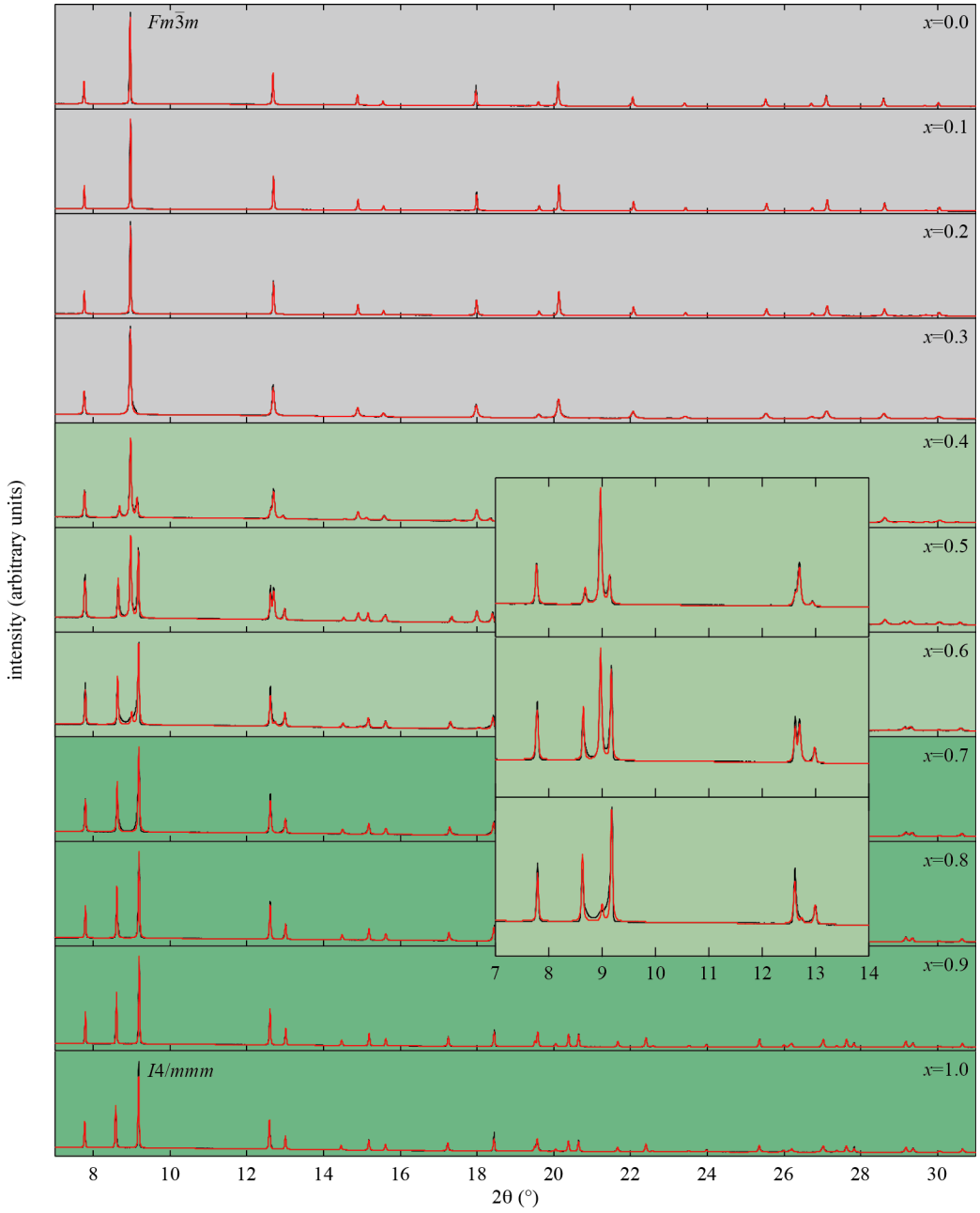


Figure C2.15: Constrained Rietveld fits of the PXRD patterns of $Zn_{1-x}Cu_x[Pt(CN)_6]$ at 100 K. Grey and green indicate cubic and tetragonal phases, respectively, and pale green represents two-phase refinements. The calculated diffraction pattern is shown in red and the experimental in black.

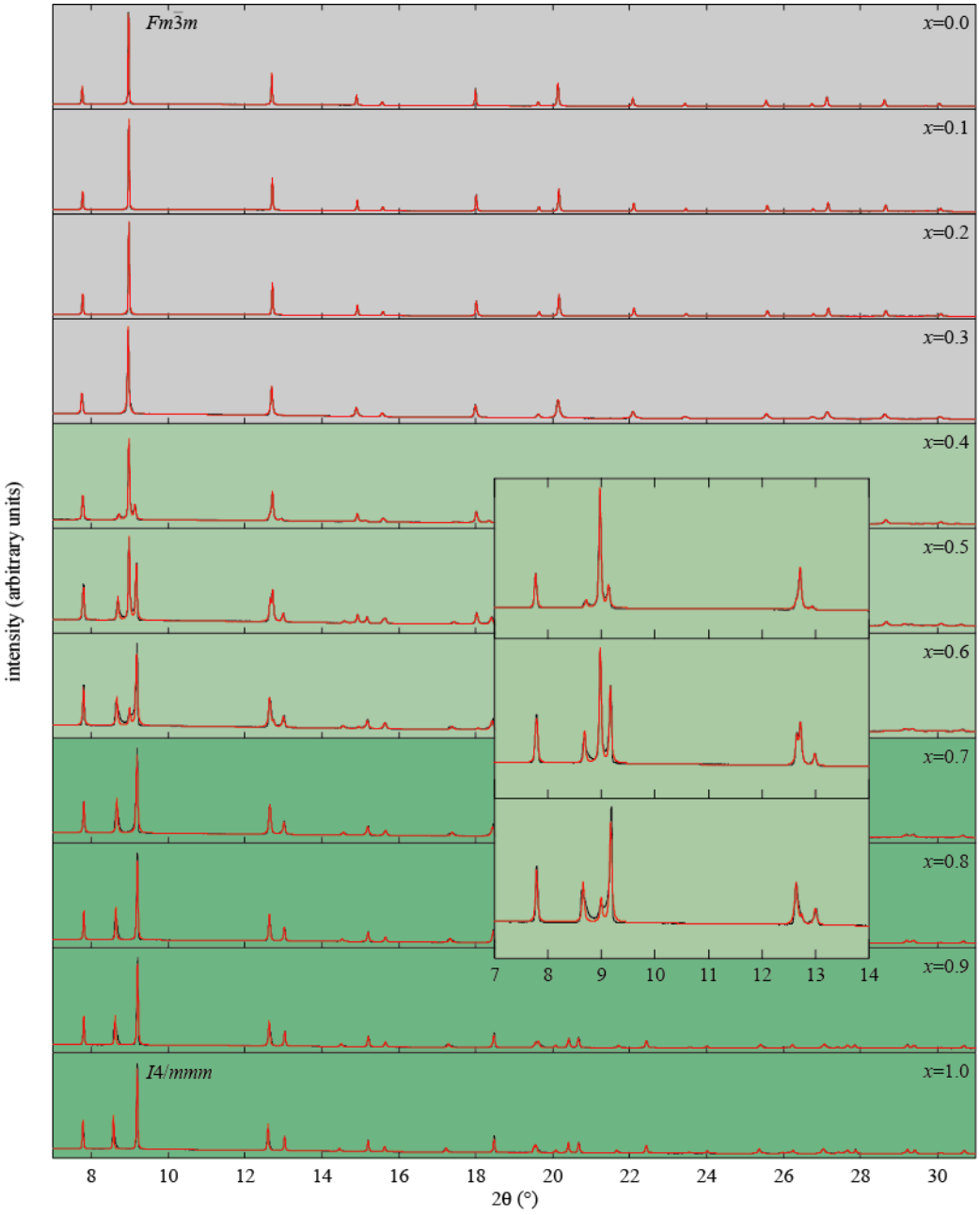


Figure C2.16: Pawley fits of the PXRD patterns of $Zn_{1-x}Cu_x[Pt(CN)_6]$ at 500 K. Grey and green indicate cubic and tetragonal phases, respectively, and pale green represents two-phase refinements. The calculated diffraction pattern is shown in red and the experimental in black.

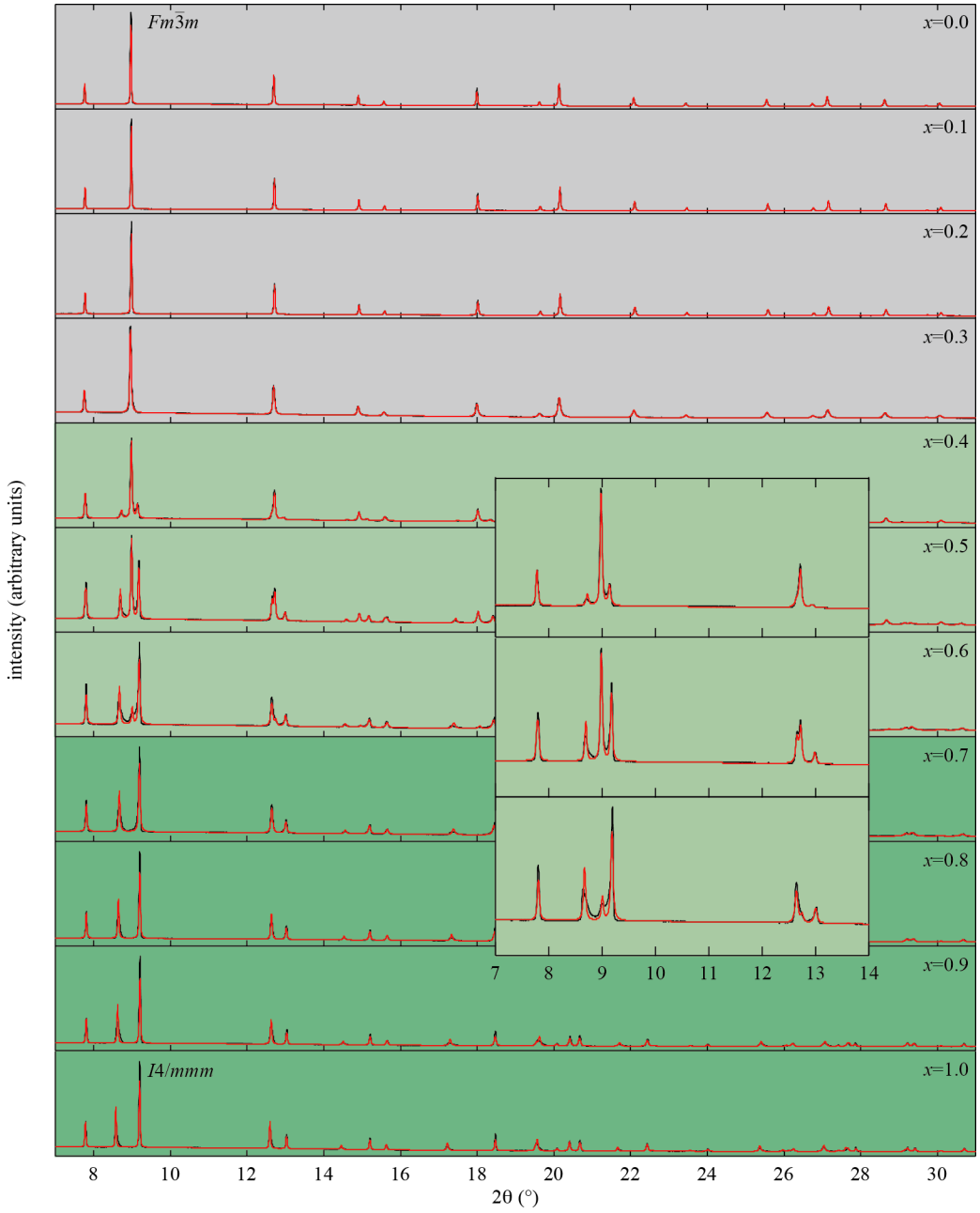


Figure C2.17: Constrained Rietveld fits of the PXRD patterns of $Zn_{1-x}Cu_x[Pt(CN)_6]$ at 500 K. Grey and green indicate cubic and tetragonal phases, respectively, and pale green represents two-phase refinements. The calculated diffraction pattern is shown in red and the experimental in black.

C2.4 $Cd_{1-x}Cu_x[Pt(CN)_6]$

$Cd_{1-x}Cu_x[Pt(CN)_6]$ is cubic for $x = 0$, but a second cubic phase is apparent from $x \geq 0.2$, unlike the other three hexacyanoplatinate series [Fig. C2.18–C2.19 and Table C2.11]. This is particularly noticeable when $x = 0.5$, where the fractions of the two cubic phases are almost equal. However, this sample presents something of an anomaly. In general, the tetragonal phase only becomes predominant at very high values of x and even at $x = 0.9$, reflections pertaining to the cubic phase can be discerned. No temperature-dependent variations were found [Fig. C2.20–C2.23 and Tables C2.12–C2.13]

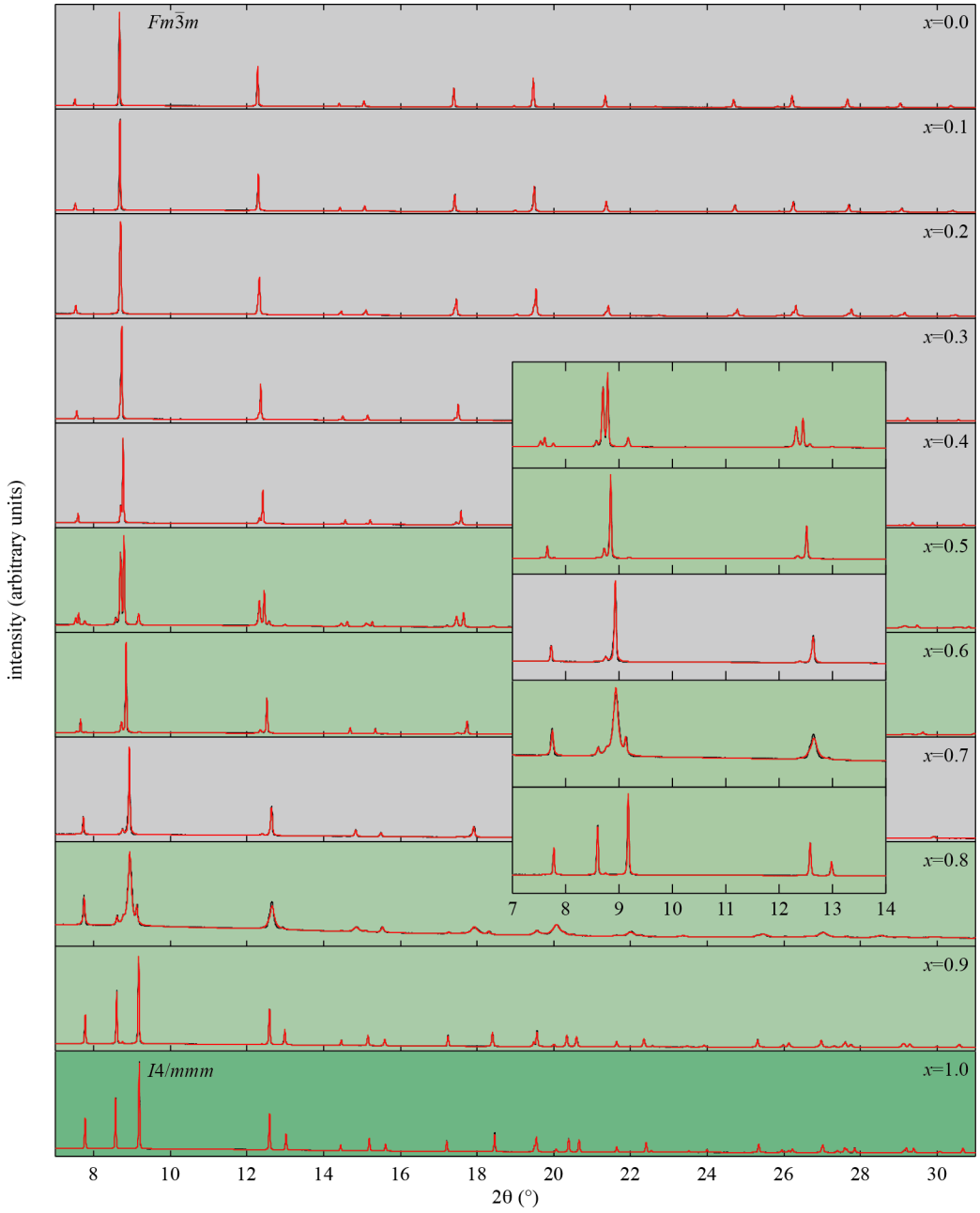


Figure C2.18: Pawley fits of the PXRD patterns of $Cd_{1-x}Cu_x[Pt(CN)_6]$ at ambient conditions. Grey and green indicate cubic and tetragonal phases, respectively, and pale green represents two-phase refinements. The calculated diffraction pattern is shown in red and the experimental in black.

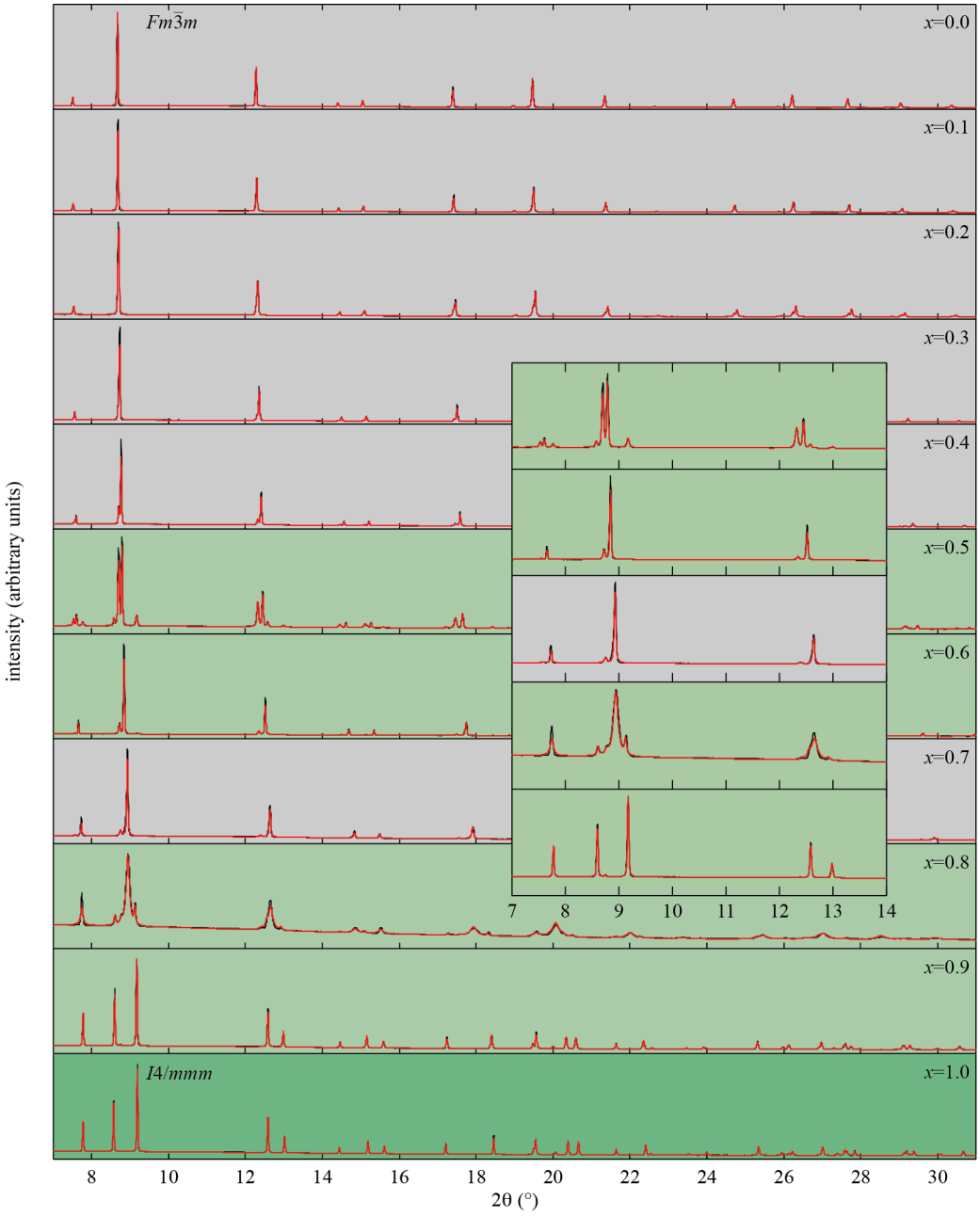


Figure C2.19: Constrained Rietveld fits of the PXRD patterns of $Cd_{1-x}Cu_x[Pt(CN)_6]$ at ambient conditions. Grey and green indicate cubic and tetragonal phases, respectively, and pale green represents two-phase refinements. The calculated diffraction pattern is shown in red and the experimental in black.

Table C2.11: Crystallographic data for $Cd_{1-x}Cu_x[Pt(CN)_6]$ at ambient conditions.

	First cubic phase			Second cubic phase			Tetragonal phase				
x_{nom}	a_{c}/Å	Strain	Phase fraction	a_{c}/Å	Strain	Phase fraction	a_{t}/Å	c_t/Å	Strain	Phase fraction	x_{AAS}
0	10.92730(3)	0.1256(8)	1								0
0.1	10.91397(3)	0.1546(9)	1								0.092(9)
0.2	10.91558(6)	0.2073(15)	0.3778	10.88570(2)	0.1156(6)	0.6222					0.022(16)
0.3	10.9023(2)	0.233(3)	0.1850	10.85764(6)	0.1299(7)	0.8150					0.24(2)
0.4	10.88447(8)	0.308(3)	0.2424	10.810280(10)	0.1186(4)	0.7576					0.35(3)
0.5	10.87159(5)	0.3148(15)	0.4453	10.76114(3)	0.1496(8)	0.4077	7.29164(13)	11.0265(3)	0.353(5)	0.1470	0.45(2)
0.6	10.8651(2)	0.389(7)	0.1597	10.71729(3)	0.1667(8)	0.8066	7.2910(16)	11.026(4)	0.82(7)	0.0337	0.55(3)
0.7	10.8285(7)	0.63(2)	0.0986	10.61507(6)	0.2884(17)	0.9012					0.73(4)
0.8	10.8063(17)	1.10(6)	0.0496	10.60198(15)	1.178(5)	0.8048	7.34638(19)	11.0137(6)	0.436(9)	0.1456	0.811(19)
0.9	10.8330(7)	0.188(14)	0.0108				7.30708(2)	11.02276(5)	0.1607(7)	0.9892	0.920(15)
1							7.27616(10)	11.02891(3)	0.0935(4)	1	1

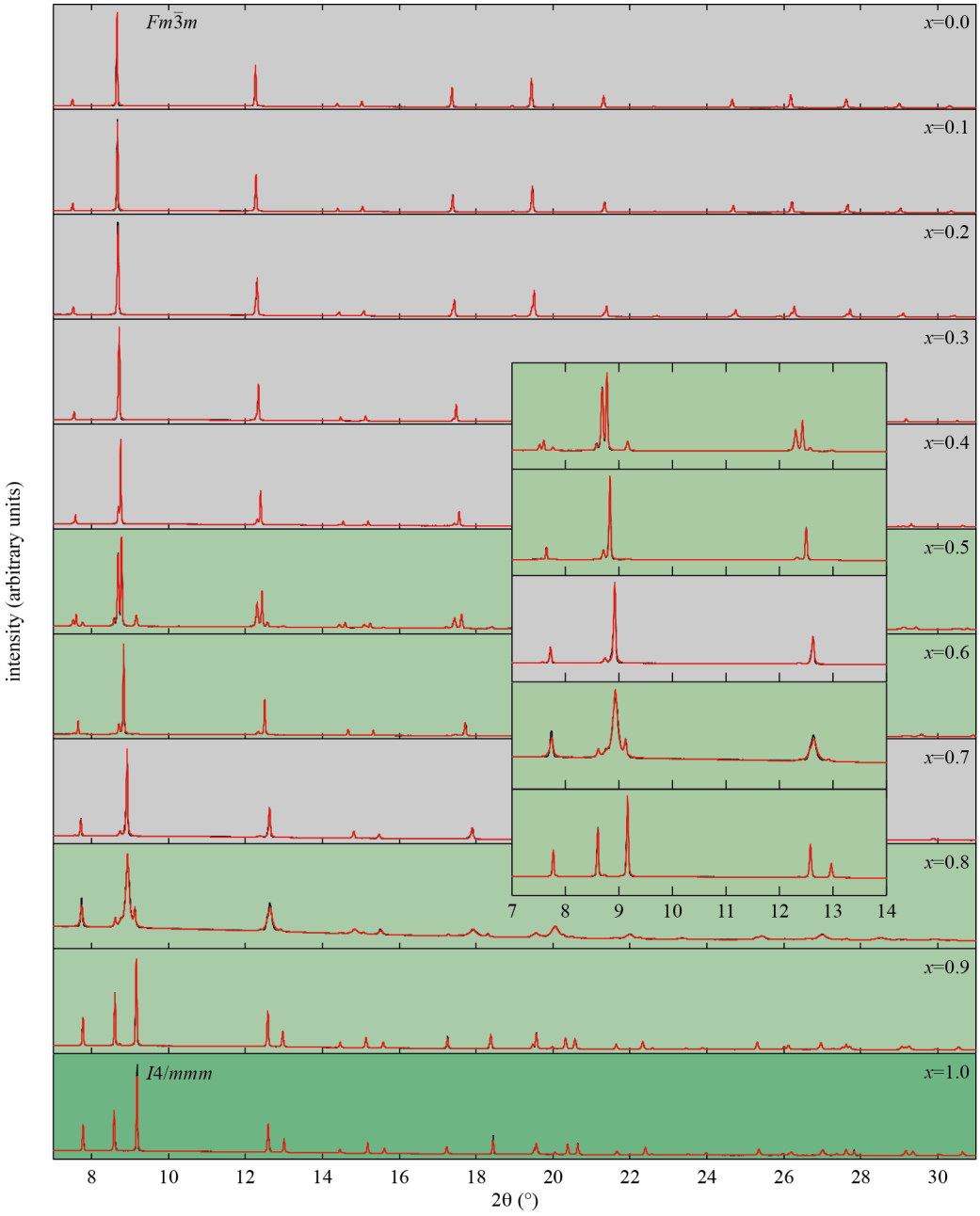


Figure C2.20: Pawley fits of the PXRD patterns of $Cd_{1-x}Cu_x[Pt(CN)_6]$ at 100 K. Grey and green indicate cubic and tetragonal phases, respectively, and pale green represents two-phase refinements. The calculated diffraction pattern is shown in red and the experimental in black.

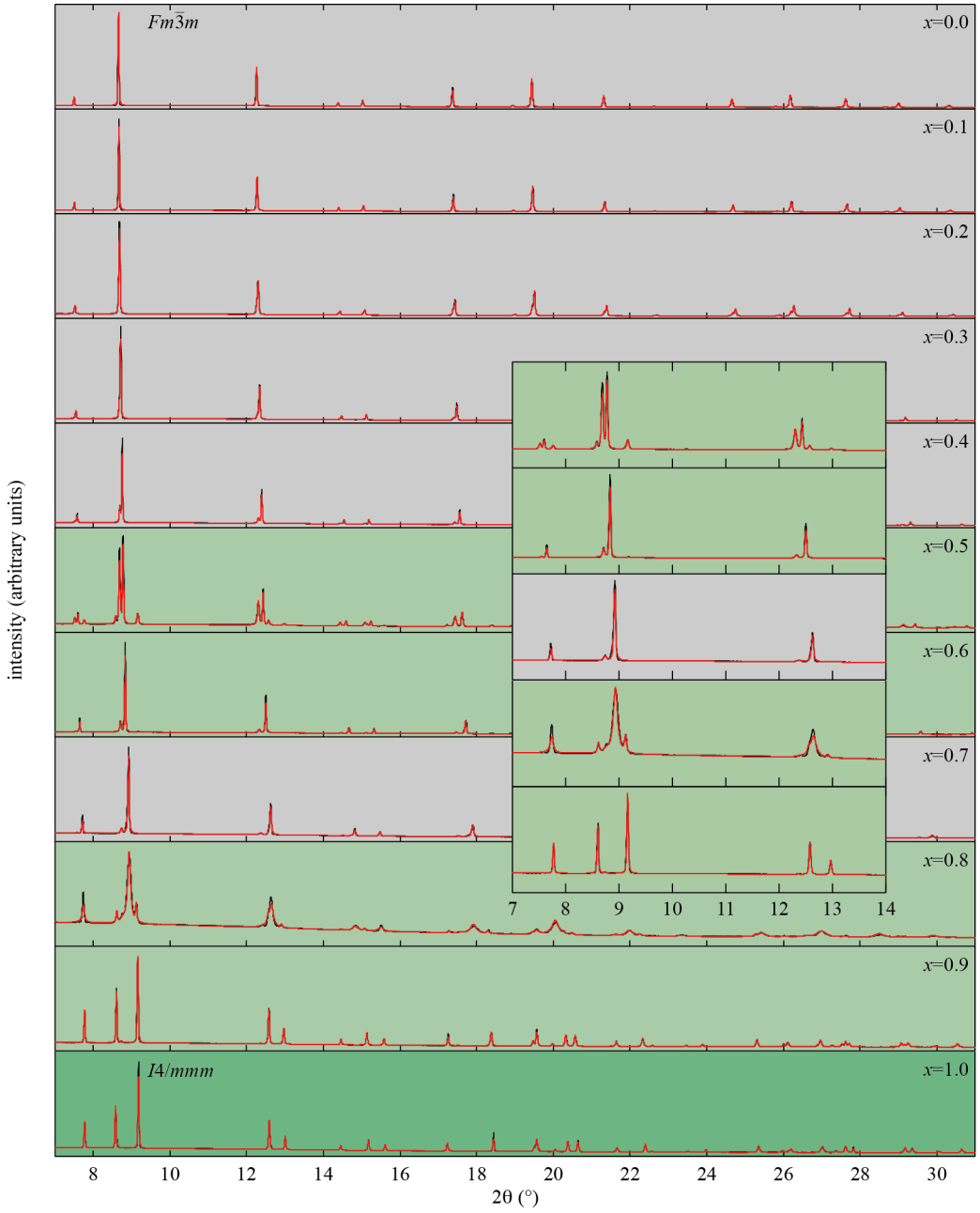


Figure C2.21: Constrained Rietveld fits of the PXRD patterns of $Cd_{1-x}Cu_x[Pt(CN)_6]$ at 100 K. Grey and green indicate cubic and tetragonal phases, respectively, and pale green represents two-phase refinements. The calculated diffraction pattern is shown in red and the experimental in black.

Table C2.12: Crystallographic data for $Cd_{1-x}Cu_x[Pt(CN)_6]$ at 100 K.

	First cubic phase			Second cubic phase			Tetragonal phase				
x_{nom}	a_{c}/Å	Strain	Phase fraction	a'_{c}/Å	Strain	Phase fraction	a_{t}/Å	c_t/Å	Strain	Phase fraction	x_{AAS}
0	10.94197(3)	0.1410(8)	1								0
0.1	10.92971(3)	0.1514(8)		1							0.092(9)
0.2	10.93137(7)	0.2092(16)	0.3783	10.90174(2)	0.1104(7)	0.6217					0.022(16)
0.3	10.91793(14)	0.243(42)	0.1807	10.87347(2)	0.1304(6)	0.8193					0.24(2)
0.4	10.90024(8)	0.331(3)	0.2510	10.82514(1)	0.1142(4)	0.7490					0.35(3)
0.5	10.88681(5)	0.3240(15)	0.4456	10.77586(3)	0.1541(8)	0.4089	7.29990(13)	11.0193(4)	0.355(5)	0.1455	0.45(2)
0.6	10.8806(2)	0.389(7)	0.1557	10.73108(3)	0.1688(8)	0.8128	7.2996(14)	11.031(4)	0.76(6)	0.0315	0.55(3)
0.7	10.8442(7)	0.64(2)	0.0951	10.62594(5)	0.2966(14)	0.9049					0.73(4)
0.8	10.807(3)	1.95(11)	0.0725	10.61066(14)	1.084(5)	0.7865	7.34803(18)	11.0027(5)	0.355(8)	0.1410	0.811(19)
0.9	10.8566(5)	0.134(14)	0.0090				7.31549(3)	11.01479(6)	0.1848(8)	0.9910	0.920(15)
1							7.28212(3)	11.01200(7)	0.1541(8)		1

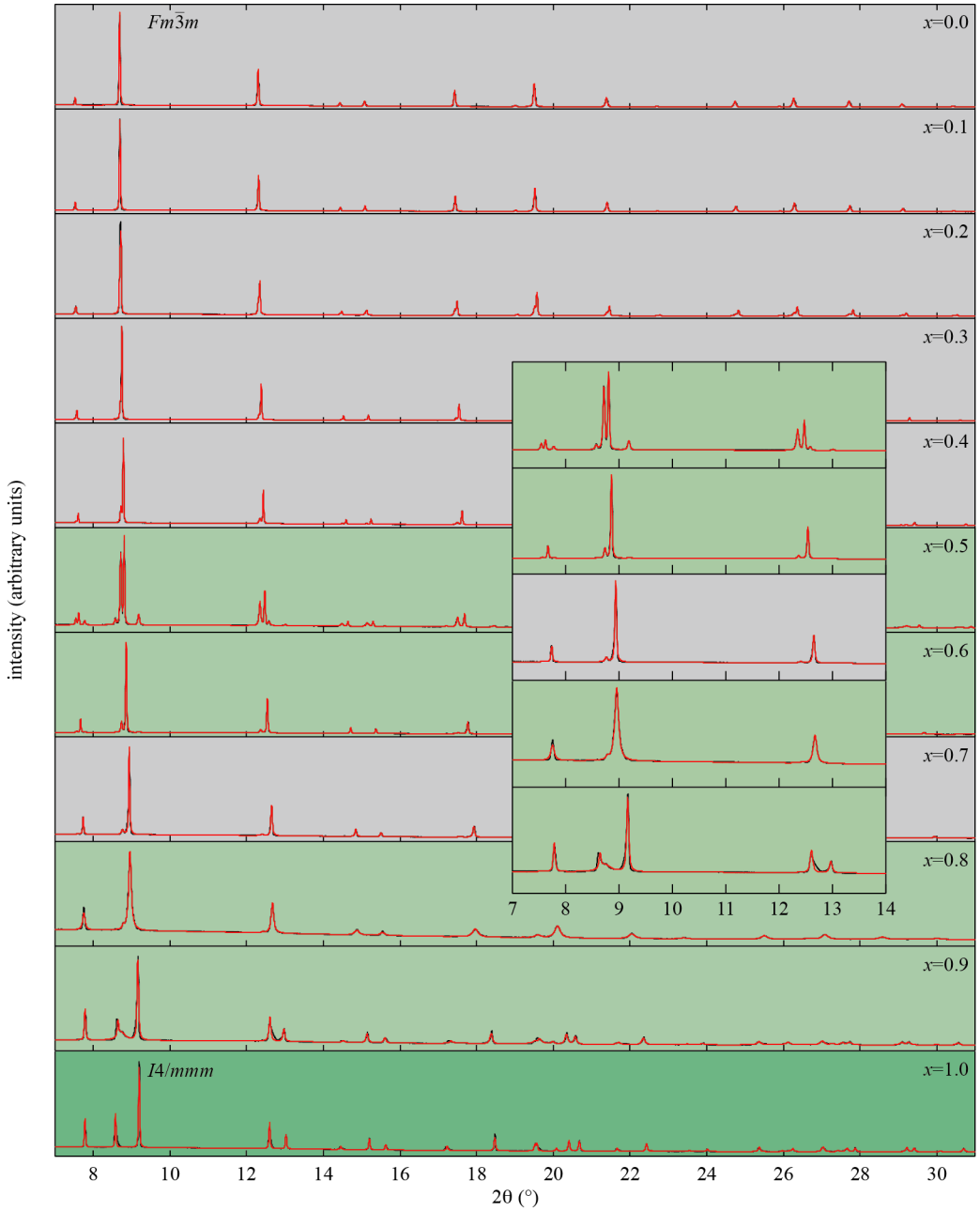


Figure C2.22: Pawley fits of the PXRD patterns of $Cd_{1-x}Cu_x[Pt(CN)_6]$ at 500 K. Grey and green indicate cubic and tetragonal phases, respectively, and pale green represents two-phase refinements. The calculated diffraction pattern is shown in red and the experimental in black.

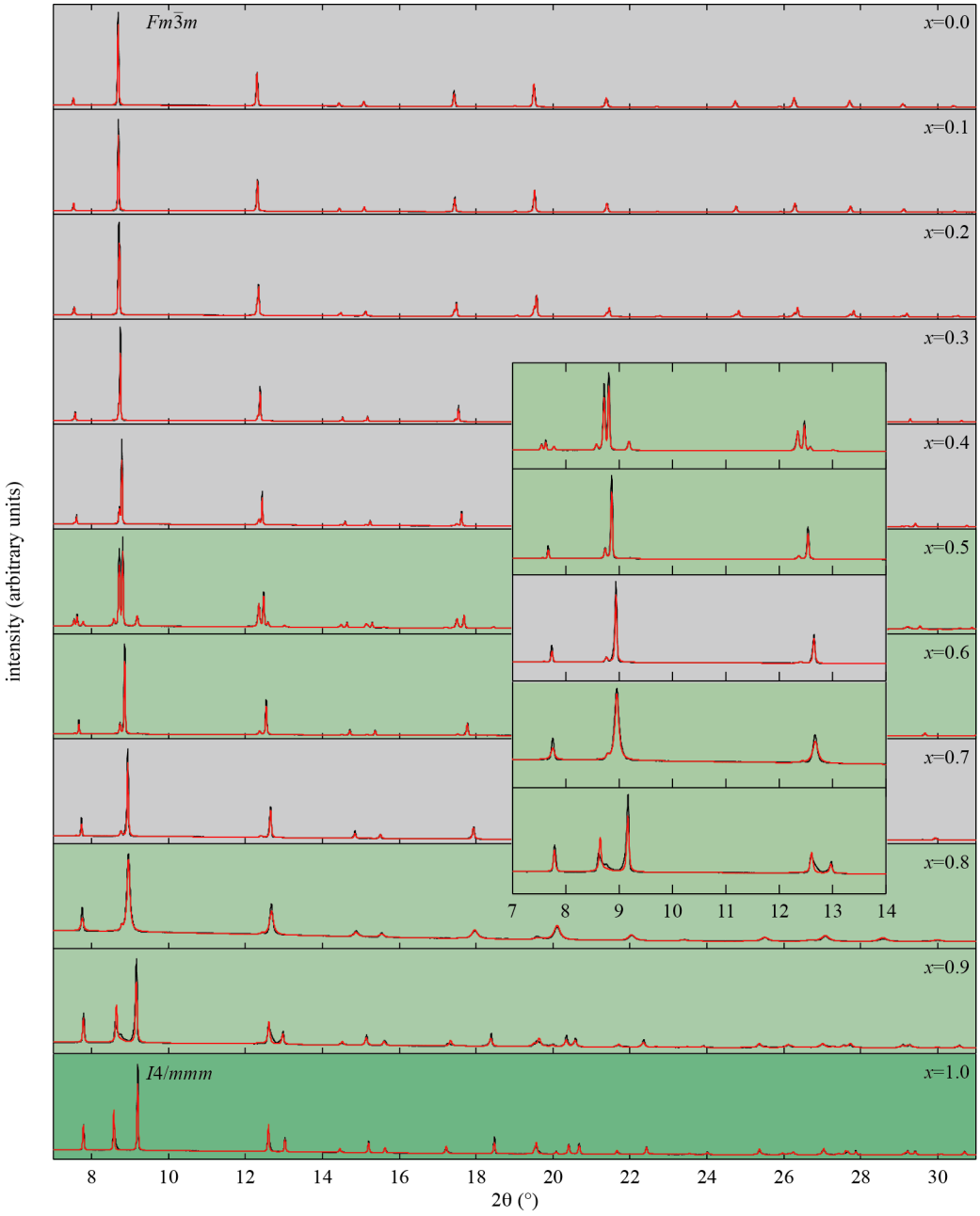


Figure C2.23: Constrained Rietveld fits of the PXRD patterns of $Cd_{1-x}Cu_x[Pt(CN)_6]$ at 500 K. Grey and green indicate cubic and tetragonal phases, respectively, and pale green represents two-phase refinements. The calculated diffraction pattern is shown in red and the experimental in black.

Table C2.13: Crystallographic data for $Cd_{1-x}Cu_x[Pt(CN)_6]$ at 500 K.

	First cubic phase			Second cubic phase			Tetragonal phase				
x_{nom}	a_{c}/Å	Strain	Phase fraction	a'_{c}/Å	Strain	Phase fraction	a_{t}/Å	c_t/Å	Strain	Phase fraction	x_{AAS}
0	10.90653(4)	0.1916(10)									0
0.1	10.89767(4)	0.1789(9)									0.092(9)
0.2	10.89938(9)	0.238(2)	0.4309	10.86670(3)	0.1030(9)	0.5691					0.022(16)
0.3	10.88003(12)	0.295(4)	0.2509	10.83534(2)	0.0868(5)	0.7491					0.24(2)
0.4	10.86469(10)	0.388(3)	0.2957	10.78785(2)	0.0906(5)	0.7043					0.35(3)
0.5	10.84822(4)	0.3119(13)	0.4451	10.73920(2)	0.0008(8)	0.3988	7.28204(13)	11.0291(4)	0.383(5)	0.1561	0.45(2)
0.6	10.8475(2)	0.381(7)	0.1597	10.69815(3)	0.1847(8)	0.8055	7.2839(17)	11.009(5)	0.92(8)	0.0348	0.55(3)
0.7	10.8154(7)	0.63(2)	0.1000	10.60440(5)	0.2722(13)	0.9000					0.73(4)
0.8	10.7914(9)	0.50(3)	0.0311	10.58251(9)	0.984(3)	0.9688	7.2635(7)	10.9318(13)	0.615(18)	0.0001	0.811(19)
0.9	10.846(2)	3.14(8)	0.1406				7.31510(8)	10.9637(4)	0.427(3)	0.8594	0.920(15)
1							7.26998(4)	11.01636(14)	0.1849(14)		1

C3 $(\mathbf{B}_{1-x}\mathbf{Cu}_x)_3[\mathbf{B'(CN)}_6]_2$

C3.1 $(\mathbf{Mn}_{1-x}\mathbf{Cu}_x)_3[\mathbf{Co(CN)}_6]_2$

Table C3.14: Crystallographic data for $(Mn_{1-x}Cu_x)_3[Co(CN)_6]_2$ at ambient conditions.

	One-phase refinement		Two-phase refinement					
x_{nom}	a/Å	Strain	a/Å	Strain	Phase fraction	a/Å	Strain	Phase fraction
0	10.42877(1)	0.1251(4)						
0.1	10.41048(5)	0.5591(15)						
0.2	10.38886(12)	0.934(4)	10.39629(11)	0.683(5)	0.7064	10.3075(13)	1.69(3)	0.2926
0.3	10.35426(14)	1.338(5)	10.36547(13)	0.991(5)	0.7291	10.2611(10)	1.77(2)	0.2709
0.4	10.3169(4)	2.423(13)	10.3596(2)	1.317(8)	0.5859	10.2100(6)	1.879(17)	0.4141
0.5	10.2708(2)	2.226(8)	10.3042(3)	1.549(8)	0.6780	10.1802(5)	1.507(15)	0.3220
0.6	10.2200(3)	2.334(9)	10.2754(6)	1.900(16)	0.5965	10.1617(4)	1.279(3)	0.4035
0.7	10.1738(2)	1.929(7)						
0.8	10.13826(19)	1.551(7)						
0.9	10.10214(13)	1.161(4)						
1	10.07700(12)	1.264(4)						

Table C3.15: Crystallographic data for $(Mn_{1-x}Cu_x)_3[Co(CN)_6]_2$ at 100 K.

	One-phase refinement		Two-phase refinement					
x_{nom}	a/Å	Strain	a/Å	Strain	Phase fraction	a/Å	Strain	Phase fraction
0	10.35149(2)	0.1625(5)						
0.1	10.36599(5)	0.6275(16)						
0.2	10.31645(9)	0.907(3)	10.32682(16)	0.621(6)	0.6032	10.2755(10)	1.209(11)	0.3968
0.3	10.30216(8)	0.986(3)	10.31097(16)	0.753(4)	0.7249	10.2544(10)	1.130(15)	0.2751
0.4	10.2393(3)	2.179(11)	10.2748(2)	1.274(7)	0.6167	10.1362(6)	1.753(16)	0.3833
0.5	10.1929(2)	2.149(7)	10.2232(3)	1.563(9)	0.6942	10.1113(6)	1.432(16)	0.3058
0.6	10.1485(3)	2.288(9)	10.2015(6)	1.836(14)	0.6149	10.0917(3)	1.177(12)	0.3851
0.7	10.1009(2)	1.761(7)						
0.8	10.07926(18)	1.410(6)						
0.9	10.05161(12)	1.165(4)						
1	10.04908(11)	1.186(4)						

Table C3.16: Crystallographic data for $(Mn_{1-x}Cu_x)_3[Co(CN)_6]_2$ at 500 K.

	One-phase refinement		Two-phase refinement					
x_{nom}	a/Å	Strain	a/Å	Strain	Phase fraction	a/Å	Strain	Phase fraction
0	10.36164(3)	0.2392(8)						
0.1	10.32615(5)	0.6368(15)						
0.2	10.31093(10)	0.992(3)	10.32358(18)	0.655(7)	0.5543	10.2702(10)	1.300(11)	0.4457
0.3	10.33015(12)	1.180(4)	10.34256(17)	0.852(6)	0.6765	10.2674(10)	1.406(16)	0.3235
0.4	10.2397(3)	2.497(12)	10.2795(3)	1.465(9)	0.6306	10.1257(6)	1.831(18)	0.3694
0.5	10.1790(2)	2.247(7)	10.2103(3)	1.659(8)	0.7123	10.0895(5)	1.432(15)	0.2877
0.6	10.1441(4)	2.428(7)	10.20058(12)	2.028(5)	0.6527	10.0822(2)	1.205(56)	0.3473
0.7	10.0909(2)	1.825(7)						
0.8	10.07225(18)	1.487(6)						
0.9	10.03838(13)	1.167(4)						
1	10.04569(11)	1.217(4)						

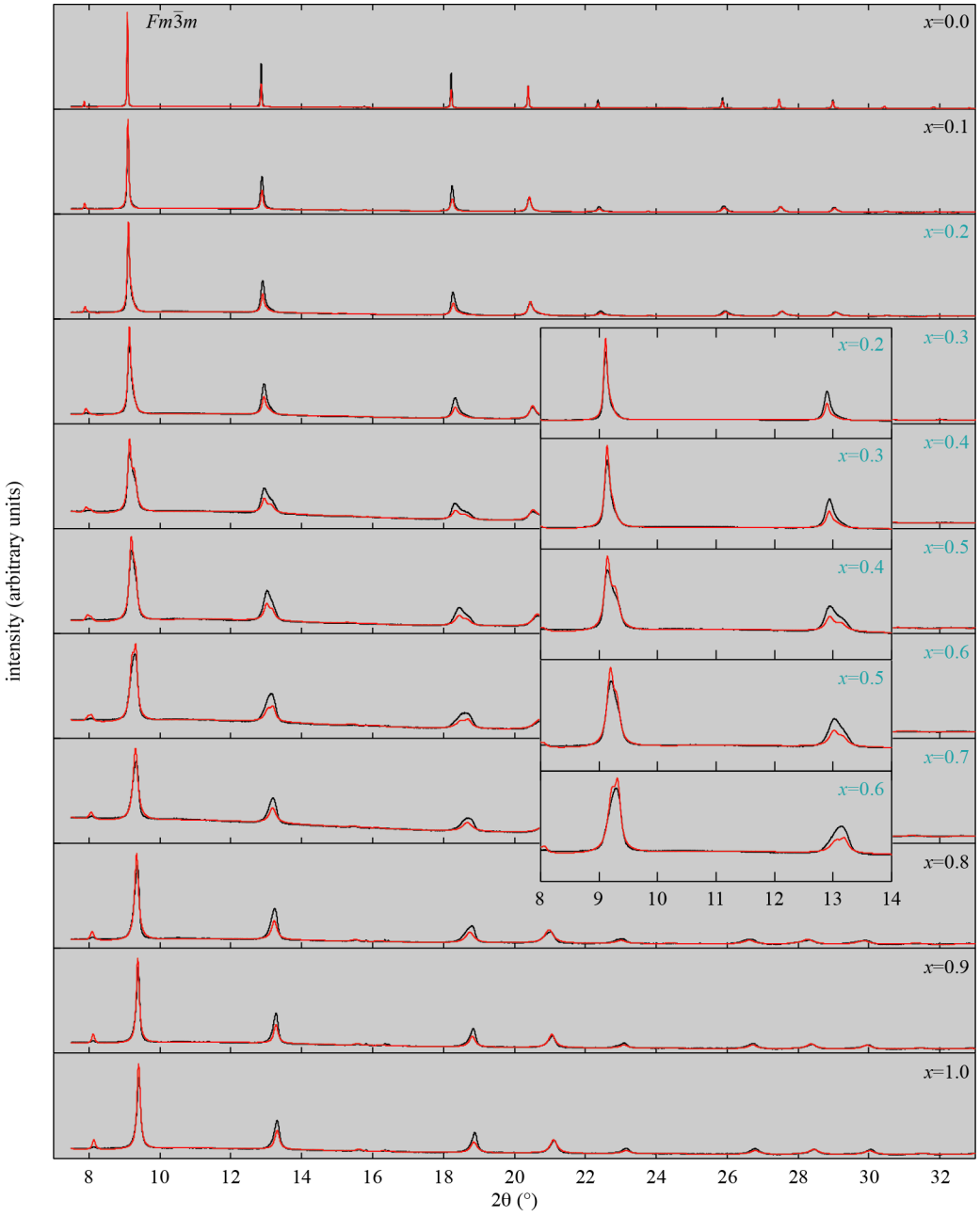


Figure C3.24: Constrained Rietveld fits of $(Mn_{1-x}Cu_x)_3[Co(CN)_6]_2$ at ambient conditions. Two-phase refinements are indicated by teal text. The calculated diffraction pattern is shown in red and the experimental in black.

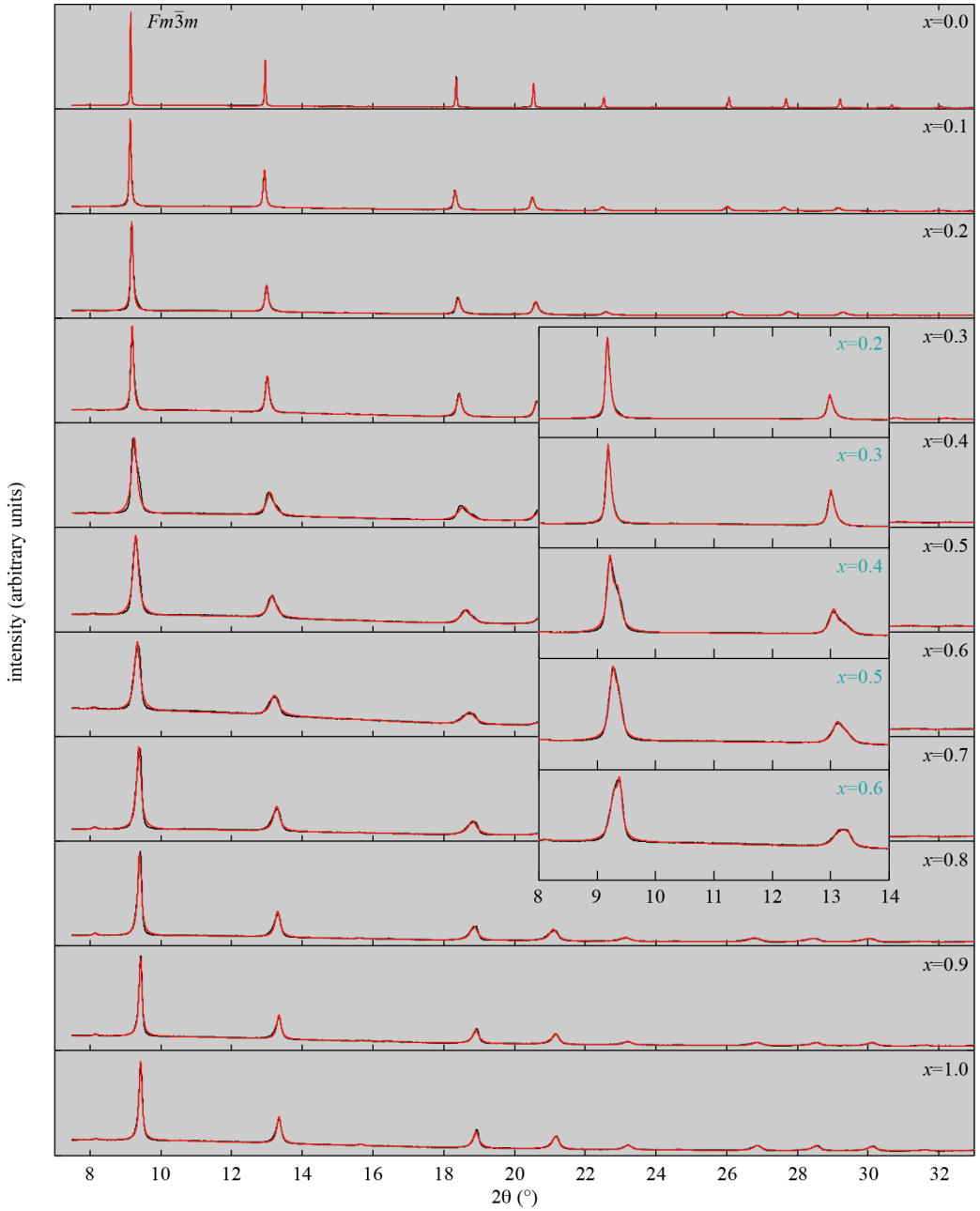


Figure C3.25: Pawley fits of $(Mn_{1-x}Cu_x)_3[Co(CN)_6]_2$ at 100 K. Two-phase refinements are shown in the inset and indicated by teal text. The calculated diffraction pattern is shown in red and the experimental in black.

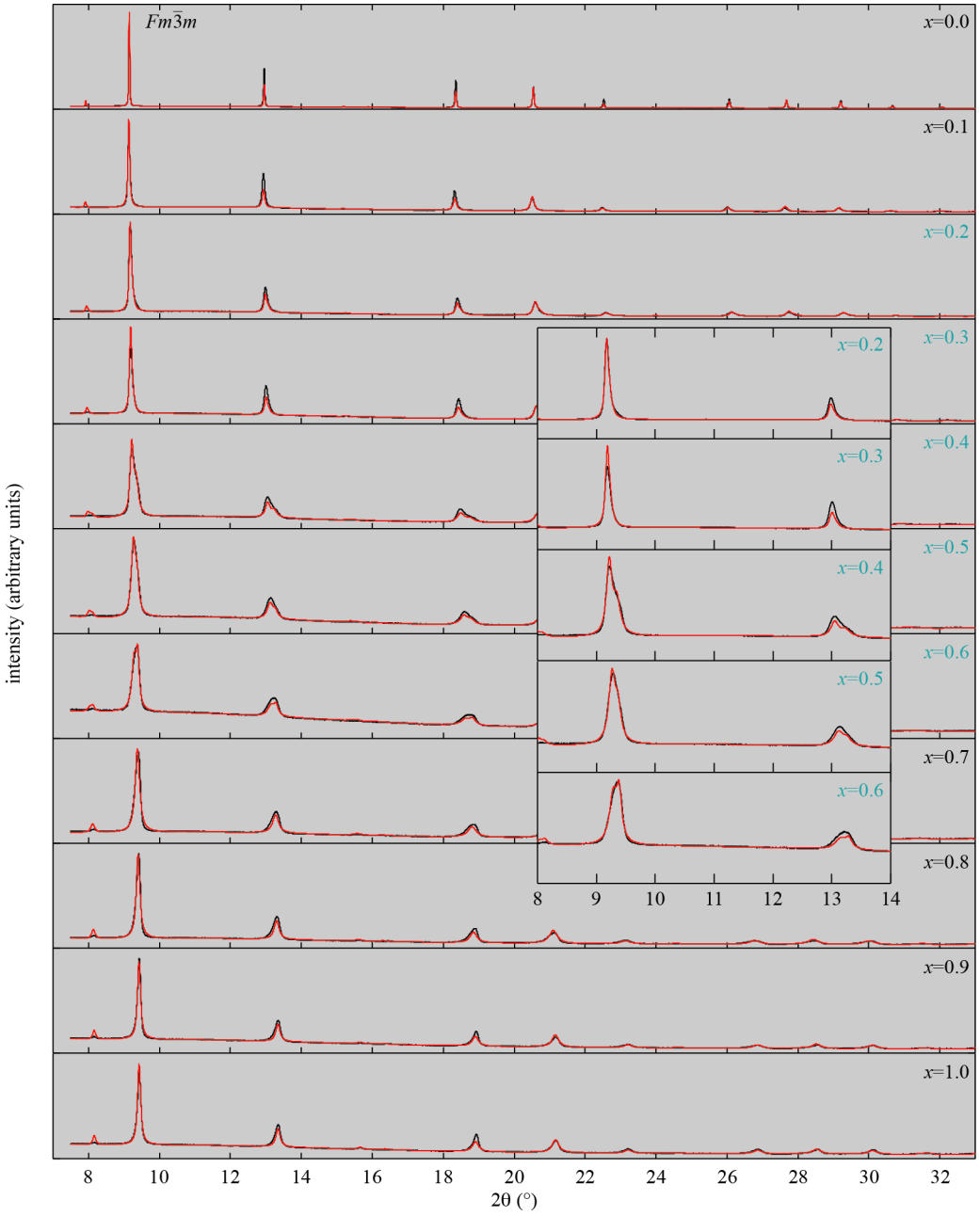


Figure C3.26: Constrained Rietveld fits of $(Mn_{1-x}Cu_x)_3[Co(CN)_6]_2$ at 100 K. Two-phase refinements are indicated by teal text. The calculated diffraction pattern is shown in red and the experimental in black.

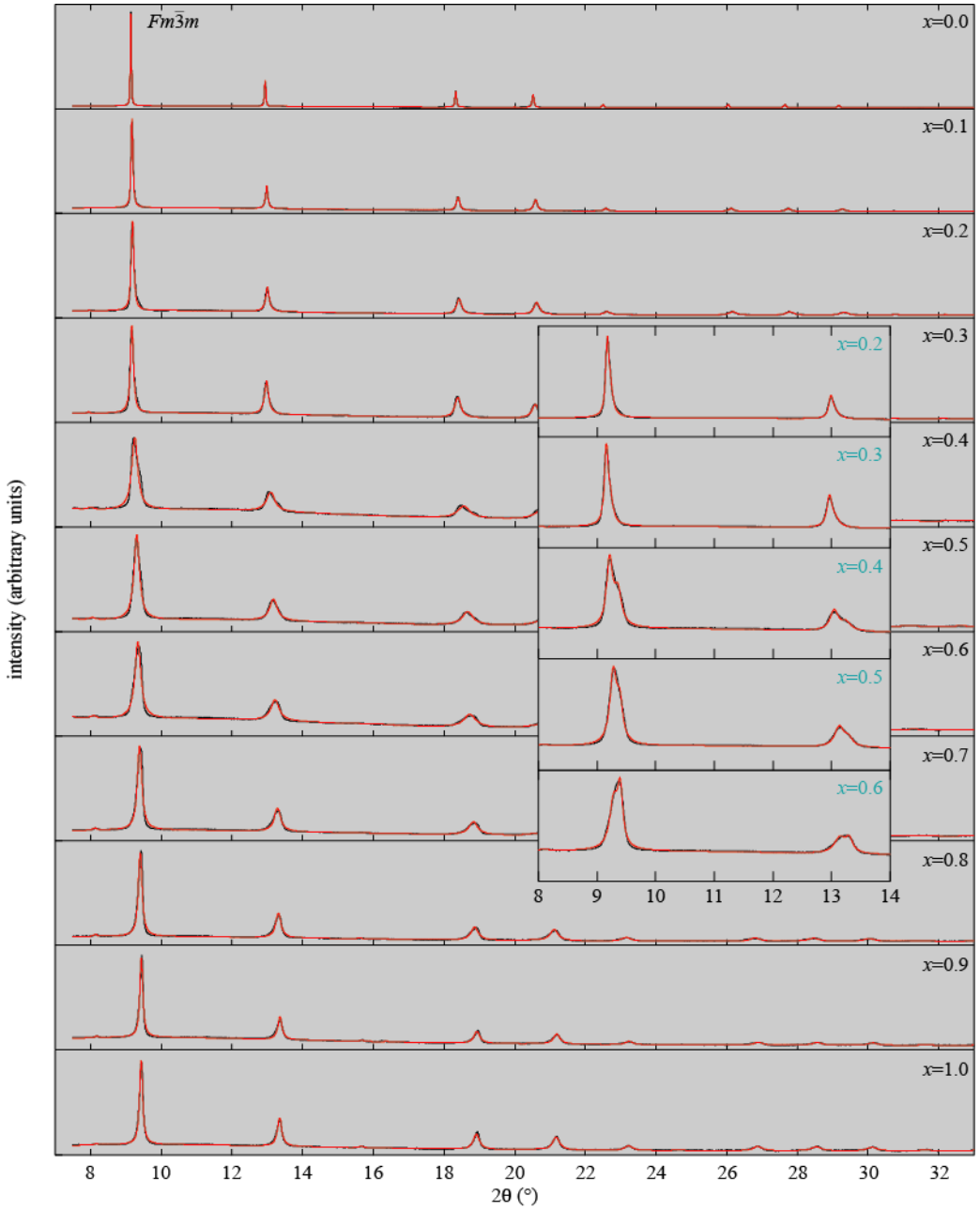


Figure C3.27: Pawley fits of $(Mn_{1-x}Cu_x)_3[Co(CN)_6]_2$ at 500 K. Two-phase refinements are shown in the inset and indicated by teal text. The calculated diffraction pattern is shown in red and the experimental in black.

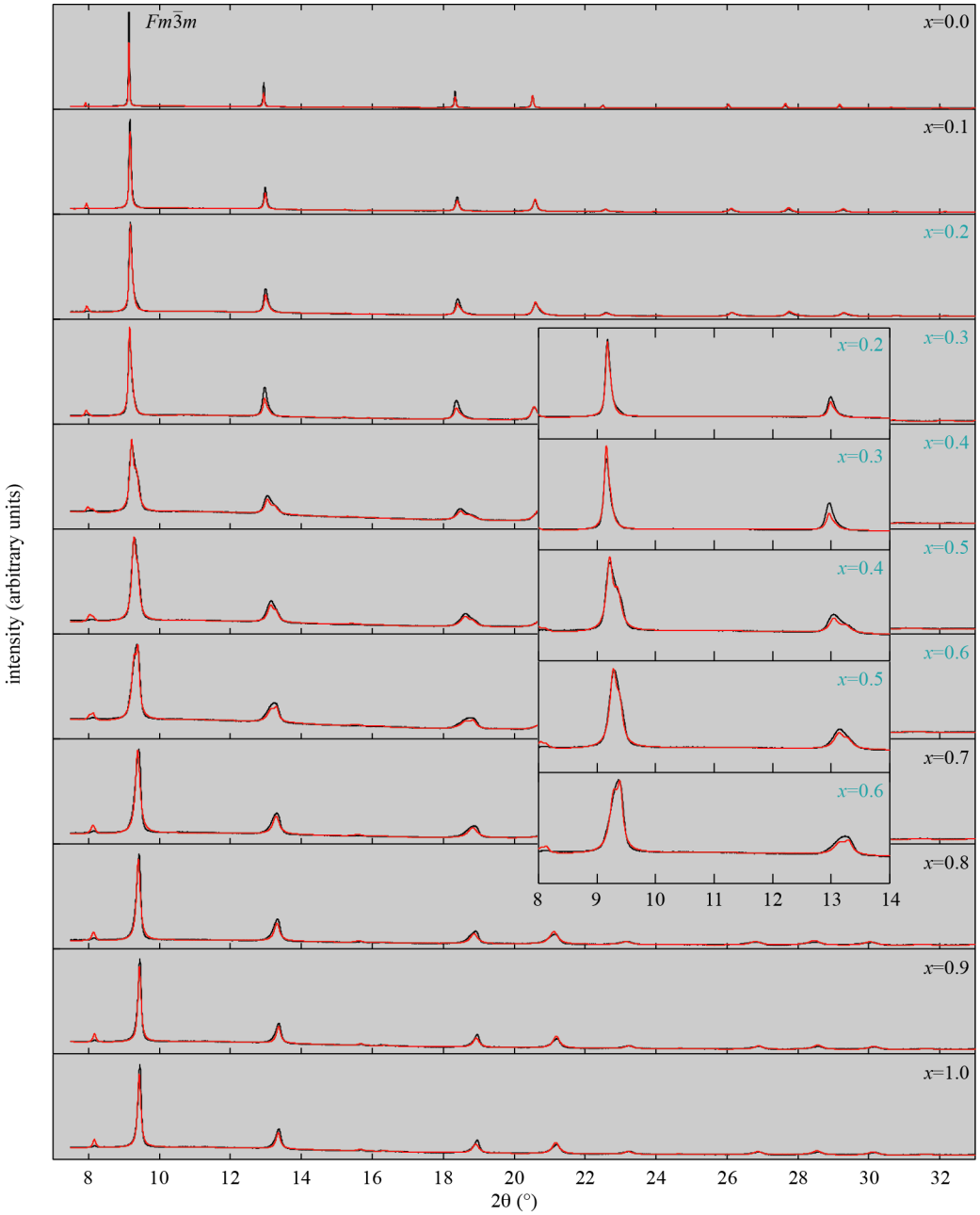


Figure C3.28: Constrained Rietveld fits of $(Mn_{1-x}Cu_x)_3[Co(CN)_6]_2$ at 500 K. Two-phase refinements are shown in the inset and indicated by teal text. The calculated diffraction pattern is shown in red and the experimental in black.

C3.2 $(Mn_{1-x}Cu_x)_3[Fe(CN)_6]_2$

At ambient conditions, $(Mn_{1-x}Cu_x)_3[Fe(CN)_6]_2$ behaves analogously to the corresponding cobaltate [Section 4.5.1]: isostructural endmembers and no composition-induced phase transitions. Likewise, two cubic isostructural phases feature at intermediate x-values, which were analysed by both one- and two-phase refinements [Fig. C3.29–C3.30 and Table C3.17], as discussed previously. However, the two phases merge upon heating and the unsplit peak shape persists at low temperature [Fig. C3.31–C3.32 and Tables C3.18–C3.19]. These patterns were refined using single-phase refinements. Notably, the background is increased and crystallinity is lower, which may be a sign of partial decomposition. Moreover, a sizeable reflection grows in at $2\theta = 16$ ($d \approx 3$ Å) in several patterns at 100 K and this cannot be satisfactory accounted for by the nearby 311 and 222 reflections. Finally, compounds with $x = 0.2$ and 0.3 exhibit a few extra peaks close to the intense 022 and 004 reflections at 13.5° and 18.5° ($d \approx 3.7$ and 2.6 Å), respectively. It is also worth noting that a subtle colour change from brown to dark blue occurred during the variable-temperature measurements. In essence, this system exhibits interesting non-ambient behaviour that merits further study; yet, there is no clear orbital disorder-order transition, which is the focus of this work. One can speculate whether the discrepant behaviour is related to charge transfer transitions, as has been observed for other hexacyanoferrate systems.[211,215]

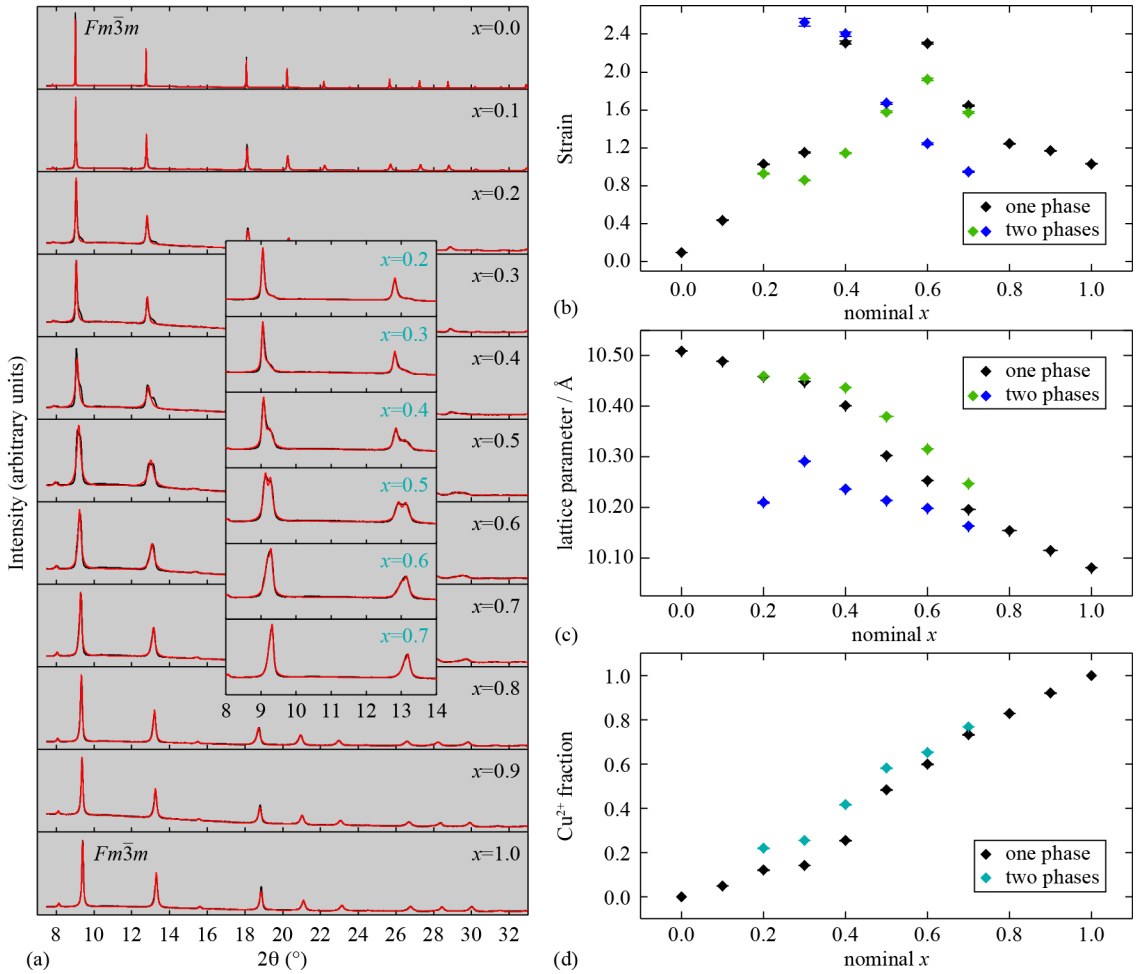


Figure C3.29: Crystallographic data for $(Mn_{1-x}Cu_x)_3[Fe(CN)_6]_2$ at ambient conditions. (a) Pawley fits of the diffraction patterns using only one phase with the inset showing two-phase fits of the samples at intermediate x. The calculated diffraction pattern is shown in red and the experimental in black. (b) The Lorentzian strain, (c) the lattice parameters, and (d) the calculated Cu concentration as a function of x. In all cases, the results from one-phase refinements are shown in black, whereas the two phases are coloured blue and green respectively.

Table C3.17: Crystallographic data for $(Mn_{1-x}Cu_x)_3[Fe(CN)_6]_2$ at ambient conditions.

	One-phase refinement		Two-phase refinement					
x_{nom}	a/Å	Strain	a/Å	Strain	Phase fraction	a/Å	Strain	Phase fraction
0	10.50930(2)	0.0934(5)						
0.1	10.48925(4)	0.4370(12)						
0.2	10.45833(13)	1.026(4)	10.46037(9)	0.928(4)	0.8303	10.2096(19)	3.52(8)	0.1697
0.3	10.44872(19)	1.148(6)	10.45611(11)	0.857(5)	0.6947	10.2917(12)	2.52(4)	0.3053
0.4	10.4011(5)	2.310(18)	10.43710(18)	1.147(7)	0.5773	10.2364(7)	2.40(2)	0.4227
0.5	10.3029(4)	2.947(17)	10.3801(3)	1.580(10)	0.5252	10.2141(4)	1.670(11)	0.4748
0.6	10.2533(3)	2.304(10)	10.3156(6)	1.924(15)	0.5747	10.1983(3)	1.244(11)	0.4253
0.7	10.19604(18)	1.646(6)	10.2475(6)	1.573(12)	0.5262	10.1634(2)	0.950(8)	0.4738
0.8	10.15417(11)	1.244(4)						
0.9	10.11540(10)	1.171(3)						
1	10.08067(9)	1.032(3)						

Table C3.18: Crystallographic data for $(Mn_{1-x}Cu_x)_3[Fe(CN)_6]_2$ at 100 K.

x_{nom}	a/Å	Strain
0	10.44666(5)	0.4114(14)
0.1	10.22290(17)	1.575(6)
0.2	10.1994(3)	1.511(10)
0.3	10.2294(4)	2.206(16)
0.4	10.2165(3)	2.082(13)
0.5	10.2261(3)	2.661(10)
0.6	10.2096(3)	2.250(13)
0.7	10.1966(3)	1.255(9)
0.8	10.1977(4)	2.675(18)
0.9	10.1500(5)	2.67(2)
1	10.04300(9)	1.000(3)

Table C3.19: Crystallographic data for $(Mn_{1-x}Cu_x)_3[Fe(CN)_6]_2$ at 500 K.

x_{nom}	a/Å	Strain
0	10.43281(4)	0.3030(10)
0.1	10.29620(10)	1.188(4)
0.2	10.2448(3)	1.484(10)
0.3	10.2537(7)	1.827(14)
0.4	10.2458(2)	2.251(9)
0.5	10.2433(4)	3.295(16)
0.6	10.2332(2)	2.476(10)
0.7	10.23520(14)	1.115(5)
0.8	10.2065(3)	3.145(14)
0.9	10.2276(5)	2.538(10)
1	10.1505(3)	2.575(12)

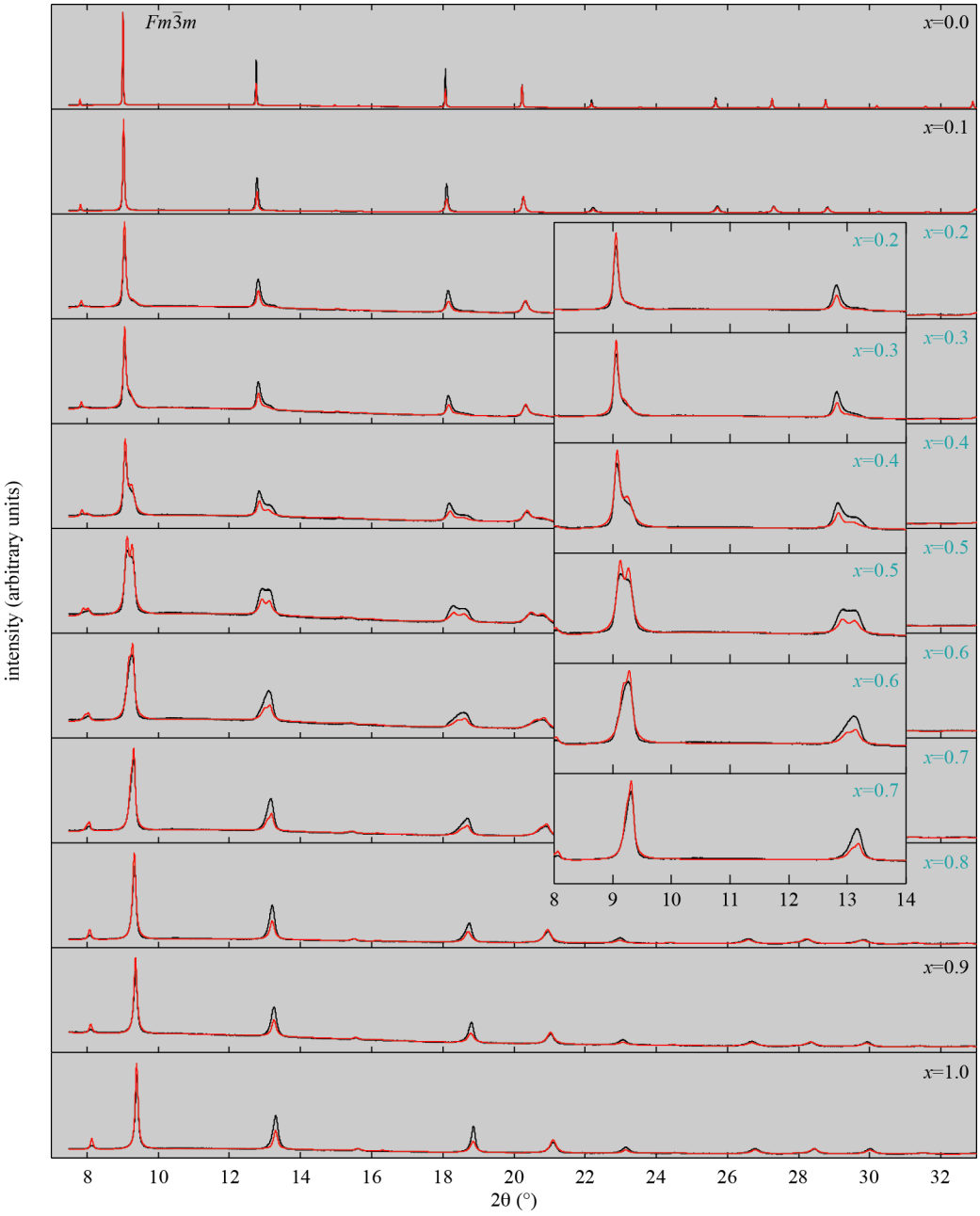


Figure C3.30: Constrained Rietveld fits of $(Mn_{1-x}Cu_x)_3[Fe(CN)_6]_2$ at ambient conditions. Two-phase refinements are indicated by teal text. The calculated diffraction pattern is shown in red and the experimental in black.

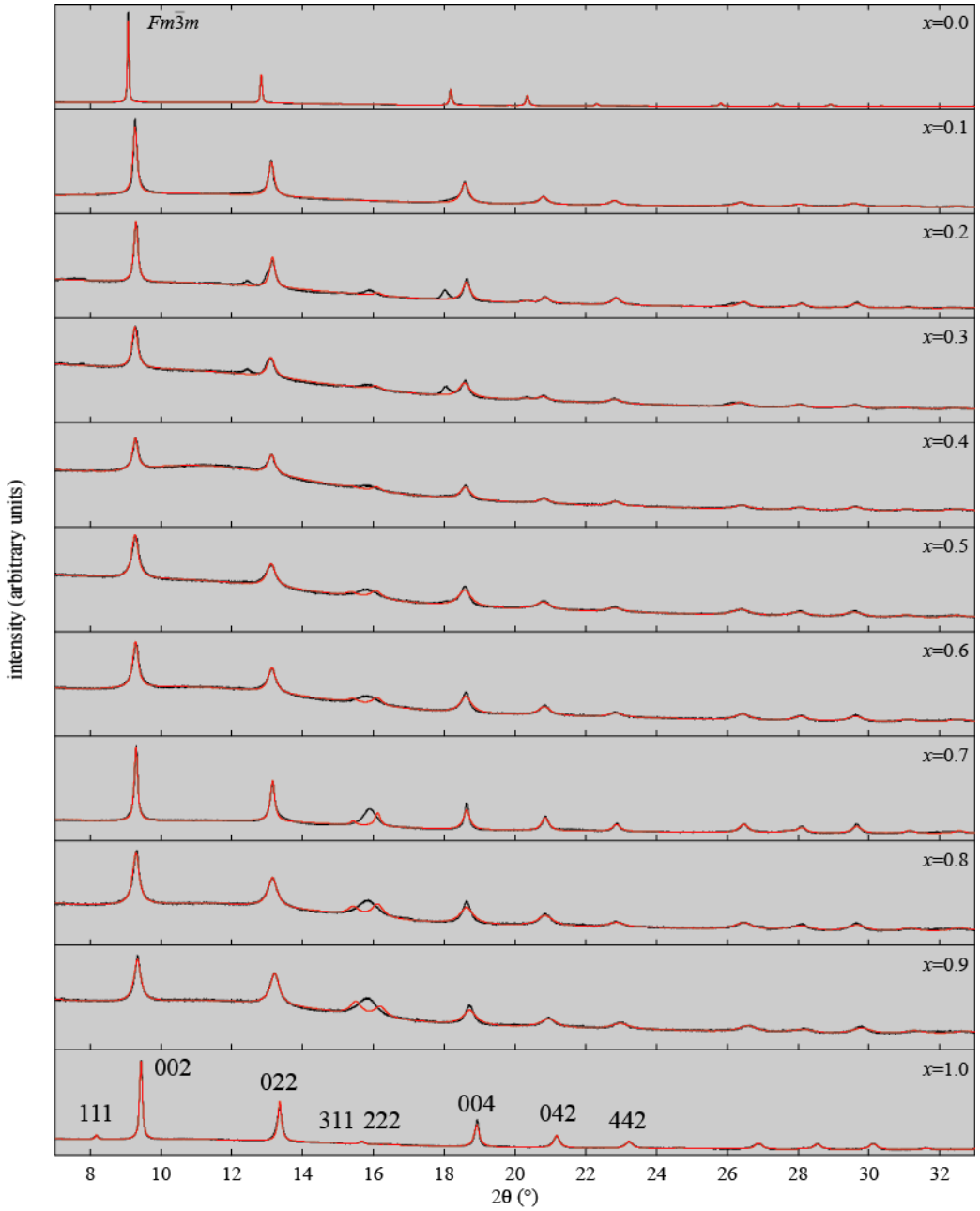


Figure C3.31: Pawley fits of $(Mn_{1-x}Cu_x)_3[Fe(CN)_6]_2$ at 100 K. The calculated diffraction pattern is shown in red and the experimental in black. Key reflections are labelled by Miller indices.

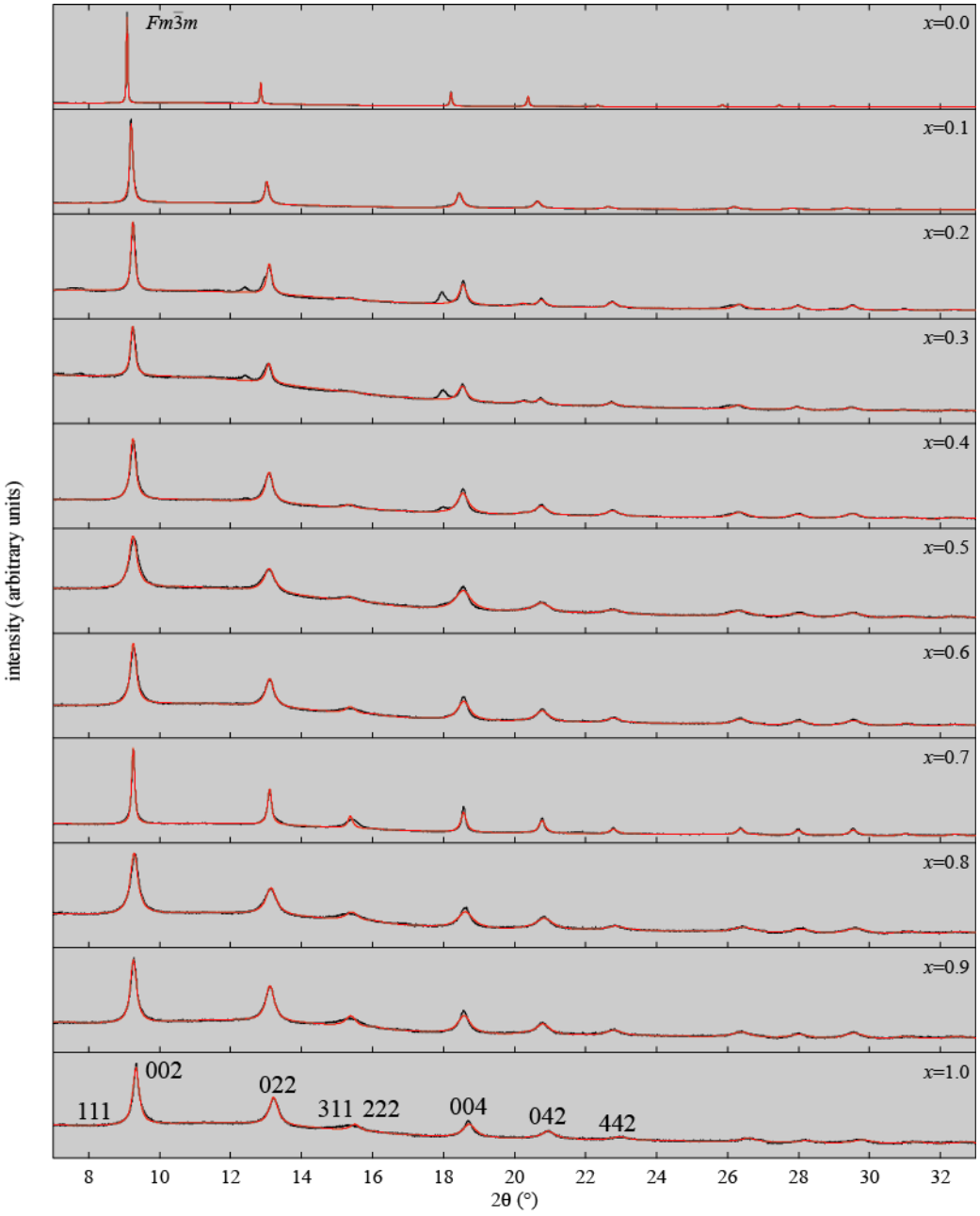


Figure C3.32: Pawley fits of $(Mn_{1-x}Cu_x)_3[Fe(CN)_6]_2$ at 500 K. The calculated diffraction pattern is shown in red and the experimental in black. Key reflections are labelled by Miller indices.

C3.3 $(Cd_{1-x}Cu_x)_3[Co(CN)_6]_2$

All members of the series $(Cd_{1-x}Cu_x)_3[Co(CN)_6]_2$ crystallise in $Fm\bar{3}m$ and there is no sign of multiple phases [Fig. C3.33 and Table C3.20]. As the two endmembers are isostructural, this system represents the simplest possible solid solution. No thermally induced phase transitions were observed [Fig. C3.34–C3.35 and Tables C3.21–C3.22].

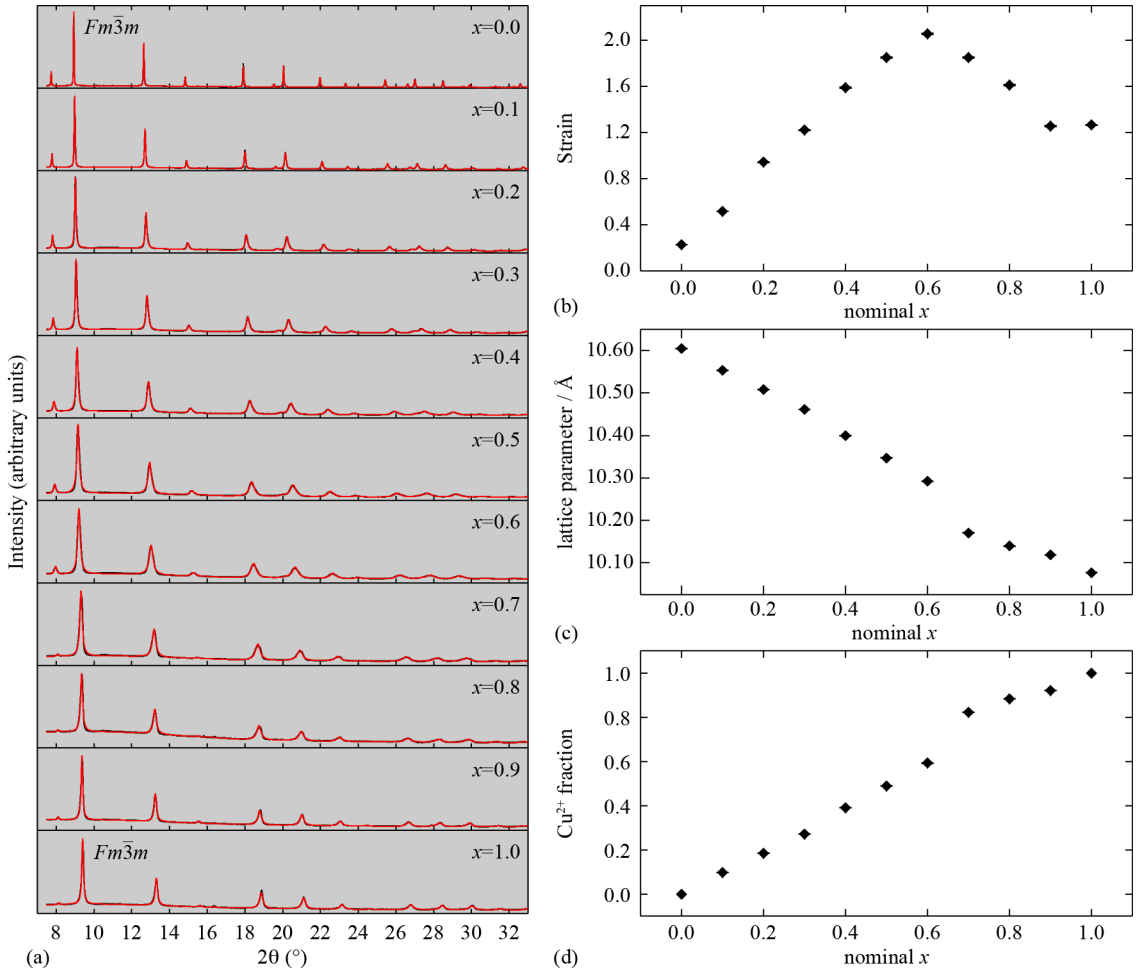


Figure C3.33: Crystallographic data for $(Cd_{1-x}Cu_x)_3[Co(CN)_6]_2$ at ambient conditions. (a) Pawley fits of the diffraction patterns at ambient conditions. The calculated diffraction pattern is shown in red and the experimental in black. (b) The Lorentzian strain, (c) the lattice parameters, and (d) the calculated Cu concentration as a function of x.

Table C3.20: Crystallographic data for $(Cd_{1-x}Cu_x)_3[Co(CN)_6]_2$ at ambient conditions.

x_{nom}	a/Å	Strain
0	10.60481(2)	0.2299(5)
0.1	10.55357(3)	0.5172(8)
0.2	10.50823(8)	0.943(2)
0.3	10.46174(9)	1.221(3)
0.4	10.39957(12)	1.588(4)
0.5	10.34731(16)	1.848(5)
0.6	10.29269(17)	2.053(6)
0.7	10.1706(2)	1.849(7)
0.8	10.13911(18)	1.610(6)
0.9	10.11917(12)	1.255(4)
1	10.07700(12)	1.264(4)

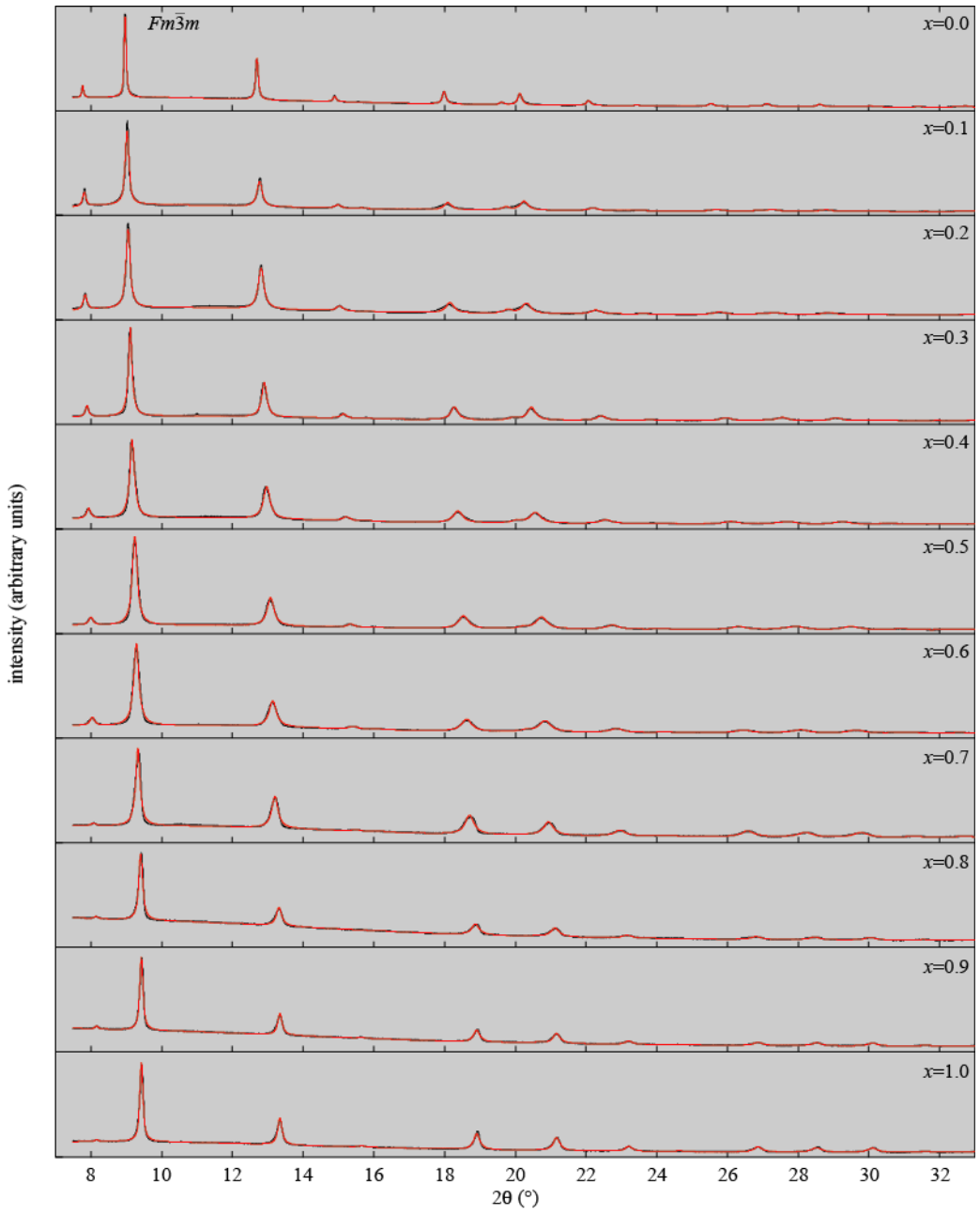


Figure C3.34: Pawley fits of the PXRD patterns of $(Cd_{1-x}Cu_x)_3[Co(CN)_6]_2$ at 100 K. The calculated diffraction pattern is shown in red and the experimental in black.

Table C3.21: Crystallographic data for $(Cd_{1-x}Cu_x)_3[Co(CN)_6]_2$ at 100 K.

x_{nom}	a/Å	Strain
0	10.56088(7)	0.733(2)
0.1	10.49861(16)	1.480(5)
0.2	10.46542(16)	1.679(5)
0.3	10.39409(13)	1.482(4)
0.4	10.33734(18)	1.951(6)
0.5	10.25148(16)	2.027(5)
0.6	10.20350(19)	2.137(6)
0.7	10.1571(2)	1.805(7)
0.8	10.06917(17)	1.527(6)
0.9	10.04932(11)	1.211(4)
1	10.04908(11)	1.186(4)

Table C3.22: Crystallographic data for $(Cd_{1-x}Cu_x)_3[Co(CN)_6]_2$ at 500 K.

x_{nom}	a/Å	Strain
0	10.53080(6)	0.4972(17)
0.1	10.46748(18)	1.419(6)
0.2	10.41036(14)	1.494(4)
0.3	10.37077(12)	1.453(4)
0.4	10.29693(16)	1.830(5)
0.5	10.24614(17)	2.070(6)
0.6	10.1839(2)	2.173(8)
0.7	10.0770(2)	1.920(7)
0.8	10.05429(18)	1.565(6)
0.9	10.03376(12)	1.224(4)
1	10.04569(11)	1.217(4)

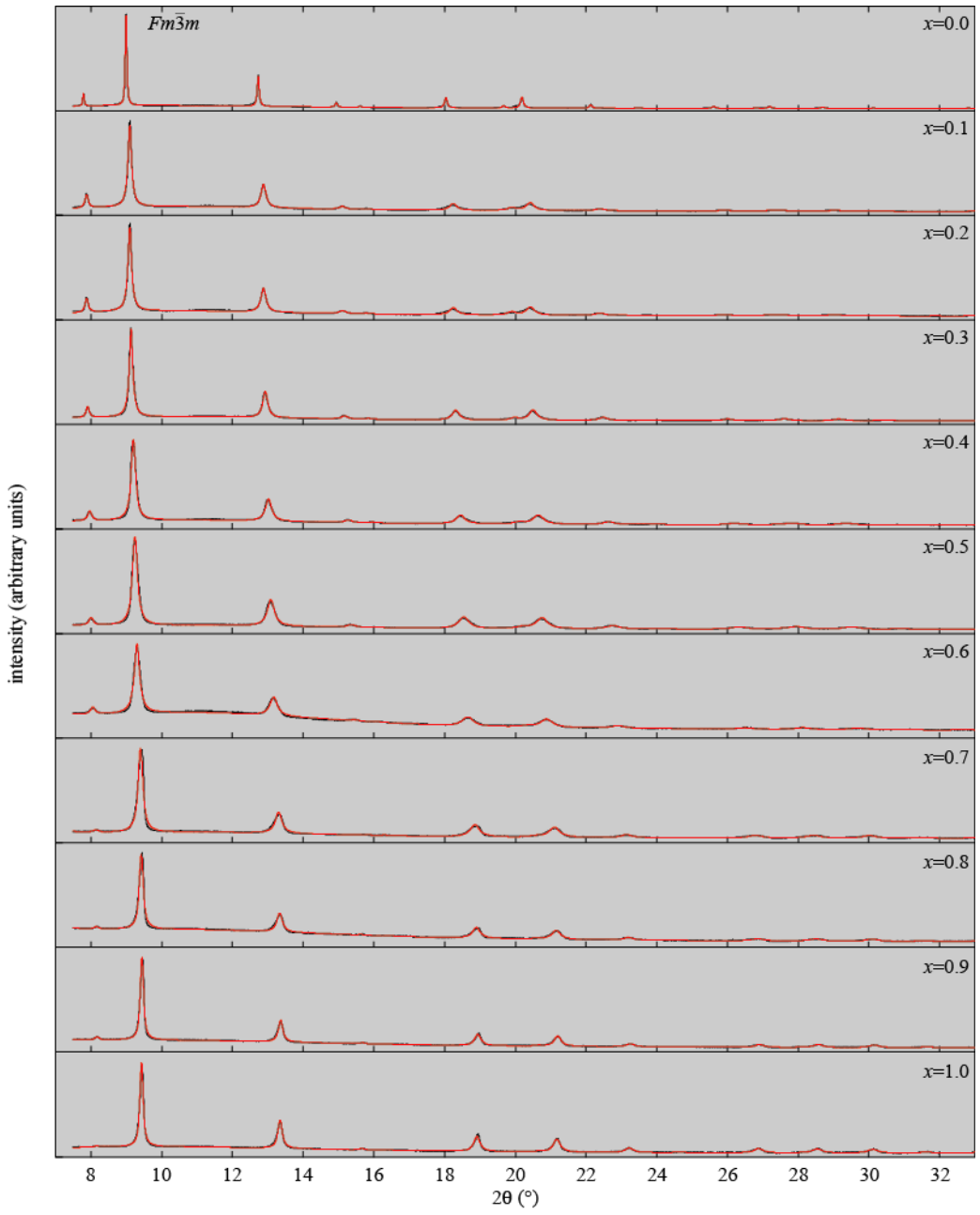


Figure C3.35: Pawley fits of the PXRD patterns of $(Cd_{1-x}Cu_x)_3[Co(CN)_6]_2$ at 500 K. The calculated diffraction pattern is shown in red and the experimental in black.

Appendix D

The following is a manuscript in preparation.

Hidden Vacancy Polymorphism of Prussian Blue Analogues

Arkadiy Simonov,[1] Trees De Baerdemaeker,[1,2] Maria Laura Rios Gomez,[3] Hanna L. B. Boström,[1] Chloe S. Coates,[1] Harry J. Gray,[1] Hans-Beat Bürgi,[4] and Andrew L. Goodwin [1,*]

[1]Department of Chemistry, University of Oxford, Inorganic Chemistry Laboratory, South Parks Road, Oxford OX1 3QR, U.K.
[2]Centre for Surface Chemistry and Catalysis, KU Leuven, Celestijnenlaan 200F, P.O. Box 2461, 3001 Leuven, Belgium
[3]Departamento de Polímeros, Instituto de Investigaciones en Materiales, Universidad Nacional Autónoma de México, Ciudad de México 04510, Mexico
[4]Department of Chemistry, University of Zurich, Winterthurerstrasse 190, CH-8057 Zürich, Switzerland

∗To whom correspondence should be addressed; E-mail: andrew.goodwin@chem.ox.ac.uk.

Prussian blue analogues (PBAs) are a broad and important family of microporous inorganic solids, famous for their gas storage (*1–5*), metal-ion immobilisation (*6, 7*), proton conduction (*8, 9*), and stimuli-dependent magnetic (*10–12*), electronic (*13*) and optical (*14*) properties. The family also includes the widely-used double-metal cyanide (DMC) catalysts (*15–17*) and the topical hexacyanoferrate/hexacyanomanganate (HCF/HCM) battery materials (*18–20*). Central to the various physical properties of PBAs is the ability to transport mass reversibly, a process made possible by the presence of a large number of structural vacancies. Normally presumed random (*21–23*), the arrangement of these vacancies is actually crucially important because it controls the connectivity of the micropore network, and hence diffusivity and adsorption profiles (*24, 25*). The long-standing obstacle to characterising PBA vacancy networks has always been the

relative inaccessibility of single-crystal samples (*26*). Here we report the growth of single crystals of a range of PBAs. By measuring and interpreting their X-ray diffuse scattering patterns, we identify for the first time a striking diversity of non-random vacancy arrangements that is hidden from conventional crystallographic analysis of powder samples. Moreover, we show that this unexpected phase complexity can be understood in terms of a remarkably simple microscopic model based on local rules of electroneutrality and centrosymmetry. The hidden phase boundaries that emerge demarcate vacancy polymorphs with profoundly different micropore characteristics. Our results establish a clear foundation for correlated defect engineering in PBAs as a means of controlling storage capacity, transport profile, and phase stability.

The true crystal structures of PBAs—as of Prussian Blue itself—have long posed a difficult and important problem in solid-state chemistry because their ostensibly simple powder diffraction patterns [Fig. 1(a)] belie a remarkable complexity at the atomic scale (*27–29*). The common parent structure is based on the cubic lattice and corresponds to the idealised composition $M[M'(CN)_6]$. Atoms of type M and M′ (usually transition-metal cations) occupy alternate lattice vertices and are octahedrally coordinated by bridging cyanide ions (CN^-) at the lattice edges [Fig. 1(b)]. There is a close conceptual parallel to the double perovskite structure (*30*); indeed the key considerations of covalency and octahedral coordination geometry that stabilise perovskites amongst oxide ceramics (*31*) also favour this same architecture for transition-metal cyanides, which accounts for the chemical diversity of PBAs (*32*). Charge balance requires that the formal oxidation states of the M and M′ cations sum to six, as in $Cd^{II}[Pd^{IV}(CN)_6]$ (*33*).

Prussian Blue is a mixed-valence cyanide of iron in its 2+ and 3+ oxidation states (*34, 35*), and so its composition cannot respect this oxidation-state sum rule. Instead the rule is circumvented by the inclusion of vacancies: the composition is well approximated by the formula $Fe^{III}[Fe^{II}(CN)_6]_{3/4}\square_{1/4}\cdot xH_2O$, where the symbol $\square$ represents a vacancy on the M′-site (*28*). Each vacancy gives rise to a micropore of effective diameter $\sim$8.5 Å (*36*) that is greater than the distance between neighbouring M′-sites

($a/\sqrt{2} \simeq 7.2$ Å). Hence a pair of neighbouring vacancies, if present, connects to form a larger micropore (*1*). A random distribution of the quarter of vacant M′-sites would imply bulk micoroporosity, since this vacancy fraction is larger than the percolation threshold for the face-centered cubic M′ sublattice $p_{\mathrm{C}} \simeq 0.20$ (*37*). But Prussian Blue is not microporous: the single-crystal X-ray diffraction study of Ref. 28 showed that vacancies tend to avoid one another by adopting a specific ordered arrangement [Fig. 1(b)]. A vacancy fraction of 1/4 is actually the greatest that can support complete vacancy isolation in this way.

PBAs with a nominal composition of $\mathrm{M^{II}[M'^{III}(CN)_6]_{2/3}\square_{1/3}} \cdot x\mathrm{H_2O}$ (hereafter abbreviated to "M[M′]") contain an even higher fraction of M′-site vacancies than Prussian Blue (*32,38*). Hence geometry dictates that these vacancies—whether distributed randomly or not—must form connected neighbour-pairs [Fig. 1(b)]. The existence and nature of any extended micropore network that then develops from these local connections depends on longer-range vacancy correlations. The collective micropore structure of PBAs is remarkably poorly understood, despite the many important properties of the family and the relevance of mass transport to these properties (*1, 20*). So what *is* known? Adsorption isotherm measurements have long indicated a significant variability in pore characteristics as a function of PBA composition (*38, 39*). Solid-state ^{113}Cd NMR measurements have shown evidence of non-statistical vacancy distributions throughout the solid solution Cd[Fe]–Cd[Co] (*40*). Weak primitive superlattice reflections have sometimes been observed and sometimes not in the powder X-ray diffraction patterns of various PBAs; their presence has usually been interpreted as evidence for (partial) Prussian-blue-type vacancy order (*26*). For the Zn[Co] DMC catalysts, the pore structures of some—and only some—samples have been found to collapse on dehydration to give a rhombohedral form with substantially reduced catalytic activity, but the reasons for sample specificity are not well understood (*23, 41*). High-resolution transmission electron (HRTEM) microscopy has demonstrated the presence of vacancy chains in some Cu-PBAs as well as their absence in other Zn-containing samples (*42*). And in the one existing single-crystal diffraction study of a PBA (*viz*. Mn[Mn]), strong diffuse scattering was observed and interpreted

in terms of Warren–Cowley correlation parameters (*43, 44*). Taken together, these observations suggest that (i) micropore network models based on random vacancy distributions are unlikely to be realistic, and (ii) there must be substantial variability amongst the pore networks of different PBAs.

In this study, we have characterised vacancy correlations in a range of PBAs by growing single crystal samples, measuring their X-ray diffuse scattering patterns, and interpreting these patterns *via* three-dimensional difference pair distribution function (3D-ΔPDF) analysis and Monte Carlo (MC) simulations. We managed to grow single crystals by employing a variety of slow-diffusion techniques (see SI); despite focusing predominantly on the hexacyanocobaltates M[Co] we will nevertheless come to discuss our results in the broader context of PBAs in general.

For every crystal we tested, the corresponding single-crystal X-ray diffraction pattern contained weak but highly-structured diffuse scattering, which is the hallmark of strongly-correlated disorder (*45, 46*). Representative $(hk0)$ cuts of our diffuse scattering patterns are shown for a selection of PBAs in Fig. 2, where we include the only other single-crystal diffuse scattering pattern ever reported for a PBA—namely for Mn[Mn] (Refs. 43,44). Drawing on the detailed analysis of Ref. 44 we can be confident that the main diffuse scattering features we observe are elastic rather than inelastic in origin. Inverse Fourier transform of the normalised diffuse scattering function yields the 3D-ΔPDF (*47*), which clearly shows the scattering to arise from vacancy correlations (and associated structural relaxation) rather than any alkali cation or solvent inclusion (see SI). In powder X-ray diffraction (PXRD) measurements, orientational averaging acts to conceal this diffuse scattering within the background function and/or to cause it to resemble primitive superlattice reflections (*44*); it is in this sense that the vacancy correlations from which the diffuse scattering arises are "hidden" from conventional PXRD analysis.

Importantly, and contrary to the expectations of Ref. 44, we find a remarkable diversity of diffuse scattering patterns amongst PBAs. This is true even for crystals with the same nominal composition but grown in separate batches (the example in Fig. 2 is a pair of Mn[Co] crystals grown at different rates). So our experimental data unambiguously show that the vacancies in PBAs are distributed in a highly

non-random manner, and that these distributions are fundamentally different for different PBA samples.

How might we understand this diversity, and what are its implications for mass transport in PBAs? To answer these questions we have developed a very simple vacancy interaction model that is nevertheless capable of explaining qualitatively the various diffuse scattering patterns observed experimentally. MC simulations driven by this set of interactions generate representative pore network configurations for each phase that can then be used to determine physical properties of relevance to mass transport and storage in PBAs. The model we have developed contains just two ingredients, each arising from simple crystal-chemical considerations. The first favours a uniform vacancy distribution—*i.e.* such that for each M-site four of its six neighbouring M′-sites are occupied and two are vacant. This contribution reflects Pauling's "electroneutrality" principle (*48*), and is consistent with earlier local-structure investigations based predominantly on Cd environment distributions in Cd[Fe_xCo_{1-x}] (*40*). The second ingredient acts to favour centrosymmetric vacancy distributions around the M-site, which we expect to be more or less important as a function of M-site chemistry (*e.g.*, crystal field effects and/or tendency for off-centering). Formally, we represent the MC energy of a given vacancy model by the expression

$$E = \sum_{\mathbf{r}\in\{\mathrm{M}\}} \left[J_1 \left(4 - \sum_{\mathbf{r}'\in\frac{1}{2}\langle 100\rangle} e_{\mathbf{r}+\mathbf{r}'} \right)^2 + \frac{J_2}{2} \sum_{\mathbf{r}'\in\frac{1}{2}\langle 100\rangle} (e_{\mathbf{r}+\mathbf{r}'} - e_{\mathbf{r}-\mathbf{r}'})^2 \right], \tag{1}$$

where the M′-site states $e_{\mathbf{r}} = 0$ (vacant) or 1 (present), and $J_1, J_2 > 0$ quantify the strength of the electroneutrality and centrosymmetry terms, respectively. The occupancy fraction $\frac{1}{N_{\mathrm{M}'}} \sum_{\mathbf{r}\in\{\mathrm{M}'\}} e_{\mathbf{r}}$ is fixed at $\frac{2}{3}$ (here $N_{\mathrm{M}'}$ is the number of M′-sites in the MC model). We proceeded to carry out a series of MC simulations driven by Eq. (1) for a range of $J' = J_1/J_2$ ratios and for various effective temperatures $T' = T/J_2$. Our results are shown in Fig. 3(a), represented in terms of the single-crystal X-ray diffuse scattering patterns calculated from an ensemble of 40 MC configurations generated at each point across an evenly-distributed mesh of suitable $J', \log(T')$ parameters.

The phase behaviour we observe from this simple MC model is remarkable for a number of reasons. Clearly the form of the diffuse scattering—and, as we will come to see, of the pore network geometry—is

an extremely sensitive function of J' and T'. This observation mirrors closely our experimental results: namely, that small variations in synthesis conditions or PBA composition are accompanied by substantial changes in the form of the diffuse scattering. Such sensitivity arises because the two interaction terms of electroneutrality and centrosymmetry actually operate in tension: they are mutually resolvable at a vacancy fraction of 25% (leading to the ordered Prussian Blue vacancy arrangement shown in Fig. 1(c)) but become frustrated as additional vacancies are added to the system. Hence the two simple crystal-chemical considerations embedded in Eq. (1) drive an unexpectedly complex configurational landscape for the $\frac{1}{3}$ M′-site vacancy fraction of PBAs that is reminiscent of geometric frustration in relaxor ferroelectrics (*e.g.* $Pb(Mg_{1/3}Nb_{2/3})O_3$ (*49*)) and relaxor ferromagnets (*e.g.* $La(Sb_{1/3}Nb_{2/3})O_3$ (*50*)).

Importantly, the experimental diffuse scattering patterns given in Fig. 2 are well approximated by our MC simulations at different specific values of J' and T' [Fig. 3(a,b)]. The implication is that considerations of electroneutrality and centrosymmetry alone are sufficient to account for the basic form and diversity of diffuse scattering patterns observed experimentally. But what determines J' and T' for a given system? PBAs for which the M-site cation is crystal-field active (Cu[Co] and Co[Co]) correspond to smaller values of J', which is sensible because crystal field (including Jahn-Teller (JT)) effects must increase the relative importance of the centrosymmetry (J_2) term in the lattice energy. By contrast, crystal-field-inactive M-site cations correspond to larger J'; the especially large values for Zn[Co] and Cd[Co] likely reflect the propensity of Zn and Cd to adopt (acentric) tetrahedral coordination in their pseudobinary cyanides $M(CN)_2$ (*51, 52*) [Fig. 3(c)]. So variation of PBA composition allows control over J', with M-site chemistry playing a more important role than that of the M′-site. In contrast, the effective MC temperature T' will reflect precursor concentration and speed of crystal growth during synthesis (high $T' \equiv$ fast growth and/or high concentration). Indeed our various Mn[M′] samples correspond to a common J' value $\simeq 1$ but differ in terms of T', with the lowest T' value obtained for the slowest-grown sample (gel diffusion). So, from a synthetic viewpoint, there is genuine scope for navigating J', T'-space through judicious choice of PBA chemistry (J') and synthesis approach (T').

Just as the calculated diffuse scattering patterns are unexpectedly diverse for our MC configurations, so too are the corresponding pore network structures [Fig. 4(a)]. Despite their considerable disorder, these networks have meaningfully different physical characteristics that we will come to discuss in greater detail below. Collectively the various different scattering patterns and pore network types identify previously-unknown phase domains of distinct vacancy polymorphs, the boundaries between which are essentially hidden from conventional PXRD analysis [Fig. 3(b); see SI for further discussion]. One specific real-space motif that recurs in different forms amongst these phases is that of "ladder" vacancies which can connect to form columnar, planar, or lattice-like micropores [Fig. 4(b)]. The physical relevance of this motif to real PBA samples is directly evident from the experimental 3D-ΔPDF function itself [Fig. 4(c)] as it is in previous high-resolution transmission electron microscopy measurements (*42*). The structure of rhombohedral Zn[Co] DMCs (*53*) contains collapsed ladder vacancies [Fig. 4(d)], suggesting that varying degrees of ladder-vacancy preorganisation in cubic Zn[Co] samples may explain their varying susceptibilities to structural collapse on dehydration.

In Fig. 3(d) we show a range of physical quantities calculated from our MC configurations as a function of J' and T'. Some of these—*e.g.* the MC energy gradient $\log(\frac{\Delta E}{\Delta T})$ or the degree of diffuse scattering localisation $L = \log\left[\frac{\sum I^2}{(\sum I)^2}\right]$—serve primarily to highlight phase boundaries, but others are particularly relevant to the transport properties of PBA phases. For example, tortuosity τ is a measure of the curvature of internal pore space (*54, 55*) and hence its variation suggests a range of both adsorption and transport profiles amongst PBAs (*25*). It is a particularly important quantity in the context of gas- or ion-storage materials because it affects the rate of mass transport (also known as conductance or volumetric flow rate (*56*)):

$$C \propto \frac{\rho}{\tau^2}, \tag{2}$$

where ρ is the number of vacancy neighbour-pairs per formula unit (*57*). We find C varies by as much as a factor of two within the high-temperature disordered "A" phase and by yet another factor of two on progressing into lower-temperature phases. In other words, the variation in diffuse scattering we observe

experimentally reflects a variation in pore network structure that accounts for a fourfold difference in transport rates. Even accessible pore volumes vary substantially: we calculate differences $> 25\%$ for this same family of configurations. Moreover, a number of vacancy polymorphs are strongly anisotropic and hence their transport properties will depend on orientation. So on the one hand this incredible variability in pore network characteristics helps explain the irreproducibility and diversity of sorption and storage properties observed experimentally. And, on the other hand, it serves to highlight the clear opportunity for optimisation of transport and storage characteristics *via* synthetic control over vacancy correlations—*i.e.* defect engineering (*58*). For most mass transport applications, our results favour a combination of low J' (*e.g.* JT-active M = Cu) and high T' (rapid precipitation), which is consistent with the empirical identification of Cu[Fe] ("CuHCF") as a high-performance battery material (*18*).

Our results identify a number of future challenges. In this study we have deliberately focussed on single-crystal PBA samples—indeed one of our key points is that PXRD is remarkably insensitive to the vacancy polymorphism of this family. So the task of establishing a robust link between vacancy correlations and (to take one example) ion-storage capacity in HCF battery components will require innovative approaches to measuring and interpreting diffuse scattering from the microcrystalline components used in real materials. Serial femtosecond crystallography (*59*) and/or low-energy electron diffraction (*60*) may help in this regard. Our analysis has also been intentionally simplistic: we have not needed to invoke the role of alkali metal inclusion in mediating vacancy stoichiometry or distributions, nor have we considered the strain implications of cooperative JT distortions (*61*). Yet these additional degrees of freedom must allow further chemical control over pore network characteristics. Indeed there is a very large number of potential variables one might use to engineer defects in PBAs—*e.g.* concentration, pH, crystal growth kinetics and media, temperature, speciation, solubility, competing ions, chelation—and establishing rules that link these variables to vacancy polymorphs represents an enormous task, albeit one with clear practical benefits. Our results raise new questions both of vacancy mobility in PBAs and of the implications of vacancy polymorphism for magnetic order, spin-state transitions, orbital order,

and photophysics in these materials. Moreover, any mechanistic understanding of DMC catalysis will require characterisation of particle surface structure, which we now find may be substantially more complex (and varied) than previously anticipated. And, stepping back, is it not also tempting to ask: are PBAs special? Or does a similar wealth of hidden polymorphism play a role in the defect chemistry of other microporous phases, such as metal–organic frameworks (*62*) and zeolites (*63*)?

Methods

Single crystal growth

Single crystal PBA samples were grown using slow diffusion methodologies. Typical preparations involved counterdiffusion of aqueous solutions of a potassium hexacyanometallate(III) and a divalent transition-metal nitrate or chloride. Crystals of Cd[Co], Mn[Co]*I*, Mn[Fe], and Zn[Co] were grown in H-cells, while those of Mn[Co], Cu[Co], Co[Co] and Mn[Mn] were grown from silica gel.

Single crystal diffuse scattering

Single crystal diffuse scattering measurements were carried out using the I19 beamline at the Diamond Light Source (U.K.) and the BM01 beamline at the European Synchrotron Radiation Facility (France). Each measurement involved a full sphere of data collection carried out in a single run. Bragg peaks were indexed and integrated using the package XDS (*64*). Reciprocal space reconstruction and averaging was performed in the software MEERKAT (*65*).

3D-ΔPDF analysis

Diffuse scattering was analysed using the 3D-ΔPDF method (*66,67*). The experimental diffuse scattering was reconstructed as stated above. Then the background air scattering was subtracted by using an empty instrument run and manually selecting the optimal scale coefficient. The resulting diffuse scattering was averaged in the $m\bar{3}m$ Laue group using outlier rejection as described by Blessing (*68*). Bragg peaks were removed using the "punch and fill" procedure: spheres of intensity around the Bragg peaks were removed

to ensure omission of thermal diffuse scattering contributions from subsequent analysis. The resulting holes were filled with the median intensity from a small surround region of reciprocal space. Finally, the 3D-ΔPDF map was calculated using fast Fourier transform. Quantitative 3D-ΔPDF refinement was carried out using the program YELL (*69*).

Monte Carlo simulations and analysis

Monte Carlo (MC) simulations were carried out using a parallel tempering approach (*70*) implemented within custom-written code. For each J' value, an ensemble of 160 configurations was generated and MC simulations carried out at a suitable distribution of temperatures T' (evenly spread in $\log T'$). Replica exchange steps were implemented following regular intervals of successful MC steps. Configurations were equilibrated for a fixed number of epochs, and 40 configurations for diffuse scattering calculations were selected from a further production run. Diffuse scattering patterns were calculated from this ensemble of configurations with $m\bar{3}m$ symmetry applied. Convergence was almost universal except for a small family of polymorph II configurations at the very lowest sampled temperatures. Surface area and accessible pore volume calculations were calculated using the ZEO++ code (*71*).

References

1. S. S. Kaye & J. R. Long, J. Am. Chem. Soc. **127**, 6506 (2005).

2. K.W. Chapman, P.D. Southon, C.L. Weeks & C.J. Kepert, Chem. Comm., 3322 (2005)

3. B. Zamora, J. Roque, J. Balmaseda & E. Reguera, Z. Anorg. Allg. Chem. **636**, 2574 (2010).

4. L. Hu, P. Zhang, Q.-W. Chen., Y-Y. Mei & N. Yan, RSC Adv. **1**, 1574 (2011).

5. F. Karadas, H. El-Faki, E. Deniz, C. T. Yavuz, S. Aparicio & M. Atilhan, Micro. Meso. Mater. **162**, 91 (2012).

6. P. A. Haas, Sep. Sci. Technol. **28**, 2479 (1993).

7. T. Vincent, C. Vincent & E. Guibal, Molecules **20**, 20582 (2015).

8. S.-I. Ohkoshi, K. Nakagawa, K. Tomono, K. Imoto, Y. Tsunobuchi & H. Tokoro, J. Am. Chem. Soc. **132**, 6620 (2010).

9. K. Ono, M. Ishizaki, K. Kanaizuka, T. Togashi, T. Yamada, H. Kitagawa & M. Kurihara, Angew. Chem. Int. Ed. **56**, 5531 (2017).

10. S. Ferlay, T. Mallah, R. Ouahés, P. Veillet & M. Verdaguer, Nature **378**, 701 (1995).

11. M. Verdaguer & G. Girolami, Magnetic Prussian Blue analogues. In J. S. Miller & Drillon, M. (eds.) Molecules to Materials V, 283–346 (WILEY-VCH Verlag GmbH & Co. KGaA, Weinheim, 2004).

12. I. Maurin, D. Chernyshov, F. Varret, A. Blezen, H. Tokoro, K. Hashimoto & S.-I. Ohkoshi, Phys. Rev. B **79**, 064420 (2009).

13. A. I. Rykov, X. Li & J. Wang, J. Solid State Chem. **227**, 35 (2015).

14. A. Bleuzen, C. Lomenech, V. Escax, F. Villain, F. Varret, C. Cartier dit Moulin & M. Verdaguer, J. Am. Chem. Soc. **122**, 6648 (2000).

15. B. Le-Khac & W. Chester, Highly active double metal cyanide catalysts. U.S. Patent 5,714,428, (1998).

16. A. Peeters, P. Valvekens, R. Ameloot, G. Sankar, C. E. A. Kirschhock & D. E. De Vos, ACS Catal. **3**, 597 (2013).

17. A. García-Ortiz, A. Grirrane, E. Reguera & H. García, J. Catalysis **311**, 386 (2014).

18. C. D. Wessells, R. A. Huggins & Y. Cui, Nature Commun. **2**, 550 (2011).

19. H.-W. Lee, R. Y. Wang, M. Pasta, S. W. Lee, N. Liu & Y. Cui, Nature Commun. **5**, 5280 (2014).

20. M. Pasta, C. D. Wessells, N. Liu, J. Nelson, M. T. McDowell, R. A. Huggins, M. F. Toney & Y. Cui, Nature Commun. **5**, 3007 (2014).

21. A. Ludi, H. U. Güdel & M. Ruegg, Inorg. Chem. **9**, 2224 (1970).

22. D. F. Mullica, W. O. Milligan, G. W. Beall & W. L. Reeves, Acta Cryst. B**34**, 3558 (1978).

23. J. Roque, E. Reguerra, J. Balmasseda, J. Rodríguez-Hernández, L. Reguera & L. F. del Castillo, Micro. Meso. Mater. **103**, 57 (2007).

24. Y. Moritomo, K. Igarashi, J. Kim & H. Tanaka, Appl. Phys. Exp. **2**, 085001 (2009).

25. Q. Xiong, T. G. Baychev & A. P. Jivkov, J. Contam. Hydr. **192**, 101 (2016).

26. F. Grandjean, L. Samain & G. J. Long, Dalton Trans. **45**, 18018 (2016).

27. J. F. Keggin & F. D. Miles, Nature **137**, 577 (1936).

28. H. J. Buser, D. Schwarzennbach, W. Petter & A. Ludi, Inorg. Chem. **16**, 2704 (1977).

29. F. Herren, P. Fischer, A. Ludi & W. Hälg, Inorg. Chem. **19**, 956 (1980).

30. C. J. Howard & H. T. Stokes, Acta Cryst. A**61**, 93 (2005).

31. J. B. Goodenough, Phys. Rev. **100**, 564 (1955).

32. A. G. Sharpe. The Chemistry of Cyano Complexes of the Transition Metals (Academic Press, London, 1976).

33. H.-J. Buser, G. Ron, A. Ludi & P. Engel, J. Chem. Soc., Dalton Trans., 2473 (1974).

34. J. L. Frisch, Miscellanea Berolinensia ad incrementum scientiarum **1**, 377 (1710).

35. B. M. Chadwick & A. G. Sharpe, Adv. Inorg. Chem. Radiochem. **8**, 83 (1966).

36. C. P. Krap, J. Balmaseda, L. F. del Castillo, B. Zamora & E. Reguera, Energy Fules **24**, 581 (2010).

37. S. C. van der Marck, Int. J. Mod. Phys. C **9**, 529 (1998).

38. S. S. Kaye & J. R. Long, Catalysis Today **120**, 311 (2007).

39. R. Roque-Malherbe, F. Lugo & R. Polanco, Appl. Surf. Sci. **386**, 360 (2016).

40. A. Flambard, F. H. Köhler & R. Lescouëzec, Angew. Chem. Int. Ed. **48**, 1673 (2009).

41. C. Marquez, M. Rivera-Torrente, P. P. Paalanen, B. M. Weckhuysen. F. G. Cirujano, D. De Vos & T. De Baerdemaeker, J. Catal. **354**, 92 (2017).

42. H. A. Calderon & E. Reguera, Microsc. Microanal. **18**, 1468 (2012).

43. P. Franz, C. Ambrus, A. Hauser, D. Chernyshov, M. Hostettler, J. Hauser, L. Keller, K. Krämer, H. Stoeckli-Evans, P. Pattison, H.-B. Bürgi & S. Decurtins, J. Am. Chem. Soc. **126**, 16472 (2004).

44. D. Chernyshov & A. Bosak, Phase Trans. **83**, 115 (2010).

45. D. A. Keen & A. L. Goodwin, Nature **521**, 303 (2015).

46. T. R. Welberry & T. Weber, Cryst. Rev. **22**, 2 (2016).

47. T. Weber & A. Simonov, Z. Krist. **227**, 238 (2012).

48. L. Pauling. The Nature of the Chemical Bond and the Structure of Molecules and Crystals: An Introduction to Modern Structural Chemistry (Cornell University Press, Ithaca NY, 1960).

49. M. Paściak, T. R. Welberry, J. Kulda, M. Kempa & J. Hlinka, Phys. Rev. B **85**, 224109 (2012).

50. P. D. Battle, S. I. Evers, E. C. Hunter & M. Westwood, Inorg. Chem. **52**, 6648 (2013).

51. H. Zhdanov, C. R. Acad. Sci. URSS **31**, 352 (1941).

52. E. Shugam & H. Zhdanov, Acta Physiochim. URSS **20**, 247 (1945).

53. C. P. Krap, B. Zamora, L. Reguera & E. Reguera, Micro. Meso. Mater. **120**, 414 (2009).

54. P. C. Carman, Flow of Gases Through Porous Media (Butterworths, London, 1956).

55. J. Bear, Dynamics of Fluids in Porous Media (Dover, New York, 1988).

56. J. H. van der Linden, G. A. Narsilio & A. Tordesillas, Phys. Rev. E **94**, 022904 (2016).

57. N. Epstein, Chem. Eng. Sci. **44**, 777 (1989).

58. Z. Fang, B. Bueken, D. E. De Vos & R. A. Fischer, Angew. Chem. Int. Ed. **54**, 7234 (2015).

59. T. Zhang, S. Jin, Y. Gu, Y. He, M. Li, Y. Li & H. Fan, IUCrJ **2**, 322 (2015).

60. Y. Yun, X. Zou, S. Hovmöller & W. Wan, IUCrJ **2**, 267 (2015).

61. D. O. Ojwang, J. Grins, D. Wardecki, M. Valvo, V. Renman, L. Häggström, T. Ericsson, T. Gustafsson, A. Mahmoud, R. P. Hermann & G. Svensson, Inorg. Chem. **55**, 5924 (2016).

62. M. J. Cliffe, W. Wan, X. Zou, P. A. Chater, A. K. Kleppe, M. G. Tucker, H. Wilhelm, N. P. Funnell, F.-X. Coudert & A. L. Goodwin, Nature Commun. **5**, 4176 (2014).

63. G. Brunklaus, H. Koller & S. I. Zones, Angew. Chem. Int. Ed. **55**, 14459 (2016).

64. W. Kabsch, Acta Cryst. D**66**, 125 (2010).

65. https://github.com/aglie/meerkat

66. A. Simonov, T. Weber & W. Steurer, J. Appl. Cryst. **47**, 2011 (2014).

67. T. Weber & A. Simonov, Z. Krist. **227**, 238 (2012).

68. R. H. Blessing, J. Appl. Cryst. **30**, 421 (1997).

69. A. Simonov, T. Weber & W. Steurer, J. Appl. Cryst. **47**, 1146 (2014).

70. D. J. Earl & M. W. Deem, Phys. Chem. Chem .Phys. **7**, 3910 (2005).

71. T. F. Willems, C. H. Rycroft, M. Kazi, J. C. Meza & M. Haranczyk, Micro. Meso. Mater. **149**, 134 (2012).

Acknowledgements

A.S., C.S.C. and A.L.G gratefully acknowledge financial support from the Leverhulme Trust U.K. (Grant No. RPG-2015-292), and T.D.B. acknowledges F.W.O.–Vlaanderen (Research Foundation Flanders) for a Postdoctoral Fellowship. A.L.G. thanks the European Research Council for funding (Grant. No. 279705) and P. D. Battle (Oxford) for valuable discussions.

Fig. 1.

Structure of Prussian Blue and its analogues. (a) X-ray powder diffraction pattern of $Mn[Co(CN)_6]_{2/3} \cdot xH_2O$ ($\equiv$ Mn[Co]), which is typical of that of most PBAs and even of PB itself. (b) The parent structure type (left) consists of interpenetrating f.c.c. arrays of M and M′ cations (pink and blue spheres, repsectively), bridged by cyanide ions (black rods). In Prussian Blue (centre), one quarter of the M′ sites are vacant, creating isolated micropores (green spheres). The M-cation coordination sites directed at these pores are typically occupied by bound H_2O, and additional water molecules occupy the centres of the micropores. In PBAs with composition $M[M'(CN)_6]_{2/3} \cdot xH_2O$ (right), another 1/12 of M′ sites are vacant. There are now too many vacancies for each micropore to remain isolated; instead neighbouring pores must connect (dark green collars) to give an extended micropore network. The characteristics of this network depends on the degree and nature of vacancy correlations.

Fig. 2.

Experimental structured diffuse scattering from Prussian Blue analogues. The experimental X-ray diffraction patterns of single-crystal PBA samples contain highly structured diffuse scattering, the form of which is strongly sample- and chemistry-dependent. Reconstructed $(hk0)$ scattering planes are shown here for eight PBA samples ($-6 < |h|, |k| < 6$). We include data for two samples with the same nominal composition Mn[Co(CN)$_6$]$_{2/3} \cdot x$H$_2$O but prepared using two different diffusion rates: the Mn[Co]$'$ crystal was grown more quickly than Mn[Co]. Also included are the data reported in Ref. 44 for Mn[Mn]. At the bottom-right corner of each panel we show the corresponding scattering-plane-averaged diffuse scattering pattern. Note the fundamental difference in information content of these single-crystal data relative to PXRD traces of the same materials [*cf.* Fig. 1(a)].

Fig. 3.

Monte Carlo simulation results and vacancy polymorph phase diagram. (a) Map of diffuse scattering calculated from MC configurations performed at a range of J', T' values. Superimposed on the map are the experimental plane-averaged diffuse scattering patterns of Fig. 2, positioned according to the best qualitative match in form of the scattering pattern. (b) Distribution of experimental PBA samples in J', T' space (left) and partitioning of the diffuse scattering map into regions of distinct vacancy polymorphs (I–VI). The vertical red line represents a hidden morphotropic phase boundary. (c) Centrosymmetric and acentric M-site coordination geometries favoured at low and high values of J', respectively (green spheres indicate M′ vacancies). The acentric coordination geometry allows migration of the M-site cation towards a pseudo-tetrahedral site (pink arrow). (d) Thermodynamic and micropore network characteristics of the J', T'-dependent MC simulations: (clockwise from top-left) normalised MC energy per formula unit E'; MC energy gradient $\log(\frac{\Delta E}{\Delta T})$; anisotropy $\sigma = \sum(I - \hat{I})^2$, where I and $\hat{I}$ are the diffuse scattering intensities respectively before and after inclusion of $m\bar{3}m$ Laue symmetry; diffuse scattering localisation $L = \frac{\sum I^2}{(\sum I)^2}$ which acts as a measure of degree of local vacancy order; fraction of surface-accessible vacancies x_{acc}; conductance C; number of vacancy-neighbour pairs per formula unit ρ; and tortuosity τ. The phase space represented by each panel corresponds to that shown in (a). Phase boundaries are shown as guides to the eye.

Fig. 4.

Real-space description of micropore network structures. (a) Representative micropore network structures for each polymorph. Only connected vacancies within a representative MC configuration are shown, and colour (red–blue) is used to illustrate computed transport rate along a common crystal axis (left–right). Polymorph II is clearly biphasic; the left-hand component (one third of the MC simulation box) has a vacancy fraction of 50%, with vacancies forming planar sheets, and the right-hand component (two thirds of the MC box) has the ordered Prussian Blue structure with 25% vacancies. The micropore network of this polymorph does not percolate along the transport axis; hence colour is used to denote independent pore structures. Polymorph VI contains one-dimensional pore channels that are not cross-linked (see inset). (b) A "ladder vacancy" fragment as described in the text. (c) The experimental 3D-ΔPDF $g(\mathbf{r})$ for Co[Co], which is representative of that for all PBAs studied here. The strongest and longest-range correlations lie along the cartesian axes (shaded), as expected for the ladder vacancy motif. (d) In the collapsed (rhombohedral) polymorph of Zn[Co], distorted vacancies also adopt ladder-type arrangements (see inset) that form intersecting columns related by the threefold rotation axes of the rhombohedral cell (*53*). The degree of related vacancy order in cubic Zn[Co] (*i.e.* with higher catalytic activity) likely influences its propensity to undergo structural collapse to this rhombohedral form on dehydration.

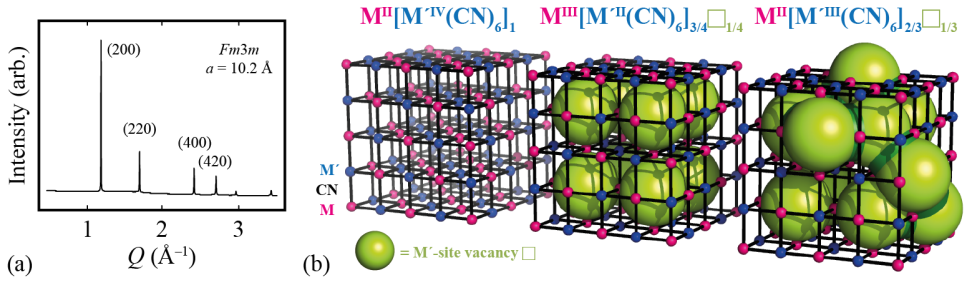

Intensity (arb.)
(200)
Fm3m
a = 10.2 Å
(220)
(400)
(420)
1
2
3
Q (Å⁻¹)
(a)
(b)
M´
CN
M
= M´-site vacancy □

FIGURE 1

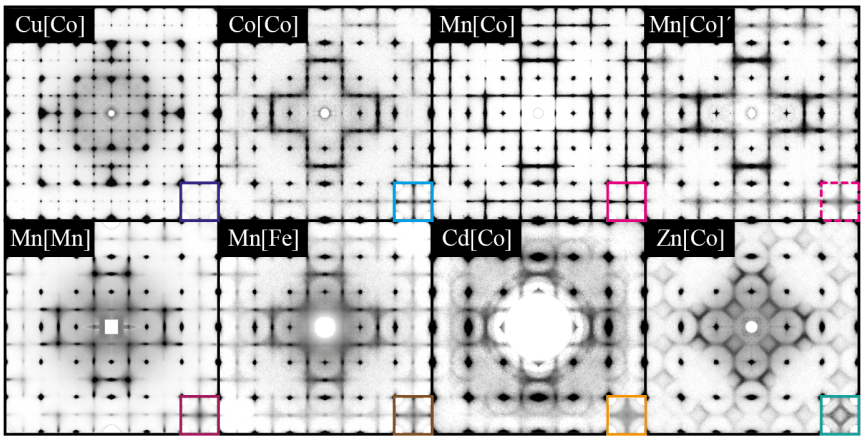


FIGURE 2

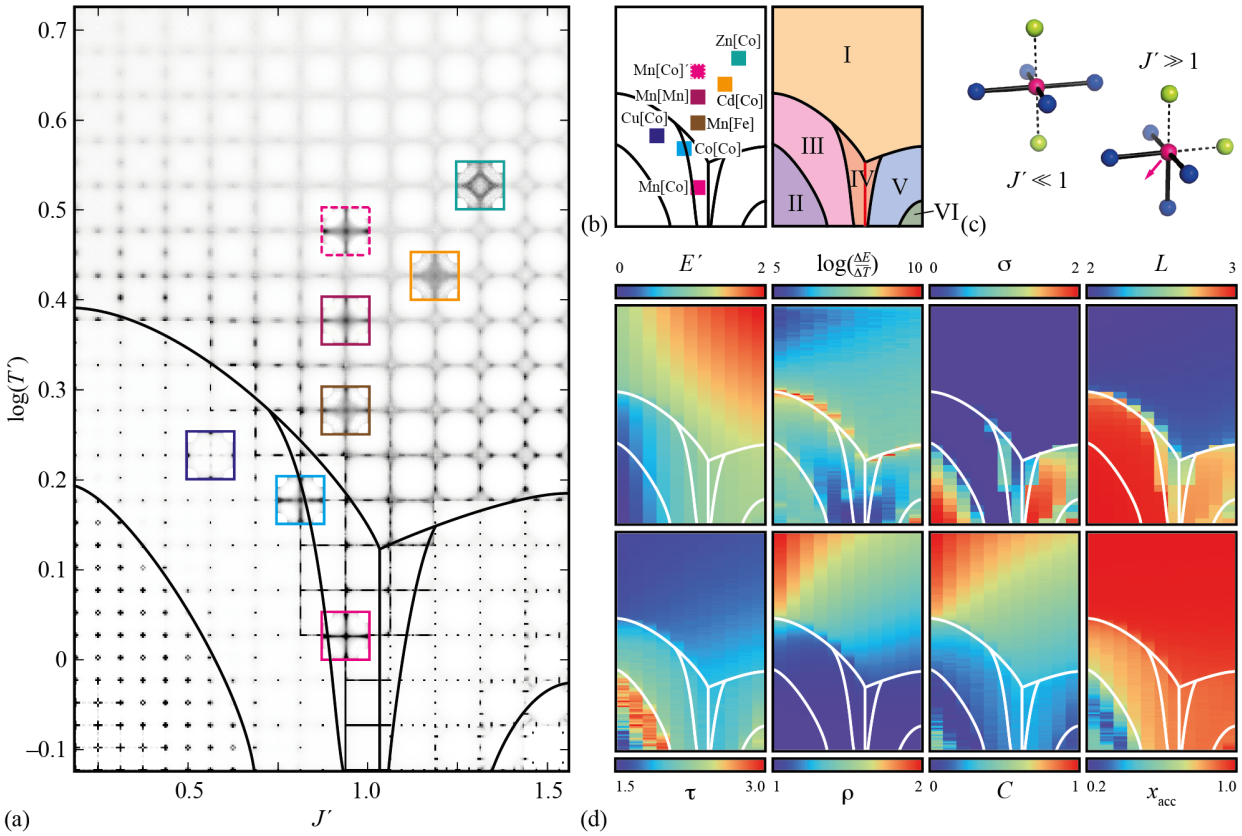

(a)
log(T′)
J′
0.7
0.6
0.5
0.4
0.3
0.2
0.1
0
−0.1
0.5
1.0
1.5
(b)
Zn[Co]
Mn[Co]′
Mn[Mn]
Cd[Co]
Cu[Co]
Mn[Fe]
Co[Co]
Mn[Co]
I
II
III
IV
V
VI
(c)
J′ ≫ 1
J′ ≪ 1
(d)
E′
log(ΔE/ΔT)
σ
L
τ
ρ
C
x_acc

FIGURE 3

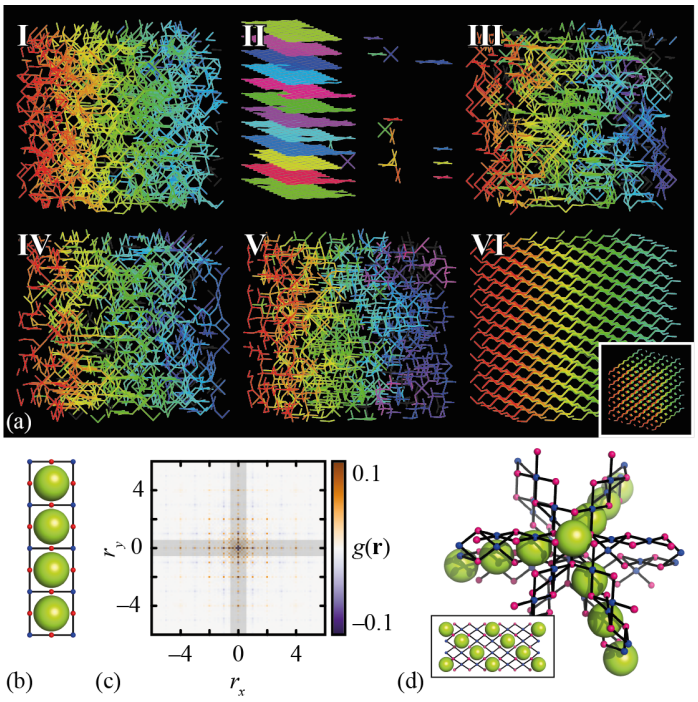


FIGURE 4

Appendix E

Table E0.1: Distortions of molecular perovskites and their corresponding irreps in both settings of the perovskite unit cell. The space group for a given order parameter direction (OPD) is also shown.

Distortion	Origin at A	Origin at B	Space group (OPD)
Symmetric strain	Γ_1^+	Γ_1^+	$Pm\bar{3}m$ (a)
Tetragonal strain	Γ_3^+	Γ_3^+	$P4/mmm$ (a,0)
Unconventional tilt	Γ_4^+	Γ_4^+	$P4/m$ (a,0,0)
Orthorhombic strain	Γ_5^+	Γ_5^+	$Cmmm$ (a,0,0)
Acoustic polar mode	Γ_4^-	Γ_4^-	$P4mm$ (a,0,0)
Octahedral deformation	Γ_5^-	Γ_5^-	$P\bar{4}m2$ (a,0,0)
A-site cation order	X_1^+	X_3^-	$P4/mmm$ (a;0;0)
Octahedral deformation	X_2^+	X_4^-	$P4_2/mmc$ (a;0;0)
Columnar shift	X_5^+	X_5^-	$Pmma$ (0,a;0,0;0,0)
Unconventional tilt	X_1^-	X_3^+	$P4/mcc$ (a;0;0)
Octahedral deformation	X_2^-	X_4^+	$P4_2/mcm$ (a;0;0)
B-site cation order	X_3^-	X_1^+	$P4/mmm$ (a;0;0)
Jahn-Teller distortion	X_4^-	X_2^+	$P4_2/mmc$ (a;0;0)
Unconventional tilt	X_5^-	X_5^+	$Pmma$ (0,a;0,0;0,0)
A-site cation order	M_1^+	M_4^+	$P4/mmm$ (a;0;0)
Conventional tilt	M_2^+	M_3^+	$P4/mbm$ (a;0;0)
Jahn-Teller distortion	M_3^+	M_2^+	$P4/mbm$ (a;0;0)
B-site cation order	M_4^+	M_1^+	$P4/mmm$ (a;0;0)
Unconventional tilt	M_5^+	M_5^+	$Cmma$ (a,0;0,0;0,0)
Octahedral deformation	M_1^-	M_4^-	$P4/nbm$ (a;0;0)
Columnar shift	M_2^-	M_3^-	$P4/nmm$ (a;0;0)
A-site displacement	M_3^-	M_2^-	$P4/nmm$ (a;0;0)
Out-of-phase shift	M_5^-	M_5^-	$Pmma$ (0,0;a,a;0,0)
A-site cation order	R_1^+	R_2^-	$Fm\bar{3}m$ (a)
Octahedral deformation	R_4^+	R_5^-	$I4/mcm$ (a,0,0)
Out-of-phase shift	R_5^+	R_4^-	$I4/mmm$ (a,0,0)
B-site cation order	R_2^-	R_1^+	$Fm\bar{3}m$ (a)
Jahn-Teller distortion	R_3^-	R_3^+	$I4/mcm$ (0,a)
Octahedral deformation	R_4^-	R_5^+	$I4/mmm$ (a,0,0)
Conventional tilt	R_5^-	R_4^+	$I4/mcm$ (a,0,0)

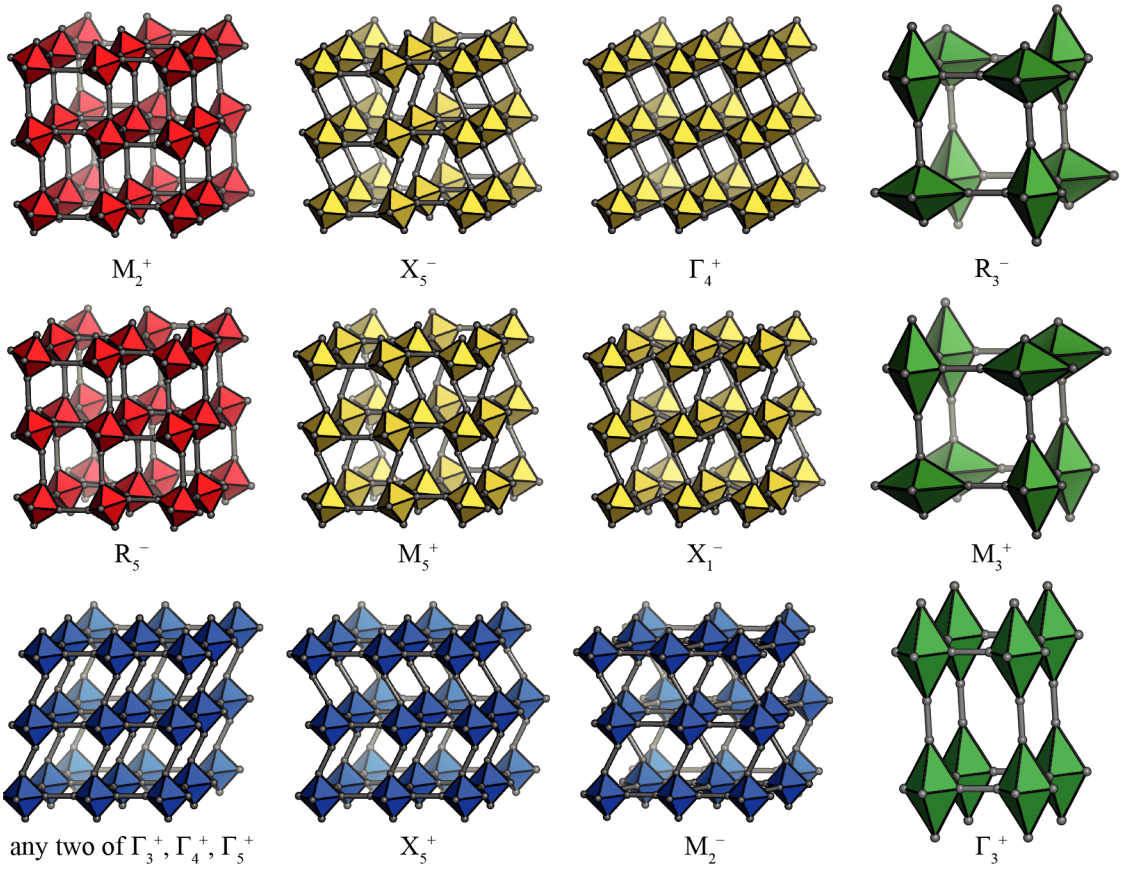


Figure E0.1: Visual representations of a selection of relevant irreps for molecular perovskites.

Table E0.2: Third-order couplings with polarisation (Γ_4^-). The coupling of one irrep from each column in a given row will generate a polar distortion, provided that crystal momentum is conserved. Coupling schemes satisfying the restrictions for the conservation of parity and crystal moments NOT listed here may still give piezoelectric space groups.

$R_{4,5}^+$	$R_{1,2,3,4,5}^-$
$R_{4,5}^-$	$R_{1,2,3,4,5}^+$
M_5^+	$M_{1,2,3,4,5}^-$
M_5^-	$M_{1,2,3,4,5}^+$
$M_{1,2}^+$	$M_{3,4}^-$
$M_{1,2}^-$	$M_{3,4}^+$
X_5^+	$X_{1,2,3,4,5}^-$
X_5^-	$X_{1,2,3,4,5}^+$
$X_{1,2}^+$	$X_{3,4}^-$
$X_{1,2}^-$	$X_{3,4}^+$

Table E0.3: Fourth-order couplings with polarisation (Γ_4^-). The coupling of one irrep from each column in a given row will generate a polar distortion, provided that crystal momentum is conserved. Coupling schemes satisfying the restrictions for the conservation of parity and crystal moments NOT listed here may still give piezoelectric space groups.

$\mathrm{X}^{+}_{1,2}$	$\mathrm{M}^{+}_{3,4,5}$	$\mathrm{R}^{-}_{1,2,3,4,5}$
$\mathrm{X}^{+}_{1,2}$	$\mathrm{M}^{-}_{3,4,5}$	$\mathrm{R}^{+}_{1,2,3,4,5}$
$\mathrm{X}^{-}_{1,2}$	$\mathrm{M}^{+}_{3,4,5}$	$\mathrm{R}^{+}_{1,2,3,4,5}$
$\mathrm{X}^{-}_{1,2}$	$\mathrm{M}^{-}_{3,4,5}$	$\mathrm{R}^{-}_{1,2,3,4,5}$
$\mathrm{X}^{+}_{3,4}$	$\mathrm{M}^{+}_{1,2,5}$	$\mathrm{R}^{-}_{1,2,3,4,5}$
$\mathrm{X}^{+}_{3,4}$	$\mathrm{M}^{-}_{1,2,5}$	$\mathrm{R}^{+}_{1,2,3,4,5}$
$\mathrm{X}^{-}_{3,4}$	$\mathrm{M}^{+}_{1,2,5}$	$\mathrm{R}^{+}_{1,2,3,4,5}$
$\mathrm{X}^{-}_{3,4}$	$\mathrm{M}^{-}_{1,2,5}$	$\mathrm{R}^{-}_{1,2,3,4,5}$
X^{+}_{5}	$\mathrm{M}^{+}_{1,2,3,4,5}$	$\mathrm{R}^{-}_{1,2,3,4,5}$
X^{+}_{5}	$\mathrm{M}^{-}_{1,2,3,4,5}$	$\mathrm{R}^{+}_{1,2,3,4,5}$
X^{-}_{5}	$\mathrm{M}^{+}_{1,2,3,4,5}$	$\mathrm{R}^{+}_{1,2,3,4,5}$
X^{-}_{5}	$\mathrm{M}^{-}_{1,2,3,4,5}$	$\mathrm{R}^{-}_{1,2,3,4,5}$
$\mathrm{X}^{+}_{1,2,3,4,5}$	$\mathrm{M}^{+}_{1,2,3,4,5}$	$\mathrm{R}^{-}_{4,5}$
$\mathrm{X}^{+}_{1,2,3,4,5}$	$\mathrm{M}^{-}_{1,2,3,4,5}$	$\mathrm{R}^{+}_{4,5}$
$\mathrm{X}^{-}_{1,2,3,4,5}$	$\mathrm{M}^{+}_{1,2,3,4,5}$	$\mathrm{R}^{+}_{4,5}$
$\mathrm{X}^{-}_{1,2,3,4,5}$	$\mathrm{M}^{-}_{1,2,3,4,5}$	$\mathrm{R}^{-}_{4,5}$